

**Dual-Polarization
Weather Radar Handbook**
2nd Edition



**Dual-Polarization
Weather Radar Handbook**

Preface to the First Edition

This first edition of the "*Dual Polarization Weather Radar Handbook*" is a major revision of Bringi, V.N., Thurai, M., Hanesen, R.: "*Improved Dual Polarization Radar Applications*", AMS – Gematronik GmbH, Neuss, Germany, 2004. We decided to change the title because the new one reflects the scope of the book much better. The *Handbook* is intended to become a useful tool in the hands of radar meteorologists who are planning to purchase or who are already operating a polarimetric Doppler radar. Such a radar is a quite sophisticated measurement tool. In order to take full advantage of its capabilities a detailed knowledge of its operating principles is required. Until today only one textbook is available which is fully dedicated to dual polarization radars: Bringi, V.N., Chandrasekar, V.: "*Polarimetric Doppler Weather Radar*", Cambridge University Press, Cambridge, UK, 2001. Although this book also covers operational aspects its focus is on the theory and on the current state of polarimetric weather radar research. The book is a valuable resource for a lot of topics treated in the *Handbook* and we strongly recommend to use this book for the investigation of details which are not covered by the *Handbook*.

The *Handbook* tries to make the principle of polarimetric weather radar operation understandable by applying a minimum on theory and a maximum of explanations. Its focus is on important aspects of the technology and of the daily operation of dual polarization radars rather than on the underlying physics. Because it will be permanently improved and supplemented we appreciate all suggestions from operators of polarimetric weather radars and from those who are planning to operate such a radar.

In comparison to "*Improved Dual Polarization Radar Applications*", we have in the *Handbook* improved the description of the polarimetric radar theory and have added several algorithm examples for the classification of radar echo types. Furthermore, the appendix was extended by a list of symbols and acronyms.

August 2005
Neuss, Germany
V.N. Bringi, M. Thurai, R. Hanesen

Preface to the Second Edition

Since the release of the first edition of the "*Dual Polarization Weather Radar Handbook*" in 2005, research has heavily continued to improve algorithms on the measurements of weather radar data. In particular, dual-polarization based algorithms for precipitation classification have been investigated for C-band and, beginning more recently, also for X-band radars. The results are promising for all radar bands (though yet rather preliminary for X-band).

As a consequence of this, we have significantly extended Chapter 7 about radar echo and precipitation classification. The sections for S-band algorithms, which had already been available in the first edition, were slightly revised and extended. A section on the identification of chaff was added. Furthermore, several new Sections about precipitation classification for C-band and for X-band radars have been added. Several typing errors have been removed. This new reference will support all users of polarimetric radars. Also, it contains valuable information for those who do not yet but are planning to benefit from the advantages of polarimetric radar systems.

July 2007

Neuss, Germany

V.N. Bringi, M. Thurai, R. Hanesen

Contents

1	Introduction	1
2	Polarimetric Radar Theory	7
2.1	Scatter cross-section of water drops	8
2.1.1	Spherical drops	8
2.1.2	Non-spherical drops	10
2.2	Drop size distribution (dsd) in rain	11
2.3	Drop shapes	15
2.4	Polarimetric radar observables	17
2.4.1	Co-polar and differential reflectivity	17
2.4.2	Cross-polar reflectivity and linear depolarization ratio	20
2.4.3	Differential propagation phase and specific differential phase	21
2.4.4	Correlation coefficient ρ_{co}	22
2.5	Other (secondary) polarimetric radar observables	23
2.5.1	Back scatter differential phase	23
2.5.2	Co-cross-polar correlation	23
2.6	Summary of applications of the polarization radar observables	25
3	Processing the Differential Propagation Phase	27
3.1	General considerations	27
3.2	The iterative filtering technique	28
3.2.1	Φ_{dp} unwrapping	30
3.2.2	'Good data' mask application	30
3.2.3	FIR Filtering	32
3.2.4	K_{dp} calculation	35
3.3	A simple smoothing technique	36
3.4	Other techniques	37
4	Correcting the Measured Reflectivity for Rain Attenuation	39
4.1	The linear Φ_{dp} method	41
4.2	The standard ZPHI method	42
4.3	I-ZPHI: The iterative ZPHI method for C and X-band radars	44
5	Correcting the Measured Z_{dr} for Differential Attenuation due to Rain	51
5.1	The linear Φ_{dp} method	51
5.2	The A_h -scaled method	54
6	Rainfall Estimation	57
6.1	Areal Φ_{dp} method	58
6.1.1	The CSU-algorithm	58
6.1.2	The RZF-algorithm	61
6.1.3	A case study	61
6.2	Higher resolution method for C and X-band radars	68
6.3	Rainfall estimation for S-band radars	72
6.3.1	The (prototype) NEXRAD DP-rain algorithm	72
6.3.2	Other algorithms	73

7	Precipitation Classification	77
7.1	Fuzzy logic schemes	78
7.2	The WSR-88D classification for S-band radar – an overview	83
7.3	Discrimination between meteorological and non-meteorological echoes – algorithms for S-band	84
7.3.1	Version 1 of the prototype WSR-88D algorithm.....	84
7.3.2	Identification of sea clutter.....	89
7.3.3	Identification of chaff.....	93
7.4	Classification between hydrometeor types – algorithms for S-band	95
7.4.1	Classification for ‘warm season’	95
7.4.2	Classification for ‘cold season’	101
7.4.3	The HDR method and combined HDR-LDR methods	107
7.5	Echo classification algorithms for C-band – an overview	109
7.6	Discrimination between meteorological and non-meteorological echoes – algorithms for C-band	116
7.6.1	The MeteoFrance approach	116
7.6.2	Identification of sea clutter at C-band	120
7.6.3	Identification of chaff.....	123
7.7	Classification between hydrometeor types – algorithms for C-band using fuzzy logic schemes.....	123
7.7.1	The Italian operational approach using Z_h , Z_{dr} , and temperature.....	123
7.7.2	The Australian BMRC C-POL scheme	127
7.7.3	The University of Alabama ARMOR scheme	129
7.7.4	The Environment Canada approach.....	131
7.8	Classification between hydrometeor types – algorithms for C-band using non-fuzzy logic schemes.....	133
7.8.1	DLR scheme.....	133
7.8.2	The HDR method and combined HDR-LDR methods	136
7.9	Preliminary results for echo classification at X-band	138
7.9.1	Classification between meteorological and non-meteorological echoes and identification of sea clutter	138
7.9.2	Recent research on hydrometeor classification	141
8	APPENDIX A – Iterative Φ_{dp} Filtering	145
9	APPENDIX B – List of Symbols and Acronyms	151
10	References	155
11	About the Authors	163

Dual-Polarization Weather Radar Handbook

An Overview of Dual-Polarization Weather Radar: Theory and applications

2nd Edition

V.N. Bringi¹, M. Thurai¹, and R. Hanesen²

1 Introduction

The electromagnetic wave is characterized by its amplitude, frequency and polarization state. When the radiated wave from the radar interacts with moving particles in the atmosphere, all three characteristics of the scattered wave change, and by monitoring this change it is possible to infer the particles' size, radial velocity, shape and orientation. The earliest weather radars in the era of the 1950s were mainly used to measure the back scatter power at a single polarization state. During the 1960-70s, the Doppler shift principle was used to measure the radial velocity of hydrometeors in addition to the back scattered power but still at a single polarization state.

By the mid-1970s, it was recognized that Doppler radar would be of great importance for operational applications. In the late 1980s, the deployment of Doppler radars for operational weather forecasting accelerated which continues to the present time. Advances in radar hardware, signal processing and display software have made the Doppler radar the 'work horse' of most operational weather services. More recently, the assimilation of the Doppler wind field into high resolution numerical model prediction has gained substantial momentum.

Prior to the early 70s there was limited research in dual-polarized radars for weather applications, the measurements being limited by the poor cross polar performance of the radar hardware, particularly the antenna/feed. The modern era of polarimetric radar using precision microwave hardware began with the Canadian work (McCormick and Hendry, 1979) starting in the late 60s-early 70s using dual-circular polarization techniques for propagation research (Ka and X-bands) and hail detection (at S-band). The Canadian work clearly showed that oblate rain drops formed a highly oriented medium and that the differential propagation phase and differential attenuation between the horizontal and vertical polarizations through such a medium could be measured at Ka and S-bands using circular polarization techniques without the need for Doppler processing (Hendry et al., 1976).

The use of dual-linear polarizations at horizontal and vertical states was proposed in the late 70s primarily because at low elevation angles these states are aligned along the principal axes of the highly oriented oblate rain medium (Seliga and Bringi, 1976,

¹ Consultants to Selex–Gemtronik

² Selex–Gemtronik

1978). The radiated polarization was alternately switched between horizontal and vertical states at the pulse repetition frequency using high power mechanical or ferrite switches; reception was via a single receiver which was configured to alternately receive the H or V returns (first implemented in the U.K. ; see Hall et al., 1980). Such a scheme enabled the accurate measurement of the reflectivities at H and V polarizations and the resulting differential reflectivity (Z_{dr}). This development rapidly led the way to detection of the melting level where non-spherical ice melted to form highly oriented oblate raindrops, hail detection, determination of the parameters of the raindrop size distribution and improved estimation of rainfall (Bringi et al 1984; Hall et al., 1984). Subsequently, several S-band Doppler radars in the US were similarly modified for dual-polarization measurements which enabled the estimation of differential propagation phase between the H and V polarizations as well as the correlation coefficient between the two signal returns (Sachidananda and Zrnić, 1986).

While most research systems use high power switches with a single transmitter or use dual-transmitters to allow for dual-polarization operation, this design was abandoned mainly because of technical and logistic problems with high power switches. The current design for dual-linear polarization offered by most manufacturers follows the NEXRAD prototype which involves transmission of slant 45 linear polarization with simultaneous reception of the H and V components of the back scattered signal via two matched receivers (originally proposed by Seliga and Bringi 1976; Doviak et al 2000). The transmitter power is split equally into two channels by a precision power divider and then applied to the two ports of a dual-linear polarized horn/OMT. The radiated state may not be pure slant 45 deg but can be any elliptical state with equal powers in the H and V components. In this configuration the sensitivity in any one receiving channel is reduced by 3 dB as compared with transmitting the full power at one polarization state. However, the dual-polarized operation is fully compatible with Doppler processing, clutter filtering and range-velocity ambiguity mitigation methods used in the current (single-polarized) Doppler radar systems.

The results achieved with this design are so promising that also other weather services are showing an increasing interest in this technology. Selex-Gemtronik has responded to this demand with the development of a new signal processor, the GDRX. In its standard configuration it features all channels required for fully polarimetric operation, making upgrades from Doppler to polarimetric data acquisition easy. The GDRX is accompanied by a new analog receiver, which is based on MMIC (monolithic microwave integrated circuit) technology in order to increase the performance and to compensate the cost for the additional receiver channel. This technology is also perfectly suited for the upgrade of legacy weather radars. The receiver/digital receiver system is so compact that it can be easily installed together with the necessary waveguide circuit behind the antenna reflector, without any modifications of the pedestal waveguide circuit. This design was first proposed by SIGMET Inc. (SIGMET, 2001).

The benefit of S-band dual-polarization radars for operational use has been investigated by the National Severe Storms Laboratory using their prototype WSR-88D radar during an extensive field campaign in Norman, Oklahoma during 2002-2003 (Ryzhkov et al., 2005a). It was shown that dual-polarized radars offer significant

advantages over single polarized Doppler radars in (a) improving data quality (distinguishing meteorological echoes from non-meteorological echoes such as clutter/AP and birds/insects), (b) classification of hydrometeor types using fuzzy logic methods, and (c) improvement of rainfall estimation over conventional Z-R relations. These advantages formed the basis for recommending the upgrade of the WSR-88D network for dual-polarization in the next few years. Fig. 1.1 illustrates the progression of the weather radar technology over the past six decades in the US.

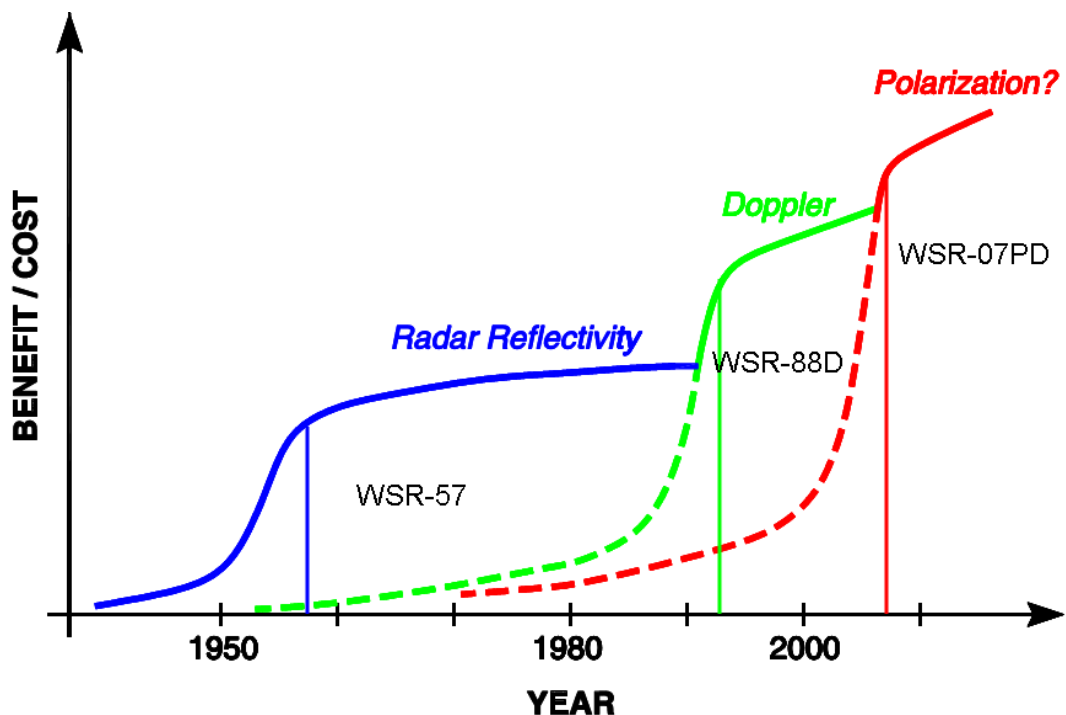


Fig. 1.1: US operational weather radar technological progression over the years.
Courtesy of Dusan Zrnić, NSSL, US.

In Europe, substantial research in dual-polarization techniques was conducted during the 1980s and 90s, for example in the UK (Goddard et al 1994), Germany (Schroth et al 1988), Italy (Guili et al., 1991), France (Pointin et al., 1988) and Austria (Randeu and Riedler, 1985). Later, the evaluation of C-band dual-polarized radars by the European operational weather agencies begun. Very recently, also X-band dual-polarized radars are integrated. Some examples are:

- (a) in France, a C-band dual-polarized radar built for MeteoFrance by Selex-Gemtronik, has been evaluated (Parent du Chatelet et al., 2004, Gourley et al., 2006). Another Dual-Polarization radar, but S-band, will be installed in 2008.
- (b) In the U.K., the Met Office and the Environment Agency have installed a C-band dual-polarized radar in Kent primarily for hydrological application.
- (c) The German Weather Service has also contracted with Selex-Gemtronik for upgrading one of their research C-band Doppler for dual-polarized capability.

- (d) The University of Helsinki has acquired a new C-band dual-polarized radar for research primarily in winter storms. Two radars of this type will be installed in Estonia in 2008.
- (e) Italy, which has a long tradition in regard to polarimetric weather radar research and operation, with the GPM-500C by Alenia/SMA being the first operational polarimetric Doppler weather radar in the world. Regione Piemonte received two modern polarimetric radars from Selex-Gemtronik. Currently most of the GPM-500C radars are upgraded. In 2006 Selex-Gemtronik started to build up a completely new Doppler weather radar network in Italy, with at least two fully polarimetric systems integrated in the network. Another existing Gemtronik radar of Regione Piemonte is going to be upgraded to a polarimetric system by end of 2007.
- (f) In Italy, Regione Piemonte recently also received a Selex-Gemtronik X-band polarimetric weather radar. Four more radars of this type are going to be delivered to the Italian Civil Protection Department (DPC).
- (g) Serbia, which applies a Selex-Gemtronik S-band polarimetric weather radar for hail detection and seeding.
- (h) Spain, which installed in 2005 a Selex-Gemtronik C-band polarimetric weather radar for precipitation retrieval algorithms.
- (i) Slovakia and Austria also recently installed C-band polarimetric radars.

There is increasing evidence that short range X-band dual-polarized systems can find a niche in hydrological application such as monitoring a small watershed or for urban hydrology, or as ‘gap filler’ radars in national networks. The application of polarimetric radar data allows to overcome a fundamental problem of X-band radars: the accurate attenuation correction. For example, the dual-polarized radar system (MP-X) operated by the National Research Institute for Earth Science and Disaster Prevention (NIED) in Japan is being used in a three-year semi-operational evaluation for rainfall estimation near the Tokyo area since 2003 (Maki et al 2005). The “Hydro” dual-polarized X-band system operated by the National Oceanic and Atmospheric Administration (NOAA) in the U.S. has already been successfully used for rainfall estimation in several different climatic regimes (Matrosov et al 2002). In France, the “Hydrix” X-band dual-polarized radar was evaluated for rainfall estimation (Le Bouar et al 2005). There is now little doubt that correction of the measured reflectivity due to rain attenuation at C and X-bands using the differential propagation phase data would by itself justify the added cost of dual-polarization at these frequencies, without even considering the other advantages such as improving data quality or hydrometeor classification. Selex-Gemtronik has developed the METEOR 50DX polarimetric X-band Doppler weather radar system as a product for this emerging market. The METEOR 50DX is an extremely compact design which can be quickly installed at almost any radar site as well as on mobile platforms.

The anticipated demand for operational dual-polarized radars at S, C and X-bands is expected to be strong in the next years as weather agencies seek to replace or enhance their existing Doppler radars with dual-polarization. There is also the beginnings of interest from the broadcast meteorological services, for example by local TV stations, for improved severe weather warnings. For these reasons, Selex-Gemtronik offers dual-polarized systems at the three frequencies as well as offering standard Doppler systems which can be made ‘dual-pol’ prepared for future upgrades. This Handbook comes at an opportune time for describing the basic theory

and the recent advances in dual-polarization radar for the non-expert in a self-contained format. It is clear that substantial algorithm development will be needed to generate useful products for the weather forecaster especially at the C and X-bands. Selex-Gemtronik anticipates that the Handbook continues to be a ‘living’ document in that it will be updated as new techniques and results become available in the future.

This Handbook is organized as follows. Chapter 2 gives an overview of dual-polarized radar theory and defines all the important measurables including a table of their applications and advantages. Chapter 3 deals with techniques for processing the differential propagation phase data to arrive at the specific differential phase (K_{dp}) which is an important measure of rain intensity. Chapter 4 describes the correction of the measured reflectivity for rain attenuation especially at C and X-bands using the measured differential propagation phase. In similar fashion, Chapter 5 deals with correcting the measured differential reflectivity (Z_{dr}) for rain attenuation. Chapter 6 describes improvements in rainfall estimation afforded by dual-polarization at S, C and X-bands along with examples. Chapter 7 deals with hydrometeor classification using fuzzy logic schemes which is an important operational application. Algorithms are presented for all three radar bands, i.e. S, C, and X-band. Appendix A gives details of an iterative filtering technique for differential propagation phase that is useful at C and X-bands. Appendix B contains a list of symbols and abbreviations/acronyms used. Finally, the references are included for proper citation of the original sources used in this Handbook, and for the reader seeking greater details than can be given herein.

A number of colleagues have graciously provided their original figures for inclusion in this Handbook: Dr Masayuki Maki of NIED, Japan; Dr Thomas Keenan of BMRC, Melbourne, Australia; Drs. Alexander Ryzhkov and Terry Schuur of NSSL, Norman, Oklahoma; and, Dr John Goddard of RAL, U.K.

A variety of figures have been obtained or adapted from Journals and Conference Proceedings of the American Meteorological Society, as can be obtained from the source given in the respective figure captions. The copyright of such figures is by American Meteorological Society and/or by the respective authors.

2 Polarimetric Radar Theory

All weather radars, conventional or otherwise, make use of the radar-range equation in order to obtain the reflectivity from an ensemble of scatterers distributed within the radar pulse volume. For a pulsed radar system, of pulse duration τ_0 , the received power from the pulse volume at a distance r_0 (see Fig. 2.1) is given by:

$$\bar{P}_r(r_0) = \frac{c\tau_0}{2} \frac{P_t G_0^2}{\lambda^2 (4\pi)^3} \frac{\pi \theta_1 \varphi_1}{8 \ln 2} \frac{\pi^5 |K_w|^2}{r_0^2} Z_e(r_0) \quad (2.1)$$

where P_t is the transmit power, G_0 is the radar antenna gain, c is the speed of light and θ_1 and φ_1 are the antenna beamwidths in the azimuth and elevation planes. The factor K_W depends on the dielectric constant of water at the radar frequency. The received power as a function of range can therefore be used to derive the range profile of the equivalent radar reflectivity, $Z_e(r)$.

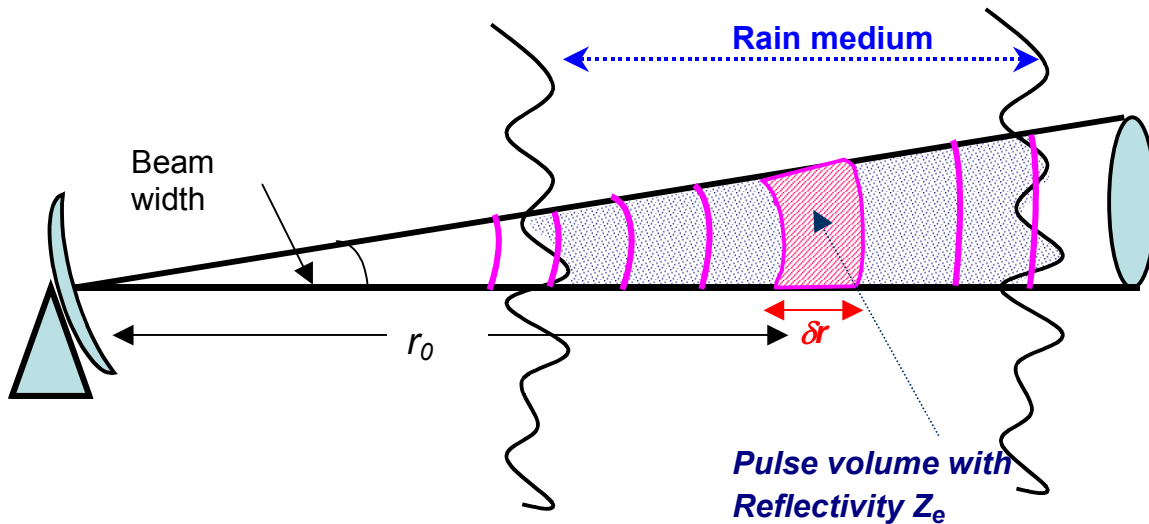


Fig. 2.1: Radar beam traversing through rain-filled medium and the reflectivity Z_e from a pulse volume at a range r_0 . The pulse volume is defined by the radar beam width and range gate interval δr .

The equivalent reflectivity factor, Z_e is the sum of contributions from all scatterers, each with its own back scatter cross-section σ . It depends not only on the distribution of the shape and size but also the type of hydrometeors present within the pulse volume. Assuming all hydrometeors are rain drops, one could relate the radar reflectivity to the rainfall rate, provided we make some assumption about the drop size distribution.

2.1 Scatter cross-section of water drops

2.1.1 Spherical drops

In the case of spherical water drops with diameters which are small compared with the wavelength (λ) of the incident wave, the back scatter cross section σ_b under Rayleigh approximation is given by :

$$\sigma_b = \left(\frac{\pi^5}{\lambda^4} \right) |K_w|^2 D^6 \quad (2.2)$$

which, as seen from the above equation, has a straight-forward D^6 dependence. When λ becomes more comparable to D , the solution for σ_b takes into account the higher order terms, which are calculated using the Mie theory. Fig. 2.2 shows the back scatter cross-section as a function of diameter for a spherical water drop, calculated for 0 °C, for S, C and X bands. For comparison, the corresponding Rayleigh scattering curves are included as dotted lines. At S-band, the Mie resonance effects become significant only for diameters greater than 10 mm. As expected, for C-band, the corresponding diameter is around 7 mm and for X-band, the diameter is significantly less (3 mm). Since typical drop size distributions in rain have diameters which can range up to 7 or 8 mm (in very heavy rain), the non-Rayleigh effects may need to be considered for C and X-band radars when converting measured reflectivity to rainfall rate. For comparison, Fig. 2.2 also includes ice spheres.

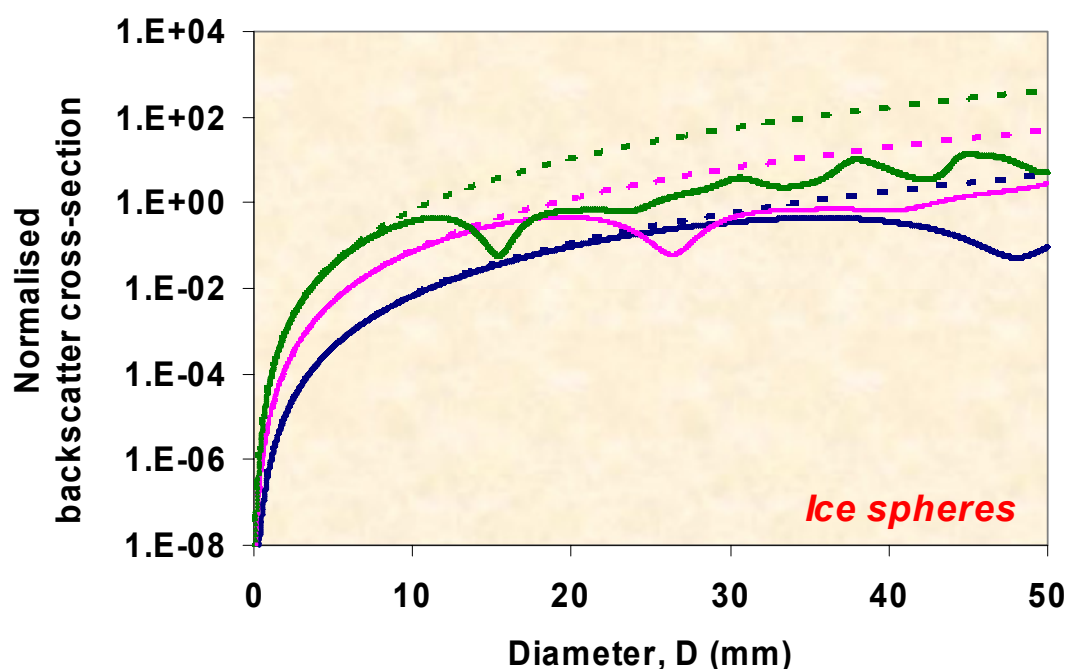
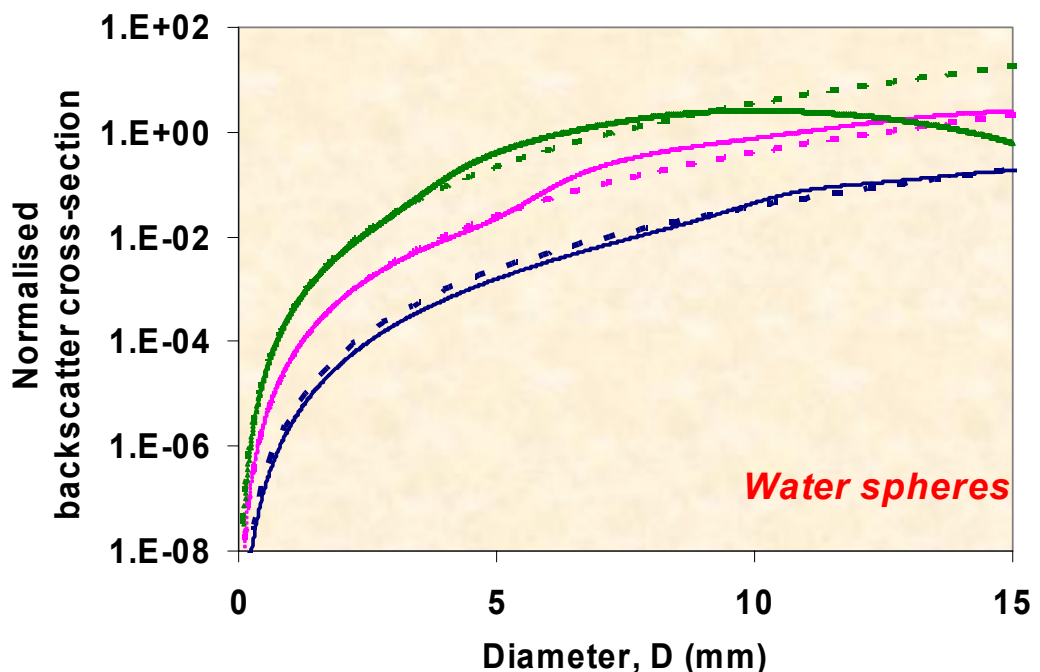


Fig. 2.2: Normalized back scatter cross-section ($= \sigma_b / \pi r^2$, r being the radius) of water spheres (top) and ice spheres (bottom) shown as solid lines at S (blue), C (magenta) and X (green) bands, from Mie solution (solid lines), compared with Rayleigh scatter cross-sections (dotted lines).

2.1.2 Non-spherical drops

In the case of the radar transmit beam having dual-linear polarization, the back scattering properties of a single scatterer is given by its scattering matrix :

$$S = \begin{bmatrix} S_{hh} & S_{hv} \\ S_{vh} & S_{vv} \end{bmatrix} \quad (2.3)$$

where h and v represent horizontal and vertical polarizations for the transmit (given by the second subscript) and the receive (given by the first subscript) signals. For a radar transmitting dual linear polarization (H and V), the elements of the scattering matrix relate the two components of the incident electric field to the back scattered electric field. For spherical drops,

$$S_{hh} = S_{vv} \quad (= S_{Sphere}) \quad (2.4)$$

and

$$S_{hv} = S_{vh} = 0 \quad (2.5)$$

and

$$\sigma_b(D) = 4\pi |S_{Sphere}(D)|^2 \quad (2.6)$$

For non-spherical drops, S_{hh} and S_{vv} will not be equal and, furthermore, S_{vh} and S_{hv} will not be zero. (Note, from reciprocity theorem, $S_{hv} = S_{vh}$, see Bringi and Chandrasekar, 2001, Section 2.2.) If we assume that every single rain drop is uniformly oriented with zero canting angle (i.e. with their axis of symmetry aligned vertically; see Fig. 2.3), then the scattering matrix will be given by:

$$S = \begin{bmatrix} S_{hh} & 0 \\ 0 & S_{vv} \end{bmatrix} \quad (2.7)$$

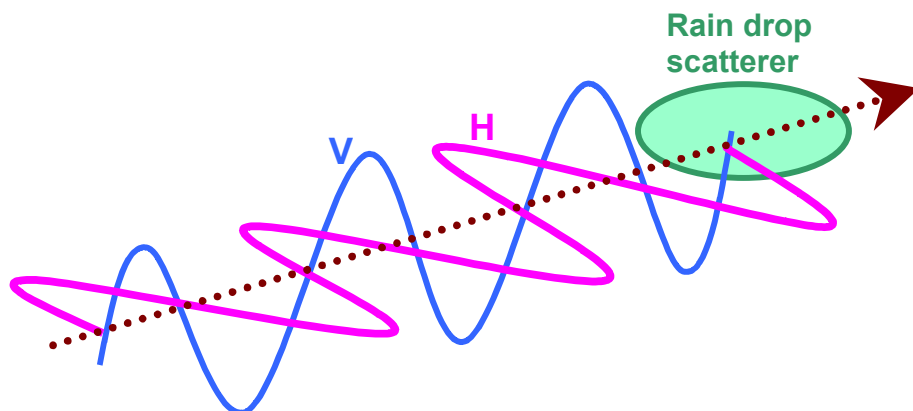


Fig. 2.3: Horizontally and vertically polarized incident waves on an oblate rain drop, Together with the direction of wave propagation.

2.2 Drop size distribution (dsd) in rain

The drop size distribution, *dsd*, is defined as the number of drops per unit volume $N(D)$ in the diameter interval D to $D + \delta D$. It is fundamental to characterizing the rain (microstructure) and to relate the integral rain parameters with each other. It is a highly variable quantity which is governed by the microphysics of rain formation and evolution.

In most cases, the *dsd* can be described, to a good approximation, by three parameter models such as the Gamma distribution. The parameters of the model are often used to relate radar reflectivity to rain rate, microwave attenuation and the liquid water content W , all of which are of practical interest. Two-parameter models are also used; these are less flexible, but still provide good fitting to natural *dsd* in a limited domain. The various ways of describing *dsds* are as follows:

- The most frequently used model is the Gamma distribution, given by,

$$N(D) = N_0 D^\mu \exp(-\Lambda D) = N_T \frac{\Lambda^{\mu+1} D^\mu}{\Gamma(\mu+1)} \exp(-\Lambda D) \quad (2.8)$$

where N_0 is the intercept parameter and Λ is related to the median diameter D_0 via the equation

$$D_0 = \frac{3.67 + \mu}{\Lambda} \quad (2.9)$$

D_0 is defined such that drops less than this value contribute to one half of the total water content. N_T is the zeroth moment which represents the number of drops per unit volume. The parameter μ (typically from -1 to 5) controls the shape of the *dsd* but is often fixed (typically $\mu = 3$) for simplicity, which makes it possible to estimate *dsd* from dual-parameter radar measurements.

- The exponential *dsd* is a special case with $\mu = 0$,

$$N(D) = N_0 \exp(-\Lambda D) = N_T \Lambda \exp(-\Lambda D) \quad (2.10)$$

with N_0 (or N_T) and Λ as the parameters defining the *dsd*.

- The Gamma *dsd* can also be normalized in a different manner (Testud et al 2001) using water content (W) as the basis for normalization rather than N_T , as follows,

$$N(D) = N_w f(\mu) \left[\frac{D}{D_m} \right]^\mu \exp \left[-(4 + \mu) \frac{D}{D_m} \right] \quad (2.11)$$

where N_w is the normalized intercept parameter given by,

$$N_w = \frac{4^4}{\pi \rho_w} \left[\frac{1000W}{D_m^4} \right] ; \quad mm^{-1} m^{-3} \quad (2.12)$$

where W is in $g m^{-3}$ and $\rho_w = 1$ is the water density in $g cm^{-3}$; D_m is the mass weighted mean diameter (in mm) defined as,

$$D_m = \frac{\int D^4 N(D) dD}{\int D^3 N(D) dD} \quad (2.13)$$

and,

$$f(\mu) = \frac{6}{4^4} \frac{(4+\mu)^{\mu+4}}{\Gamma(\mu+4)} \quad (2.14)$$

In the case of exponential distributions, the most frequently quoted dsd is the Marshall-Palmer (M-P) distribution. This is a special case where N_0 is set to 8000 $mm^{-1} m^{-3}$ and $\Lambda (mm^{-1})$ given by the power law $\Lambda = 4.1 R^{-0.21}$, where R is in $mm h^{-1}$. Inserting this power-law for Λ into the exponential dsd (equation (2.10)), and resolving for the definition of reflectivity Z as the sixth moment of dsd , yields an intrinsic M-P $Z-R$ relation of $Z = 296 R^{1.47}$. Although the M-P model is a reasonable statistical representation for certain climates, it is not applicable for all rain types.

Knowledge of the dsd enables one to relate the rainfall rate R and the specific attenuation k via the equations,

$$R = 0.6 \times 10^{-3} \pi \int v(D) N(D) D^3 dD ; \quad mm h^{-1} \quad (2.15)$$

and,

$$k = 4.343 \times 10^3 \int \sigma_{ext}(D) N(D) dD ; \quad dB km^{-1} \quad (2.16)$$

where $v(D)$ is the terminal velocity in $m s^{-1}$, D is in mm , $N(D)$ in $mm^{-1} m^{-3}$, and σ_{ext} is the extinction cross-section in m^2 . The equivalent radar reflectivity Z_e is given by,

$$Z_e = \frac{\lambda^4}{\pi^5 |K_w|^2} \int \sigma_b(D) N(D) dD ; \quad mm^6 m^{-3} \quad (2.17)$$

where σ_b is the back scatter cross-section in mm^2 , K_w is the dielectric factor of water and λ is the radar wavelength in mm .

Finally, the liquid water content W is given by,

$$W = 10^{-3} \frac{\pi \rho_w}{6} \int D^3 N(D) dD ; \quad g m^{-3} \quad (2.18)$$

For Rayleigh scattering, a power law form for $v(D)$ and normalized gamma dsd , the relationship between the reflectivity factor, Z ($= Z_e$) and R simplifies to:

$$Z = \frac{a(\mu)}{\sqrt{N_w}} R^{1.5} \quad (2.19)$$

where $a(\mu)$ is a function dependent only on μ (see Section 7.1.4 of Bringi and Chandrasekar 2001). For exponential dsd ($\mu = 0$ and $N_w = N_0 = 8000$), the above reduces to,

$$Z = 240 R^{1.5} \quad (2.20)$$

Note that this relation is different from the intrinsic M-P relation $Z = 296 R^{1.47}$, because the former assumes a power-law for the drop fall velocity. The coefficient of the $Z-R$ power law varies as a result of variations in N_w with different rain types. The exponent is also a variable quantity, and varies typically between 1.5 (for constant N_w) and 1 (for N_w varying linearly with R).

The variability of the dsd is illustrated in Fig. 2.4 in the $\log_{10}\langle N_w \rangle$ versus $\langle D_m \rangle$ plane. The cases are separated into (a) stratiform and (b) convective rain types. For case (a), the $\log_{10}\langle N_w \rangle$ shows an inverse (near-linear) relation with $\langle D_m \rangle$. For reference, two constant N_w lines are shown, one for the M-P N_w of 8000 and another for N_w of 1000. The corresponding $Z-R$ relationships reflect the different microphysics involved in stratiform rain formation, for example, the melting of large snow flakes giving rise to large rain drops as indicated by $\langle N_w \rangle = 1000$ and $\langle D_m \rangle = 1.75 \text{ mm}$ as opposed to the melting of smaller rimed ice particles (giving rise to smaller drops) indicated by $\langle N_w \rangle = 8000$ and $\langle D_m \rangle = 1.2 \text{ mm}$.

For convective rain, maritime and continental clusters can be identified in Fig. 2.4b. Maritime rain can be identified by D_m in the range 1.5-1.75 mm and N_w around $20,000 \text{ mm}^{-1} \text{ m}^{-3}$, whereas continental rain shows D_m in the range 2-2.75 mm and N_w around 2000. Both cases in Fig. 2.4 clearly show that a single $Z-R$ relationship cannot be used to estimate rainfall rates without incurring large error. For example, in convective rain, if a continental $Z-R$ relationship is incorrectly used for the maritime regime, the rainfall rate will be underestimated by at least a factor of 2. This was a real operational problem in the case of the Fort Collins, Colorado, flash flood event of 28 July 1997 when the standard NEXRAD $Z-R$ relationship ($300 R^{1.4}$) was incorrectly applied to an unusual 'maritime' type event (i.e. large concentration of small drops). Conventional operational radars routinely use gauge adjusted $Z-R$ relationships to overcome this problem but real time implementation can be difficult to achieve in practice.

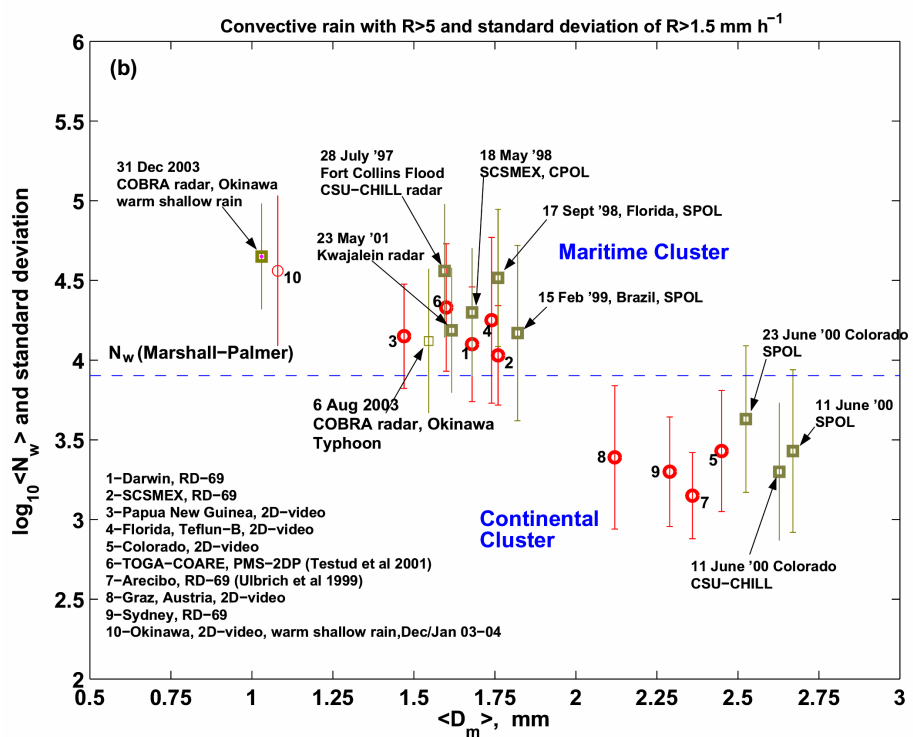
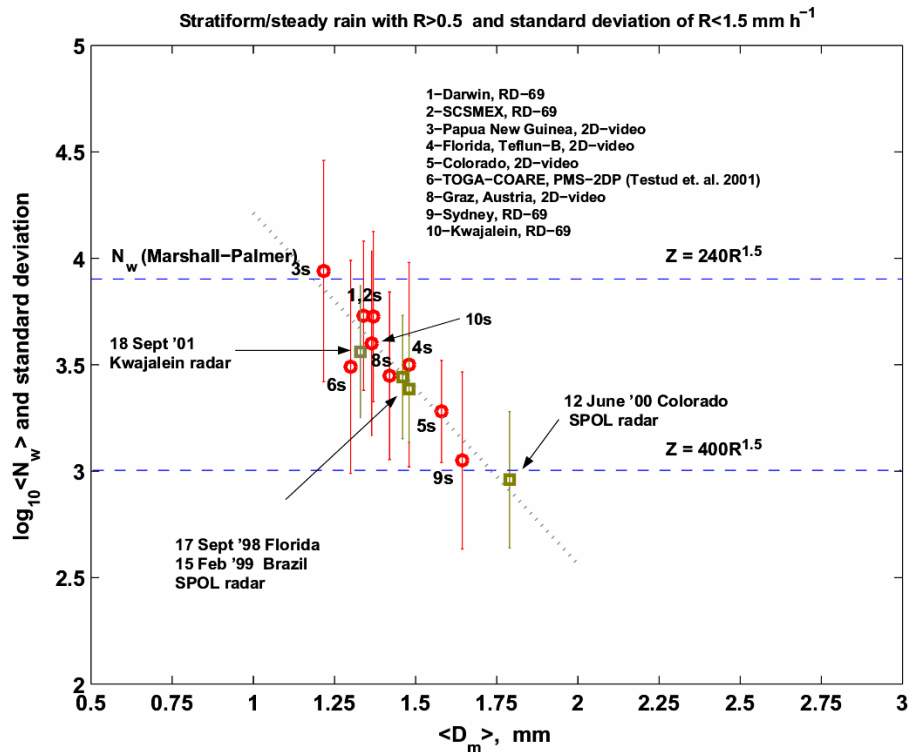


Fig. 2.4: (a) The average value of $\log_{10} N_w$ (with $\pm 1\sigma$ std dev bars) versus average D_m from disdrometer data (numbered open circles) and dual-polarization radar retrievals (open squares as marked) for stratiform rain. Dotted line is the least squares fit.
(b) As in (a) except data for convective rain. Note that N_w is the 'normalized' intercept parameter and D_m is the mass-weighted mean diameter of a 'normalized' gamma dsd .

2.3 Drop shapes

The single measure of reflectivity (Z) at one polarization (usually horizontal polarization) being dependent on both N_w and D_m can lead to large errors in the estimate of attenuation and rain rate. To overcome this problem (and as mentioned earlier in this Section), the advanced weather radars make use of the oblateness of the rain drops and its monotonic relationship with the equivalent drop diameter. Fig. 2.5a shows some of the initial work on drop shapes, derived from wind tunnel measurements of Pruppacher and Beard (1970). It shows the clear dependence of the oblateness on drop size (i.e. larger the size, more the oblateness).

Since then, many publications have appeared containing empirically derived formulas to relate the mean axis ratio to D_e . In addition, theoretical work has been done, the most quoted being the numerical model of Beard and Chuang (1987) for equilibrium shapes. The variation is shown in Fig. 2.5b. More recently, Thurai and Bringi (2005) measured the mean axis ratios of water drops falling from an 80 m bridge using a 2-dimensional video disdrometer (Randeu et al 2002, Kruger and Krajewski 2002). It was found that the drops, after reaching steady state oscillations, followed the upper bound region of the Beard and Chuang curves. This experimental curve conducted in artificial rain is also shown in Fig. 2.5b.

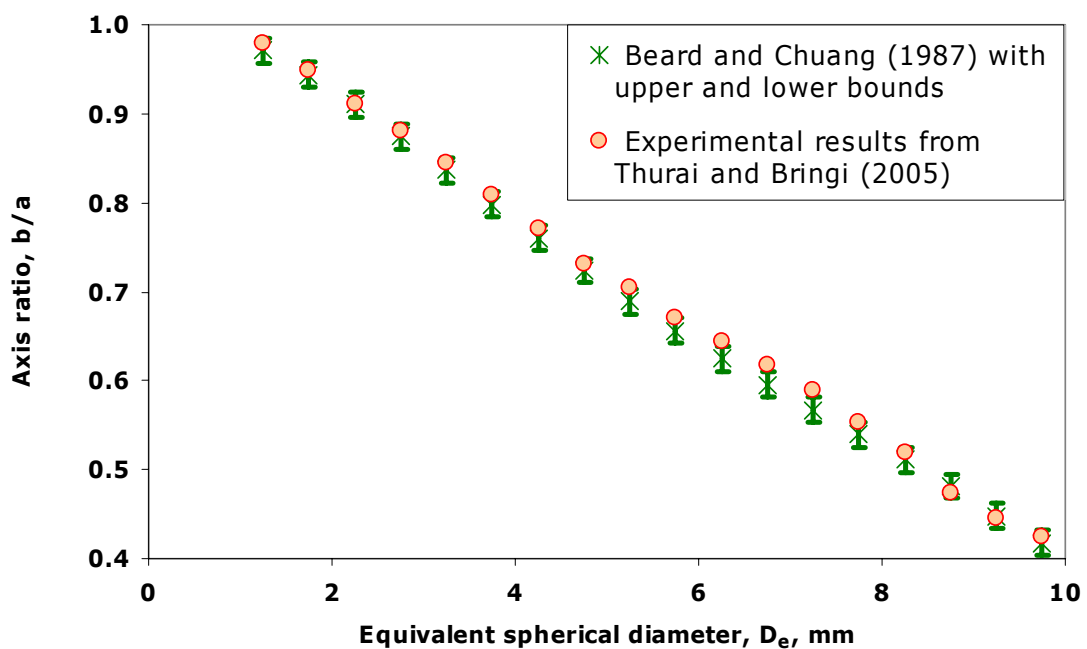
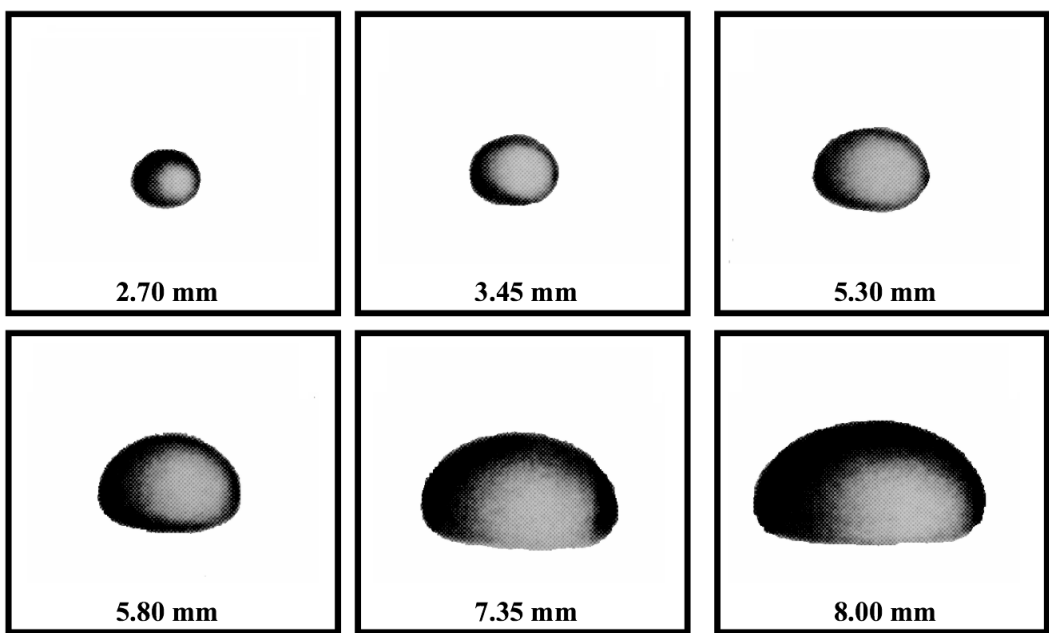


Fig. 2.5: (a) Wind tunnel measurements of drop shapes, from Pruppacher and Beard (1970), showing the oblateness dependence on drop size. Image ©copyright Royal Meteorological Society and John Wiley and Sons, Inc.

(b) Axis ratio versus equivalent spherical diameter from a fit to the numerical model of Beard and Chuang (1987) for equilibrium raindrop shapes. Note that D_e is the equi-volume spherical diameter given by $\frac{\pi}{6}D_e^3 = \frac{4\pi}{3}a^2b$, where a and b are the semi-minor and semi-major axes, respectively. Also included are the results from an artificial rain experiment reported in Thurai and Bringi (2005) using 2-dimensional video disdrometer.

2.4 Polarimetric radar observables

2.4.1 Co-polar and differential reflectivity

The oblateness gives rise to a difference in the back-scatter signal between horizontal and vertical polarizations. This additional parameter measured by a dual-polarization radar, is called the differential reflectivity Z_{dr} which is defined in dB scale as $10 \log_{10} (Z_h/Z_v)$. For a single particle, the differential reflectivity is given by:

$$Z_{dr} = 10 \log_{10} \left(\frac{|S_{hh}|^2}{|S_{vv}|^2} \right) \quad (2.21)$$

For a distribution of scatterers within the radar pulse volume, ensemble averaging is used to define the quantity Z_{dr} . This is obtained from the ratio between the co-polar reflectivities of the H- and V-polarizations, Z_h and Z_v respectively. Referring to the earlier equation (2.17) for the equivalent radar reflectivity, we can now include the polarization dependent term as follows:-

$$Z_h = \frac{\lambda^4}{\pi^5 |K_w|^2} \int \sigma_b^{hh}(D_e) N(D_e) dD_e ; \quad mm^6 m^{-3} \quad (2.22a)$$

$$Z_v = \frac{\lambda^4}{\pi^5 |K_w|^2} \int \sigma_b^{vv}(D_e) N(D_e) dD_e ; \quad mm^6 m^{-3} \quad (2.22b)$$

where

$$\sigma_b^{hh}(D_e) = 4\pi |S_{hh}(D_e)|^2 \quad (2.22c)$$

and

$$\sigma_b^{vv}(D_e) = 4\pi |S_{vv}(D_e)|^2 \quad (2.22d)$$

The Z_{dr} then becomes,

$$Z_{dr} = 10 \log_{10} \left(\frac{Z_h}{Z_v} \right) \quad (2.23)$$

Typical values of Z_{dr} for the various sizes of rain drops and hail are shown in Fig. 2.6.

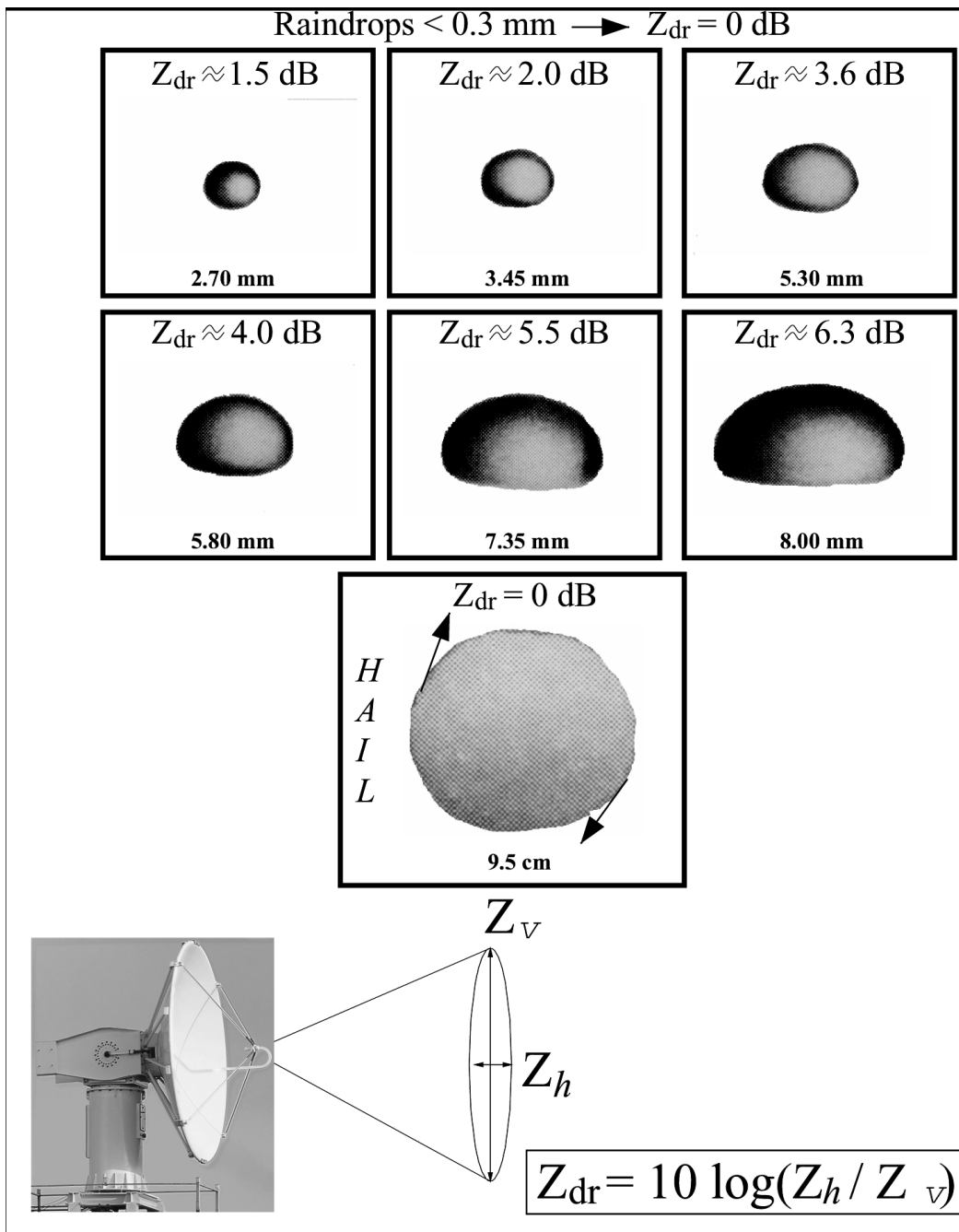


Fig. 2.6: Summary of typical Z_{dr} values of raindrops of various sizes and hail. The black arrow on the hail particle represent the tumbling motions as it falls in a thunderstorm. Adapted from Wakimoto and Bringi (1988).

The measure of Z_{dr} enables the estimation of D_m , which is one of the key parameters describing the dsd . It is more accurate at S-band where Rayleigh scattering holds, as opposed to C- and X-bands where Mie scattering effects introduce more uncertainty. Fig. 2.7 shows calculations of Z_{dr} versus D_m at the three frequencies, assuming the Beard and Chuang (1987) drop shapes and disdrometer measurements of drop size distributions from many different climatic regimes (a sub-set of the data used in Fig. 2.4).

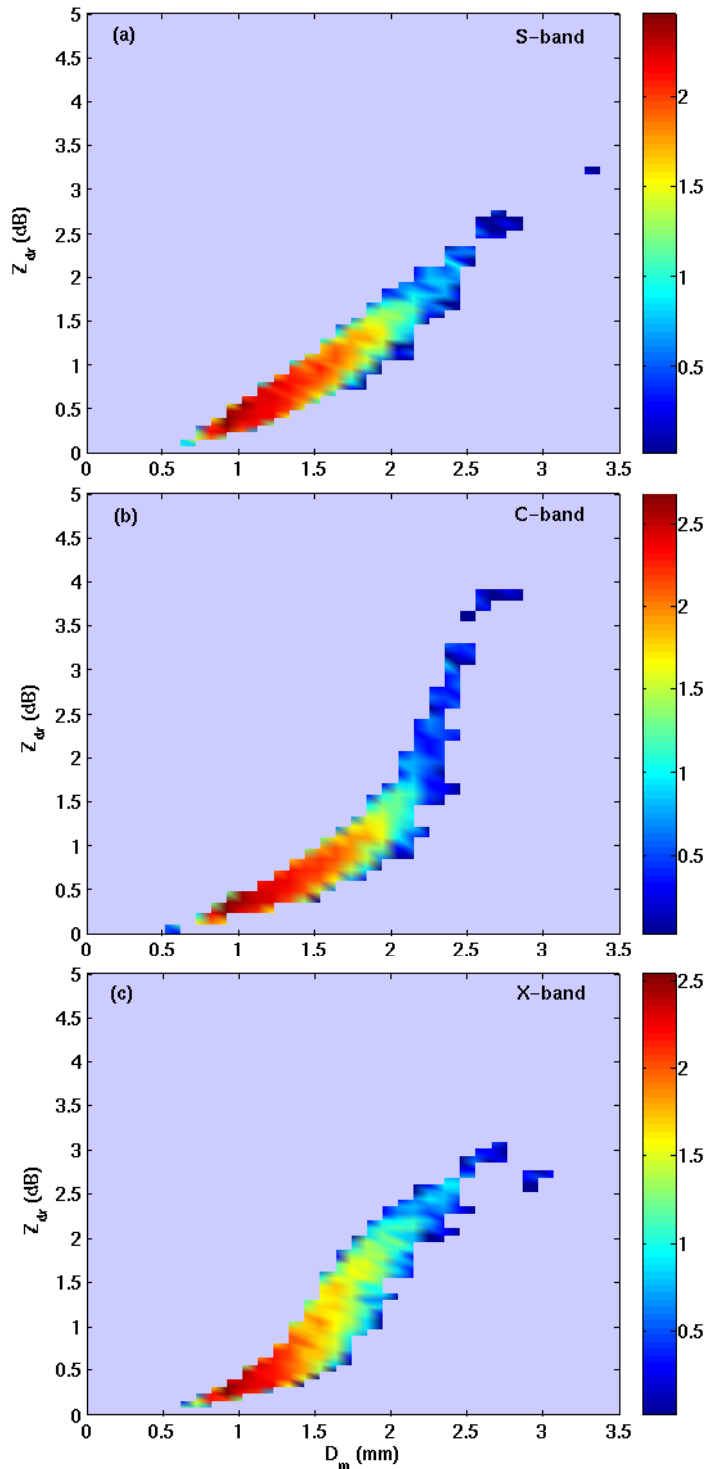


Fig. 2.7: Calculations of Z_{dr} versus the mass weighted mean diameter D_m at S-, C- and X-bands, for measured drop size distributions from a variety of climatic regimes. The color filling contours the frequency of occurrence of $Z_{dr} - D_m$ pairs on a log scale.

2.4.2 Cross-polar reflectivity and linear depolarization ratio

In the above section it was considered that rain drops are oblate spheroids having zero canting angle with respect to the vertical. For scatterers which have a finite canting angle (i.e. with their axis of symmetry tilted from the vertical), the scattering process will cause a small but finite fraction of the transmit (or incident) energy to be depolarized, the contribution of which could be resolved in the direction of the orthogonal polarization. The amount of depolarization will depend on a number of factors, namely, the hydrometeor size, the axis ratio, the degree of canting and the radar beam elevation. This will result in non-zero values for the magnitudes of S_{hv} and S_{vh} in the scattering matrix, defined in Section 2.1.2. Such depolarization is measured in terms of the so-called linear depolarization ratio, abbreviated to LDR . For a single scatterer, the LDR_{vh} from horizontal to vertical polarization is given by:

$$LDR_{vh} = 10 \log_{10} \left(\frac{|S_{vh}|^2}{|S_{hh}|^2} \right) \quad (2.24)$$

For an ensemble of scatterers, the cross-polar reflectivity is derived in an analogous way to the co-polar reflectivity, as follows:

$$Z_{hv} = \frac{\lambda^4}{\pi^5 |K_w|^2} \int \sigma_b^{hv}(D) N(D) dD ; \quad mm^6 m^{-3} \quad (2.25)$$

where

$$\sigma_b^{hv}(D) = 4\pi |S_{hv}(D)|^2 \quad (2.26)$$

and, more generally, it has been shown that (Tragl, 1990)

$$Z_{vh} = Z_{hv} \quad (2.27)$$

The overall LDR_{vh} and LDR_{hv} are defined by the corresponding ratios between the cross-polar reflectivity and the co-polar reflectivity (in the absence of any depolarization of the propagation to and from the radar), and are given by:

$$LDR_{hv} = 10 \log_{10} \left(\frac{Z_{hv}}{Z_h} \right) \quad \text{and} \quad LDR_{vh} = 10 \log_{10} \left(\frac{Z_{vh}}{Z_v} \right) \quad (2.28)$$

Although LDR is sensitive to the degree of canting, in most cases of rainfall measurements, it can be difficult to detect the cross-polar component because of limitations due to antenna cross-polar performance. Melting snowflakes on the other hand often cause sufficient LDR to be detected with relative ease. The measurement of LDR is more useful for precipitation classification (see Chapter 7) than for improving rainfall estimates.

2.4.3 Differential propagation phase and specific differential phase

The oblateness of the drops also causes a difference in the amplitude and phase of the propagating signal, with the result that the horizontally polarized wave will suffer (i) higher attenuation and (ii) phase lag relative to the vertically polarized wave. This gives rise to (i) differential attenuation and (ii) differential propagation phase (Φ_{dp}) between the H and V polarized waves. The latter is conceptually depicted below in Fig. 2.8.

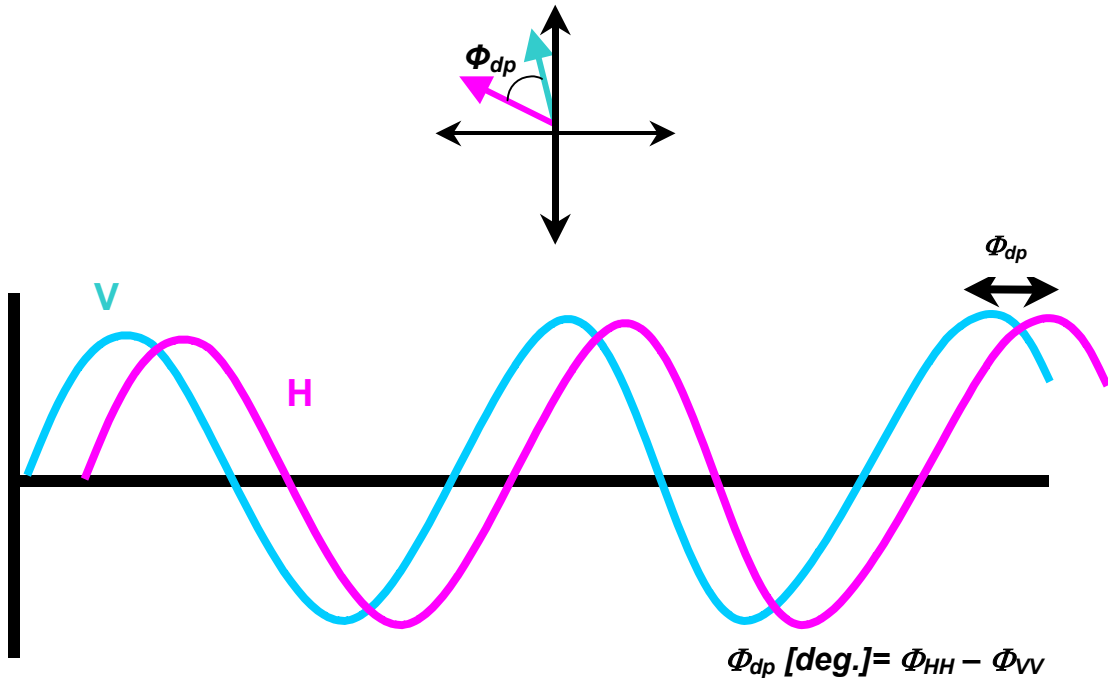


Fig. 2.8: Conceptual phasor diagram showing the propagation phase delay between the H and V polarized waves.

Φ_{HH} , Φ_{VV} : cumulative differential phase shift for the total round trip between radar and resolution volume.

$\Phi_{HH} - \Phi_{VV}$: differential phase shift upon back scatter + differential phase shift along the propagation path

The specific differential phase (K_{dp} ; $^{\circ}/\text{km}$) is related to the derivative of Φ_{dp} along range, $K_{dp} = \frac{1}{2} \frac{d}{dr} \Phi_{dp}$, and is an important measure of the rain rate. It is defined as,

$$K_{dp} = \frac{2\pi}{k_0} \int \text{Re}[\hat{h} \cdot \vec{f} - \hat{v} \cdot \vec{f}] N(D) dD \quad (2.29)$$

where \hat{f} is the forward scattering amplitude, k_0 is the wave number in free space ($k_0 = 2\pi/\lambda$), and \hat{h} and \hat{v} are the unit vectors along the horizontal and vertical

directions in the plane of polarization, respectively. Since \hat{f} is proportional to k_0^2 , an inverse relation of K_{dp} with wavelength results. Owing to that, K_{dp} is more pronounced at C- and X-bands as compared with S-band and, consequently, the X-band K_{dp} can be used to estimate significantly lower rain rates (typically, as low as 2 mm/h).

In rainfall, the differential propagation phase Φ_{dp} is known to be a monotonically increasing function of range. If the rain rate is uniform along the path, Φ_{dp} increases by a fixed amount per unit distance along range and K_{dp} is constant.

2.4.4 Correlation coefficient ρ_{co}

Another parameter which can be measured by a dual-polarization radar is the co-polar correlation coefficient ρ_{co} (zero-lag if polarization switching is used), which is the correlation between horizontally and vertically polarized return signals. This is defined as (Sachidananda and Zrnic, 1985):

$$\rho_{co} = \frac{\langle S_{vv} S_{hh}^* \rangle}{\sqrt{\langle |S_{hh}|^2 \rangle \langle |S_{vv}|^2 \rangle}} \quad (2.30)$$

Here the brackets $\langle \rangle$ represent the expected values, assuming that the hydrometeor properties such as size, shape and canting angle are statistically distributed. The asterisk * denotes the complex conjugate. Apart from the distribution of shape and the canting angles, ρ_{co} is also influenced by the oscillation of large drops and the phase difference in the back scatter signals (referred to as back scatter differential phase) between H and V polarizations. Moreover, it is influenced by particle mixture (e.g. rain/hail mixture) and by irregular particle shapes (e.g. hail, graupel). The ρ_{co} is therefore useful for identifying non-rain hydrometeors. Measurements made in rain using horizontally pointing radar beam indicate that ρ_{co} can range from 0.98 (Balakrishnan and Zrnic (1990)) to 0.995 (Illingworth and Caylor, 1991, using a high resolution S-band radar). Note, the physical cause of de-correlation is that the back scatter fields from the two orthogonal polarizations do not vary in unison. Low values of ρ_{co} are observed in bright-band regions and in rain / hail mixtures (around 0.9 at S-band). For randomly orientation of particles in the plane of polarization, there is a simple relationship between ρ_{co} and LDR , given by (Aydin and Tang, 1997):

$$|\rho_{co}| = 1 - 2 \times 10^{0.1(LDR)} \quad (2.31)$$

2.5 Other (secondary) polarimetric radar observables

2.5.1 Back scatter differential phase

The term ρ_{co} as defined in the above equation (2.30) is a complex quantity, the magnitude of which represents the correlation coefficient ρ_{co} . In the absence of differential propagation phase, it can be represented as:

$$\rho_{co} = |\rho_{co}| e^{i\delta} \quad (2.32)$$

where δ is the phase difference in H and V polarizations caused by back scattering, known as ‘back scatter differential phase’,

$$\delta = \arg\left(\langle S_{vv} S_{hh}^* \rangle\right) \quad (2.33)$$

In the presence of differential propagation phase from the radar to the range resolution volume of interest, the estimator for $\arg(\rho_{co})$ gives the sum of δ and Φ_{dp} .

The parameter δ becomes significant in Mie region, i.e. when the radar wavelength is comparable to the size of the scatterers. It is largely negligible in rain at S-band whereas at X-band and even at C-band, it can become noticeable in the measured Φ_{dp} range profiles as a local perturbation on the monotonically increasing differential propagation phase (discussed later in Appendix A). Although not used for quantitative estimation of rainfall rates, the parameter δ helps to identify non-precipitation echoes, such as those arising from birds.

2.5.2 Co-cross-polar correlation

For polarization radars which have the added capability of receiving the cross-polar signal component, the two co-cross-polar correlation coefficients ρ_x^h and ρ_x^v can also be determined. These are defined as:

$$\rho_x^h = \frac{\langle S_{hh}^* S_{hv} \rangle}{\sqrt{\left[\langle |S_{hh}|^2 \rangle \langle |S_{hv}|^2 \rangle \right]}} \quad (2.34a)$$

$$\rho_x^v = \frac{\langle S_{vv}^* S_{hv} \rangle}{\sqrt{\left[\langle |S_{vv}|^2 \rangle \langle |S_{hv}|^2 \rangle \right]}} \quad (2.34b)$$

They are primarily dependent on the characteristics of hydrometeor orientation, i.e. the canting angle distribution. In particular, the mean and the *rms* width of the canting angle distribution in rain can be estimated approximately from ρ_x^h and ρ_x^v (Ryzhkov, et al 2002a), when combined with Z_{dr} and LDR . Other applications are (i) detection of aligned crystals – indicated by pronounced ρ_x^h and ρ_x^v signatures – which could be used to locate electrically charged regions in clouds and (ii) radar hardware assembly quality checks (in particular antenna/feed) such as undue coupling between the two orthogonal channels. Note this requires simultaneous measurements of the co- and cross-polar signals in two separate receivers; Doppler processing is not necessary (see Section 6.1.2 of Bringi and Chandrasekar, 2001).

2.6 Summary of applications of the polarization radar observables

There are many applications of the added parameters that a polarization radar can measure. The primary use relates to the improvement in quantifying rainfall rates. Other important applications are hydrometeor classification and discrimination between meteorological and non-meteorological echoes. Chapters 6 and 7 will discuss these applications in detail. Table 2.1 below summarizes the applications of the various radar observables.

Table 2.1: Applications and advantages of Radar observables

Parameter	Z _h	Z _{dr}	K _{dp} /Φ _{dp}	ρ _{co}	LDR	δ	ρ _{x^h} , ρ _{x^v}
Applications and advantages							
To improve estimates of rainfall rates	×	×	×				
Hydrometeor classification, eg. hail, wet/dry snow	×	×	×	×	×		
To determine melting level heights		×		×	×	×	
To correct for rain attenuation and/or rain on radome effects			×				
Self consistency checks of Z calibration in rain	×	×	×				
To identify ground clutter and/or anomalous propagation		×	×	×			
To discriminate sea clutter effects and AP over-sea			×	×	×		
To identify biological scatterers such as birds and insects		×	×			×	
To overcome problems due to beam-blockage			×				
To identify regions of oriented ice crystals in clouds			×				×

3 Processing the Differential Propagation Phase

3.1 General considerations

In rainfall, the differential propagation phase Φ_{dp} is known to be a monotonically increasing function of range (see Section 2.4.3). However, measurements always show some fluctuations in Φ_{dp} which depend on system coherence (e.g., Magnetron or Klystron transmitter), signal-to-noise ratio, number of integration samples etc., as well as atmospheric parameters such as Doppler spectral width. These measurement fluctuations are typically around 3-6 degrees, which implies that the range profile of Φ_{dp} must be 'smoothed' or filtered before its range derivative (or, K_{dp}) can be calculated.

There are a number of 'smoothing' techniques such as

- (a) moving average (weighted and non-weighted),
- (b) median filter and
- (c) finite impulse response (FIR) filter.

In some applications such as the mean areal rain rate over a watershed, only the total increase in Φ_{dp} over the area is of interest and not its range derivative at each range resolution volume. For higher resolution rainfall estimates, the range derivative must be computed after filtering the Φ_{dp} along range. A number of techniques for filtering the Φ_{dp} along range are available generally based on a least squares fit of a straight line over a successive number of range samples. The range interval over which the K_{dp} estimate is derived is a compromise between the desired need for high range resolution and the need for a statistically stable estimate. Additionally, at higher frequencies such as C (near 5 GHz) or X (near 10 GHz)-bands, the monotonically increasing range profile of Φ_{dp} is often perturbed by back scatter differential phase between H and V polarized waves from very large raindrops or melting graupel/hail particles (see, equation 4.65 on page 178 of Bringi and Chandrasekar, 2001). Such back scatter differential phase tends to bias the K_{dp} estimates rather strongly. The simple least-squares fit of a straight line to successive range samples of Φ_{dp} will not remove the back scatter differential phase component. This is not an issue at S-band except for rain mixed with large hail or within the melting region in stratiform events.

The standard deviation of the K_{dp} estimate (assuming path length $L = N \Delta r$ where Δr is the range sample spacing and N the number of range samples in L) is given theoretically as (see Section 6.6.2 of Bringi and Chandrasekar, 2001):

$$SD(\hat{K}_{dp}) = \frac{SD(\hat{\Phi}_{dp})}{L} \sqrt{\frac{3}{N - \frac{1}{N}}} \quad (3.1)$$

Fig. 3.1 shows $SD(\hat{K}_{dp})$ versus L for several values of Δr . For typical Δr of 150 m and L of 3 km, the $SD(\hat{K}_{dp})$ is estimated to be around 0.25 °/km, which corresponds to a

rainfall intensity of about 5.0 mm/h at X-band, 10 mm/h at C-band, and 15 mm/h at S-band.

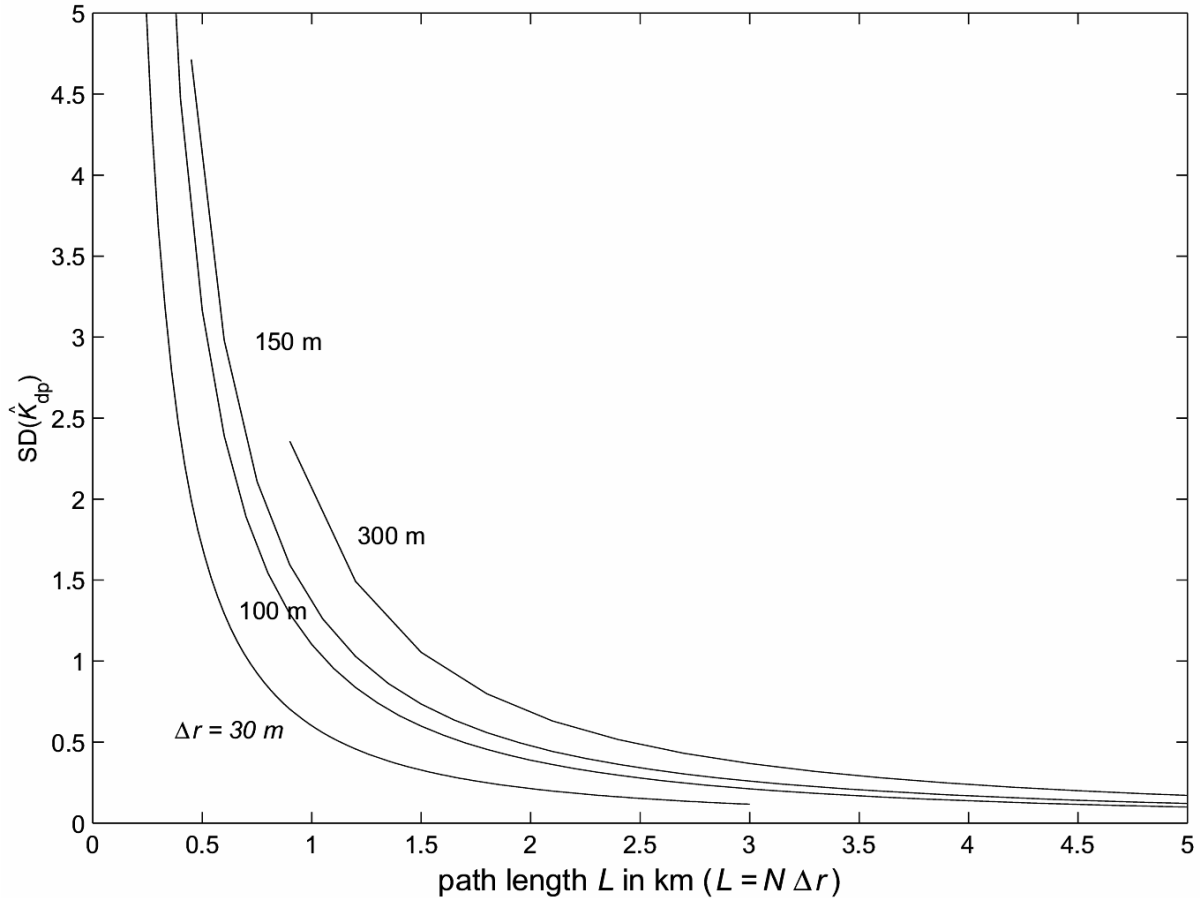


Fig. 3.1: Standard deviation of K_{dp} estimate obtained as the slope of a straight line fit to the Φ_{dp} profile, shown as a function of path length. The various curves show the effect of different range sample spacings for a fixed path length.

3.2 The iterative filtering technique

Hubbert and Bringi (1995) describe an iterative filtering technique for suppressing unexpected large deviations of Φ_{dp} from its monotonic increasing range profile in rain that might be ascribed to back scatter differential phase or some other system causes. An alternate consensus method is described in May et al. (1999) that overcomes the problem of 'outliers' in the Φ_{dp} data. While the examples given in this Section are based on C-band radar data, they can also be applied to X-band as well as S-band.

A simple diagram of the steps involved in Φ_{dp} processing is shown in Fig. 3.2. The processing is carried out on the basis of individual range profiles of Φ_{dp} , signal-to-

noise ratio (SNR) and the co-polar correlation coefficient. Some of the procedures in Fig. 3.2 are elaborated below in Sections 3.2.1 to 3.2.4.

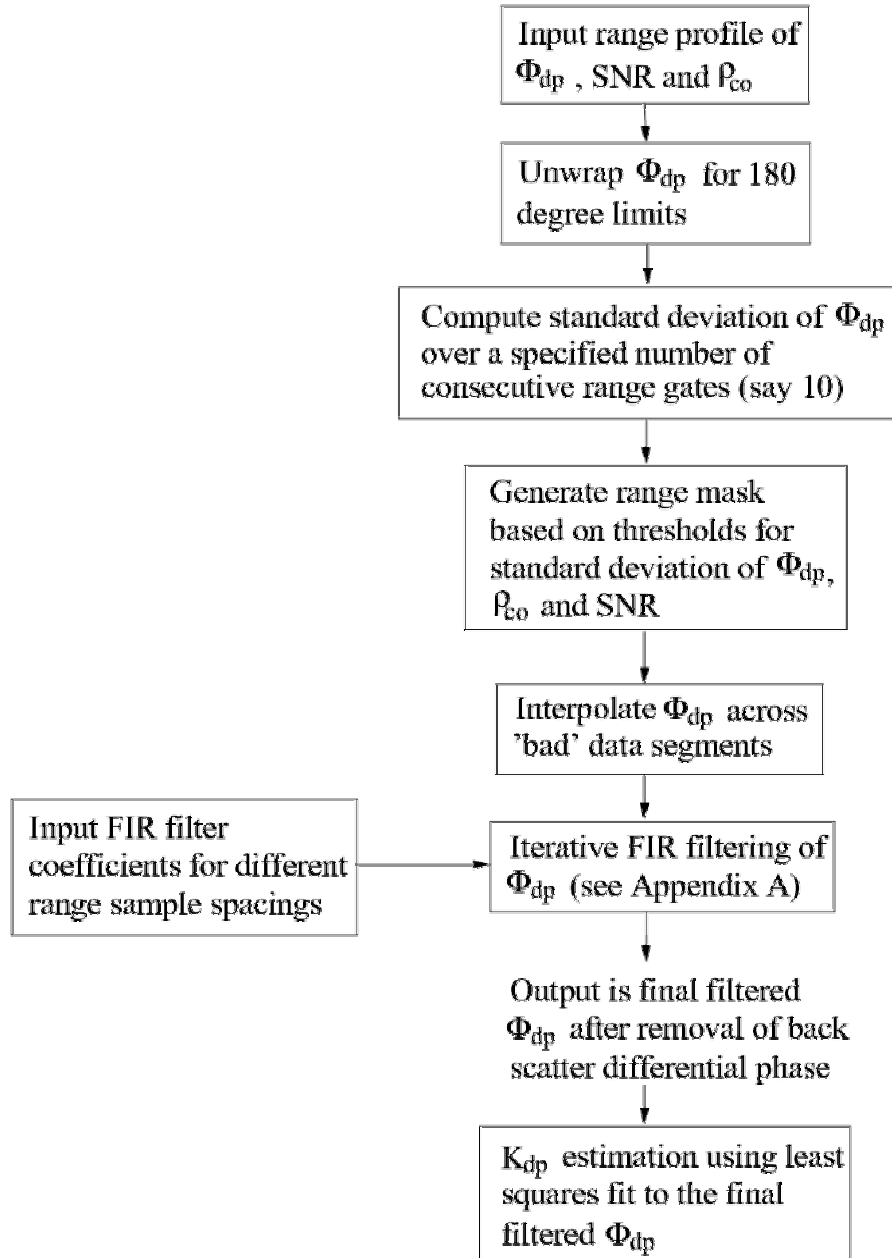


Fig. 3.2: Steps for Φ_{dp} filtering and K_{dp} estimations.

3.2.1 Φ_{dp} unwrapping

Before any range filtering on Φ_{dp} is done, the Φ_{dp} data has to be unwrapped when it increases to 180° in the case of pulse to pulse switching or 360° in the case of simultaneous transmit/receive configuration. For pulse-to-pulse switching, the Φ_{dp} algorithm involves one half of the sum of the two phase estimates (one from HV* sequence and one from H*V sequence). Thus the resulting Φ_{dp} is unique only in the interval of 180° . In the case of simultaneous transmit/receive scheme, only one phase estimator is involved, giving a 360° interval. The Φ_{dp} unwrapping is straightforward since the range profile is known to be monotonically increasing with range in rain.

3.2.2 'Good data' mask application

Next, a 'good' data mask is generated along range which separates signal returns from weather echoes and non-weather targets (e.g., clutter). An example is shown in Fig. 3.3 which illustrates the 'good' data mask based on the standard deviation of Φ_{dp} computed over ten consecutive range samples. In addition to thresholding based on standard deviation of Φ_{dp} (typical threshold of 10° – 20°), both SNR and copolar correlation coefficient (ρ_{co}) are used to establish the 'good' data mask ($SNR > 3\text{ dB}$, $\rho_{co} > 0.8$ – 0.9). These thresholds should be determined based on radar system performance, overall system sensitivity, the sampling strategy and clutter environment (for example, land versus sea clutter). High system coherence as afforded by Klystron transmit systems is preferable to magnetron based systems and hence lower thresholds can be tolerated. From analyses experience based on different dual-polarized radar systems, the good data mask is not very sensitive to the selected thresholds. For 'bad' data segments, the Φ_{dp} is linearly interpolated between the two neighboring 'good' data segments. Fig. 3.4 shows a PPI scan of (a) measured Φ_{dp} , (b) the Z_h before applying the 'good' data mask and (c) the Z_h after applying the mask. These data are from the Bureau of Meteorology Research Center (BMRC) C-POL radar (data are provided courtesy of Dr. T. Keenan of the BMRC). These and subsequent data have been typically time-averaged over 64 pulses per polarization state with PRT of 1 ms.

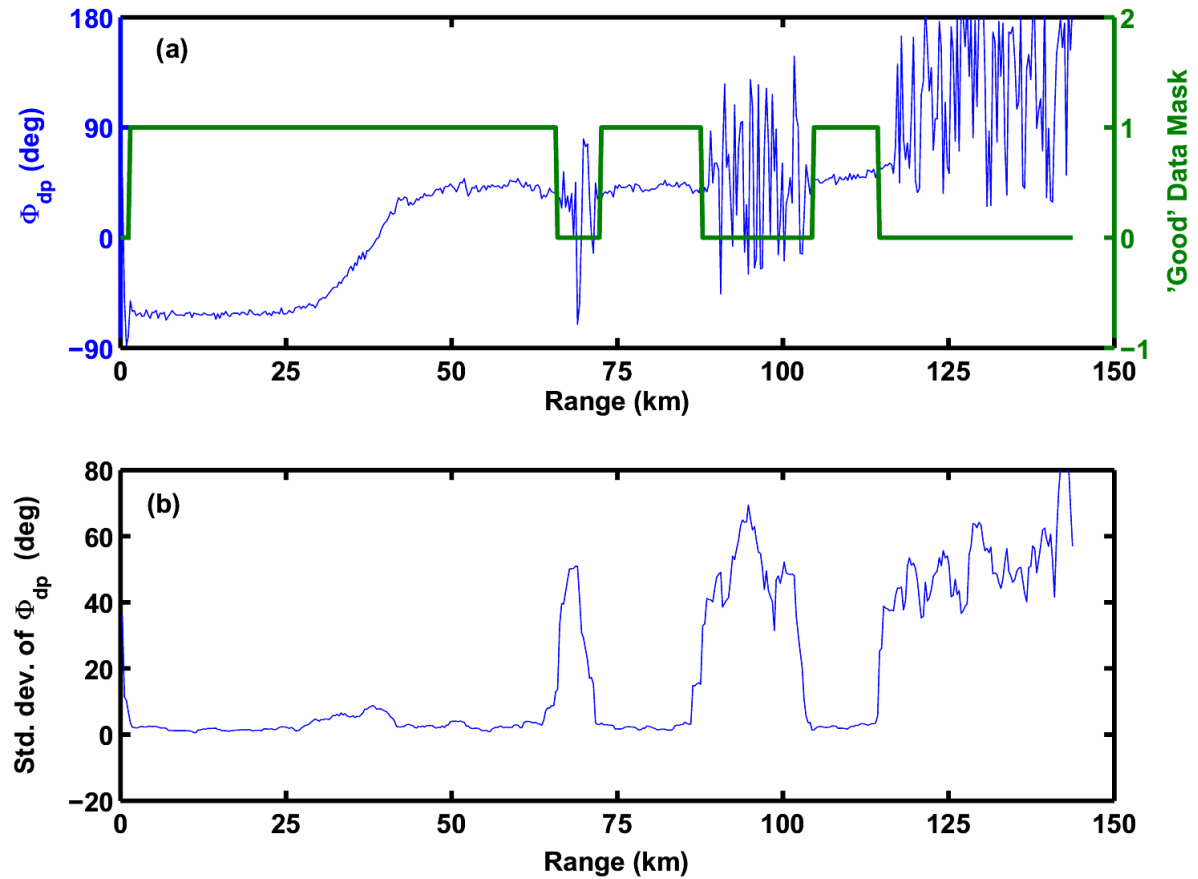


Fig. 3.3: Range profile from the BMRC/C-POL radar located on Dongsha Island for the South China Sea Monsoon Experiment. Data from 18 May 1998 at elevation angle of 0.5°. (a) measured Φ_{dp} and 'good' data mask. (b) standard deviation of Φ_{dp} from 10 consecutive range samples. The 'good' data mask is based on standard deviation $< 20^\circ$ and SNR > 3 dB. Data courtesy of Thomas Keenan of BMRC.

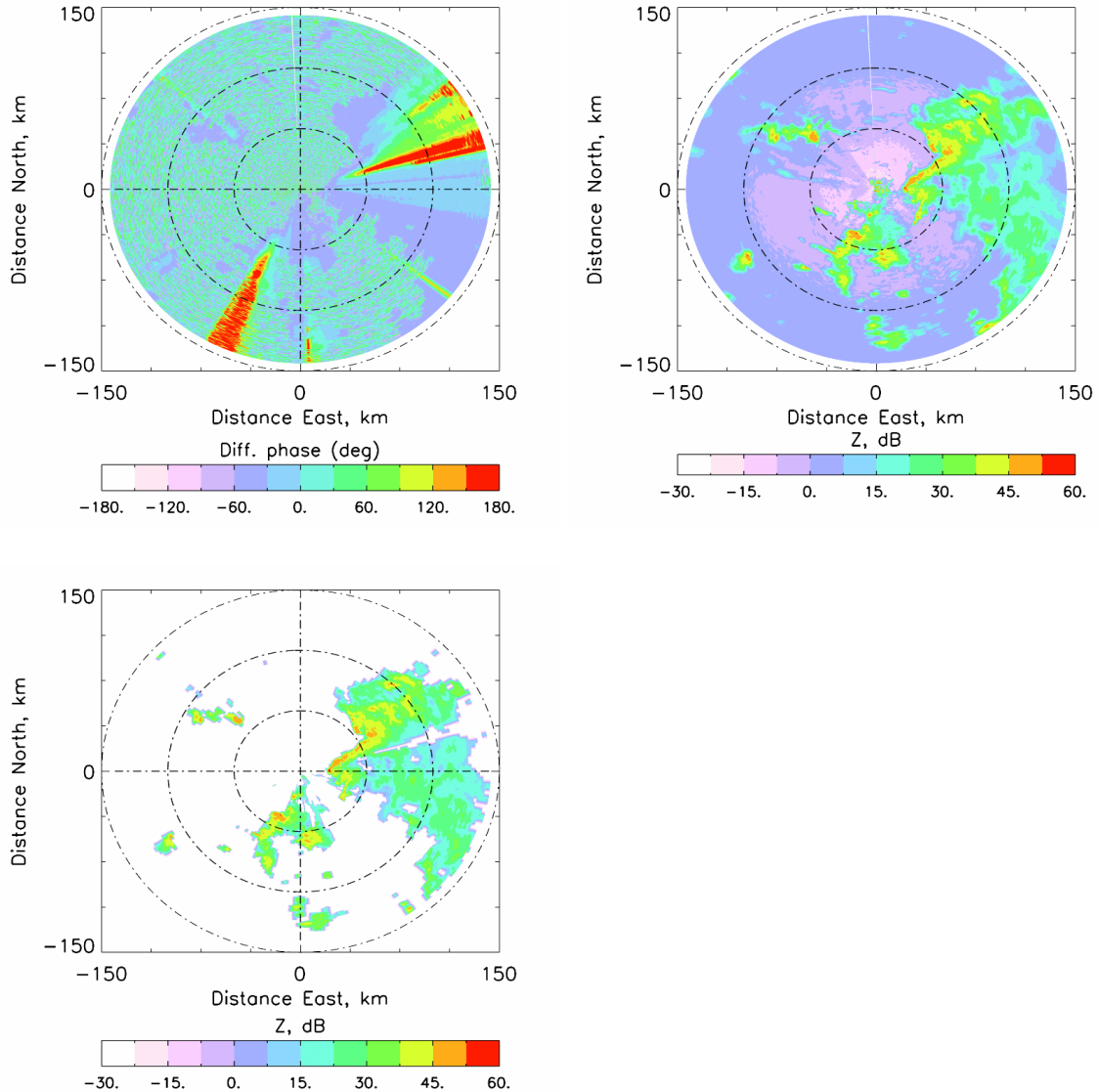


Fig. 3.4: PPI data at elevation angle of 0.6° from the BMRC/C-POL radar located in Darwin, Australia on February 3, 2000. (a) measured Φ_{dp} , (b) measured Z_h and (c) measured Z_h with 'good' data mask applied as illustrated in Fig. 3.3. Data courtesy of Thomas Keenan of BMRC.

3.2.3 FIR Filtering

Next, we select a finite impulse response (FIR) range filter which suppresses the 'high frequency' fluctuations in Φ_{dp} from one range sample to the next while still preserving the monotonically increasing property of Φ_{dp} with range. The FIR range filter falls within the class of weighted moving average filters except that the weights are based on a desired spectral response. The magnitude response of one such 20th order FIR filter designed for 150 m range sample spacing is shown in Fig. 3.5. It is designed to sharply 'attenuate' spatial variations of 1.5 km and less by 12 dB or more. The -3 dB point is set at 2.85 km. FIR filters for other range sample spacings can be pre-designed and software-selected irrespective of the radar frequency.

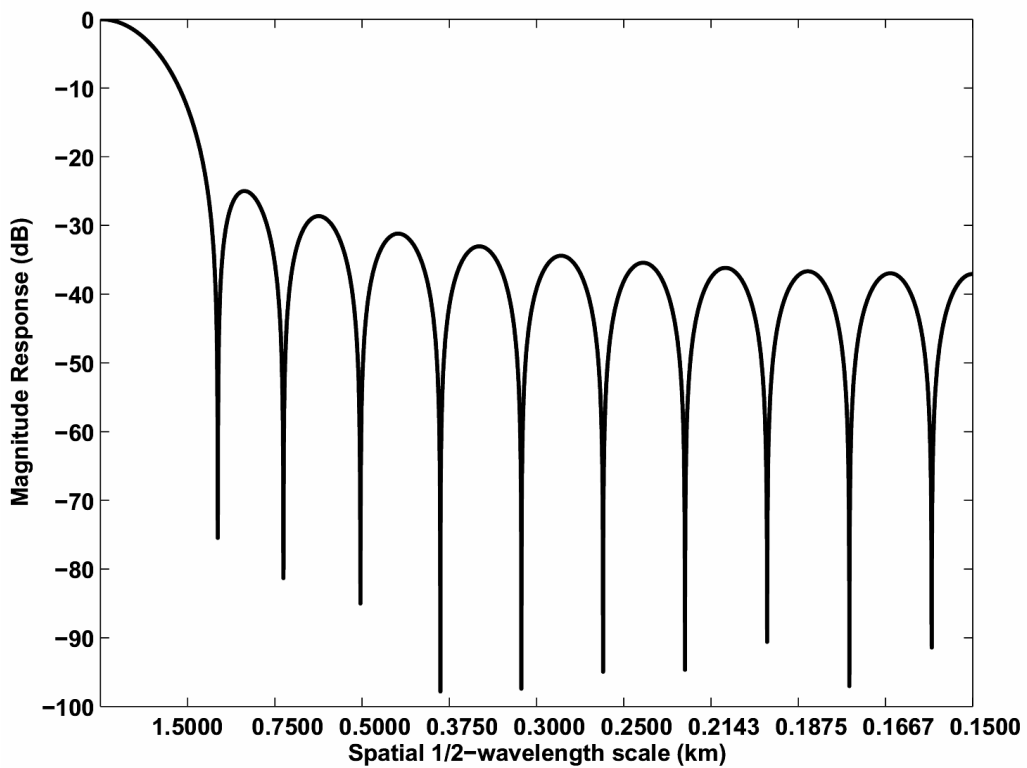


Fig. 3.5: The magnitude response of a twentieth-order finite impulse response filter (FIR) from Hubbert and Bringi (1995).

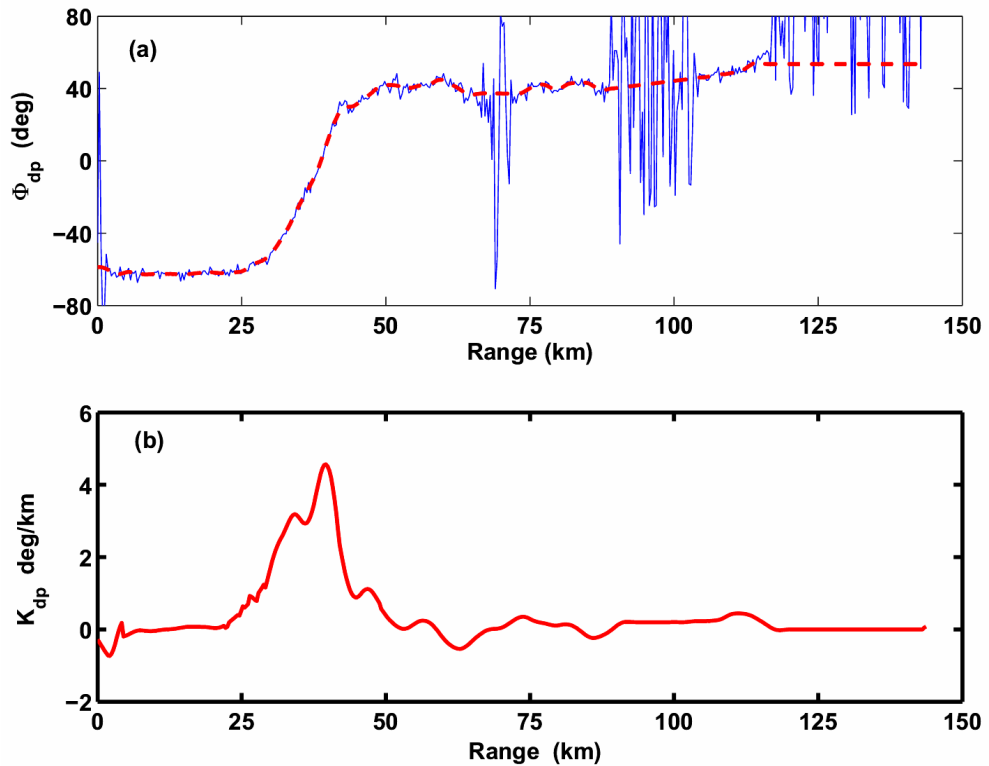


Fig. 3.6: (a) Range profile of 'raw' Φ_{dp} along with the iterative filtering method for the same case shown in Fig. 3.3. No significant scattering differential phase is noted. (b) K_{dp} profile is shown. Data courtesy of Thomas Keenan of BMRC.

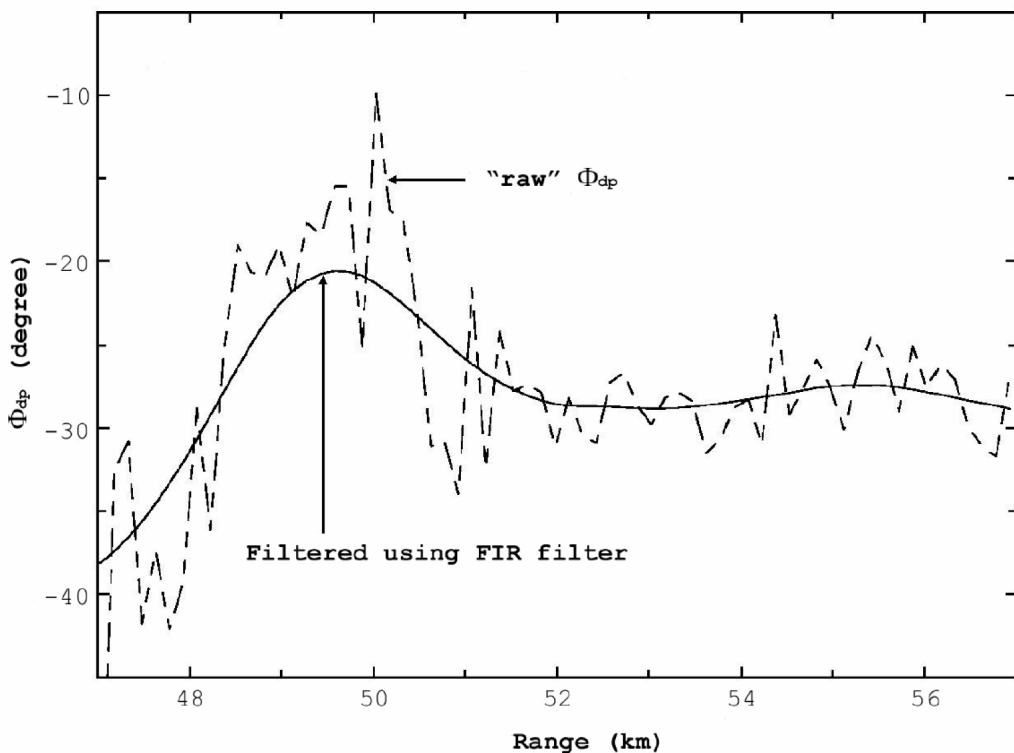


Fig. 3.7: Example range profile of 'raw' Φ_{dp} and filtered version using the FIR filter in Fig. 3.5. From Hubbert and Bringi (1995).

Fig. 3.6a shows an example range profile of 'raw' Φ_{dp} along with the FIR filtered version (same case as in Fig. 3.3) where there is no back scatter differential phase present. Fig. 3.7, however, shows an example where there is significant back scatter phase detected between 49 to 50 km along with the FIR filtered curve without suppressing this effect. If the K_{dp} were derived from this filtered curve there will be a large positive value centered at 48.5 km and nearly symmetric negative value centered at 50.5 km which is unreasonable. Fig. 3.8 shows the final iterative filtering result which is designed to 'suppress' the back scatter differential phase and, at the same time, ensures that the differential propagation phase increases monotonically with range (solid line in Fig. 3.8). The iteration methodology is explained in more detail in Appendix A.

At S-band where Rayleigh scattering largely holds, the back scatter differential phase is negligible; hence the number of iterations required for convergence is reduced from typically 10 for C- and X-bands to 2 for S-band.

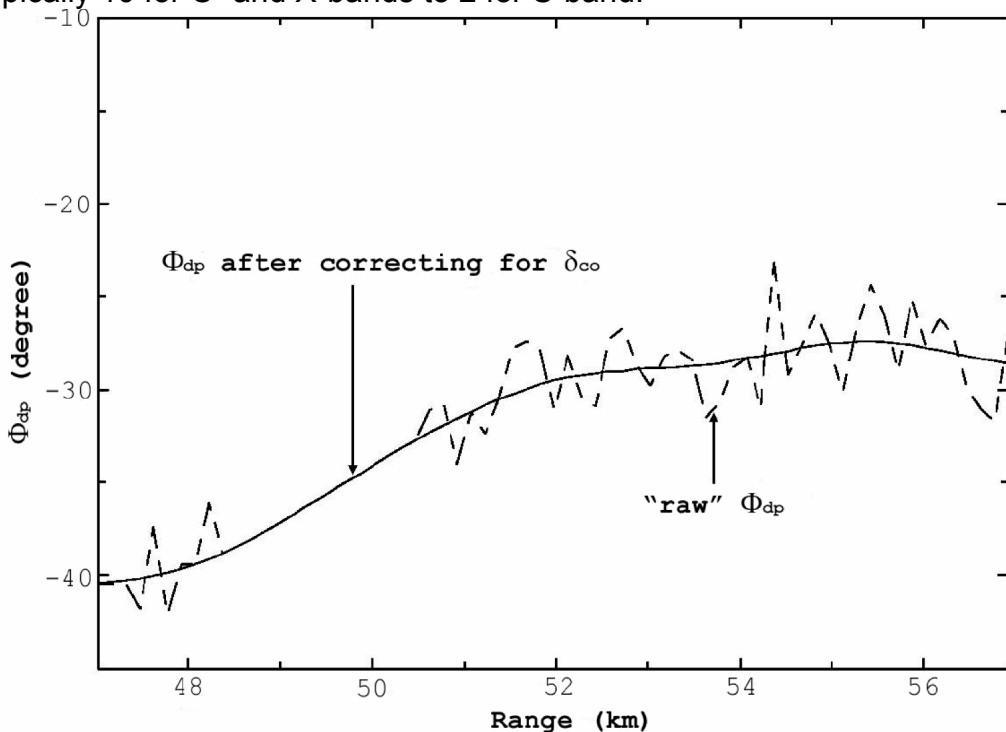


Fig. 3.8: Result after applying an iterative filter algorithm to correct the Φ_{dp} for back scatter differential phase (δ_{co}) in the range interval 48-50.5 km. The corrected solid line is Φ_{dp} from which K_{dp} is estimated. From Hubbert and Bringi (1995).

3.2.4 K_{dp} calculation

Once the iteratively filtered Φ_{dp} profile is obtained, the K_{dp} is finally calculated based on a least squares linear fit to a varying number of consecutive range samples based on the reflectivity value (e.g., 10 samples if $Z_h > 45 \text{ dBZ}$, 20 samples for $30 < Z_h < 45 \text{ dBZ}$ and 30 samples for $Z_h < 30 \text{ dBZ}$). Such 'telescoping' further

smoothes the final K_{dp} especially for lighter rain segments (see Fig. 3.6b). Fig. 3.9 shows a PPI scan of the resulting K_{dp} (the same case for which 'raw' Φ_{dp} and Z_h were shown earlier in Fig. 3.4). Note that the BMRC/CPOL radar employs a near real-time implementation of the iterative filtering technique and K_{dp} estimation.

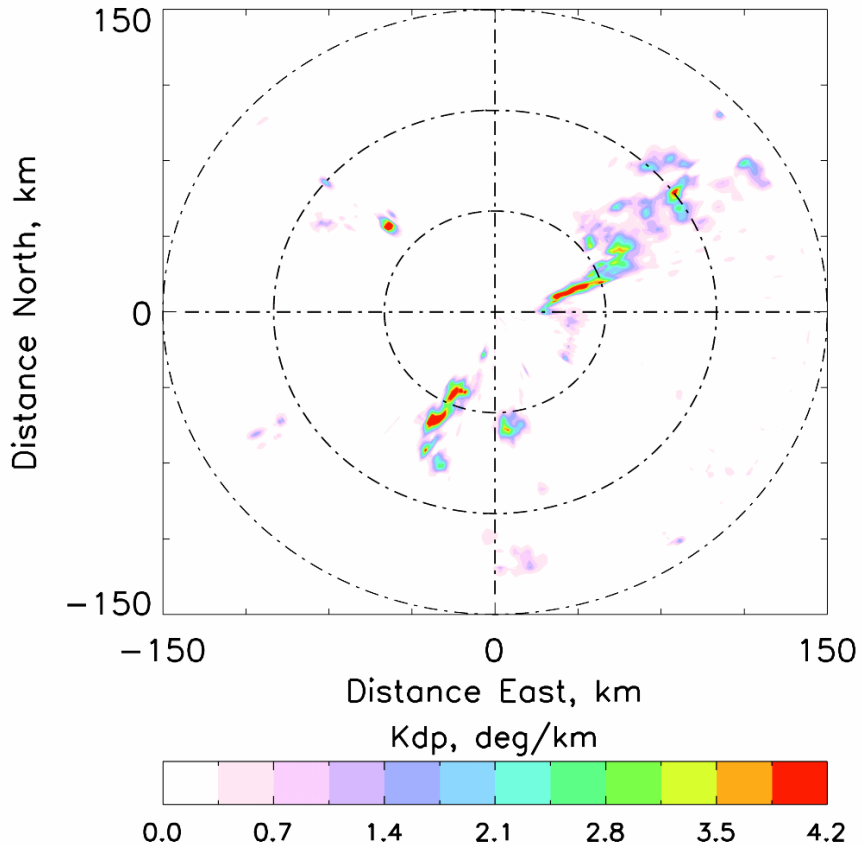


Fig. 3.9: PPI data showing the K_{dp} field (the same case as in Fig. 3.4) using the iterative filtering method. The rain rate for K_{dp} of $4^\circ/\text{km}$ is estimated to be 100 mm/h . Data courtesy of Thomas Keenan of BMRC.

3.3 A simple smoothing technique

The iterative FIR method is a relatively complicated process which has been applied to data at C-band and X-band to suppress back scatter differential phase or other abnormal system related phase fluctuations . If no prior filtering is done, then the K_{dp} estimates can be very noisy and inaccurate. To illustrate the contrast, Fig. 3.10 shows the K_{dp} image derived from the 'raw' Φ_{dp} data using the simplest estimate of the range derivative. This is obtained from the slope over 8 consecutive range samples. The noisiness of these K_{dp} estimates clearly indicate that a more elaborate range filtering process is needed.

3.4 Other techniques

A variety of other techniques for estimating K_{dp} from noisy range profiles of Φ_{dp} are available in the literature, e.g. May et al (1999), Timothy et al (1999) or Matrosov et al (2002). If there are no significant effects due to back scatter differential phase, these other techniques result in similar K_{dp} estimates provided the range window over which the smoothing is applied is the same. At S-band, Ryzhkov and Zrnic (1996) have described a scheme to pre-filter the raw Φ_{dp} data followed by estimating the slope of a least-squares straight line fit over a range window of 9 and 25 gates depending on the reflectivity value (9 for $Z_H > 40$ dBZ and 25 for $Z_H < 40$ dBZ). For real time applications, further evaluations on the specific radar system are needed before an optimal K_{dp} estimator can be recommended, at least for C and X bands.

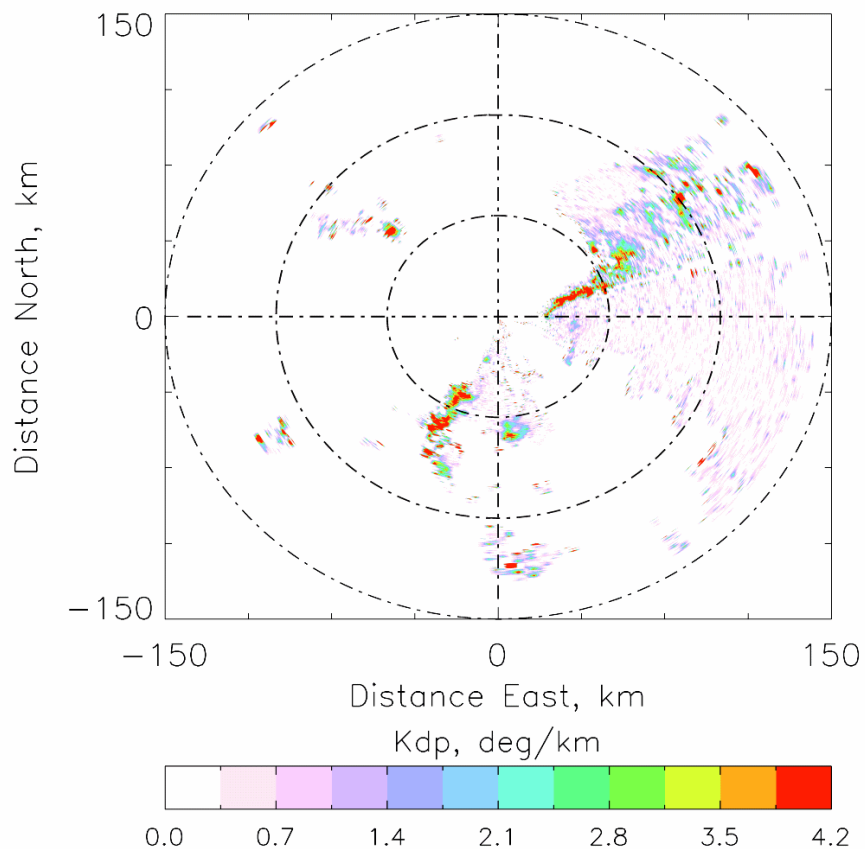


Fig. 3.10: PPI data showing the K_{dp} field using the slope of the 'raw' Φ_{dp} over eight range samples. Compare with Fig. 3.9. Data courtesy of Thomas Keenan of BMRC.

4 Correcting the Measured Reflectivity for Rain Attenuation

Attenuation occurs as a result of the way in which the radar signal (i.e. the electromagnetic wave) interacts with the rain-filled medium through which the signal propagates. Rain can be thought of as being composed of dielectric scatterers, whose complex permittivity is the same as that of water. The interaction of water dipoles with the electromagnetic wave governs the propagation effects. Primarily, this consists of a scattering component and an absorption component. These are both frequency dependent quantities, particularly at frequencies above 1 GHz.

The specific attenuation (A_h or A_v) in dB/km is defined as,

$$A_{h,v} = 4.343 \times 10^3 \int \sigma_{\text{ext}}^{h,v} N(D) dD \quad (4.1)$$

where $\sigma_{\text{ext}}^{h,v}$ is the extinction cross section for horizontal or vertical polarization. There is also a direct relationship between A_h (or, A_v) and Φ_{dp} in rain and this provides an important constraint on attenuation-correction algorithms. The differential attenuation also causes Z_{dr} to decrease with increasing propagation into the rain medium; this can also be corrected for by using the Φ_{dp} measurement. At S-band, attenuation effects are much smaller than at C- or X-band and can be neglected except for intense rain events. Fig. 4.1 shows calculations of specific attenuation for various rainfall rates, using a range of measured size distributions of raindrops.

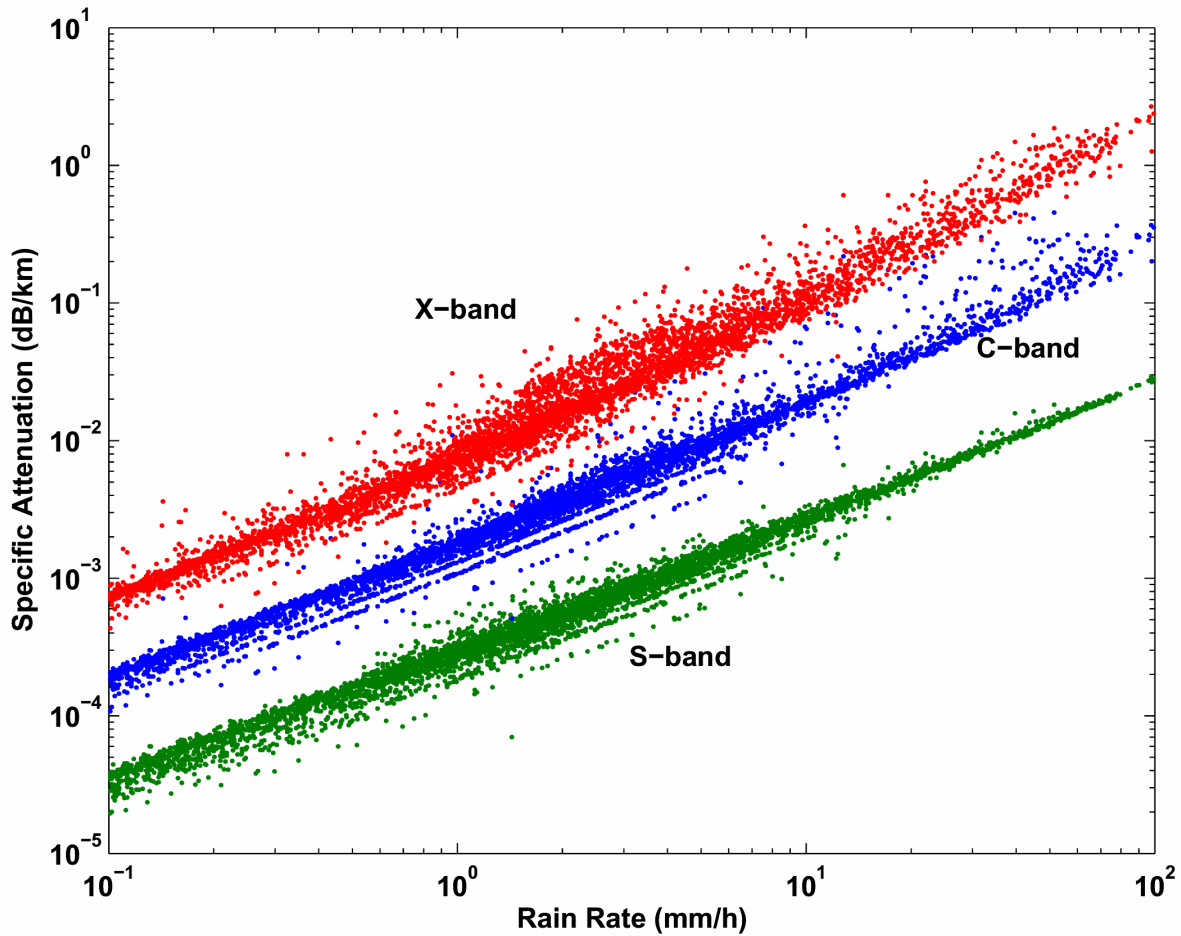


Fig. 4.1: Specific attenuation versus rain rate at 2.7 (S-band), 5.5 (C-band) and 9.3 GHz (X-band) for drop size distributions measured by 2D-Video disdrometer at a number of locations which include Graz, Austria; Papua New Guinea; Florida; and Joss disdrometer data from Darwin, Australia. The 2D-video data from Graz and Papua New Guinea is courtesy of Joanneum Research; the 2D-video data from Florida is courtesy of University of Iowa; and Joss disdrometer data from Darwin is courtesy of Bureau of Meteorology Research Center, Melbourne. Each data point is based on 3-minute averaged *dsd*. The specific attenuation is at H-polarization for oblate raindrops at 0° elevation angle.

In the case of dual-polarized radar, the measured differential propagation phase along the path (being independent of signal attenuation) can be used to estimate the path attenuation directly or it can be used as a constraint to stabilize attenuation-correction procedures. From scattering theory, the specific attenuation (A_h in dB/km) of the H-polarized wave can be approximately linearly related to the K_{dp} (in °/km) as $A_h = \alpha K_{dp}$. The linearity is excellent at X and C-bands; the exponent b of a power law fit, $A_h = \alpha K_{DP}^b$, is 1.02 at 9.3 GHz and 0.99 at 5.5 GHz, Jameson (1992). The linearity is not as good at S-band, with $b = 0.84$.

Table 4.1 lists the different attenuation-correction methods along with their main advantages/disadvantages.

Table 4.1: Methods for correcting Z_h for attenuation

Method	Main advantage	Main disadvantage	Reference
Linear Φ_{dp} with fixed α	Simplicity; easy to implement in real-time	Unconstrained; can over or underestimate attenuation.	Bringi et al. 1990
Empirical linear Φ_{dp} with average α . Estimated from measured Z_h and Φ_{dp}	Moderately simple. Tends to correct for mean attenuation	Not straight-forward for real-time implementation. Inaccuracies due to non-homogeneous precipitation	Ryzhkov and Zrnić 1995 (for S-band) Carey et al. 2000 (for C-band)
Standard ZPHI	Constrained. Does not depend on Z calibration Undergoing (near) real-time testing	α is fixed apriori; does not account for temperature and drop shape effects. N_0 constant assumption.	Testud et al. 2000
Iterative ZPHI	Constrained. α is estimated optimally; accounts for drop shape and temperature effects Does not depend on Z calibration Near real-time implementation tested on BMRC-CPOL radar.	N_0 constant assumption. More computation intensive.	Bringi et al. 2001a

4.1 The linear Φ_{dp} method

By integrating over range, it is clear that the path-integrated attenuation (or, *PIA*) can be directly estimated from the change in Φ_{dp} if α can assumed to be constant. The attenuation-correction scheme then becomes very simple:

$$Z_h(r) = Z'_h(r) + 2\alpha \int_0^r K_{dp}(s)ds \quad (4.2a)$$

$$= Z'_h(r) + \alpha [\Phi_{dp}(r) - \Phi_{dp}(0)] \quad (4.2b)$$

where $Z'_h(r)$ is the observed reflectivity at range R in dBZ, $Z_h(r)$ is the corrected value and $\Phi_{dp}(0)$ is the system Φ_{dp} value. In this simple approach (termed the linear Φ_{dp} method) $K_{dp}(r)$ does not need to be computed. For stability and for suppression of the back scatter differential phase fluctuations, the filtered $\Phi_{dp}(r)$ should be used instead of the 'raw' Φ_{dp} . The coefficient α can vary between 0.01-0.04 dB/ $^\circ$ at S-band, 0.04-0.15 at C-band, and between 0.14-0.60 at X-band (Jameson 1992, Carey et al. 2000; Park et al. 2004). Typical values for α are 0.018 dB/ $^\circ$ at S-band, 0.08 at C-band and 0.25 at X-band. If it is assumed that the rain medium is uniform, then α can be estimated by fitting a straight line to pairs of data (Z'_h , Φ_{dp}) obtained from each

resolution volume along the path (α will be the slope of the least squares fit). Ryzhkov and Zrnić (1995) suggest that data points be chosen so that the corresponding K_{dp} lie in a narrow interval (1-2 °/km at S-band). Carey et al. (2000) have applied it at C-band. While this empirical method is difficult to implement, it does tend to estimate the average α for the specific data set. The dependence of α on the drop size distribution is significant only for large D_0 values ($D_0 > 3.0\text{ mm}$) which occurs only infrequently (big drop region). Ryzhkov and Zrnic (1995) deduced very high values for α at S-band which was attributed to rain mixed with melting ice. The prototype S-band NEXRAD algorithm uses equation (4.1) for attenuation correction with a locally 'tuned' α of 0.04 dB/km in Oklahoma.

4.2 The standard ZPHI method

In this approach (termed as ZPHI method), a power-law relation between A_h and Z_h is needed (of the form $A_h = a Z_h^b$) for rain, which may be obtained from simulations. The ZPHI method for correction of reflectivity at h-polarization is as follows. Consider a path from r_0 to R . The measured reflectivity Z'_h at range R can be expressed as (the subscript h is omitted in the following equation),

$$Z'(r) = Z(r) \exp\left(-0.46 \int_{r_0}^r A(s) ds\right) \quad (4.3)$$

where $Z(r)$ is the 'true' or intrinsic reflectivity at range R and $A(s)$ is the specific attenuation. Starting from the above equation an expression for $A(r)$ can be derived as (for details see Section 7.4.2 of Bringi and Chandrasekar 2001):

$$A_h(r) = \frac{[Z'_h(r)]^b (10^{0.1b\alpha \Delta \Phi_{dp}(r_0; r_m)} - 1)}{I(r_0; r_m) + (10^{0.1b\alpha \Delta \Phi_{dp}(r_0; r_m)} - 1) I(r; r_m)} \quad (4.4)$$

where r_0, r_m are the begin and end points along the beam and,

$$I(r_0; r_m) = 0.46 b \int_{r_0}^{r_m} [Z'_h(r)]^b dr \quad (4.5)$$

The above specific attenuation, when converted to P/A by integration along range, is constrained by the measured Φ_{dp} which stabilizes the attenuation-correction algorithm (Testud et al 2000). Only the exponent b is needed in the formulation; b is quite stable with respect to variations in both the dsd as well as temperature (e.g., at S-band $b = 0.74$; at C and X-bands $b = 0.78$, Testud et al. 2000).

Le Bouar et al. (2001) have used such segmentation along with stratiform/convective separation using their standard ZPHI algorithm. Their algorithm provides an estimate of the 'normalized' intercept parameters (N_w or N'_o ; same as N_0 for exponential dsd) for each segment. It is not clear if such additional complexity is needed for attenuation correction.

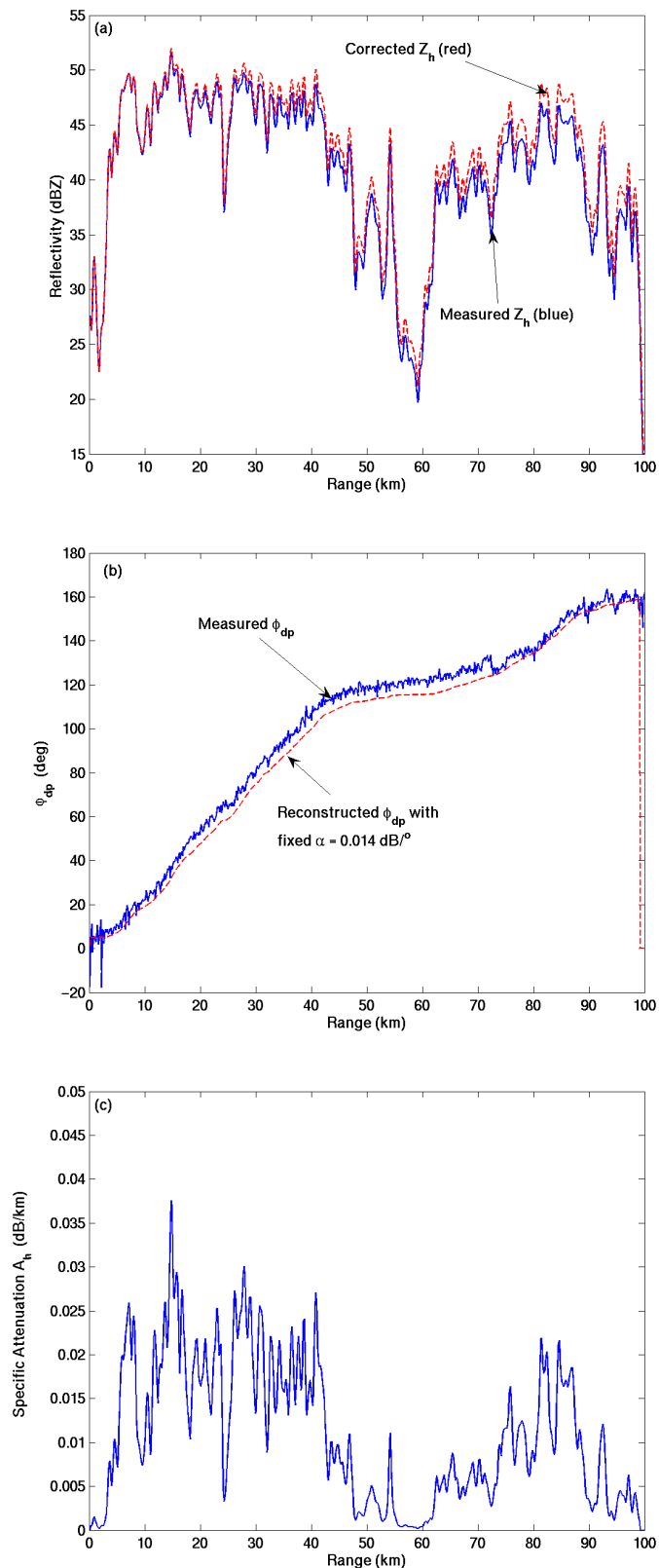


Fig. 4.2: Range profile from NCAR/SPOL radar for a squall line event in Brazil taken on 26 January 1999 at an elevation of 1.1° : (a) measured and attenuation-corrected Z_h , (b) measured Φ_{dp} and reconstructed Φ_{dp} with preset $\alpha = 0.014 \text{ dB}^{\circ}$ and (c) the specific attenuation. Data made available from NCAR.

Evaluation of attenuation-correction methods at S-band using the CSU-CHILL and SPOL radar indicate that the linear Φ_{dp} algorithm with preset $\alpha = 0.014 \text{ dB}^\circ$ is appropriate when total $\Phi_{dp} < 25\text{--}50^\circ$; for large Φ_{dp} , the standard ZPHI method is preferred because of the constraint used. An example is shown in Fig. 4.2 using the NCAR/SPOL radar. The observations were taken in Brazil during a squall line event. The top panel shows the observed (or measured) reflectivity for horizontal polarization and the corrected reflectivity. The middle panel shows the measured and reconstructed Φ_{dp} profiles and the bottom panel shows the specific attenuation determined using equation (4.4). At 90 km distance, the cumulative correction for the reflectivity is just over 2 dB.

4.3 I-ZPHI: The iterative ZPHI method for C and X-band radars

For better accuracy, another method of attenuation correction is proposed which estimates an 'optimal' α from the measured data itself using an iterative extension of the ZPHI method (Bringi et al 2001a). At S-band, application of this method is not necessary due to the relatively small attenuation. Instead, the linear Φ_{dp} Method or the standard ZPHI method is sufficient. Thus this chapter focuses on C- and X-band application.

While the coefficient a (of the relation $A_h = a Z_h^b$) is not needed in the formulation of the I-ZPHI method, it is implicitly assumed that a is constant along the path. In terms of an exponential dsd form for example, it implies that the N_0 is constant along the path but D_0 is allowed be variable. Note that N_0 and D_0 are defined in $N(D) = N_0 \exp(-3.67D/D_0)$ which is the Marshall-Palmer exponential form. Such an assumption is necessary here as the exact specific attenuation depends on the dsd and such information is not available apriori. Note that the I-ZPHI method does not assume apriori the exponential form for the dsd . For greater accuracy it is possible to separately treat different convective cells that occur along the path using the I-ZPHI algorithm.

However, as mentioned previously the I-ZPHI method of determining an 'optimal' α will improve the accuracy of attenuation-correction. Since the range of α is known apriori, we compute $A_h(r; \alpha)$ for all values in the range α_{\min} to α_{\max} . Then we compute 're-constructed' range profiles of $\Phi_{dp}^c(r; \alpha)$ as,

$$\Phi_{dp}^c(r; \alpha) = 2 \int_{r_0}^r \frac{A_h(s; \alpha)}{\alpha} ds ; \quad \alpha_{\min} \leq \alpha \leq \alpha_{\max} \quad (4.6)$$

The optimal value of α is selected by minimizing the difference (*Error* in equation (4.7) below) between the 're-constructed' Φ_{dp}^c range profiles and the (filtered) version of the measured Φ_{dp} over the path from r_0 to r_m :

$$Error = \sum_{j=1}^N \left| \Phi_{dp}^{filt}(r_j) - \Phi_{dp}^c(r_j; \alpha) \right| \quad (4.7)$$

Once the optimal α is determined, the range profile of $A_h(r; \alpha_{opt})$ is obtained and the correction follows from:

$$Z_h(r) = Z'_h(r) + 2 \int_{r_0}^r A_h(s; \alpha_{opt}) ds \quad (4.8)$$

where r_0 is the initial range at the beginning of the path. The idea here is that not only is the attenuation-correction constrained by the total Φ_{dp} across the path, but in addition, the 're-constructed' profile of Φ_{dp} (which depends on α) is made to be as close to the measured Φ_{dp} profile as possible. The following examples illustrate the application of the I-ZPHI method.

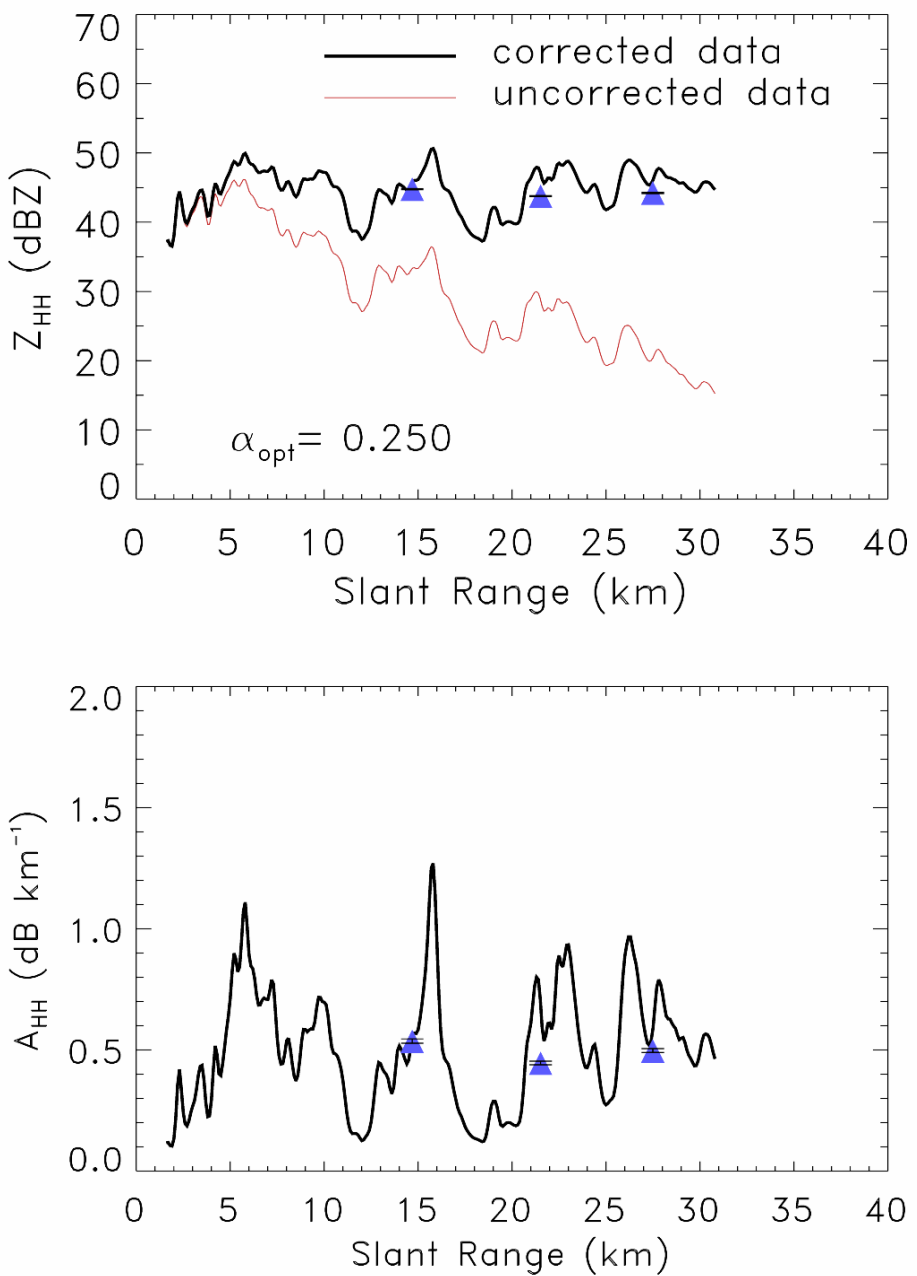


Fig. 4.3: Range profile from the MP-X band radar located in Tsukuba, Japan for the typhoon event of 11 September 2001. Elevation angle is 2.5°, azimuth angle is 294° (see PPI data in Fig. 4.5). (a) measured (observed) and attenuation-corrected Z_h , and (b) specific attenuation. The three solid triangle marks are computed from Joss disdrometers located along the radial at 294° (see Fig. 4.5). Adapted from Park et al (2005).

Fig. 4.3a shows an example of uncorrected and corrected Z_h versus range from an X-band radar in a Typhoon event near Tsukuba, Japan (Park et al 2004) using the above correction methodology. This radar (MP-X) is operated by the National Research Institute for Earth Science and Disaster Prevention (NIED), Tsukuba,

Japan and the data shown here are provided courtesy of Dr. Masayuki Maki of NIED; see Iwanami et al (2001). This radar uses slant 45° transmission (pulse width of $0.5 \mu\text{s}$) with two receivers for the H and V polarizations. The PRF is 1800 s^{-1} and typical integration is 256 samples with azimuthal sampling of 0.5° .

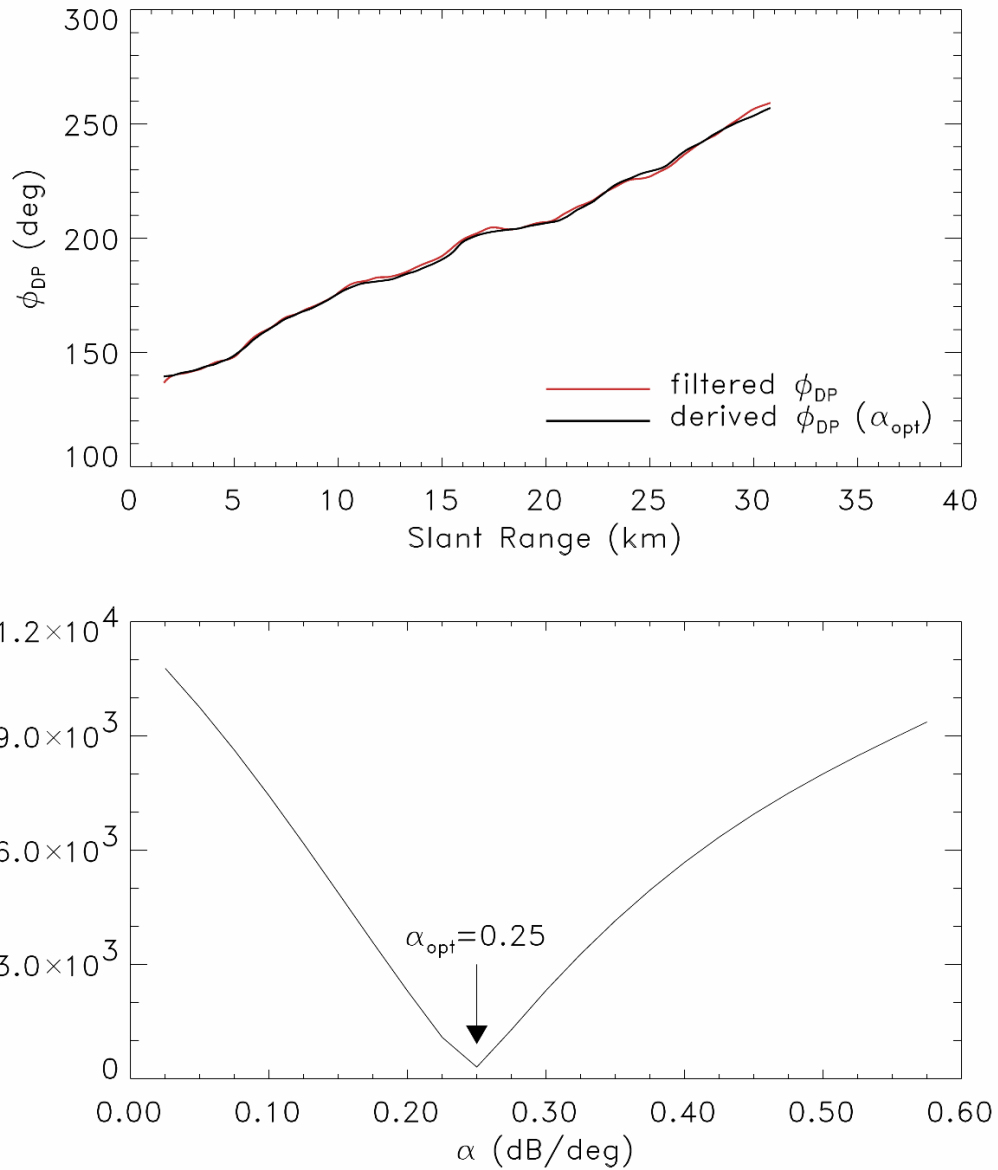


Fig. 4.4: As in Fig. 4.3 except (a) compares the measured Φ_{dp} with the re-constructed Φ_{dp} (see equation (4.6)) using the optimal α . (b) shows the Error in equation (4.7) versus α to illustrate determination of the optimal α . Adapted from Park et al (2005).

The range profile in Fig. 4.3 was chosen as there were three disdrometers located along the path permitting an evaluation of the attenuation-correction method. Reflectivity computed from the measured drop size distributions at the three locations are shown and seen to agree quite well (within 1-2 dB) with the attenuation-corrected Z_h . The optimal α for this path is estimated at 0.25 dB° . Fig. 4.3b shows the specific

attenuation (A_h) profile using the optimal α (in equation (4.8)) and it is seen to agree well with calculations of A_h using the disdrometer-measured drop size distributions at the three locations. Fig. 4.4a compares the measured Φ_{dp} with the 're-constructed' or 'derived' Φ_{dp} with optimal α (see equation (4.6)) which demonstrates excellent agreement and gives confidence in the estimated specific attenuation profile. Fig. 4.4b shows the error versus α (see equation (4.7)) demonstrating that an optimal α value can be determined for this beam. It has also been determined that the optimal α varies quite smoothly from one azimuthal angle to the next.

Fig. 4.5 shows a sector PPI sweep from the same typhoon event (at elevation angle of 2.5°) of the observed Z_h (or, $Z_{HH,uncorr}$ in left panel) and the attenuation-corrected Z_h (or, $Z_{HH,corr}$, right panel) along with the locations of the three disdrometers. Note, in particular, how the correction procedure 'restores' the reflectivity field along the radial line (at 294° azimuth) as shown. Loss of signal due to extreme attenuation can also be noted beyond the range of 25 km in the sector 270°–290°.

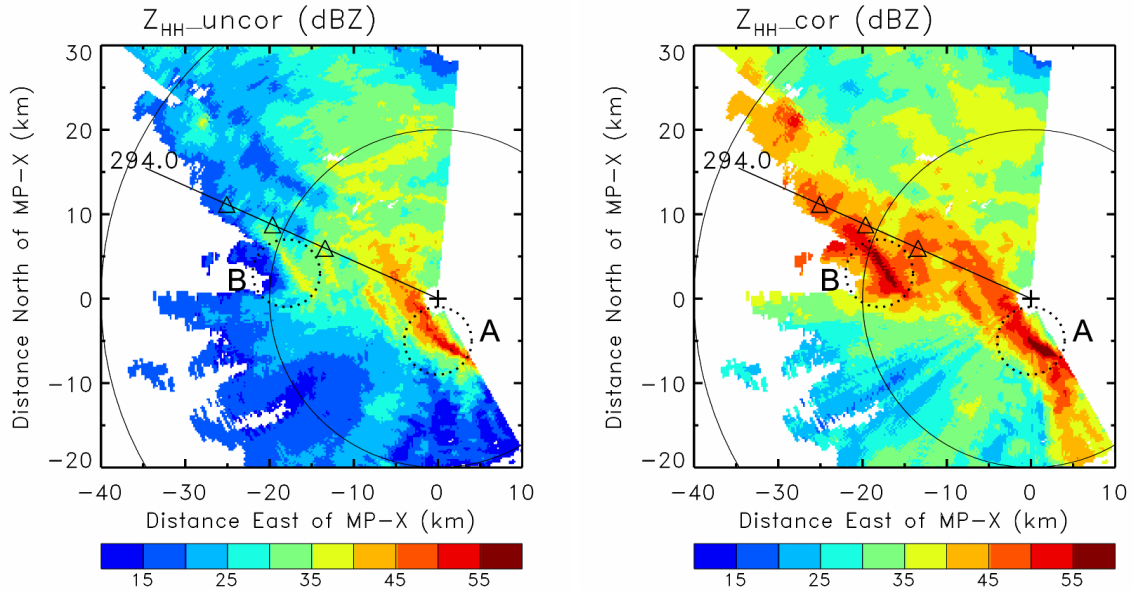


Fig. 4.5: PPI scan from the 11 September 2001 typhoon event using the MP-X band radar. Left panel shows the measured (observed) Z_h and, right panel shows the attenuation-corrected Z_h . The three triangles mark the location of the Joss disdrometers. Adapted from Park et al (2005)

The attenuation-correction procedure at C-band is, in principle, the same as at X-band except for the change in the α range. Fig. 4.6 shows, (a) the observed and corrected reflectivity range profiles, and (b) the measured Φ_{dp} and the 're-constructed' Φ_{dp} for an optimal α of 0.055 dB/° (about a factor of 5 lower than at X-band). These data are from the BMRC/C-POL radar located in Darwin, Australia. The total Φ_{dp} excursion across the entire range path is 180° in this case. Note the 10 dB correction in reflectivity at the end of the beam. Note, also, the excellent agreement between the measured Φ_{dp} and the 're-constructed' Φ_{dp} along the entire path demonstrating

the stability of the technique. Fig. 4.7 shows a PPI scan from this same event with (a) showing the observed reflectivity and (b) the corrected reflectivity.

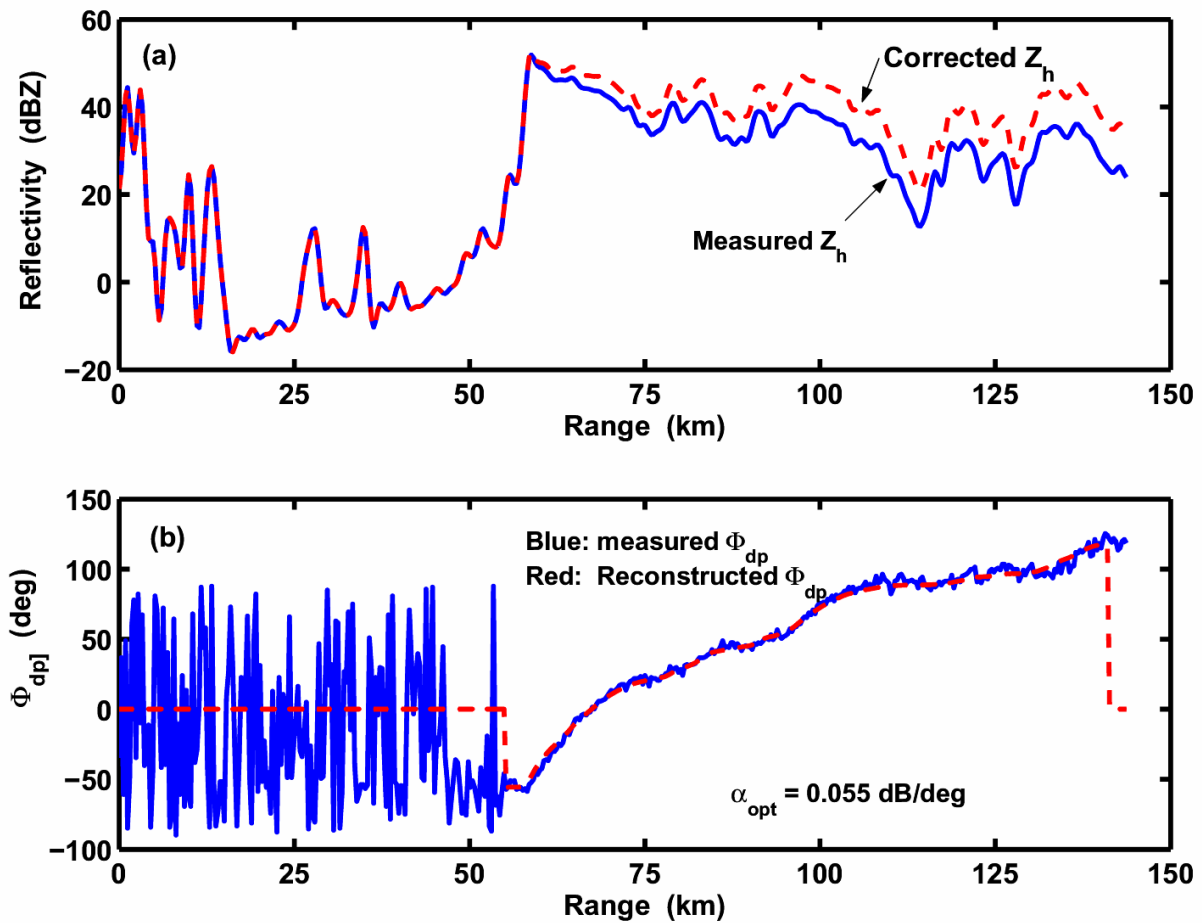


Fig. 4.6: Range profile along azimuth angle of 60° (see PPI scan in Fig. 3.4) illustrating (a) the measured and attenuation-corrected Z_h , and (b) measured Φ_{dp} and reconstructed Φ_{dp} (using equation (4.6) with optimal α of 0.055 dB/deg). Data from the BMRC/C-POL radar located in Darwin.

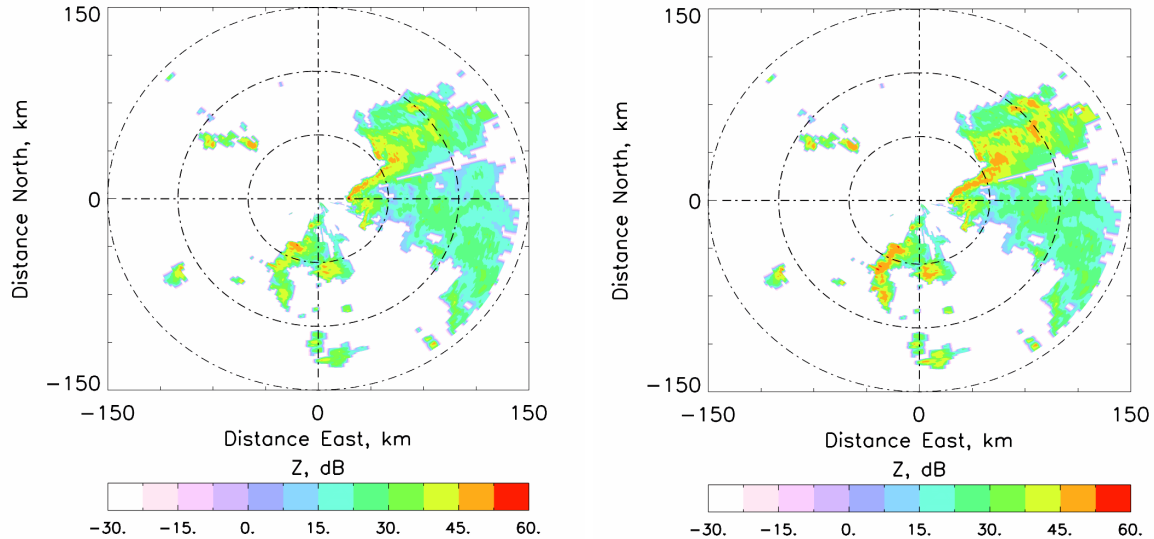


Fig. 4.7: As in Fig. 3.4 except (a) measured Z_h , and (b) attenuation-corrected Z_h . Data from the BMRC/C-POL radar located in Darwin.

From an operational perspective, the major advantage of the attenuation-correction scheme described here is its stability, and non-dependence on an absolute calibration of the radar (i.e., the radar constant used to convert measured power to equivalent reflectivity factor). However, there must be enough signal in the H and V-receivers to enable the measurement of Φ_{dp} at the end of the path, i.e., the path attenuation, especially at X-band, must not be large enough to incur loss of signal. This consideration limits the use of X-band in convective rain to short ranges (around 50-60 km) but is not, generally, a factor at C-band. Typically, the results shown here are valid for SNR of at least 3 dB but this threshold could be pushed down even further (i.e., same SNR as that needed for reliable mean Doppler velocity estimation). Since only range-filtered Φ_{dp} profiles are used, a larger measurement fluctuation (or, standard deviation) can be tolerated for the Φ_{dp} resulting in a smaller number of samples for integration and shorter dwell times. Good accuracy can be achieved, in practice, with 64 samples for integration, PRT of 1 ms and antenna rotation rates of around 15 °/s leading to angular beam spacing of 1°.

5 Correcting the Measured Z_{dr} for Differential Attenuation due to Rain

Highly oriented oblate raindrops along the beam cause the H-polarized wave to attenuate more than the V-polarized wave. In essence, the path-integrated differential attenuation between H and V waves is nearly linearly proportional to the path-integrated Φ_{dp} , or the specific differential attenuation A_{dp} is nearly linear with K_{dp} , i.e.

$$A_{dp} = A_h - A_v = \beta K_{dp} = [\beta / \alpha_{opt}] A_h \quad (5.1)$$

where A_{dp} is given in dB/km . The expression on the right side of this equation results from $A_h = \alpha_{opt} K_{dp}$. The coefficient β has nominal values of 0.003 $dB/^{\circ}$ at S-band, 0.02 at C-band and 0.035 at X-band. If the non-linearity is considered using a power law fit $A_{dp} = \beta K_{dp}^b$, the exponent b is 1.05 at 2.8 GHz (S-band), 1.23 at 5.5 GHz (C-band) and 1.15 at 9.3 GHz (X-band; Jameson 1992). This small non-linearity is usually neglected, i.e. equation (5.1) is used.

5.1 The linear Φ_{dp} method

Similar to α , the coefficient β can be considered to be constant along the beam. Then, the corrected Z_{dr} results from the measured Z'_{dr} quite simply,

$$Z_{dr}(r) = Z'_{dr}(r) + \beta [\Phi_{dp}(r) - \Phi_{dp}(0)] \quad (5.2)$$

For the same reason that α lies within a range of values so does the coefficient β (0.02–0.05 at X-band and 0.01–0.03 at C-band and 0.001–0.004 $dB/^{\circ}$ at S-band). Similar to α , the coefficient β is dependent on the dsd only for $D_0 > 3 mm$ which occurs only infrequently (big drop region). In homogeneous rain β can be estimated as the slope of the least squares fit to pairs of (Z'_{dr}, Φ_{dp}) data obtained from resolution volumes along the beam/scan (Ryzhkov and Zrnić 1995; Carey et al. 2000). Ryzhkov and Zrnic (1995) deduced very high values for $\beta = 0.004 dB/^{\circ}$ at S-band which was attributed to rain mixed with melting ice. The prototype S-band NEXRAD algorithm uses (4.2) for attenuation correction with a locally ‘tuned’ β of 0.004 $dB/^{\circ}$ in Oklahoma, which is at the higher end of the range for β quoted earlier. This is due to the high probability of large drops and small melting hail in Oklahoma thunderstorms.

One method of estimating β , involves an extension of the method proposed by Smyth and Illingworth (1998). Considering the far end of the precipitation, i.e. setting r to r_m in equation (5.2), the total differential attenuation $\Delta Z_{dr} = Z_{dr}(r_m) - Z'_{dr}(r_m)$ can be evaluated, since an estimation of the ‘true’ $Z_{dr}(r_m)$ at the end of the path can be derived. If, for example, the end of the last ‘good’ data segment contains very light drizzle, $Z_{dr}(r_m)$ should tend to 0 dB (spherical drops) which is the assumption used by Smyth and Illingworth (1998). If the end of the last ‘good’ data segment is in moderate rain, its ‘true’ Z_{dr} will be greater than 0 dB . An estimate of the ‘true’ $Z_{dr}(r_m)$

can be obtained from the corrected reflectivity $Z_h(r_m)$ by setting up a relation between mean Z_{dr} and mean Z_h . Fig. 5.1, Fig. 5.2 and Fig. 5.3 show Mie scattering simulation results at S-, C- and X -bands using 2D-video disdrometer data acquired from a wide range of climates such as Graz (Austria), Papua New Guinea, Florida, and Joss disdrometer from Darwin (Australia). Also shown are the mean fits used to predict $Z_{dr}(r_m)$ from $Z_h(r_m)$.

Once the 'true' $Z_{dr}(r_m)$ at the far end of the precipitation has been derived, an estimate of β for the beam can be obtained:

$$\beta = \frac{\Delta Z_{dr}(r_m)}{[\Phi_{dp}(r_m) - \Phi_{dp}(0)]} \quad (5.3)$$

which is then used to correct the measured Z_{dr}' according to equation (5.2). This method for Z_{dr} correction is referred to here as the constrained SI (Smyth and Illingworth) method.

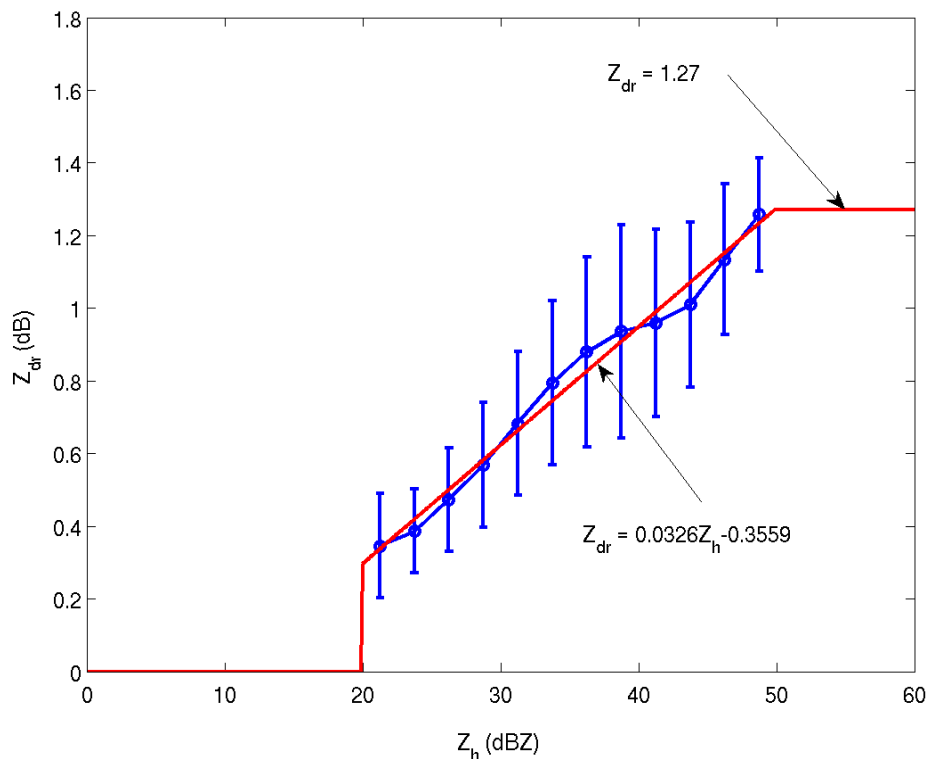


Fig. 5.1: Simulation of mean Z_{dr} vs. Z_h at 2.8 GHz (S-band) based on Joss disdrometer data from Darwin, Australia. The straight line is used to predict $Z_{dr}(r_m)$ from the corrected $Z_h(r_m)$. Note that we assume $Z_{dr}(r_m) = 0$ dB for $Z_h(r_m) < 20$ dBZ at the end of the last 'good' data segment.

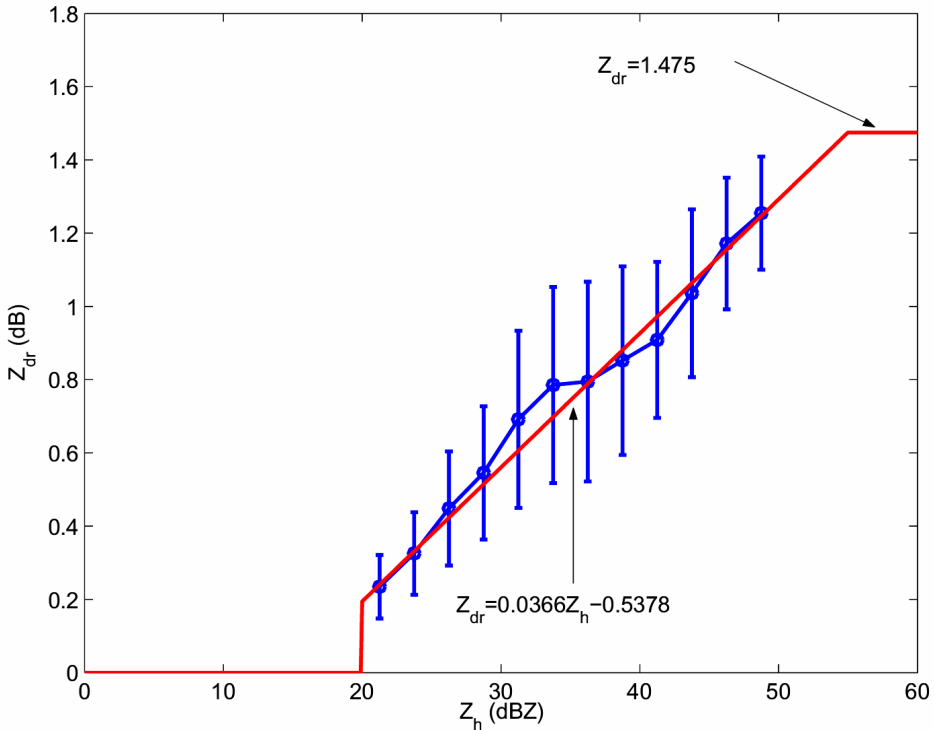


Fig. 5.2: Simulation of mean Z_{dr} vs. Z_h at 5.6 GHz (C-band) based on Joss disdrometer data from Darwin, Australia. The straight line is used to predict $Z_{dr}(r_m)$ from the corrected $Z_h(r_m)$. Note that we assume $Z_{dr}(r_m) = 0 \text{ dB}$ for $Z_h(r_m) < 20 \text{ dBZ}$ at the end of the last 'good' data segment.

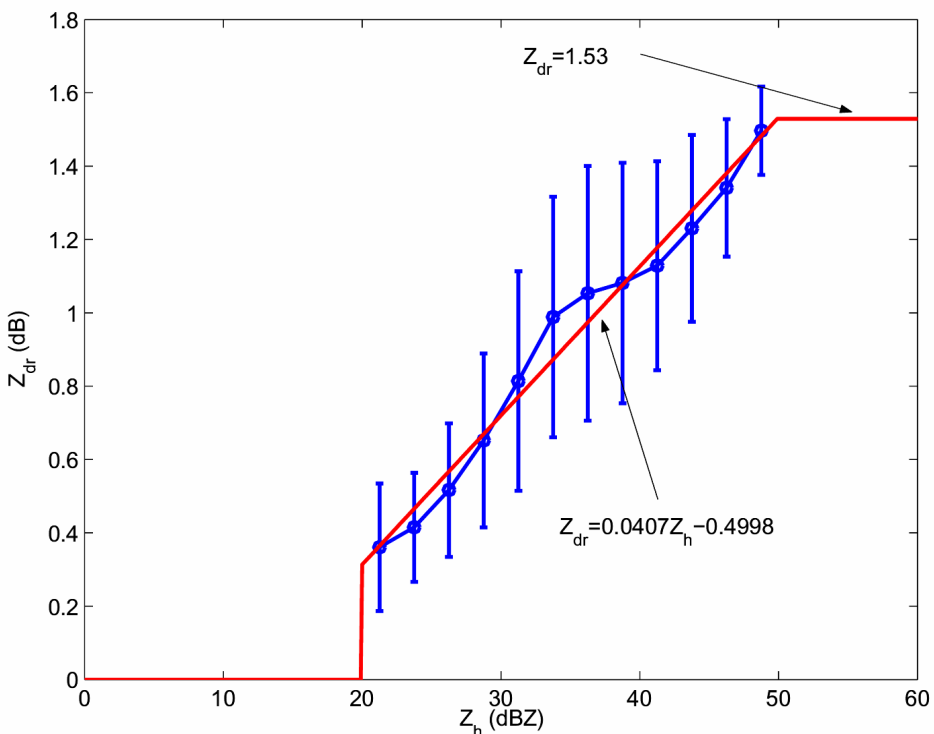


Fig. 5.3: As in Fig. 5.2 except at 9.3 GHz (X-band). Simulations use 2D-Video disdrometer data from Graz, Papua New Guinea, Florida and Joss disdrometer data from Darwin.

5.2 The A_h -scaled method

Since the specific attenuation profile, $A_h(r)$, can be first calculated using the iterative ZPHI method (or the standard ZPHI / linear Φ_{dp} method at S-band), it follows from the linearity between A_{dp} and A_h (see equation (5.1)) that the $A_h(r)$ can simply be scaled downward to estimate $A_{dp}(r)$, resulting in the Z_{dr} correction as follows:

$$Z_{dr}(r) = Z'_{dr}(r) + 2 \int_0^r A_{dp}(s)ds \quad (5.4)$$

$$= Z'_{dr}(r) + 2\gamma \int_0^r A_h(s)ds \quad (5.5)$$

where $\gamma = \beta/\alpha_{opt}$, with β determined as in equation (5.3). In practice, it is convenient to set γ to a suitable initial value ($\gamma_1 = 1$, say) and compute $Z_{dr}^1(r_m)$ using equation (5.5). The optimal γ can then be obtained as:

$$\gamma_{opt} = \frac{\Delta Z_{dr}(r_m)}{|Z_{dr}^1(r_m) - Z'_{dr}(r_m)|} \quad (5.6)$$

The A_h – scaled method of Z_{dr} correction is different from the linear Φ_{dp} method described earlier as it assumes that $A_h(r)$ is calculated first using the iterative ZPHI method whereas in the linear Φ_{dp} method such apriori estimation of $A_h(r)$ is not required. An example of using the A_h – scaled method is illustrated in Fig. 5.4a which shows a range profile of observed Z'_{dr} and corrected Z_{dr} from the NIID/MP-X radar (same typhoon event as shown in Fig. 4.5) with 'optimal' $\gamma = 0.119$. That the Z_{dr} correction is reasonable is demonstrated by the close agreement with the Z_{dr} calculated from drop size distributions measured by Joss disdrometers at the three marked locations along the beam. Fig. 5.4b shows the range profile of A_{dp} . As a consequence of the right side of equation (5.1), this is simply a scaled version of the A_h already estimated (see Fig. 4.3b).

Fig. 5.5 shows a sector PPI scan of observed Z'_{dr} (left panel) and corrected Z_{dr} (right panel) for the same typhoon event. Note again how the constrained SI procedure 'restores' the Z_{dr} field, especially in the azimuth sector 180° – 300° .

From an operational perspective, the use of Z_{dr} at X-band may be limited to hydrometeor classification (e.g., hail detection) rather than rainfall estimation since the correction for differential attenuation is approximate and is not expected to be accurate to within ± 0.2 dB that is needed for improving rainfall estimation.

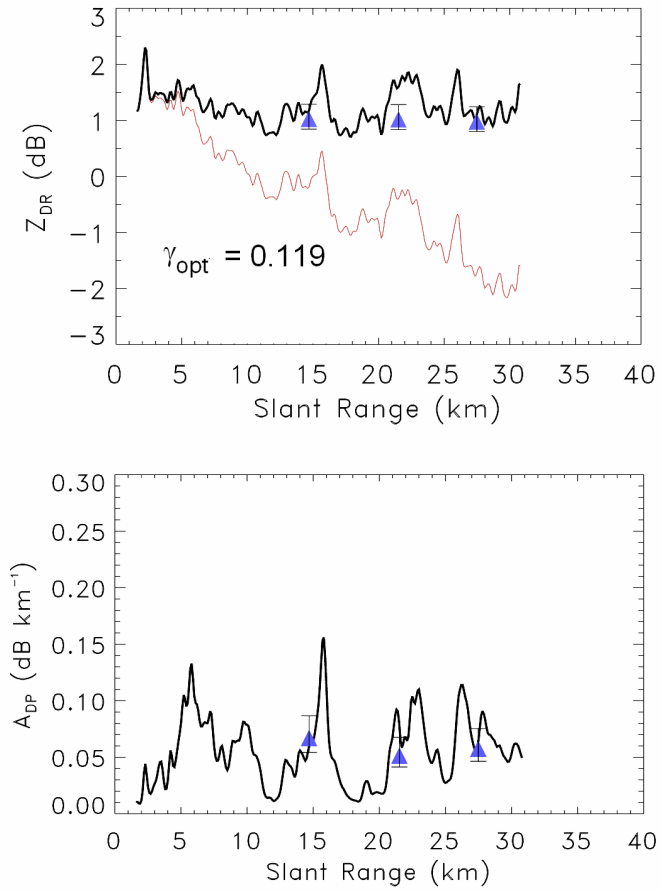


Fig. 5.4: As in Fig. 4.3 except (a) shows measured (observed) Z'_{dr} and Z_{dr} corrected for differential attenuation. (b) Profile of specific differential attenuation (A_{dp}). From Park et al. (2005).

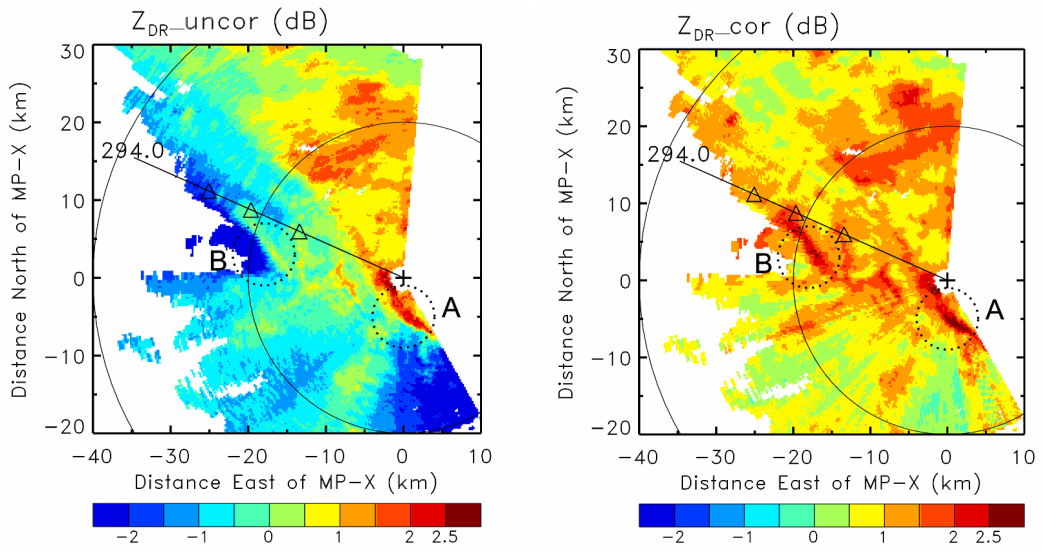


Fig. 5.5: As in Fig. 4.5 except left panel shows measured (observed) Z'_{dr} and right panel shows Z_{dr} corrected for differential attenuation. From Park et al. (2005).

An example of using the scaled A_h method for Z_{dr} correction at S-band is shown in Fig. 5.6. The top panel shows the measured Z_{dr} and the corrected Z_{dr} whilst the bottom panel shows the specific differential attenuation determined using equation (5.3). The range profiles correspond to the squall-line event in Brazil referred to earlier in Section 4.2 (see Fig. 4.2). At 90 km distance, the cumulative correction for differential reflectivity is less than 0.5 dB.

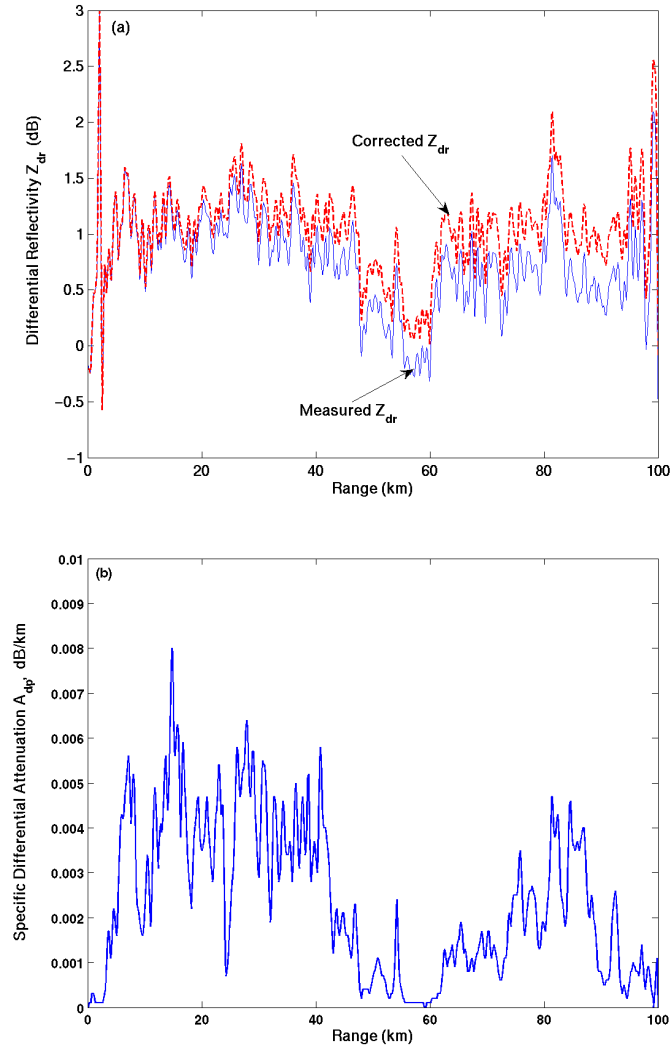


Fig. 5.6: Range profile from NCAR/SPOL radar for a squall line event in Brazil taken on 26 January 1999 referred to in Fig. 4.2: (a) measured and corrected Z_{dr} , and (b) the specific differential attenuation. Data made available from NCAR.

6 Rainfall Estimation

For a single-polarized radar, the rain rate is estimated using a $Z-R$ power law relation, which is theoretically derivable given a form for the drop size distribution, and assuming Rayleigh scattering (D^6 law) and a power law form for the terminal fall speed of drops ($D^{0.67}$). Even with a perfectly calibrated radar, it is well-known that use of an 'untuned' $Z-R$ relation can lead to unacceptable biases in the rainfall amounts. Also, provision must be made for using different $Z-R$ relations for stratiform rain versus convective rain based on the microphysics of rain formation (see Fig. 2.4). For convective rain, different $Z-R$ relations need to be used for maritime or continental rain types. At X-band and in more intense rain at C-band, the situation is exacerbated because of the need for correction due to rain attenuation. Within the interior cores of convective precipitation (especially at mid-latitudes) the probability of hail mixed with rain is high and the resulting Z might be truncated (say at 55 to 60 dBZ) to avoid a large 'hail' bias in rainfall amounts using a $Z-R$ relation. In cold season precipitation, the rain/snow boundary has to be identified to avoid rainfall estimation errors which is generally not possible when using reflectivity data alone. Also, at far ranges the beam intercepts the 'bright-band' causing an overestimate in rain amounts unless corrected for. Many of these factors that limit the application of single-polarized radar for rainfall estimation can be overcome by use of dual-polarized systems.

The use of K_{dp} to estimate rainfall has a number of advantages over power measurements:

- independent of receiver and transmitter calibrations,
- unaffected by attenuation,
- relatively immune to beam blockage,
- unbiased by ground clutter cancellers,
- unbiased by presence of hail or other 'spherical' ice particles in the resolution volume, and
- improved detection of anomalous propagation (AP) (see Zrnić and Ryzhkov 1999).

At this time there is no general consensus on an 'optimal' algorithm for estimating rainfall at C or X-bands, though there are several different but related methods that have been evaluated (Matrosov et al 2002, Anagnostou et al 2004, and Park et al 2004 for X-band; May et al 1999, Bringi et al 2001b, and Testud et al 2000 at C-band). The situation at S-band is more complete and an operational algorithm (see Section 6.3.1) is being used on the prototype WSR-88D system in Norman, Oklahoma operated by the National Severe Storms Laboratory of NOAA (Ryzhkov et al 2003). Here we take the conservative approach and propose two application scenarios, (a) areal rainfall accumulation over watershed-type areas building up from smaller polar areas (typically 5-10 km x 5-10°), and (b) higher resolution rain rate estimation along the beam (typically 3km x 1°).

6.1 Areal Φ_{dp} method

The areal rainfall, AR , can be defined as,

$$AR = \iint R(x, y) dx dy \quad (6.1)$$

where $R(x, y)$ is the instantaneous rain rate field. The mean areal rain rate, \bar{R} , is defined as AR divided by the corresponding area. The use of polar coordinates is suitable for low elevation angle radar data acquired in the conventional PPI scan mode. If r is the range and θ is the azimuth angle, the areal rainfall in polar coordinates is,

$$AR = \int_{r_1}^{r_2} \int_{\theta_1}^{\theta_2} R(r, \theta) r dr d\theta \quad (6.2)$$

If a linear relationship between R and K_{dp} is assumed of the form $R = c K_{dp}$, and using $K_{dp} = \frac{1}{2} \frac{d}{dr} \Phi_{dp}$, equation (6.2) can be expressed as,

$$AR = \frac{c}{2} \int_{\theta_1}^{\theta_2} d\theta \int_{r_1}^{r_2} \frac{d}{dr} \Phi_{dp}(r, \theta) r dr \quad (6.3a)$$

$$= \frac{c}{2} \int_{\theta_1}^{\theta_2} d\theta \int_{r_1}^{r_2} r d\Phi_{dp}(r, \theta) \quad (6.3b)$$

Integrating by parts results in,

$$AR = \frac{c}{2} \int_{\theta_1}^{\theta_2} \left\{ [r_2 \Phi_{dp}(r_2, \theta) - r_1 \Phi_{dp}(r_1, \theta)] - \int_{r_1}^{r_2} \Phi_{dp}(r, \theta) dr \right\} d\theta \quad (6.4)$$

In the above formula, for a given beam with constant θ , AR depends on its boundary values at r_1 and r_2 as well as on the area under the Φ_{dp} versus range profile. As the azimuthal angle changes from θ_1 to θ_2 , an areal sweep of Φ_{dp} over the rain region occurs naturally performing a spatial integration of the rainfall. Thus, it is not necessary to estimate $K_{dp}(r)$ which is a "noisy" field because it is obtained as one-half of the range derivative of $\Phi_{dp}(r)$. Instead, the $\Phi_{dp}(r)$ can be easily smoothed in range (Section 3) and an accurate estimate of AR becomes readily available.

6.1.1 The CSU-algorithm

A certain amount of error arises in the above method since the $R-K_{dp}$ relation is somewhat non-linear. To reduce this error, a piece-wise linear fit is proposed as illustrated in Fig. 6.1. The data points are based on 2-minute averaged drop size distributions (*dsd*) from a Joss disdrometer located in Darwin, N. Territory, Australia. These data are representative of an entire rainy season in Darwin. The K_{dp} calculations are performed at a frequency of 5.5 GHz (C-band) and assuming that raindrop axis ratios (for $1 \leq D \leq 4 \text{ mm}$) obey the relation given in Andsager et al. (1999), and for $D < 1 \text{ mm}$ or $D > 4 \text{ mm}$ the relation given in Beard and Chuang

(1987). In addition, a Gaussian canting angle distribution is assumed with zero mean and standard deviation of 10° . This model is believed to be applicable for tropical rainfall. The multiplicative coefficient c in equation (6.4) is selected from the piecewise fit based on the average K_{dp} value in the range interval r_1 to r_2 for any given beam. When AR is divided by the corresponding area, it will be termed the \bar{R}_{csu} algorithm or simply the CSU-algorithm (Bringi et al 2001b). Fig. 6.2 and Fig. 6.3 give the piece-wise linear fit at X-band and S-band respectively.

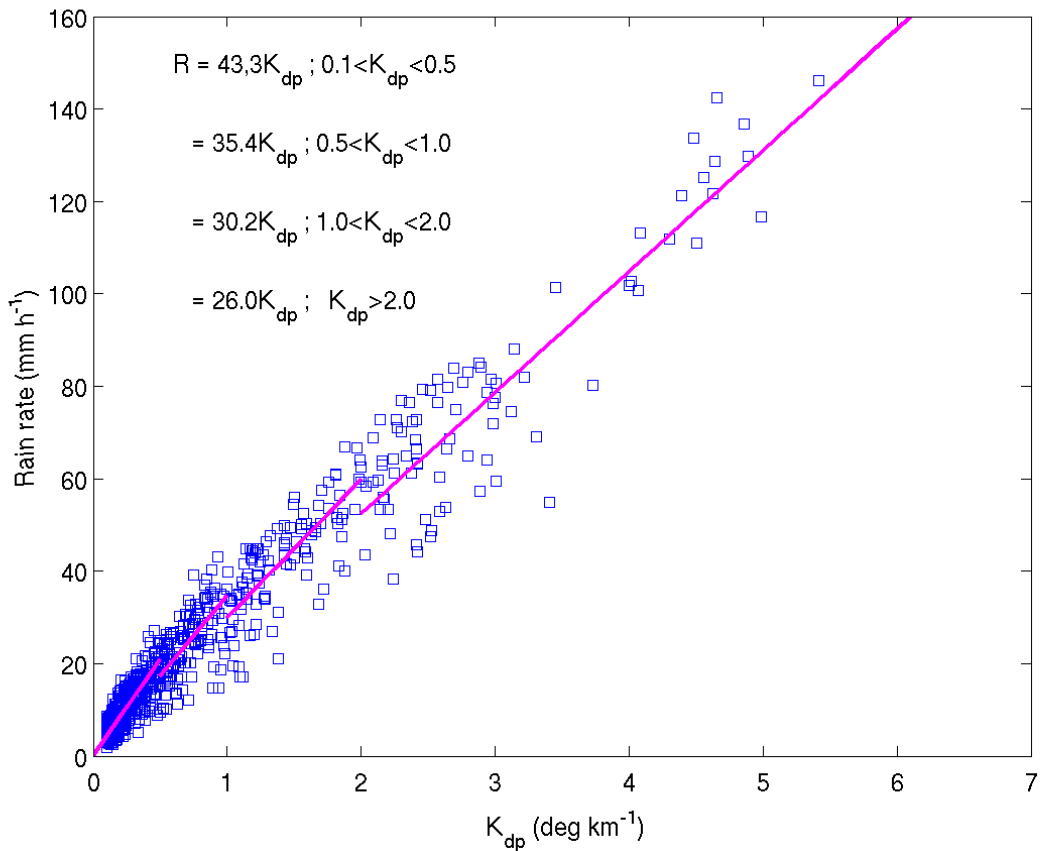


Fig. 6.1: Scattering simulations at C band based on measured drop size distributions from Darwin (each data point refers to a 2-min averaged *dsd*). Also, the piecewise linear fit is illustrated. A nonlinear fit to the data points results in $R = 32.4 K_{dp}^{0.83}$.

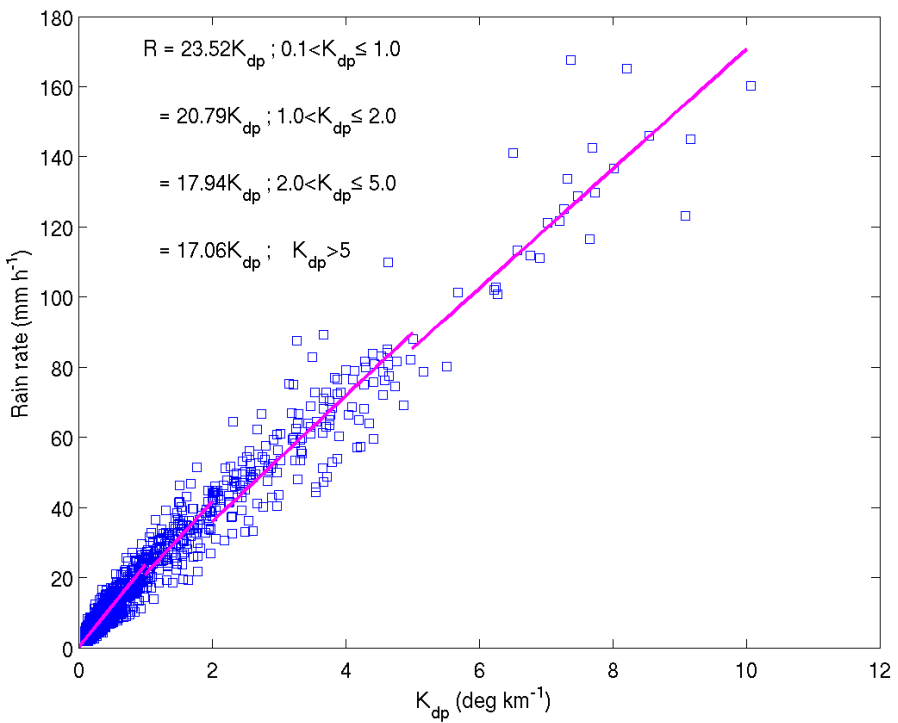


Fig. 6.2: As in Fig. 6.1 except data from Florida, Papua New Guinea, Graz and Darwin and simulated at X-band (9.3 GHz). A nonlinear fit to the data points results in $R = 21.4 K_{dp}^{0.88}$.

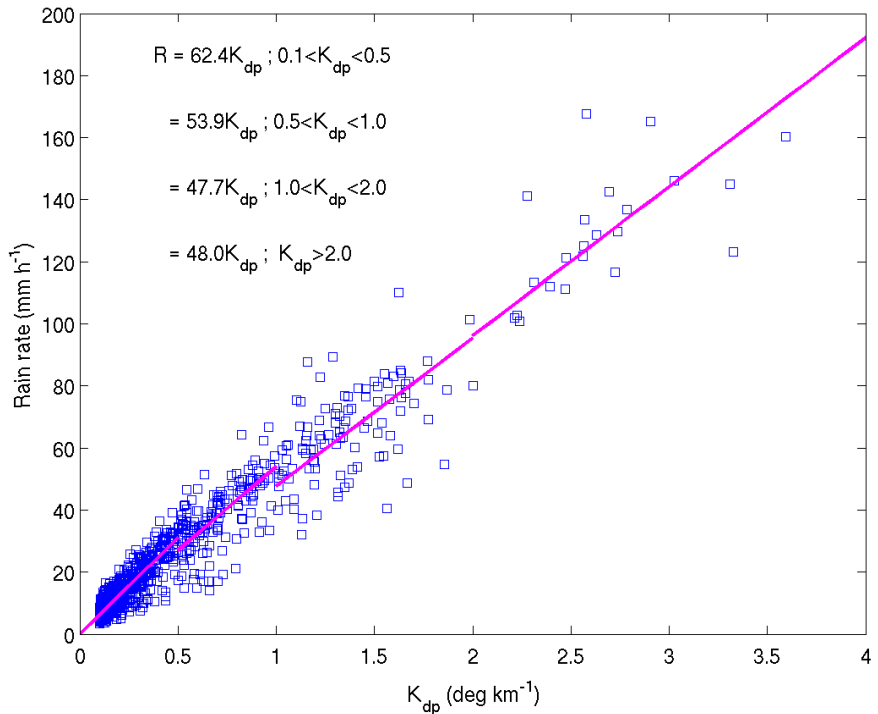


Fig. 6.3: As in Fig. 6.1 except at S-band (2.8 GHz). A non-linear fit to the data points results in $R = 52 K_{dp}^{0.88}$.

6.1.2 The RZF-algorithm

An alternate formula for AR proposed and evaluated at S-band by Ryzhkov et al. (2000), henceforth referred to as RZF-algorithm, is based on a non-linear relation; at C-band it is $R = a K_{dp}^b$ (here, $a = 32.4$, $b = 0.83$ from scattering simulations described above). It is assumed that $K_{dp}(r, \theta)$ is constant for a given θ . It follows that equation (6.2) can be simplified as,

$$AR_{rzf} = \int_{\theta_1}^{\theta_2} d\theta \int_{r_1}^{r_2} a K_{dp}^b(r, \theta) r dr \quad (6.5)$$

$$= \frac{a}{2} (r_2^2 - r_1^2) \int_{\theta_1}^{\theta_2} K_{dp}^b(\theta) d\theta \quad (6.5b)$$

$$= \frac{a}{2} (r_2 + r_1)(r_2 - r_1) \int_{\theta_1}^{\theta_2} d\theta \left[\frac{\Phi_{dp}(r_2, \theta) - \Phi_{dp}(r_1, \theta)}{2(r_2 - r_1)} \right]^b \quad (6.5c)$$

$$= \frac{a}{2} \frac{r_2 + r_1}{2} [2(r_2 - r_1)]^{1-b} \int_{\theta_1}^{\theta_2} [\Phi_{dp}(r_2, \theta) - \Phi_{dp}(r_1, \theta)]^b d\theta \quad (6.5d)$$

The above AR divided by the corresponding area will be referred to as the \bar{R}_{rzf} algorithm or simply the RZF-algorithm. In this formula, only the boundary values of Φ_{dp} occur for each beam and, it is simpler to implement this formula as compared with equation (6.4). However, the range-weighting, which is exact in equation (6.4), is constant in equation (6.5), i.e., the range-weighting is constant at $(r_2 + r_1)/2$. If $(r_2 - r_1)$ is small, then equation (6.5) becomes more exact, but the accuracy of the approximation depends not only on $(r_2 - r_1)$ but also on how different the actual $K_{dp}(r)$ profile is from being a constant. For both areal Φ_{dp} estimators, the measurement error is virtually negligible because of the areal integration and prior smoothing of the Φ_{dp} range profiles.

6.1.3 A case study

The data shown here are from the C-POL radar³ located near Darwin, Australia and operated by the Bureau of Meteorology Research Center (Keenan et al. 1998). The gage network consists of 20 gages within a 100 km^2 area located about 40 km southeast of the radar as illustrated in Fig. 6.4. The polar area used in the estimate of areal rainfall is also shown in this figure. The gages were 203-mm-diameter tipping-bucket type and the time of accumulation of 0.2 mm of rainfall is recorded. The gages are routinely calibrated and strict data quality control procedures were used to reject faulty gage data. For each gage, 1-min rain rates R_g were available as time series. Raindrop size distribution data were also available from a Joss disdrometer located in this network; over 2000 2-min averaged $N(D)$ were available for analysis representing a variety of rain types occurring in this region (i.e., thunderstorms, continental and oceanic squall lines).

³ Please see the BMRC web page at <http://www.bom.gov.au/>

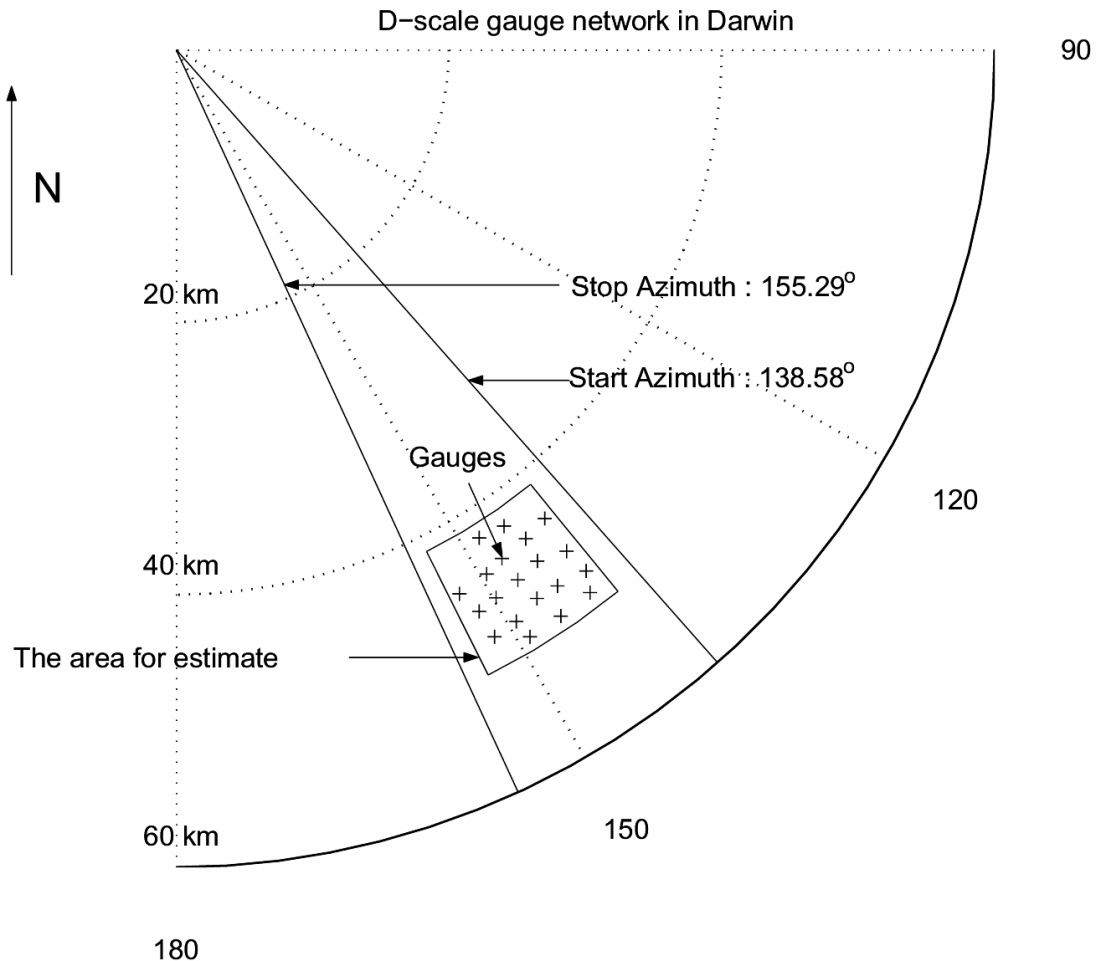


Fig. 6.4: Illustrates the dense gauge network near Darwin, and the boundaries of the polar area used for estimating the area rainfall. From Bringi et al. (2001b).

The C-POL radar data stream consists of Z_h , Z_{dr} and Φ_{dp} at range increments of 300 m. It employs a high-power switchable ferrite circulator for alternating transmission of 1 microsecond H and V polarized pulses at PRF of 1000 Hz. The number of integration samples are 64H and 64V samples (128 msec dwell) with azimuthal beam spacing of 1° (which means a sampling time of about $\frac{3}{4}$ min for one PPI sweep). The Φ_{dp} data are filtered in range using the iterative filtering algorithm described in Section 3. The reflectivity is corrected for attenuation effects using the method described in Section 4.

A threshold in $\Delta\Phi_{dp} = \Phi_{dp}(r_2) - \Phi_{dp}(r_1) > 2^\circ$ is applied for each 10 km long beam for application of the formulas in equation (6.4) and equation (6.5). Because the Φ_{dp} is filtered in range, the fluctuations in measured Φ_{dp} are reduced considerably to $< 1^\circ$. Below the 2° threshold value of $\Delta\Phi_{dp}$, a climatological Z_h - R relation may be used to determine the rain rate. Here, the coefficient and exponent of the power law are determined from Darwin disdrometer data resulting in $Z_h = 305 R^{1.36}$. The piece-wise linear fit shown in Fig. 6.1 is used to determine the value of c to be used in equation

(6.4) based on the average K_{dp} value for the beam. The coefficient a and exponent b used in equation (6.5) are based on a non-linear fit to disdrometer-based scattering simulations at C-band which results in $R = 32.4 K_{dp}^{0.83}$.

Radar data from the lowest available elevation (0.5°) tilt, or sweep, were used, and within the polar area in Fig. 6.4 a total of 12-15 beams per sweep were generally available for the azimuthal integration. The low elevation angle sweep data were available every 10 minutes, i.e., the radar sampling interval was 10 minutes. The areal rainfall in equation (6.4) and equation (6.5) obtained for each sweep was divided by the polar area in Fig. 6.4 resulting in a time series of mean areal rain rate (\bar{R}_{csu} or \bar{R}_{rzf}) spaced every 10 minutes.

The radar/gage data used in this study were obtained during the summer rainy season in Darwin (December 1998 - March 1999). Twelve convective rain events were available for analysis. A variety of rain types are represented in this dataset, e.g., continental and oceanic squall lines. As mentioned earlier, the threshold value for $\Delta\Phi_{dp}$ of 2° was selected for application of equation (6.4) and equation (6.5); otherwise, the rain rate was based on $Z_h = 305 R^{1.36}$ obtained from disdrometer-measured drop size spectra. This $\Delta\Phi_{dp}$ threshold corresponds to a rain rate threshold of about 5 mm h^{-1} . On average, the number of beams in the polar area where the $\Delta\Phi_{dp}$ threshold was exceeded was around 70 % of the total number of beams for the entire event.

A typical time series of \bar{R}_{csu} for one event (18 February 1999) is shown in Fig. 6.5 where the samples are spaced 10 min apart. Standard error bars for the radar-based estimate of areal rain rate are also shown. The fluctuation of the error in the $R(K_{dp})$ estimator about the true rain rate R is due to both the parameterization error (ε_p) as well as the radar measurement error (ε_m). The parametric error is due to the form of the $R-K_{dp}$ relation, e.g., $R = c K_{dp}^b$, and is based on simulations using the gamma drop size distribution model whose parameters (N_w , D_m , μ) are widely varied. Most of the error in this method is due to ε_p . The standard error due to parameterization, $\sigma(\varepsilon_p)$, decreases with increasing R , and is around 35 % for R around 20 mm h^{-1} . The measurement error component is negligible compared with the parameterization error. The standard error bars in Fig. 6.5 also account for the fact that the radar estimates the mean areal rain rate, i.e., the variance of the parameterization error has been reduced by M where M is the number of uncorrelated samples. Here, M is estimated as $(10/3)^2 \approx 11$ ($10 \times 10 \text{ km}^2$ is the area, while 3.0 km is a typical decorrelation distance for convective rain cells in this region).

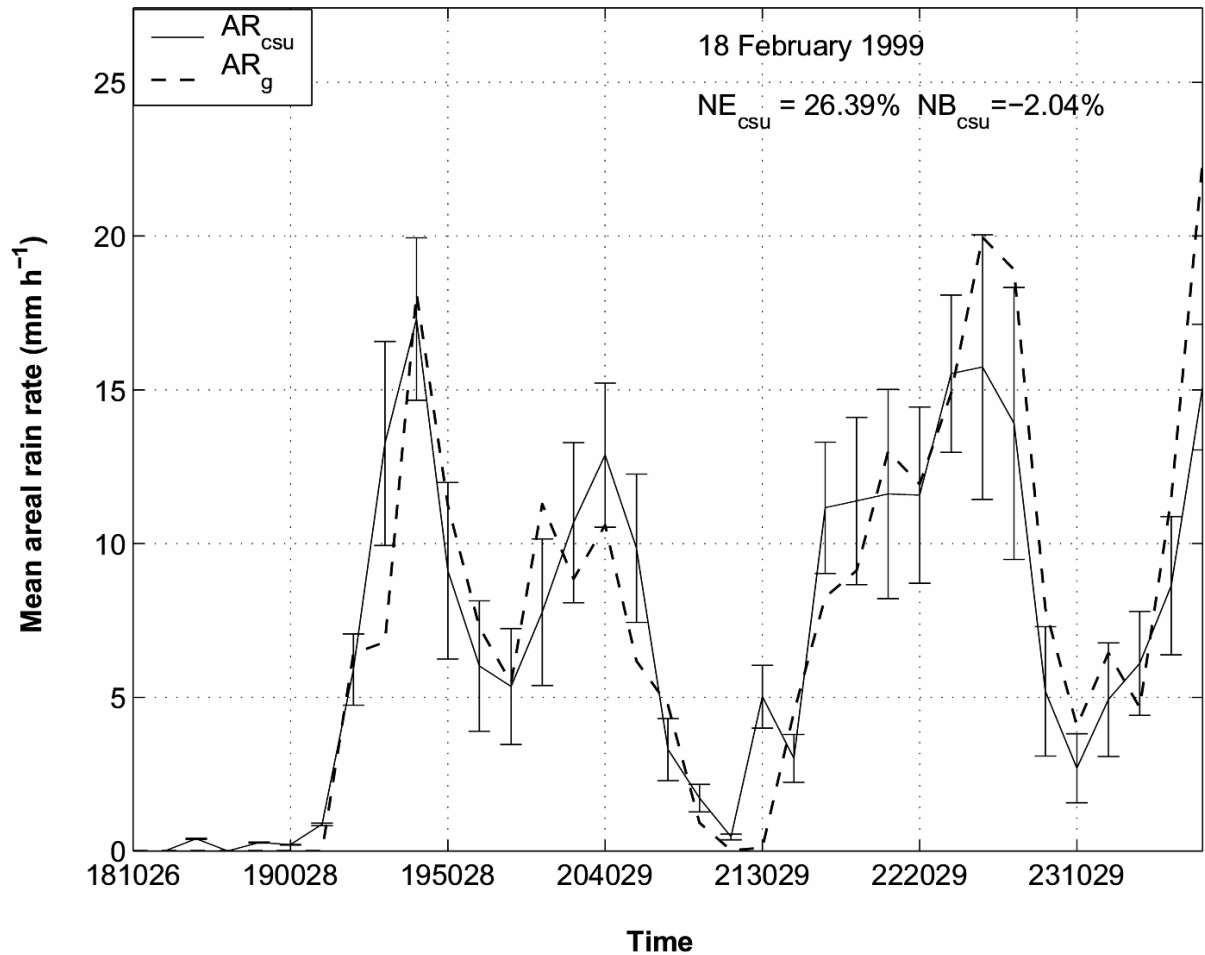


Fig. 6.5: Time series of mean areal rain rate ($\overline{R}_{\text{csu}}$ from the CSU estimator and from the gauge network (\overline{R}_g) vs. time for the storm event of 18 Feb. 1999. The radar sampling interval is 10 min. Standard error bars on $\overline{R}_{\text{csu}}$ reflect both the parameterization error as well as the measurement error. From Bringi et al. (2001b).

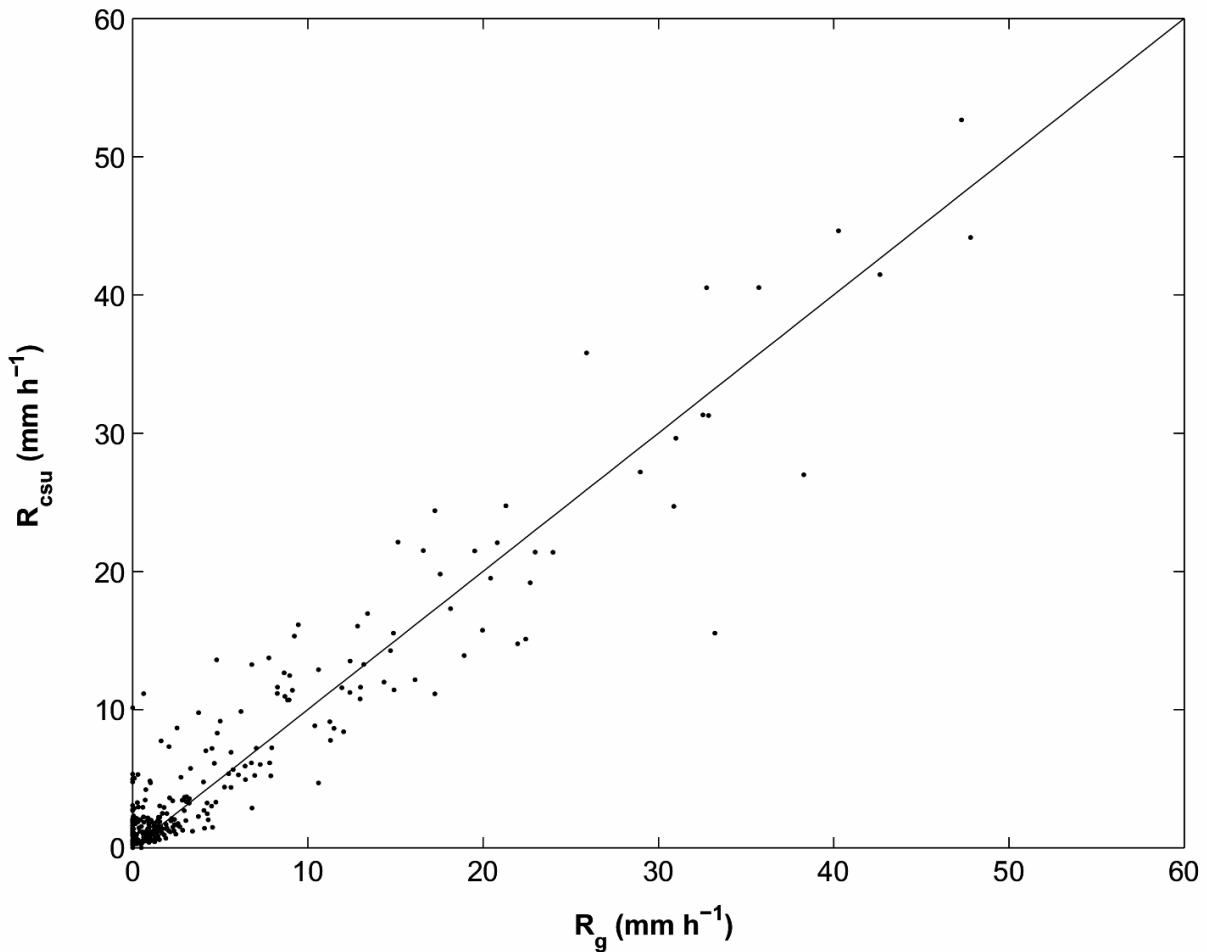


Fig. 6.6: Scatterplot of \bar{R}_{csu} vs. \bar{R}_g from all 12 events. The normalized error is 37 %, and the normalized bias is 5 %. From Bringi et al. (2001b).

Fig. 6.6 shows \bar{R}_{csu} versus \bar{R}_g for all of the 12 events. The normalized error (NE) is defined here as,

$$NE = \frac{\frac{1}{N} \sum_{i=1}^N |\bar{R}_{csu} - \bar{R}_g|}{\frac{1}{N} \sum_{i=1}^N \bar{R}_g} \quad (6.6)$$

and the normalized bias (NB) as,

$$NB = \frac{\frac{1}{N} \sum_{i=1}^N (\bar{R}_{csu} - \bar{R}_g)}{\frac{1}{N} \sum_{i=1}^N \bar{R}_g} \quad (6.6b)$$

For the data shown in Fig. 6.6, the NE is 37 % while the NB is 5 %.

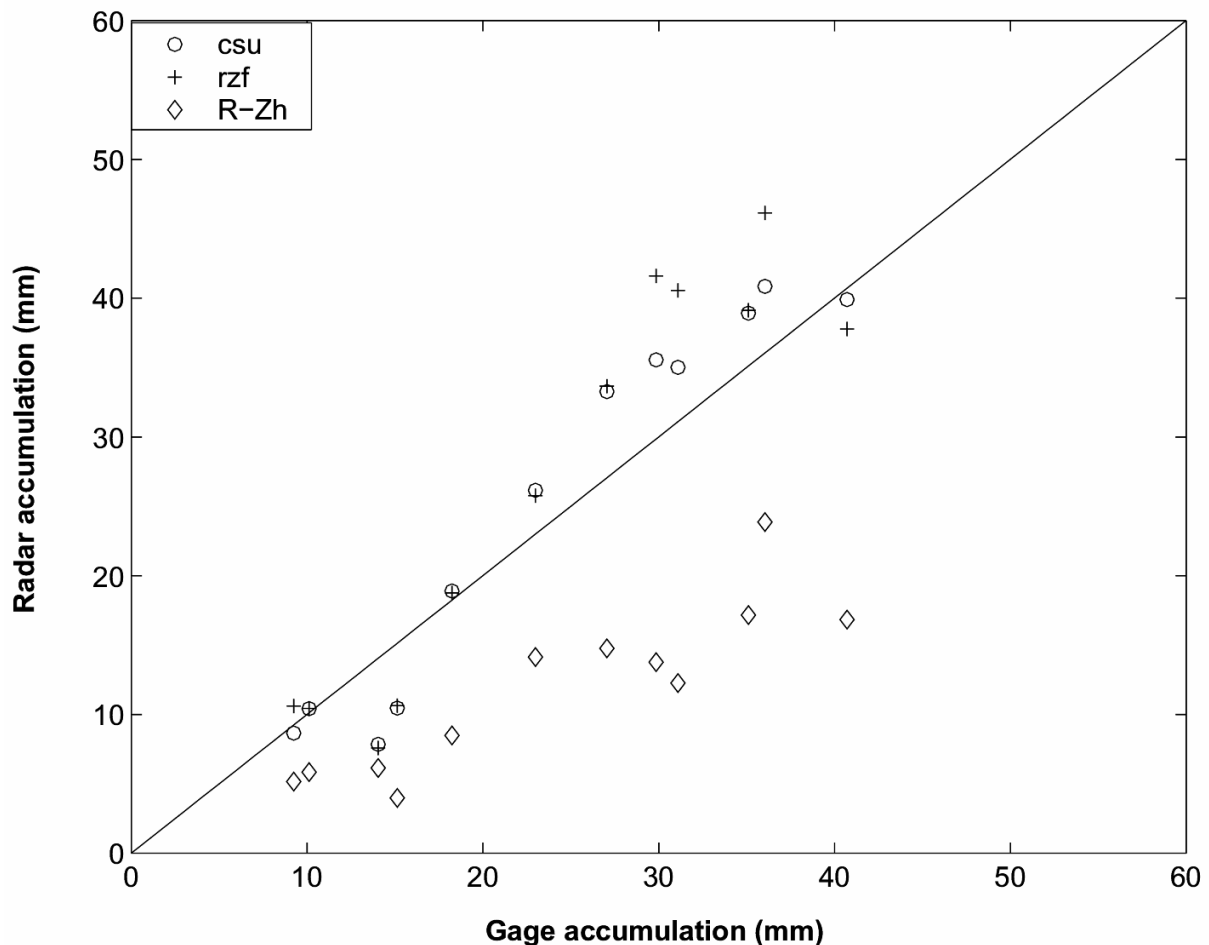


Fig. 6.7: The storm total rain accumulation from radar vs. gauge network accumulation for 12 storm events. The normalized error is 14.1 % and the normalized bias is 5.6 % for the CSU estimator. From Bringi et al. (2001b).

Fig. 6.7 compares the rain accumulation (based on samples of radar \bar{R} and rain gage \bar{R}_g spaced 10 min apart) for the 12 events; the normalized error is 14.1 % and normalized bias is 5.6 % for the CSU estimator. Note that the gage-based accumulation is based on \bar{R}_g sampled at the radar sampling interval of 10 min. Since the expected sampling error of the gage network itself is around 5-7 %, the results of Fig. 6.7 show that the radar estimation of storm total accumulation over the $10 \times 10 \text{ km}^2$ area is very accurate using the \bar{R}_{csu} algorithm. Comparable values for the normalized error and normalized bias when using the RZF algorithm (\bar{R}_{rzf}) are 21 % and 11.4 %, respectively. Corresponding error and bias values for the Z_h-R algorithm are 51 % and -50.8 %. Note that the $Z = 305 R^{1.36}$ relation was derived from disdrometer data for this region (without stratiform/convective rain separation). Fig. 6.8 shows mean areal rain rate (\bar{R}_{csu}) with polar resolution of $10\text{km} \times 10^\circ$ derived from a PPI scan collected by the BMRC/C-POL radar during the South China Sea Monsoon Experiment. Such a product is expected to be useful for hydrological application.

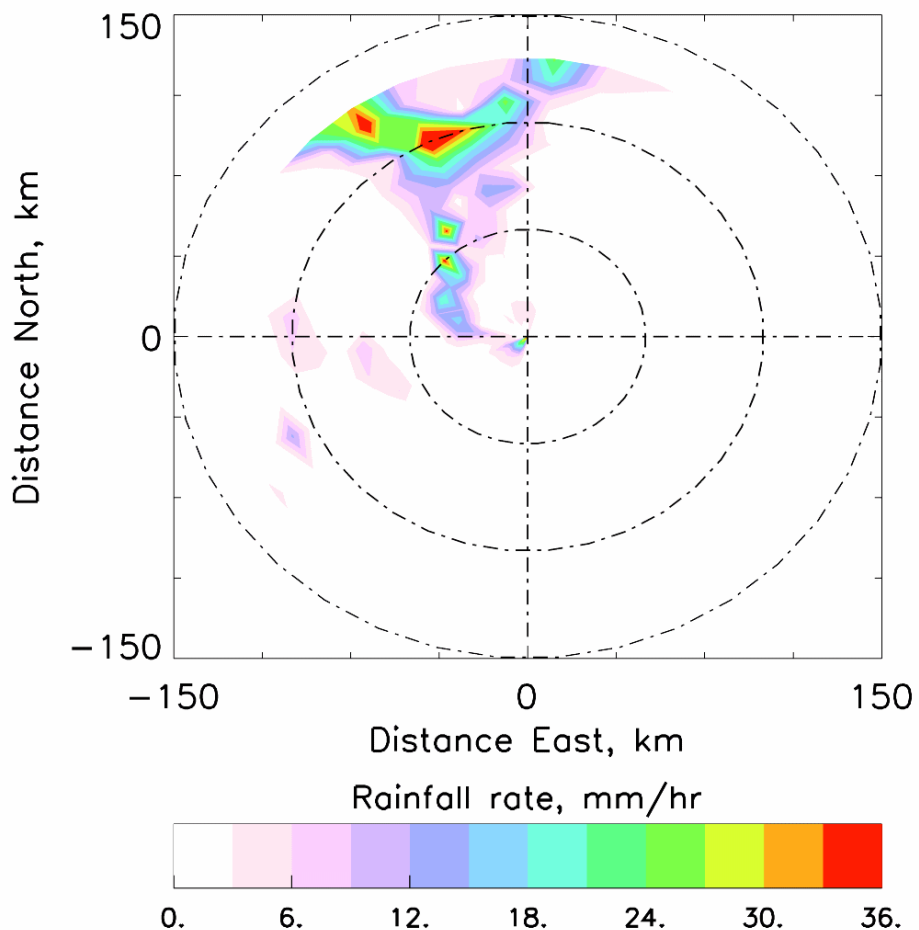


Fig. 6.8: PPI plot of mean areal rain rate from polar areas of $10 \text{ km} \times 10^\circ$ using the areal Φ_{dp} method (see equation (6.4)). Data from the BMRC/C-POL radar located on Dongsha Island for the South China Sea Monsoon Experiment. Data from 18 May 1998. Note that contour filling has been applied for display.

The areal rainfall estimator can also be applied at X-band using the piece-wise linear fit shown in Fig. 6.2. The range increment can be selected as 5 km with the same $\Delta\Phi_{dp}$ threshold of 2° . The azimuth sector can be selected as 5 beam spacings (approximately 1° apart). In this way the user-defined watershed area can be accommodated with the basic resolution being $5\text{km} \times 5^\circ$. One caveat is that the $R-K_{dp}$ fit recommended here has only been validated at C-band for tropical rainfall and accounts for the effects of drop oscillations and drop canting due to turbulence. In the mid-latitudes where convective rain forms from melting of ice particles (graupel or small hail) the effects of oscillations may be suppressed and a modified $R-K_{dp}$ relation may be applicable, especially if rain is mixed with ice precipitation. Note that the areal rainfall estimator proposed here will not be 'biased' by the presence of 'spherical' ice particles since such particles will not contribute to the differential propagation phase.

6.2 Higher resolution method for C and X-band radars

If higher resolution (approximately 3 km along the beam) rain rate estimates are desired then the $R-K_{dp}$ relation can be used directly. If the K_{dp} estimate is 'noisy' then a threshold can be selected below which an appropriate Z-R relation can be used which is valid for the corresponding rain type (where the measured Z must be corrected for attenuation first). Note that the algorithm proposed in this chapter is suitable for C- and X-band radars. For S-band radars, it is not necessarily the optimal. Instead, one of the algorithms described in the next section could be used for higher resolution rainfall applications at S-band.

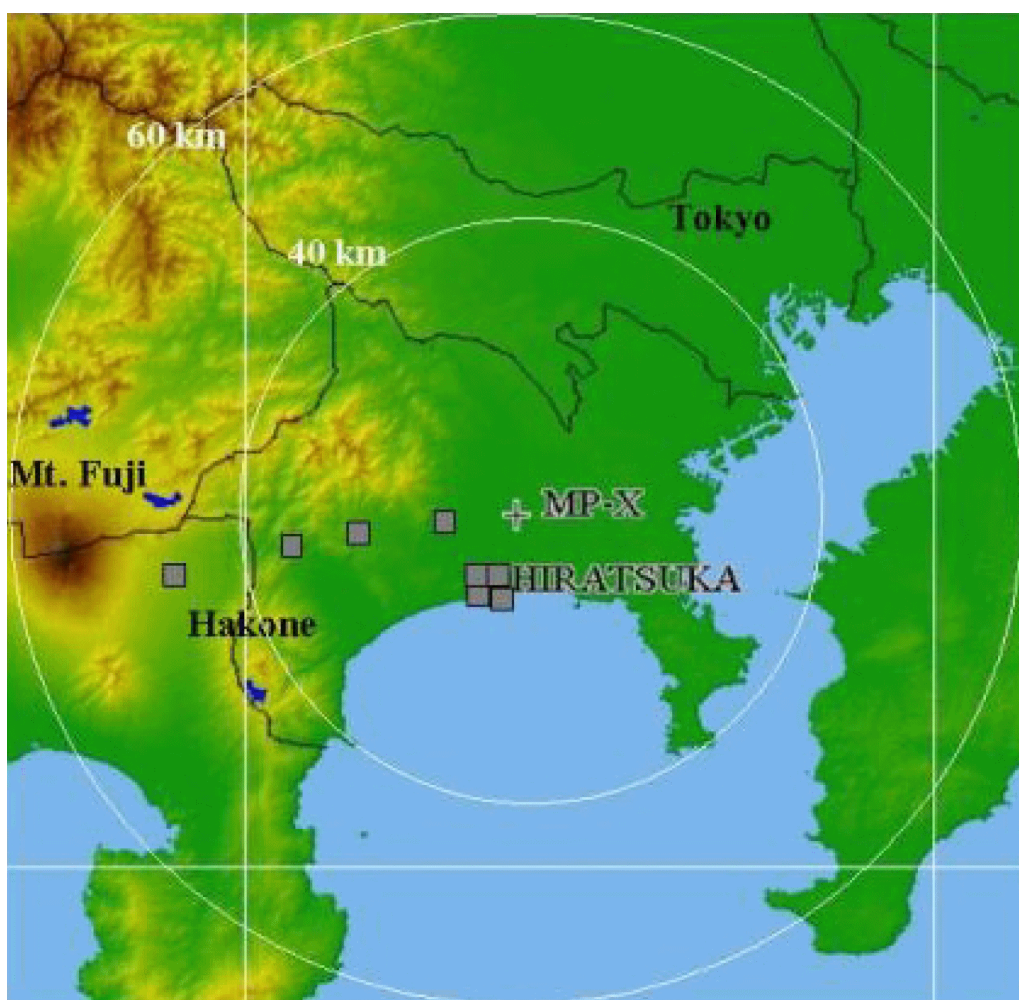


Fig. 6.9: Location of the MP-X band radar at Ebina, Kanagawa Prefecture, Japan and the location of 8 rain gages (solid squares) of the Pukyong National University of Korea. Adapted from Park et al (2005).

The following algorithm has been proposed and evaluated by Park et al (2004) using the NIED MP-X-band radar near the Tokyo region during the summer of 2003. The PRF was 1800 s^{-1} and typical integration was 100 samples with azimuthal sampling

of 1° . The site and location of the radar/gages is shown in Fig. 6.9. The algorithm is based on analysis of Joss disdrometer data (using 3 instruments) in Tsukuba, Japan,

$$R(K_{dp}) = 19.6 K_{dp}^{0.82}; \quad \text{mm/h} \quad (\text{if } K_{dp} > 0.3^\circ/\text{km}) \quad (6.7)$$

with K_{dp} in $^\circ/\text{km}$ and Z_h in $\text{mm}^6 \text{m}^{-3}$.

If $K_{dp} < 0.3^\circ/\text{km}$ then,

$$Z_h = 416 R^{1.22}; \quad dBZ_h < 35dBZ \quad (6.8)$$

$$= 104 R^{1.78}; \quad dBZ_h > 35dBZ \quad (6.8\text{b})$$

The above Z - R relations are representative of stratiform ($416 R^{1.22}$), and maritime convective ($104 R^{1.78}$) rain types. Three long-duration rain events (2 stratiform and 1 typhoon) were available for comparison with 8 gages located as shown in Fig. 6.9. Fig. 6.10 shows PPI scans of rain rate using the uncorrected Z_h (top panel) data with the Z - R relation in equation (6.8) whereas the bottom panel shows the rain rate with corrected Z_h . Note the rather dramatic restoration of the rain rate field when Z_h is corrected for attenuation.

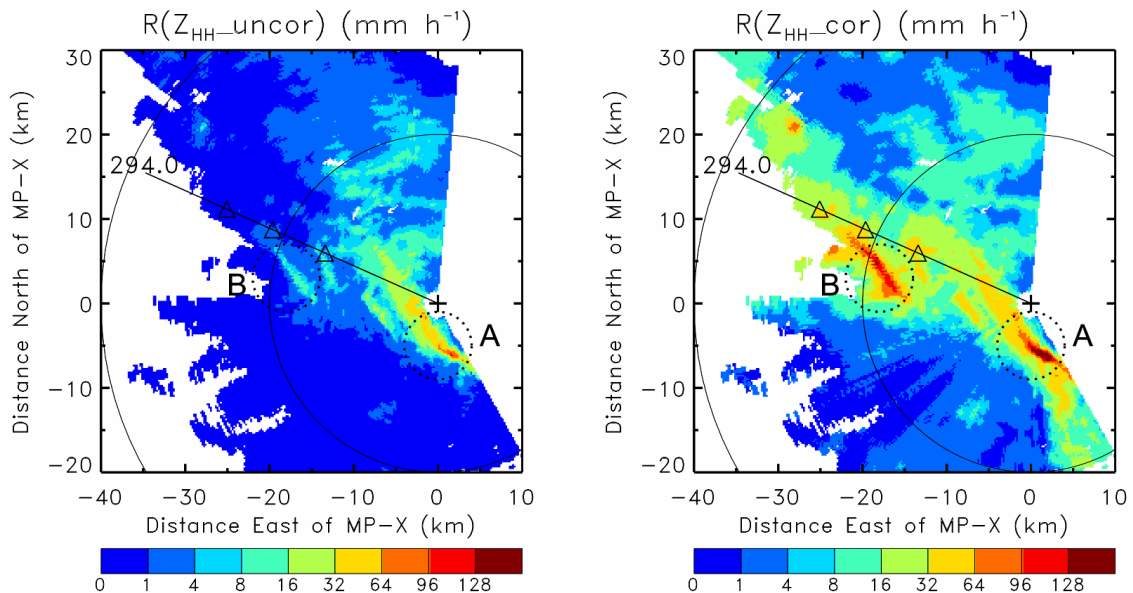


Fig. 6.10: PPI scan of rain rate using uncorrected Z (left) and corrected Z (right) using equation (6.8). Adapted from Park et al (2005).

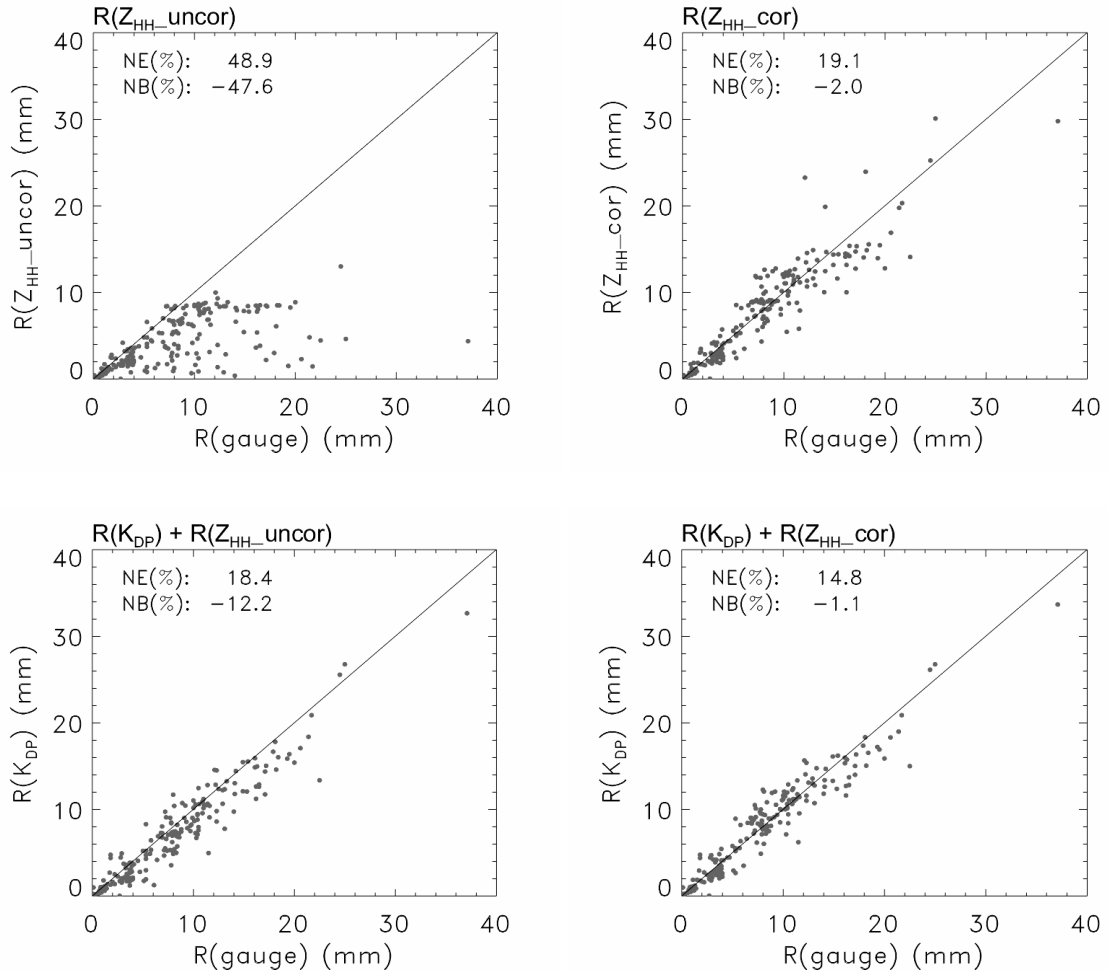


Fig. 6.11: Comparison of hourly accumulations using radar versus gages for three long-duration rain events. (a) Z-R comparison with gages using the measured Z_h only and equation (6.8), (b) using $R(K_{dp})$ relation in equation (6.7) along with uncorrected Z_h as in equation (6.8), (c) Z-R used alone but with Z corrected for attenuation, and (d) $R(K_{dp})$ along with Z-R as in equation (6.7), equation (6.8) but Z is corrected for attenuation. From Park et al (2005).

The comparison of 1-hourly accumulations over each of the 8 gage locations for the three events is shown in Fig. 6.11. The K_{dp} was calculated as described in Section 3 and the measured Z has been corrected as described in Section 4. Panel (a) shows the Z-R relation comparison using the observed (i.e., uncorrected Z) and as expected a severe underestimate of radar-estimated amounts occurs (-50 %). Panel (b) shows the rather dramatic improvement that occurs if the K_{dp} -based algorithm above is used even with Z-R relation uncorrected for attenuation and applied when K_{dp} is 'noisy'. The normalized bias is greatly reduced to near -10 % and the normalized standard error to 15 %. Panel (c) shows the results if the Z-R estimator alone is used after correcting Z for attenuation and may be compared to panel (a). This shows the need for attenuation-correction at X-band which is well-known, but also demonstrates the accuracy of the correction methodology (using the Φ_{dp} constraint) described in Section 4. Finally panel (d) shows the combined $R(K_{dp})$ and attenuation-corrected Z-

R algorithm (as in equation (6.7) and equation (6.8)) results which show the lowest bias (-1.4 %) and standard error (13 %).

Another radar/gage comparison was performed at C-band by May et al (2002) using the BMRC/C-POL radar and the $R-K_{dp}$ algorithm ($R = 34.6 K_{dp}^{0.83}$) which was compared with a fixed $Z-R$ relation $Z = 416 R^{1.22}$ (based on disdrometer analysis for the Maritime Continent Thunderstorm Experiment, north of Darwin, Australia). They found that their $R-K_{dp}$ algorithm gave a normalized bias of 14 % (radar overestimate) and fractional standard error of 21 % for storm total accumulation (21 gages over 680 km^2 area; 4 long-duration storm events). The fixed $Z-R$ relation, after correcting for attenuation and beam blockage (at the second tilt angle 1.5° – 2.2°) gave fractional standard error of 50 %. They noted that at the lowest tilt angle (0.7°) the reflectivity-based estimate was severely biased (but not the K_{dp} -based estimator) even with beam blockage and attenuation-correction procedures in place. Thus, one main advantage of using K_{dp} is that it is relatively unaffected by beam blockage effects as compared with power measurements permitting rainfall estimates at low elevation angles ($< 0.5^\circ$).

Because of its many advantages over power measurements, the use of K_{dp} to estimate rainfall is central for operational applications especially at C and X-bands even though the 'optimal' algorithm has not been fully established as yet. The form $R = a K_{dp}^b$ is an empirical power law whose multiplicative coefficient a depends on the model used for drop shapes (e.g. see Fig. 2.5), and to some extent on the range of the dsd parameters used in the simulations (e.g. whether this range is based on a theoretical gamma dsd model or based on disdrometer dsd measurements). Table 6.1 gives representative values for a and b at C and X-band.

Table 6.1: Parameters of rain rate relations

Frequency (GHz)	$a K_{dp}^b$	Drop Shape Model *	DSD	Location	Gage Validation	Reference
9.375	$19.6 K_{dp}^{0.82}$	ABL+BC	Joss Disdrometer	Tokyo	Yes	Park et al. (2004)
9.375	$12.3 K_{dp}^{0.81}$	Equilibrium	Joss Disdrometer	Wallops Island, Virginia, USA	Yes	Matrosov et al. (2002)
9.375	$18.9 K_{dp}^{0.85}$	ABL+BC	Joss Disdrometer	Darwin, Australia	Yes	Maki et al. (2004)
5.5	$32.4 K_{dp}^{0.83}$	ABL+BC	Joss Disdrometer	Darwin, Australia	Yes	Bringi et al. (2001b)
5.5	$34.6 K_{dp}^{0.83}$	Keenan	Joss Disdrometer	Tiwi Island (100 km North of Darwin)	Yes	May et al. (1999)
5.5	$31.2 K_{dp}^{0.7}$	RAL	Gamma	–	No	Illingworth and Blackman (2002)

*) ABL stands for the fit recommended by Andsager et al. (1999) for $1 \text{ mm} < D < 4 \text{ mm}$. BC stands for Beard and Chuang (1987) equilibrium fit to their numerical model, $D < 1 \text{ mm}$ and $D > 4 \text{ mm}$. Keenan stands for the empirical fit used by Keenan et al. (1997). RAL stands for the empirical fit recommended by Goddard et al. (1995)

6.3 Rainfall estimation for S-band radars

6.3.1 The (prototype) NEXRAD DP-rain algorithm

The proposed rain retrieval algorithm for the WSR-88D NEXRAD radar (Ryzhkov et al., 2003, Ryzhkov et al., 2005b) is a synthetic algorithm which uses different empirically derived equations depending on the rainfall rate determined using the conventional Z - R relation. The following set of equations describes the synthetic algorithm:

$$R = \frac{R(Z)}{0.4 + 5.0 |Z_{dr} - 1|^{1.3}} \quad \text{for } R(Z) < 6 \text{ mm/h} \quad (6.9)$$

$$R = \frac{R(K_{dp})}{0.4 + 3.5 |Z_{dr} - 1|^{1.7}} \quad \text{for } 6 < R(Z) < 50 \text{ mm/h} \quad (6.9b)$$

$$R = R(K_{dp}) \quad \text{for } R(Z) > 50 \text{ mm/h} \quad (6.9c)$$

where

$$R(Z) = 0.017 Z^{0.714} \quad (6.9d)$$

$$R(K_{dp}) = 44.0 |K_{dp}|^{0.822} \text{ sign}(K_{dp}) \quad (6.9e)$$

with Z in units of $\text{mm}^6 \text{ m}^{-3}$ and R in mm/h , and Z_{dr} being the differential reflectivity ratio in linear units. Equation (6.9d) is the inversion of the ‘standard’ NEXRAD Z - R relation. The $\text{sign}(K_{dp})$ term in (6.9e) tends to reduce the bias in rain accumulation when K_{dp} is noisy and fluctuating about 0 (note that this yields to negative rain rates R). Z and Z_{dr} in the above equations are first corrected for attenuation using the linear- Φ_{dp} method, with $\alpha = 0.04 \text{ dB}^\circ$ as in Section 4.1 and $\beta = 0.004 \text{ dB}^\circ$ as in Section 5.1. In addition, Z and Z_{dr} are smoothed with a moving average window of 3 and 5 gates respectively (gate spacing is 267 m). The Φ_{dp} is smoothed and least squares fitted over 9 or 25 successive gates to estimate the K_{dp} . The 9 gate smoothing is used to give a ‘lightly’ filtered estimate for $Z > 40 \text{ dBZ}$ and the 25 gate smoothing is used to give a ‘heavily’ filtered estimate for $Z < 40 \text{ dBZ}$. Another option is to use the non-iterative version of the FIR filter described in Appendix A; the non-iterative version is sufficient since the back scatter differential phase is close to zero at S-band (except sometimes in the melting region).

This synthetic algorithm has been proposed based on the results of testing of a large amount of data obtained using the polarimetric prototype of the WSR-88D radar located in Norman, Oklahoma. The data were collected in the simultaneous transmission and short dwell time mode. The denominator term in (6.9a,b) contains empirically derived factors which adjust the $R(Z)$ or $R(K_{dp})$ estimate for deviations of the averaged D_0 (see equation (2.9)) from the expected value (Fulton et al 1999). This synthetic algorithm is yet to be validated in other climatic regimes.

The algorithm testing was carried out by comparing against a dense rain gauge network. The synthetic algorithm outperformed a number of other algorithms in terms of 5 statistical criteria: lowest bias, standard deviations and RMS errors for point (hourly) and mean areal estimates. The algorithm performance depends on the calibration accuracy of Z_{dr} , estimated to be within 0.2 dB for the prototype WSR-88D. In the case of reflectivity, high calibration accuracy (better than 1 dB) is only needed for rain rates less than 6 mm/h.

For 1° beam antenna, the synthetic algorithm was proposed for ranges less than 125 km. At larger ranges - up to 200 km - the $R(K_{dp})$ algorithm is recommended. The $R(K_{dp})$ estimates are also recommended for 'cold season' rain with low bright band. Further details are given in Ryzhkov (2003). Note that this is limited to cases with a considerable amount of rain within the radar beam. If the radar beam is almost entirely filled with non rain medium, then dual polarization data can be used to classify the precipitation type and vertical profile correction methods can be used for estimating the rain rate at the surface (see for example Kitchen et al 1994).

6.3.2 Other algorithms

Ryzhkov (2003) has considered and evaluated a number of different polarimetric rainfall algorithms of the type $R(K_{dp})$, $R(Z, Z_{dr})$ and $R(K_{dp}, Z_{dr})$. The algorithms were based on 2D-video disdrometer data from Oklahoma and different models for the drop axis ratio versus diameter relationship (referred to as mean drop shape relationships). Based on statistical analysis of errors, they found the following algorithms best agreed with the gauge data:

$$R(K_{dp}) = 45.3 |K_{dp}|^{0.786} \text{sign}(K_{dp}) \quad (6.10)$$

$$R(Z, Z_{dr}) = 0.0142 Z^{0.77} Z_{dr}^{-1.67} \quad (6.10b)$$

$$R(K_{dp}, Z_{dr}) = 136 |K_{dp}|^{0.968} Z_{dr}^{-2.86} \text{sign}(K_{dp}) \quad (6.10c)$$

where Z in units of $\text{mm}^6 \text{m}^{-3}$, Z_{dr} is the differential reflectivity ratio in linear units, R is in mm/h and K_{dp} in %/km . The coefficients and exponents are based on non-linear least squares fit but the power law forms assumed above are only loosely based on scattering theory and fall speed assumptions. In the case of equation (6.10)a,c a more palatable alternative to the use of $\text{sign}(K_{dp})$ is to use a default Z-R relationship for K_{dp} less than a certain threshold value, e.g. 0.3 %/km for S-band.

Fig. 6.12 (from Ryzhkov, 2003) shows the RMS error performance for point and areal estimates of hourly rain accumulation for different algorithms. The big reduction in the RMS error is apparent when polarimetric variables are introduced. Furthermore, the NEXRAD DP-Rain algorithm, denoted by $R(Z, K_{dp}, Z_{dr})$, gives the lowest RMS error, both for areal and for point hourly rain accumulation.

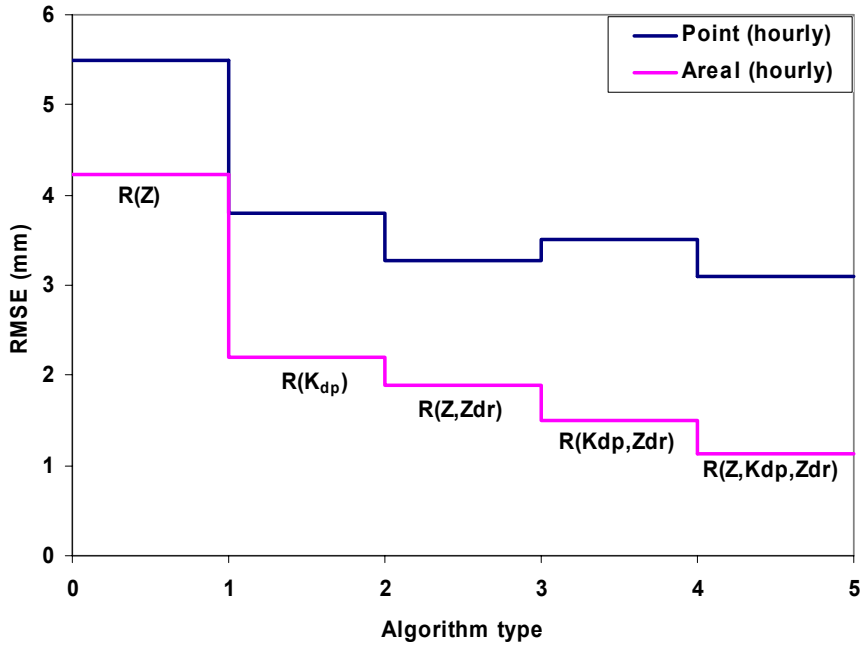


Fig. 6.12: RMS errors of point and areal hourly rainfall accumulations for various algorithms. Adapted from Ryzhkov et al, 2005b.

Fig. 6.13 compares the rain rate estimates derived using the Z-R and the NEXRAD DP algorithm for the same event as in Fig. 4.2 and Fig. 5.6, i.e. the squall line of 26 January 1999 in Brazil; a slightly different beam from the same scan was used for the rain rate comparisons. The Z and Z_{dr} fields have been smoothed to the same extent as K_{dp} . In addition, the K_{dp} is calculated using the FIR filter for this case. Generally, the NEXRAD algorithm gives systematically higher estimates of rain rate than the Z-R relationship, which is due to the fact that the standard NEXRAD Z-R relation is not suitable for tropical regimes (cf. Fig. 2.4).

Fig. 6.13 also includes another method, namely the RAL (Rutherford Appleton Laboratory) method which assumes a monotonic relationship between the ratio R/Z and Z_{dr} :

$$R = Z \cdot f_{RAL}(Z_{dr}) \quad (6.11)$$

Based on a large amount of datasets and inter-comparisons between Joss-distrometer (as well as a rapid response rain gauge) and simultaneously recorded Z and Z_{dr} from the Chilbolton radar (Goddard et al, 1994) located in Southern England, a look up table has been constructed. The comparisons have been performed over many years and are locally tuned to the Chilbolton area, nevertheless, this approach does not make any assumptions regarding the form or the type of Z and Z_{dr} dependence on rainfall rate (unlike equations (6.9)-(6.10)). Instead, it only assumes that the dsd follows the Gamma distribution, with a fixed value for μ , see equation (2.8).

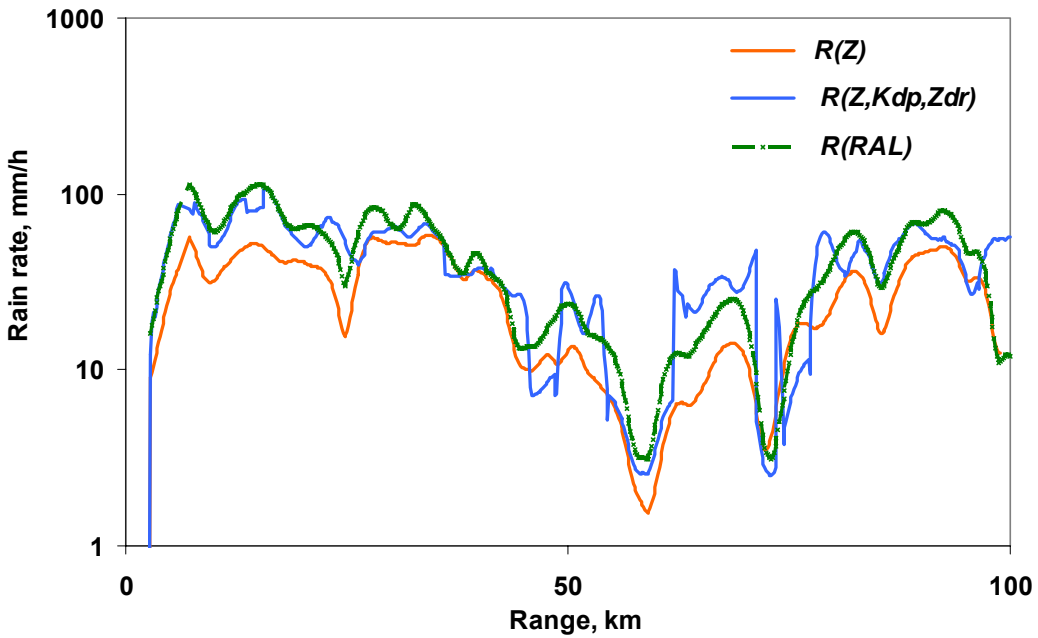


Fig. 6.13: Rain rate estimates from NEXRAD Z-R and the NEXRAD DP-rain algorithm (see equation (6.9)) and the RAL method with $\mu=5$ (see below) from the same event (but a slightly different beam) as that shown in Fig. 4.2 and Fig. 5.6.

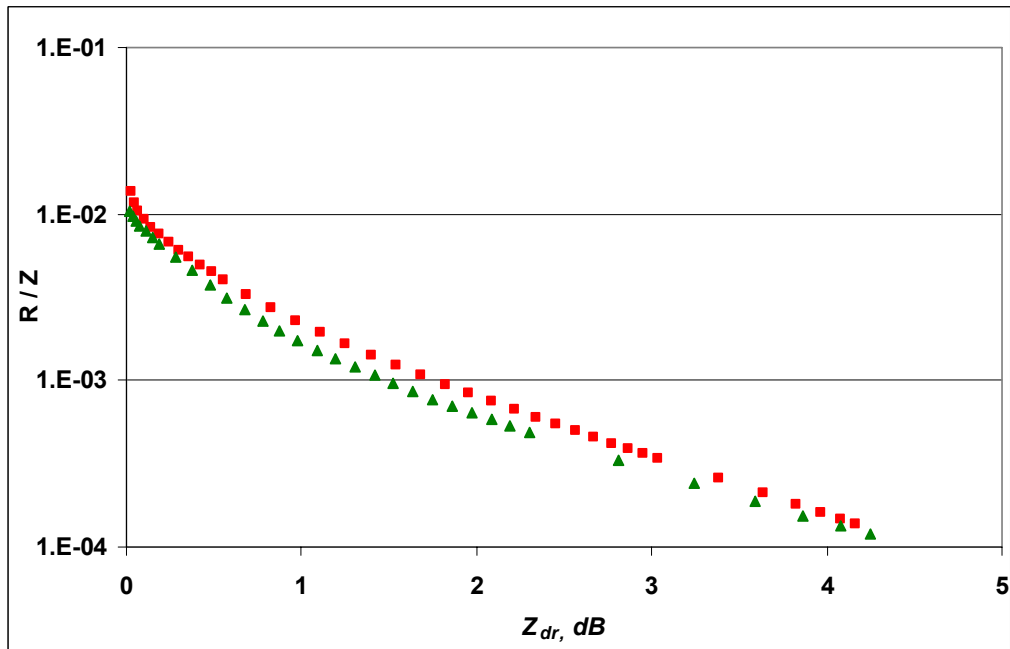


Fig. 6.14: The RAL look up table data for $\mu=0$ (red) and $\mu=5$ (green). Data courtesy of John Goddard, RAL.

Fig. 6.14 shows $f_{RAL}(Z_{dr})$, i.e. the R/Z ratio variation with Z_{dr} from the look up table for $\mu=0$ and $\mu=5$. The $\mu=5$ table has been applied to the ' $R(RAL)$ ' curve in Fig. 6.13. Generally speaking, the agreement between the NEXRAD DP algorithm and the RAL

method is good, considering that the algorithms have been tuned for different geographical locations (southern England versus central Oklahoma).

The data shown in Fig. 6.14 can be well approximated by a fourth order fit for the range $0 < Z_{dr} < 4.2$ dB:

$$\log_{10}(f_{RAL}|_{\mu=0}) = 0.0107 Z_{dr}^4 - 0.112 Z_{dr}^3 + 0.434 Z_{dr}^2 - 1.097 Z_{dr} - 1.906 \quad (6.12)$$

$$\log_{10}(f_{RAL}|_{\mu=5}) = 0.0073 Z_{dr}^4 - 0.0858 Z_{dr}^3 + 0.381 Z_{dr}^2 - 1.09 Z_{dr} - 1.982 \quad (6.12b)$$

Note that these fits are very similar to the result from Illingworth and Blackman (2002, their equation (18) and their figure 5).

Table 6.2 lists the main advantages and disadvantages of the various rain rate algorithms. These are the main algorithms which could be suitable for S-band operational systems. Several other algorithms for research-based systems have been evaluated (for example Bringi et al 2004, Brandes et al 2002, Gorgucci et al 2001).

Table 6.2: Pros and cons of various rain rate algorithms at S-band

Class of algorithm	Main advantages	Main disadvantages
$R(K_{dp})$	<ul style="list-style-type: none"> • Unaffected by absolute calibration • Unaffected by hail or bright-band • Not sensitive to partial beam blockage • Unaffected by anaprop 	<ul style="list-style-type: none"> • Considerable smoothing is required at expense of range resolution • Sensitive to mean drop shape relation
$R(Z, Z_{dr})$	<ul style="list-style-type: none"> • Robust and accurate with respect to <i>dsd</i> variations • No smoothing technique required 	<ul style="list-style-type: none"> • Need for high calibration accuracy for Z (± 1 dB) and Z_{dr} (± 0.2 dB) • Need to identify hail or other ice particles. • Affected by partial beam blockage
$R(K_{dp}, Z_{dr})$	<ul style="list-style-type: none"> • Unaffected by absolute calibration • Less sensitive to drop shape relation and <i>dsd</i> variations 	<ul style="list-style-type: none"> • Need for high calibration accuracy for Z_{dr} (± 0.2 dB) • Poorer resolution due to the need for comparable smoothing intervals for K_{dp} and Z_{dr} • Need to identify hail or other ice particles
$R(Z, K_{dp}, Z_{dr})$	<ul style="list-style-type: none"> • Recommended for prototype NEXRAD due to high accuracy • Robust with respect to absolute calibration, <i>dsd</i> variations, drop shapes and hail contamination 	<ul style="list-style-type: none"> • Need for high calibration accuracy for Z_{dr} (± 0.2 dB) • Poorer resolution due to the need for comparable smoothing intervals for K_{dp} and Z, Z_{dr}
R using look up tables based on Z, Z_{dr} (RAL-method)	<ul style="list-style-type: none"> • Robust and accurate with respect to <i>dsd</i> variations • No smoothing technique required • No need to assume power-law or any analytical form for Z and Z_{dr} dependence on rainfall rate 	<ul style="list-style-type: none"> • Need for high calibration accuracy for Z_{dr} (± 0.2 dB) • Affected by partial beam blockage • Need to identify hail or other ice particles

7 Precipitation Classification

Polarimetric observables can be used to classify the precipitation, i.e. to classify different type of hydrometeors. This is rooted in the fact that different types of hydrometeors possess different size, shape, fall mode and dielectric constant distributions from which the polarimetric radar observables can be calculated using scattering theory. For example, raindrops are oblate and highly oriented giving positive Z_{dr} signatures whereas hailstones are non-spherical but tumble as they fall giving rise to Z_{dr} near 0 dB (see also Fig. 2.6). Note that when a mixture of hydrometeor types fills the radar resolution volume (e.g., rain+hail), then the radar observables (except for K_{dp} which is based on forward scattering) are all weighted by the properties of the largest particles in the mixture (in this case, hail). Hence, all radar-based classification methods should be interpreted in this ‘bulk’ reflectivity-weighted sense. The earliest attempt at identification of hydrometeor types using Z and Z_{dr} data is the work of Hall et al (1984).

In a more general sense, polarimetric radar data can be used just to distinguish between meteorological and non-meteorological targets, e.g. to classify radar returns into

- those of meteorological origin (or, precipitation),
- echoes due to unfiltered normal ground clutter or anomalous propagation (AP) clutter, and
- echoes due to biological scatterers (insects, birds).

For example, the ‘good’ data mask application discussed in Section 3.2.2 (see Fig. 3.3) is based on a ‘primitive’ version of such ‘meteo/non-meteo’ classification using simple thresholds applied to the copolar correlation coefficient, the standard deviation of Φ_{dp} and the SNR, applied along each beam of data (earlier referred to as ‘good’ or ‘bad’ data segments along the beam).

As another example, the polarimetric scattering properties of clutter/AP are very different from insects/birds, and both in turn are very different from precipitation targets. Insects in the boundary layer have been known to give rise to very large Z_{dr} signatures even exceeding 10 dB at certain ‘look’ angles (Mueller and Larkin 1985; or Lang et al 2004). They can be modeled as prolate spheroids and their symmetry axis tends to align with the mean wind direction in the boundary layer. For this reason the azimuthal pattern of Z_{dr} from insects tends to exhibit two symmetric maxima located at azimuths perpendicular to the mean wind direction. Their reflectivities are quite low because of their low concentrations. Migrating birds are also known to exhibit very striking polarimetric signatures especially in the back scatter differential phase (see, Zrnic and Ryzhkov 1998) enabling the possibility of discrimination between birds (large $\delta \approx 100^\circ$ with moderate Z_{dr} of 3-4 dB) and insects (moderate $\delta < 30^\circ$, very large Z_{dr} of 5-10 dB).

In general, one uses always different polarimetric variables as input, i.e. a so-called input vector. By appropriate combination, the values of the input vector are used to

identify the echo as one of different types, i.e. one of the output classes. For the combination, different method exists with the fuzzy logic scheme being the mostly used.

Radars operating at different frequencies, such as S-band, C-band and X-band, may obtain the polarimetric variables with different values. For example, the differential phase is roughly proportional to the frequency. Also, Mie scattering effects can cause different results for different wavelengths. Thus precipitation classification cannot be used with unique algorithms for the different radar types. Instead, different classification algorithms exist for S-band, C-band, and X-band, respectively. For that reason, this chapter contains several sections about the classification algorithms for the different radar types.

7.1 Fuzzy logic schemes

Classification between precipitation, clutter/AP and biological echoes should be more accurate as compared to classification between a large number of hydrometeor types. In the first case, the values of the observables differ significantly, whereas the values of the polarimetric observables that delineate the different hydrometeor types are not sharply defined or overlap. Examples of such overlap are given in Fig. 7.1 valid at S-band. A simple decision logic-based approach using pre-defined boundaries as in Fig. 7.1 would be inaccurate or ambiguous unless restricted to just a few dominantly expected hydrometeor types (e.g., rain, hail, wet snow).

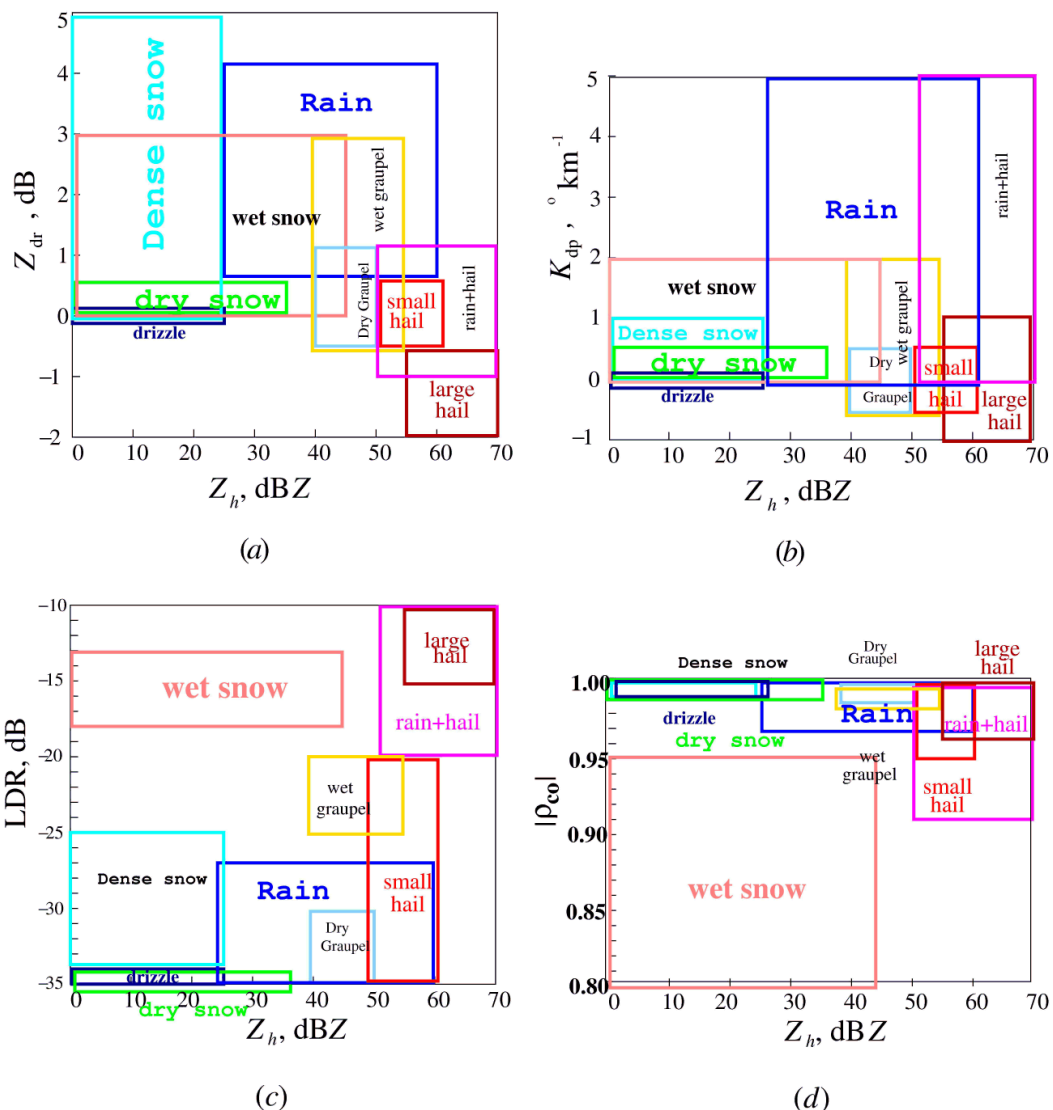


Fig. 7.1: Hydrometeor classification decision boundaries in the (a) Z_{dr} - Z_h , (b) K_{dp} - Z_h , (c) LDR - Z_h and (d) ρ_{co} - Z_h planes for S-band, from Straka and Zrnic (1993).

For that reason, ‘fuzzy’ logic methods (Mandel 1995) have been used. Such methods consider the overlap of the boundaries between hydrometeor types and thus are more suitable for classification purposes. Fig. 7.2 illustrates a conceptual model of the fuzzy logic method for hydrometeor classification between two classes only such as rain and hail where the inputs are assumed to be the three radar observables Z_h , Z_{dr} and LDR .

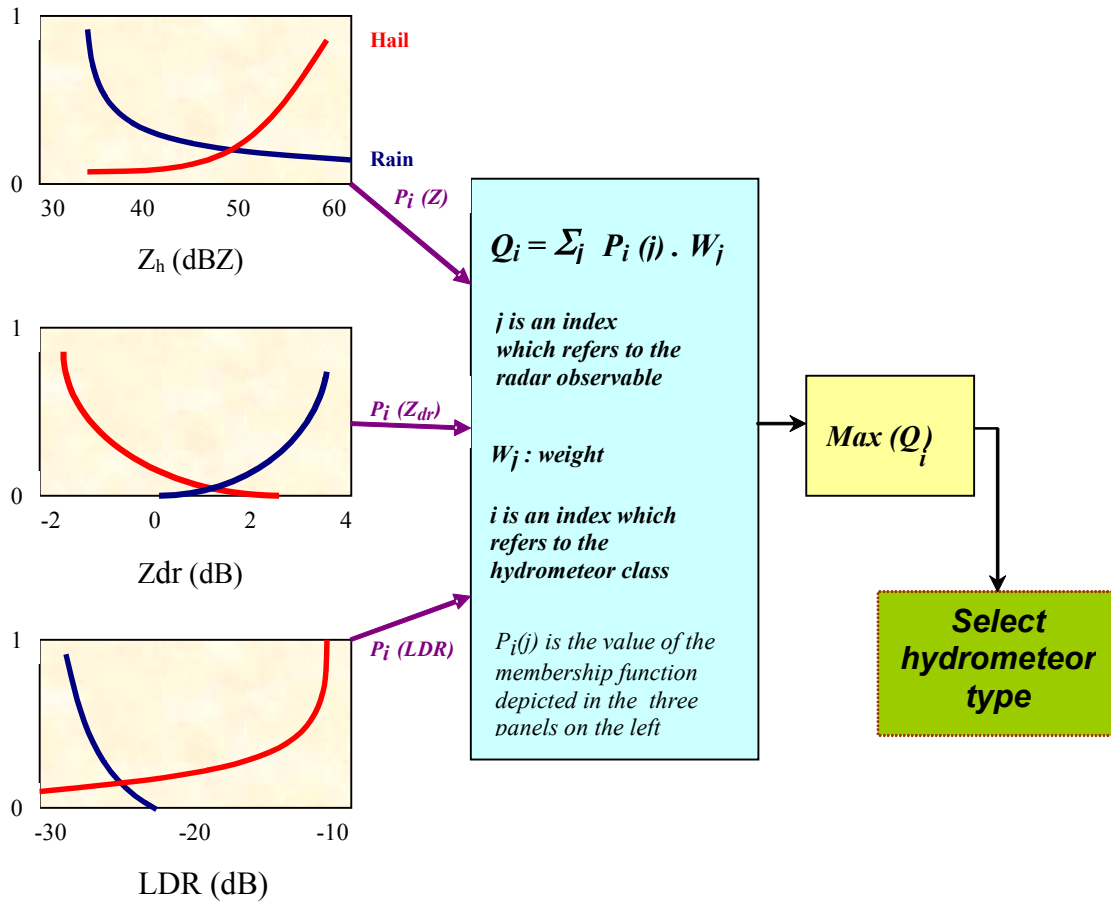


Fig. 7.2: Conceptual block diagram of a fuzzy-logic classifier for rain and hail. Left panels show the membership functions, the middle panel shows the aggregation procedure and the last panel shows the selection of the hydrometeor Type. Adapted from Vivekanandan et al (1999).

For each class, membership functions are defined that quantify the ‘conditional probability’ that the echo belongs to a particular class given the values of the input observations. For example, for the rain class the conditional probability, *Prob [echo class is rain | $Z_h=x$]*, defines one membership function while *Prob [echo class is hail | $Z_h=x$]* defines the second membership function as illustrated in Fig. 7.2. The membership functions differ from conditional probabilities in that they are un-normalized and have values between 0 and 1. They offer a way to ‘fuzzify’ the input value of Z_h .

For example an input value of 35 dBZ would imply that the conditional ‘probability’ for the echo belonging to the rain class is 0.9 while for the hail class it is much lower at 0.1. Similarly, membership functions are defined for the other two observables Z_{dr} and LDR as conceptually illustrated in Fig. 7.2. If the input ‘vector’ is, for example, $Z_h=35$ dBZ, $Z_{dr}=0$ dB and $LDR=-28$ dB, we no longer ask the statistical question ‘what is the probability that this input vector can be classified as rain or hail’; rather

we ‘fuzzify’ the input vector using the membership functions and quantify the six ‘conditional probabilities’ as follows (P being the membership value):

$$\text{Prob [echo class is rain } | Z_h=35 \text{ dBZ}] = P_{\text{rain}} (Z_h=35) = 0.9$$

$$\text{Prob [echo class is hail } | Z_h=35 \text{ dBZ}] = P_{\text{hail}} (Z_h=35) = 0.1$$

$$\text{Prob [echo class is rain } | Z_{dr}=0 \text{ dB}] = P_{\text{rain}} (Z_{dr}=0) = 0$$

$$\text{Prob [echo class is hail } | Z_{dr}=0 \text{ dB}] = P_{\text{hail}} (Z_{dr}=0) = 0.3$$

$$\text{Prob [echo class is rain } | LDR=-28 \text{ dB}] = P_{\text{rain}} (LDR=-28) = 0.8$$

$$\text{Prob [echo class is hail } | LDR=-28 \text{ dB}] = P_{\text{hail}} (LDR=-28) = 0.1$$

The next step is to weight the above 6 membership values according to the ‘confidence’ of the measurement, e.g., Z_h and Z_{dr} might have weight value of 1 whereas LDR might have weight value of 0.8. For illustration assume that the weights are unity in this example. Next, the aggregation values (Q) for rain and hail classes are computed by summing the three P_{rain} and three P_{hail} values above resulting in $Q_{\text{rain}} = 0.9+0+0.8 = 1.7$ and $Q_{\text{hail}} = 0.1+0.3+0.1 = 0.5$. The final classification of rain or hail is based on the class that has the $\max(Q)$ value, i.e., in this case the final classification is ‘rain’. The last step is called ‘defuzzification’ since only one hydrometeor class is allowed.

In the above example, the membership functions are one-dimensional. Several fuzzy logic schemes use two-dimensional membership functions, where one dimension usually is the reflectivity. For example, Fig. 7.1 can be thought of as non-fuzzy ‘two-dimensional membership areas’ with sharp boundaries. By contrast, a 2-D membership function with fuzzy boundaries is illustrated for moderate rain in Fig. 7.3.

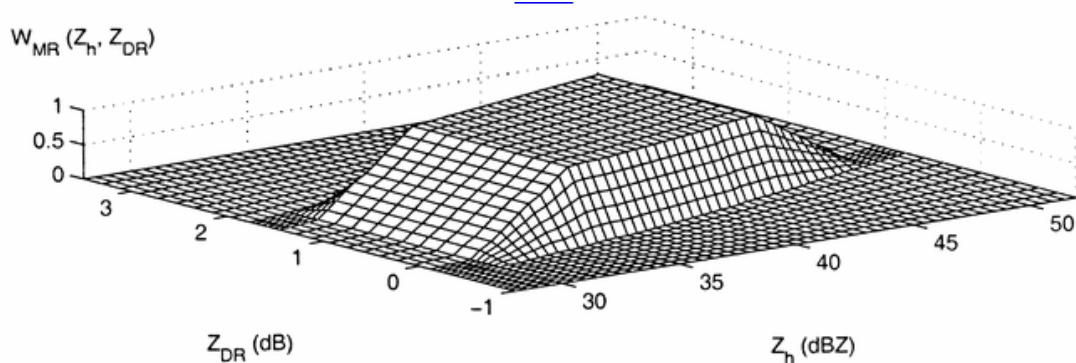


Fig. 7.3: 2-D membership function for moderate rain, from Zrnic et al (2001).

From this illustrative example it is clear that there are 4 important steps, namely,

- (i) selection of the input vector of observations,
- (ii) definition of the membership functions,
- (iii) selection of the weights for each measurement, and
- (iv) the method of aggregation.

In the above example, the membership functions are assumed to be one-dimensional, weights are unity and the aggregation value (Q) is defined as $\text{sum}(P)$. The different research versions of the fuzzy logic implementation referred to earlier differ in their selection of the input vector of observations, selection of the output hydrometeor classes, definition of 1 or 2-D membership functions, selection of the weights for the different observables, and the method of aggregation (sum or product). These research versions are being updated based on new observations and experience.

A very comprehensive set of tables and graphs giving the expected range of values of Z_h , Z_{dr} , K_{dp} , LDR and ρ_{co} for a large variety of hydrometeor types (rain, hail, graupel, ice crystals, wet/dry snow etc) is given in Straka et al (2000) which have been used for building membership functions for ‘fuzzy’ logic schemes (Vivekanandan et al 1999; Zrnic et al 2001; Liu and Chandrasekar 2000; Lim et al 2005; Schuur et al 2003). In the US the main fuzzy logic developers for research S-band radars are the National Severe Storms Laboratory (NSSL), National Center for Atmospheric Research (NCAR) and Colorado State University (CSU). A C-band version has been developed at the Australian Bureau of Meteorology Research Centre (Keenan 2003) for their CPOL radar (data from this radar were reported in Section 3.2.2 and 6.1.3). Only the NSSL has developed a semi-operational version for their prototype dual-polarized WSR-88D which will be the focus herein.

Direct validation of the classification methods has proven to be very difficult because of lack of suitable validation datasets. Limited validation has been described by Lim et al (2005) using hydrometeor imaging probes on storm-penetration aircraft. More extensive surface validation has been possible for hail detection and separation of rain and snow boundaries (Ryzhkov et al 2005a). Indirect validation based on knowledge of precipitation physics in certain types of storms (e.g., supercells, squall lines, MCS etc) together with continuity in space and time has been used to infer the ‘reasonableness’ of the classification schemes.

7.2 The WSR-88D classification for S-band radar – an overview

Table 7.1 illustrates the three different versions of the fuzzy logic scheme used on the semi-operational WSR-88D system (Schuur et al., 2003; Ryzhkov et al., 2005a).

Table 7.1: List of radar echo types identified with the prototype WSR-88D fuzzy logic classifier (from Ryzhkov et al., 2005a).

<i>Version 1</i> “Meteo – non-meteo”	<i>Version 2</i> “Warm season”	<i>Version 3</i> “Cold season”
“RA” – Rain “AP” – Ground clutter / AP “BS” – Biological scatterers	1. “AP” – Ground clutter / AP 2. “BS” – Biological scatterers 3. “BD” – “Big drops” 4. “LR” – Light rain 5. “MR” – Moderate rain 6. “HR” – Heavy rain 7. “HA” – Rain / hail	1. “AP” – Ground clutter / AP 2. “BS” – Biological scatterers 3. “DS” – Dry aggregated snow 4. “WS” – Wet snow 5. “SR” – Stratiform rain 6. “CR” – Convective rain 7. “RH” – Rain / hail

The simplest “Version 1” classifies meteorological and non-meteorological echoes. This version has been demonstrated to be very robust for ‘flagging’ or ‘blanking out’ non-meteorological echo from the conventional meteorological products.

The two other, more sophisticated versions provide a hydrometeor type classification in addition to the non-meteorological classes. Version 2, called “Warm season”, can be applied to conditions where mainly thunderstorms or tropical cyclones are expected. Version 3, called “Cold season”, can be applied for situations with mid-latitude frontal systems, which exhibit large areas of stratiform precipitation with low snow-melting layer heights (or snowfall to the ground level) and moderate convective systems (e.g. rain and graupel showers).

The selection of the input ‘feature’ vector (i.e., the vector of radar observables input to the fuzzy logic scheme) is the first important step.

Table 7.2 gives the input vector for all three Versions. They include Z_h , Z_{dr} , ρ_{co} as well as $SD(Z_h)$ and $SD(\Phi_{dp})$ where SD stands for standard deviation or texture parameter that characterizes the small-scale fluctuations of Z_h and Φ_{dp} along the radar beam. For $SD(Z_h)$ the data are averaged along the radar beam using a 1-km running average window (range samples are spaced 256 m apart) and then subtracting the smoothed value of Z_h from the ‘raw’ values. For $SD(\Phi_{dp})$, the averaging window is 2 km. Both Z_{dr} and ρ_{co} are smoothed in range using a five-point running window; in addition they are both corrected for noise (no classification is done if $SNR < 5$ dB). Both Z_h and Z_{dr} are corrected for rain attenuation using the simple linear Φ_{dp} scheme with fixed coefficients applicable for Oklahoma convective rainfall ($\alpha=0.04$, $\beta=0.004$ dB/deg, see Table 4.1 and equation (5.2)). Classification is done only on the first two PPI elevation tilts of 0.5 and 1.5 deg.

Table 7.2: List of input variables for the prototype WSR-88D fuzzy logic classifier (from Schuur et al 2003).

<i>Version 1</i> “Meteo – non meteo” Input Variables	<i>Version 2</i> “Warm season” Input Variables	<i>Version 3</i> “Cold season” Input Variables
1. Z_h 2. Z_{dr} 3. ρ_{co} 4. $SD(Z)$ 5. $SD(\phi_{dp})$	1. Z_h 2. Z_{dr} 3. ρ_{co}	1. Z_h 2. Z_{dr} 3. ρ_{co} 4. $SD(Z)$

In the following sections, these three methods are explained in detail. Some other methods developed for research applications are also described.

7.3 *Discrimination between meteorological and non-meteorological echoes – algorithms for S-band*

7.3.1 Version 1 of the prototype WSR-88D algorithm

The prototype WSR-88D version uses trapezoid-shaped membership functions as illustrated in Fig. 7.4 with four points along the horizontal axis that have to be specified (X_1 - X_4). The trapezoid-shaped membership functions for the three classes are shown in Fig. 7.5. These are based on careful analysis of scatter plots of dual-polarized radar data collected for many hours during several days of observations. The points X_2 and X_3 are obtained subjectively from experience, examination of scatter plots and consideration of statistical errors in the estimates of the various input variables (see Table 1 of Zrnic et al 2001). Different radar systems may have different levels of statistical or other errors in the dual-polarized parameters (e.g., Klystron versus Magnetron based transmitters, or slant 45 transmission versus alternate transmission of H and V polarized waves, or antenna polarization purity less than the WSR-88D antenna). It is believed that the fuzzy logic scheme should be ‘tolerant’ of such differences without the need for too much ‘fine tuning’.

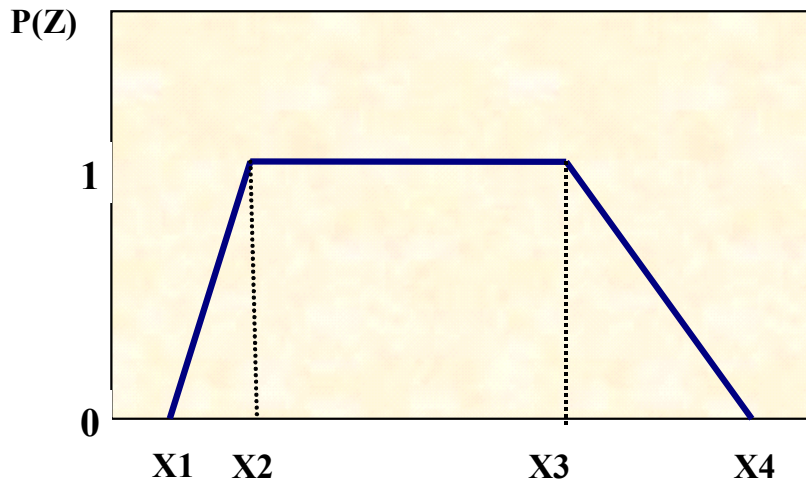


Fig. 7.4: Typical trapezoidal membership function

Examination of Fig. 7.5 shows that $SD(\Phi_{dp})$ is excellent for separating meteorological echo from ground clutter/AP echo (see also Fig. 3.3 or Fig. 3.4 in Section 3.2.2). The Z_{dr} is quite efficient at separating biological scatterers from ground clutter/AP with very little overlap. From Fig. 7.5 the ρ_{co} is similarly efficient at separating meteorological echo from biological scatterers. The $SD(Z_h)$ has been previously found to be useful for detection of AP echoes (using non-polarimetric radar) and for that reason is also used in the polarimetric application. While Z_h alone cannot separate meteo and non-meteo echoes, the combination of Z_h and Z_{dr} is much more efficient especially if a 2D-membership function is constructed for meteorological echo (rain here; see, for example, the correlated behavior of Z_{dr} with Z_h for rain as shown in Fig. 5.1 in Chapter 5). In practice, the four parameters, X1-X4, along the horizontal Z_{dr} axis (in the membership function for rain) are specified to be known functions of Z_h . In Version 1, equal weights are given to all 5 input variables. Although none of the input variables by themselves can clearly separate the three classes, their combination within the context of a fuzzy logic approach is expected to be very efficient especially for events where AP is often embedded within rain regions (this is a very challenging problem for non-polarimetric radars).

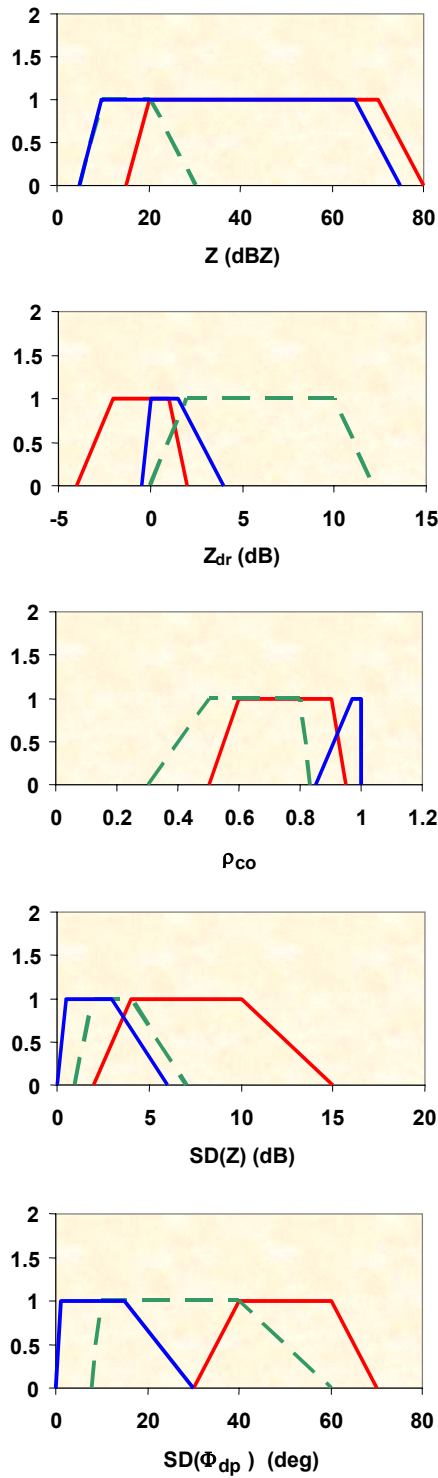


Fig. 7.5: Membership functions for the three classes : meteorological scatterers (blue), biological scatterers (dashed green) and ground clutter / AP (red), shown as a function of Z_h (top), Z_{dr} (second), ρ_{co} (third), standard deviation (SD) of Z_h (fourth) and SD of Φ_{dp} (bottom), from Schuur et al (2003).

Fig. 7.6 shows 4-panels of Z_h , Z_{dr} , ρ_{co} and Classification results for a case with clutter/AP, biological echoes and rain. The reflectivity PPI gives only very limited information for identification. The Classification algorithm, however, identifies extended regions of AP embedded in rain along with biological scatterers (mostly insects in this event). Fig. 7.7 shows another example with extensive regions of AP located SW of the radar.

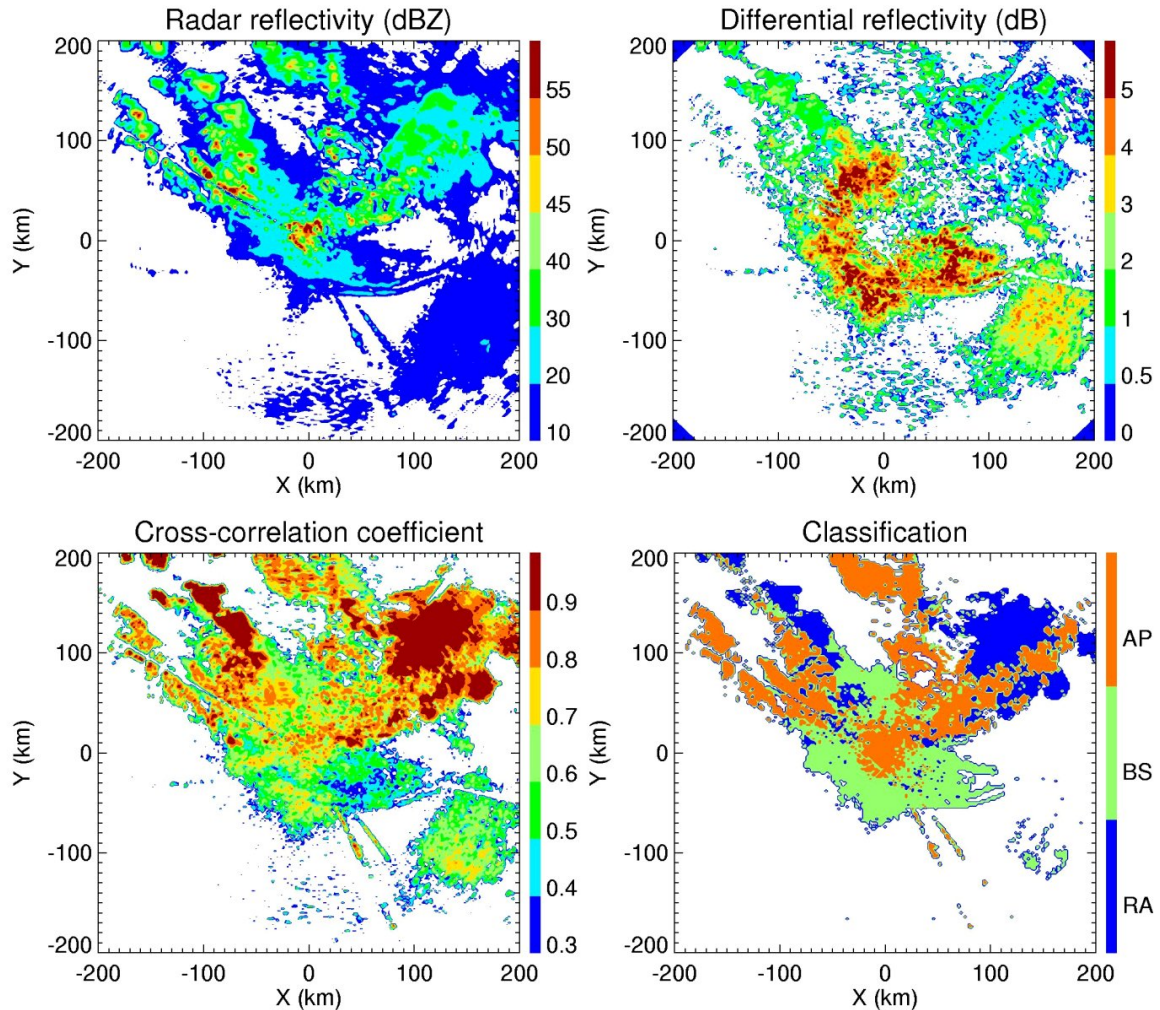


Fig. 7.6: PPI plot of Z_h , Z_{dr} , ρ_{co} and classification from the proto-type dual-polarized WSR 88D located in Norman Oklahoma. For the classes (AP, BS, RA) see Table 7.1. Image from Schuur et al (2005a).

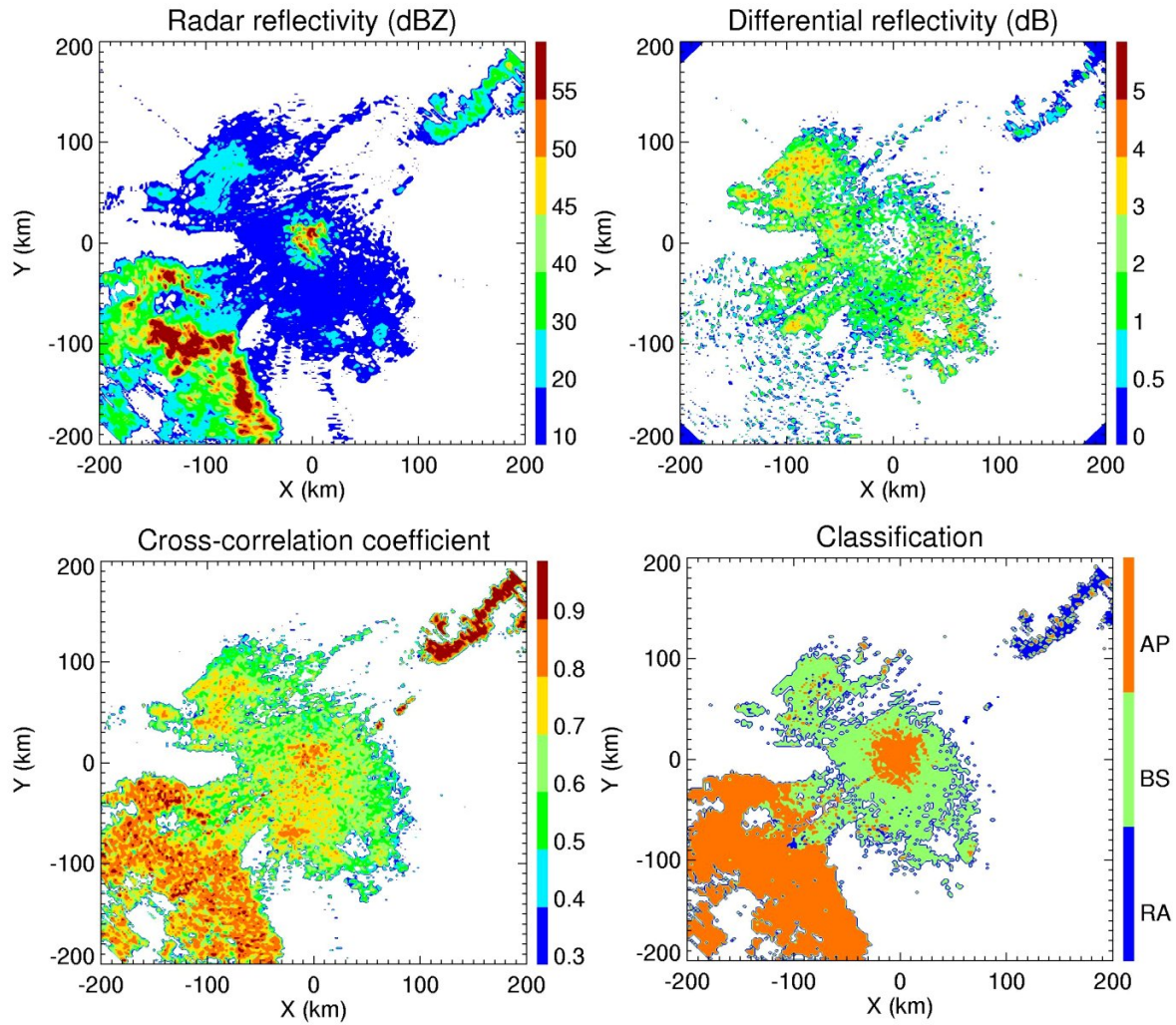


Fig. 7.7: Another PPI example of Z_h , Z_{dr} , ρ_{co} and Classification from the proto-type dual-polarized WSR 88D located in Norman Oklahoma. Adapted from Schuur et al (2005a).

Schuur et al (2003) analyzed in detail eight events that exhibited extensive areas of radar echo caused by AP or biological scatterers along with spatially separated rain echo. For each event animations were found to exhibit good spatial and temporal ‘coherency’ of the three classified fields. Further, they estimate that the number of pixels identified as non-meteorological in origin within pure rain areas was < 1%. Similarly, they estimated the number of pixels identified as pure rain within AP areas was < 1% (i.e., proportion of mis-classification). These statistics were only valid provided the SNR > 10 dB. At reduced SNR > 5 dB, the proportion of misclassification increased to 5%. They attributed this deterioration to the fact that Z_{dr} and ρ_{co} are strongly biased by noise, and that noise correction done during post-processing was not always accurate enough at lower signal levels.

7.3.2 Identification of sea clutter

Microwave propagation over the ocean surface is greatly affected by the vertical profile of the atmospheric refractivity and the oceanic surface state (e.g., Burk et al 2003). For radars located along the coast, distinguishing between ‘normal’ sea clutter, clutter caused by anomalous propagation (AP), echo from very shallow marine boundary layer clouds, and normal precipitation forms an important application for polarimetric radars especially at low elevation angles.

An S-band fuzzy logic classifier for distinguishing between sea clutter, marine boundary layer clouds and precipitation has been developed and undergone limited testing by Ryzhkov et al. (2002b) using data from the NCAR S-POL radar system. The radar was located for a field project near the Pacific shoreline near Seattle, Washington, USA. Ryzhkov et al. (2002b) found that $SD(\Phi_{dp})$ provided “amazingly sharp delineation between sea and weather echoes at a distance of 30 km” (see, also, the range profile of Φ_{dp} in Fig. 4.6 from 15-50 km which is also due to ‘normal’ sea clutter to the NE of Darwin, Australia). They also found that $SD(Z)$ was much larger for sea clutter as compared with precipitation echo. Their fuzzy logic testing was done with the input vector of observations being: $SD(\Phi_{dp})$, ρ_{co} , LDR , Z_{dr} , $SD(Z)$ and mean Doppler velocity. They found that the polarimetric-based scheme exhibited ‘superior performance’ as compared with a non-polarimetric based fuzzy logic classifier (with input vector being: $SD(Z)$ and mean Doppler velocity). An example is shown in Fig. 7.8. Sea clutter is classified from 0-30 km, followed by clouds from 30-60 km and precipitation from 140-150 km. Fig. 7.9 shows raw radar data along the radial marked in Fig. 7.8. It is clear that sea clutter has high LDR, high $SD(\Phi_{dp})$, and low ρ_{co} . From statistical analyses, low values of ρ_{co} cause high fluctuations in Φ_{dp} . On the other hand, non-precipitating cloud has significantly lower $SD(\Phi_{dp})$ and somewhat higher ρ_{co} , whereas precipitation has very low $SD(\Phi_{dp})$, low LDR , and ρ_{co} close to unity. Note that in the non-precipitating cloud, the low SNR causes large statistical fluctuations in Φ_{dp} and ρ_{co} . Fig. 7.10 shows the radar parameters and measurements as a scattergram in terms of SNR for the PPI scan in Fig. 7.8. From their data and discussion it appears that the Version 1 input vector and the membership functions as in Fig. 7.5 discussed earlier should be easily adaptable to the classification of sea clutter/AP from precipitation echo at both S and C-bands.

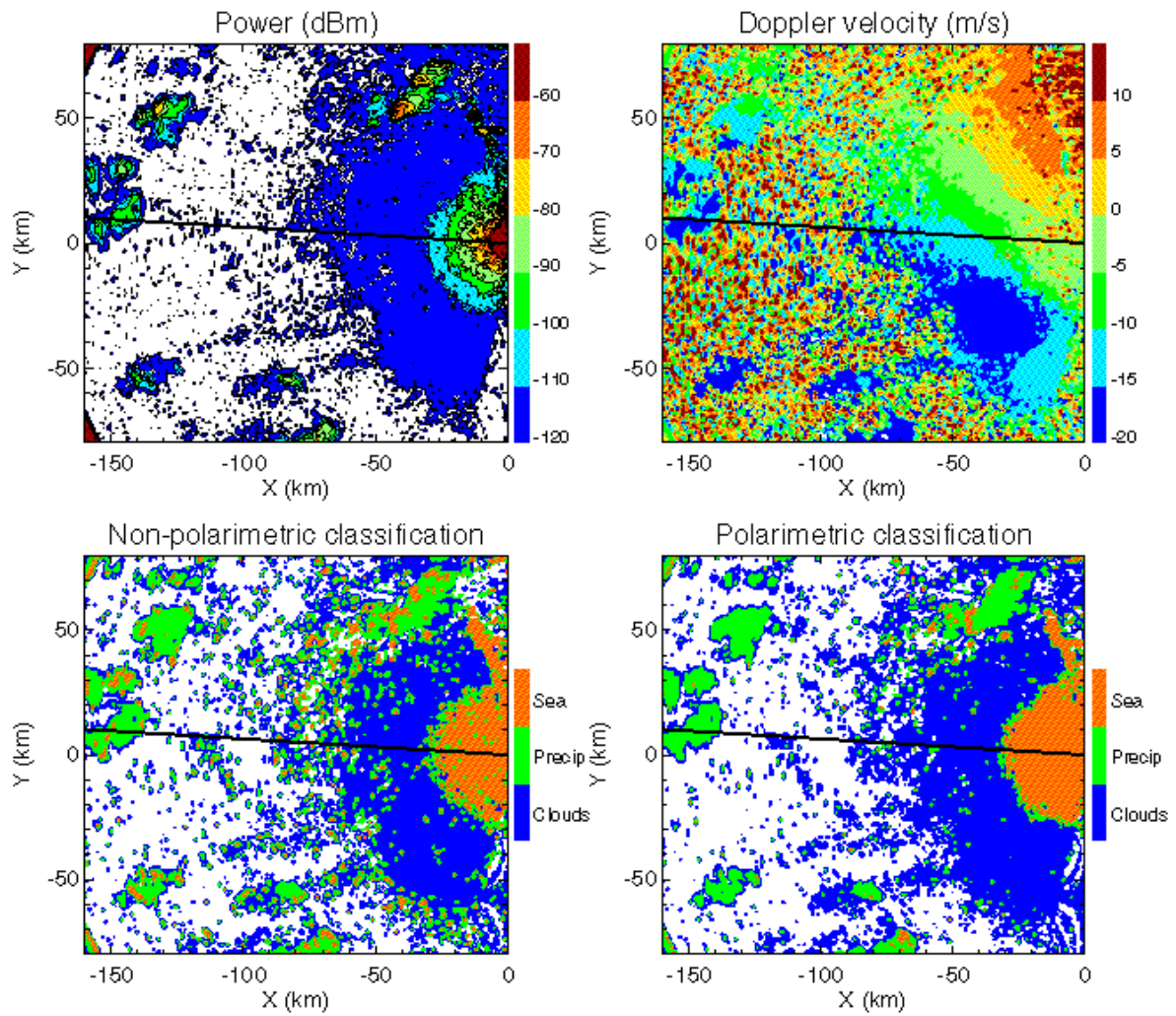


Fig. 7.8: PPI plot of received power (dBm), mean Doppler velocity and the results of polarimetric based classification at low elevation angle compared to non-polarimetric based classification. From Ryzhkov et al. (2002b); image ©copyright 2002 URSI.

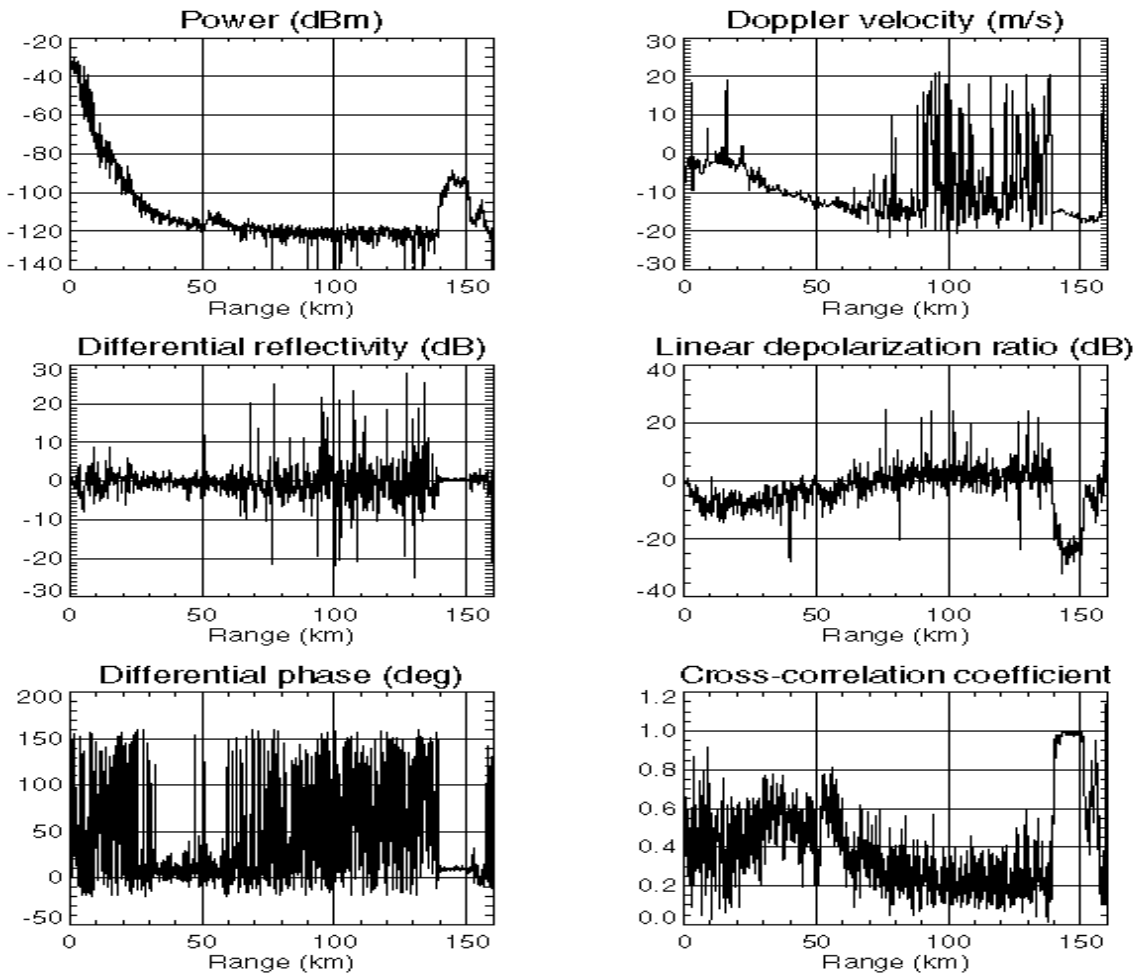


Fig. 7.9: Range profile of received power (dBm), mean Doppler velocity, Z_{dr} , LDR , ϕ_{dp} , and ρ_{co} . along the radial marked as thick solid line in Fig. 7.8. From Ryzhkov et al. (2002b); image ©copyright 2002 URSI.

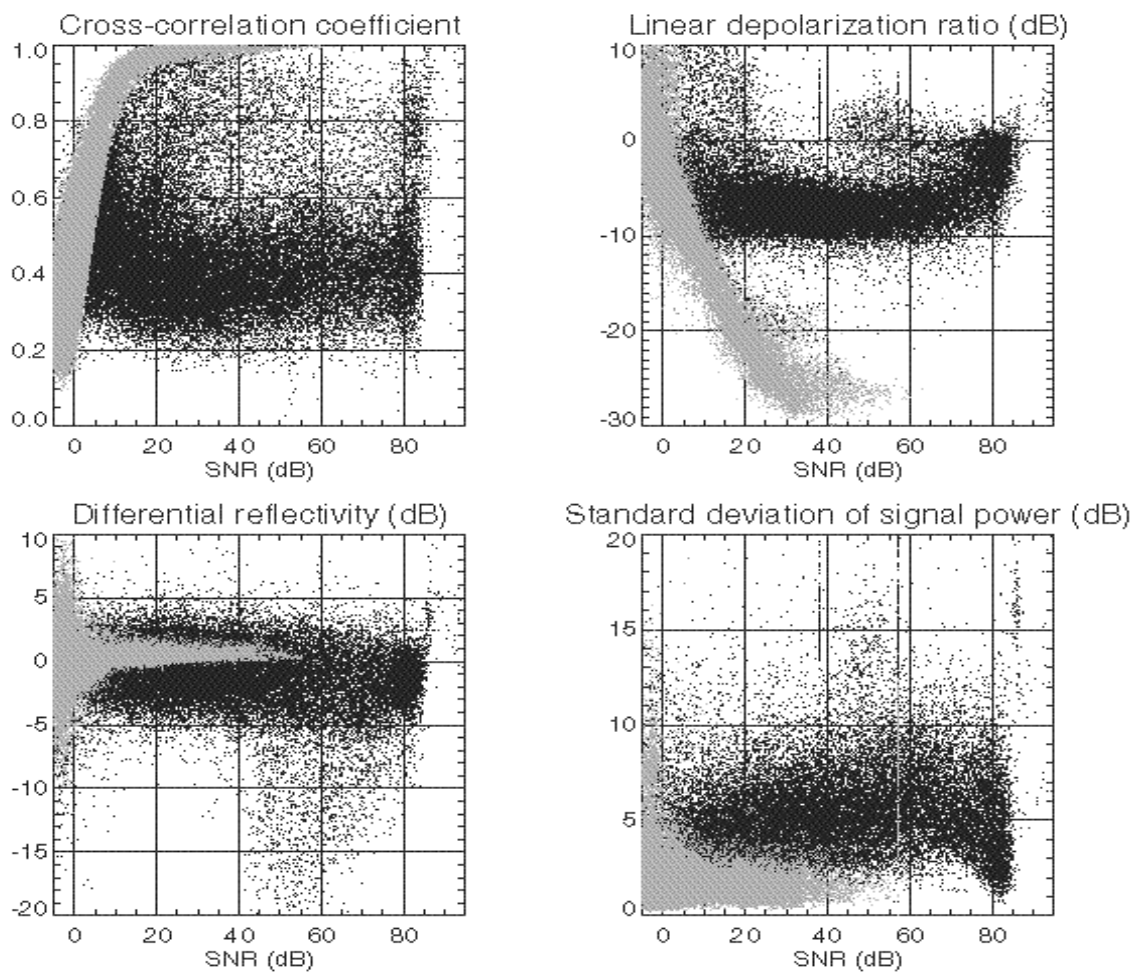


Fig. 7.10: Scattergram of various radar parameters and measurements in precipitation (grey dots) and sea clutter (black dots) versus SNR, corresponding to Fig. 7.8. From Ryzhkov et al. (2002b); image ©copyright 2002 URSI.

7.3.3 Identification of chaff

Chaff dispersion is used by the military for countermeasures but for weather radar it contaminates the rainfall accumulation amounts and as such must be identified and removed. Chaff can be modeled as thin cylinders of length $\frac{1}{2}$ wavelength long ('resonant' dipole) and usually aluminium-coated to make them 'appear' as a perfect conductor at radar wavelengths. A priori it will not be known that chaff is 'resonant' at the weather radar frequency. There is a substantial literature on the properties of chaff, i.e., their dispersion rate, fall modes, detection, etc., for military applications but not for polarimetric weather radar. The only modeling and experimental work we are aware of at linear (H/V) polarizations is that of Zrnic and Ryzhkov (2004) for S-band. They have modeled chaff particles both as 'resonant' dipole with assumed sinusoidal distribution of induced current, and as Rayleigh particles of prolate shape (length \ll wavelength). Their model results for these two cases are not very different and as such may be applied also to shorter wavelengths such as C-band.

The polarimetric variables are sensitive to the fall mode (or, orientation angle distribution) and some assumptions must be made such as the axis of the thin cylindrical chaff particles is assumed to be uniformly distributed in the horizontal plane, while the azimuth angle is uniformly distributed between 0 and 2π . The polar angle θ (measured from the local vertical direction to the cylinder axis) is assumed to be uniform between $\pi/2 - \theta_0$ and $\pi/2 + \theta_0$. These assumptions are similar to the fall mode of 'needle' ice crystals in the atmosphere (Fig. 7.70 in Bringi and Chandrasekar 2001 illustrates the fall mode assumption). The angle θ_0 is referred to as the 'flutter angle' by Zrnic and Ryzkova (2004) and the various polarimetric variables such as Z_{dr} , LDR and ρ_{co} are calculated as a function of this 'flutter angle' assuming that the radar elevation angle is 0° . Note that if θ_0 is 0 then there is no 'flutter' whereas if θ_0 is $\pi/2$ the orientation distribution is isotropic. In the latter case the $Z_{dr} = 0$ dB whereas LDR reaches its maximum value of -5 dB with $\rho_{co} = 1 - 2L = 0.36$ (see, also, equation (2.31)), where L is the ratio form of LDR .

The experimental data in chaff was collected with the prototype WSR-88D radar with the region of chaff being well separated from a snow band. The reflectivity of chaff was found to be very similar to that of snow but the polarimetric variables were found to be very different especially the low values of ρ_{co} (mean of 0.36!) in chaff and correspondingly large statistical fluctuations in Φ_{dp} (i.e., a broad distribution). This implies that chaff may be identified by very low values of ρ_{co} (typically 0.2 to 0.5) and large values of $SD(\Phi_{dp})$, in fact similar to sea clutter described in the previous section. From their experimental data the 'flutter' angle of chaff was inferred to be in the range $65\text{--}75^\circ$, i.e., not quite isotropic orientation distribution. The prototype WSR-88D, while having the LDR -mode capability, it was not exercised for this particular event. However, from the low ρ_{co} values and large inferred 'flutter' angles, the LDR values should be very large (~ -5 to -7 dB) which is rarely found in precipitation. Thus, LDR may be a useful input variable in a fuzzy logic scheme along with ρ_{co} and $SD(\Phi_{dp})$.

Fig. 7.11 shows a 4-panel PPI of Z_h , Z_{dr} , Φ_{dp} and ρ_{co} from the WSR-88D in an event with snow bands to the north of the radar, close in ground clutter and chaff 'cloud' to the southwest of the radar. Note that construction of even a two-dimensional

membership function using Z_h and Z_{dr} (e.g., see Fig. 7.3) cannot easily differentiate chaff from the snow band or rain, because of substantial overlap in the Z_h - Z_{dr} measurement plane. It is rather puzzling that Z_{dr} values in chaff can be quite positive (> 4 dB in some regions) in spite of the inferred isotropic orientation in which case $Z_{dr} \sim 0$ dB. Note, also, from Fig. 7.11 that the $SD(\Phi_{dp})$ inferred from the Φ_{dp} panel between chaff and ground clutter might appear to be similar with significant overlap. Zrnic and Ryzhkov (2004) comment that in the case of chaff, the high $SD(\Phi_{dp})$ is mainly due statistical fluctuations caused by very low values of ρ_{co} , whereas ground clutter can have much higher values of ρ_{co} along with high $SD(\Phi_{dp})$ which is attributed to the large variability of the back scatter differential phase (see equation (2.33) for the definition) and much less due to statistical fluctuations. It appears that an observational-based methodology such as used by MeteoFrance would lead to construction of density functions (and corresponding membership functions) that would lead to a robust classification of chaff with input variables being ρ_{co} , $SD(\Phi_{dp})$ and LDR . Such data in chaff (except LDR) have been collected by MeteoFrance but not reported upon yet.

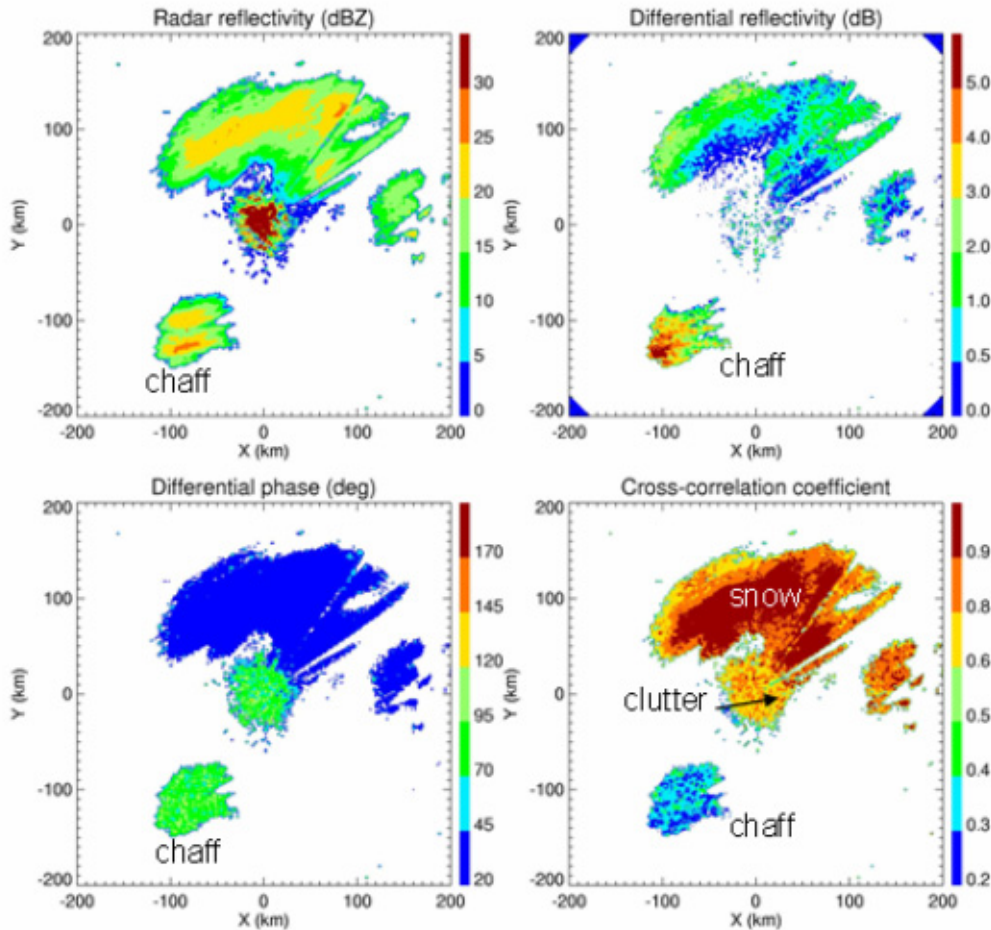


Fig. 7.11: Fields of polarimetric variables from regions of ground clutter, chaff, and snow. Data were obtained with the prototype WSR-88D during the JPOLE experiment on Feb 6, 2003 at 21:00 UTC from a scan at 0.5 deg elevation. From Zrnic and Ryzhkov (2004).

7.4 Classification between hydrometeor types – algorithms for S-band

The fuzzy logic-based methodology affords the capability to distinguish between different types of hydrometeors (see central and right column of Table 7.1 listing the hydrometeor classes used by Versions 2 and 3 for the WSR-88D application).

7.4.1 Classification for ‘warm season’

The membership functions for Version 2 ‘warm season’ are given in Fig. 7.12 but for clarity only the functions for three hydrometeor classes are shown, i.e., big drops (BD), moderate rain (MR) and rain/hail mixture (HA).

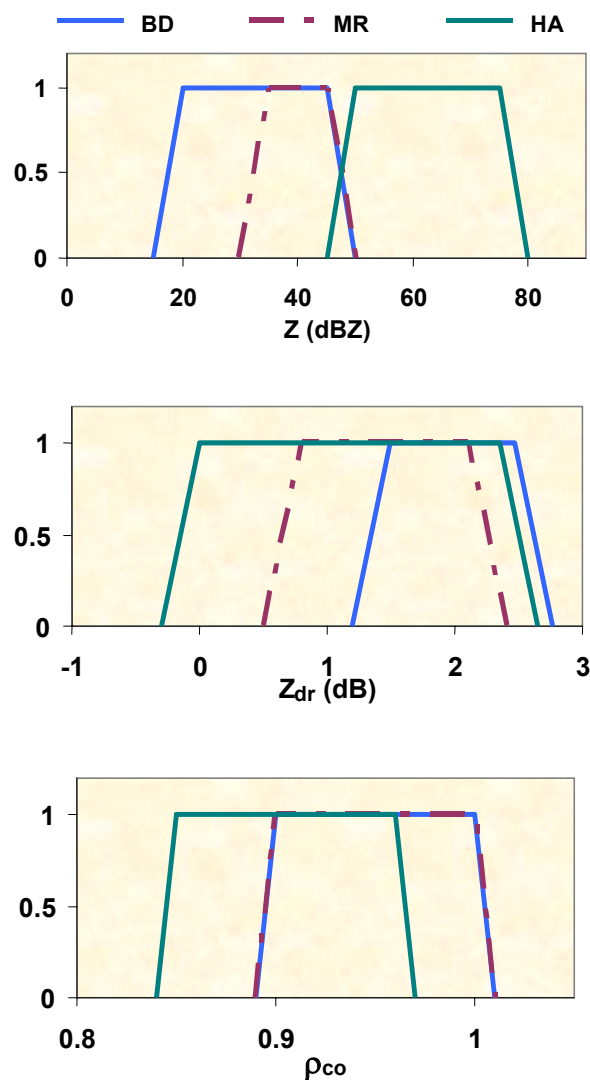


Fig. 7.12: Membership functions for the three classes in version 2 – warm season: big drops (BD), moderate rain (MR) and rain/hail mixture (HA) shown as a function of Z_h (top), Z_{dr} (middle), ρ_{co} (bottom), from Schuur et al (2003). The other warm season classes are not included.

The ‘big drops’ refer to regions where the raindrop size distribution is dominated by a very low concentration of large drops. Such regions can be associated with drop sorting in rapidly growing echoes where low-to-mid level updrafts lift smaller-sized drops into the cold regions (-5 to -10C) of the cloud. This gives rise to the so-called vertically erect, positive Z_{dr} columns which have large Z_{dr} values at the lower levels as big drops fall against the updraft. Such columns are thought to supply frozen drop embryos which enter the main updraft and grow into larger hail stones by rapidly accreting the cloud water (e.g., Hubbert et al 1998). The big drop classification appears to have prognostic value for weather forecasters dealing with hail formation in organized convection (e.g., squall lines, supercells). Fig. 7.13 shows a vertical cross section through a hailstorm in Southern Germany which illustrates the location of the positive Z_{dr} column with big drops near the bottom of the column (see region around east-west distance of 47 km; note that these data are from a C-band radar).

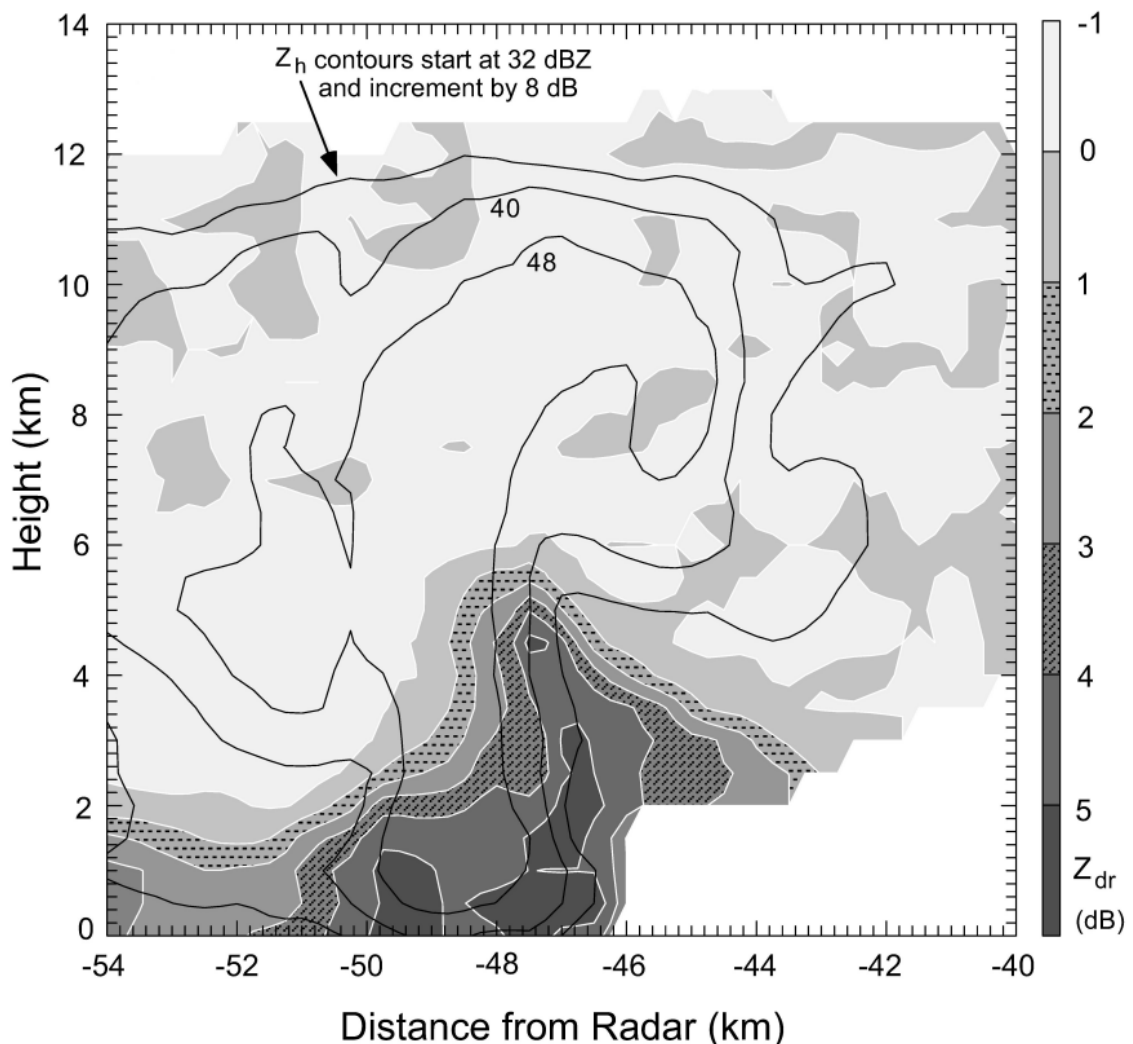


Fig. 7.13: Vertical section of radar data taken through the core of a hailstorm near Munich, Germany with contours of Z and overlay of Z_{dr} . Data taken with the C-band DLR radar, from Hubbert et al (1995).

The rain/hail class in Version 2 can refer to rain mixed with hail or to hail occurring with little or no rainfall. The earliest application of Z and Z_{dr} data was to hail detection (Hall et al 1984; Bringi et al 1984) as it was relatively simple to detect the hail shaft with high Z and Z_{dr} values close to 0 dB or even negative. Fig. 7.14 shows a RHI section through a hailstorm in Southern England. Note the high Z values (around 56 dBZ) accompanied by lowered Z_{dr} values (0 to 0.5 dB) near range of 32-33 km (marked as Region B) which is preceded by heavy rainfall indicated high Z and high Z_{dr} values (marked as Region A).

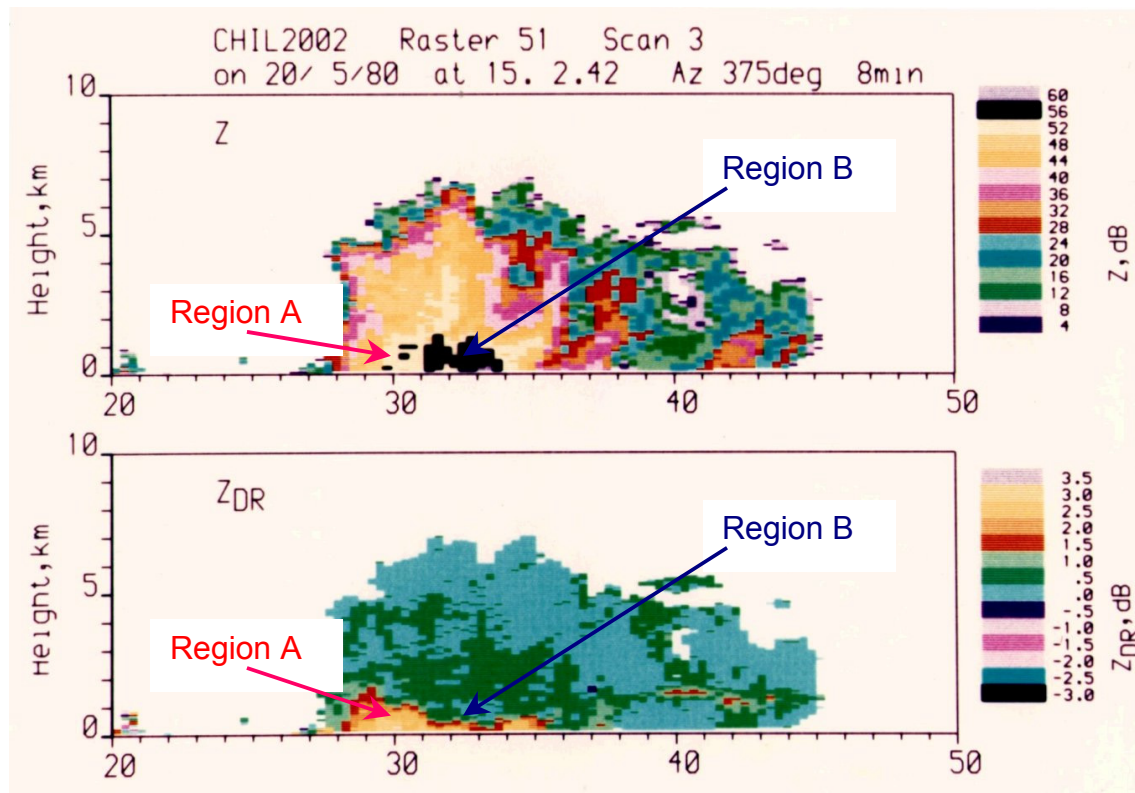


Fig. 7.14: RHI scan taken through a hail shaft in a strong convective storm, in Southern England, with the RAL S-band radar located in Chilbolton, UK, courtesy of Rutherford Appleton Laboratory, UK. These are the earliest reported measurements of Z and Z_{dr} in hail.

Fig. 7.15 shows the time variation of Z and Z_{dr} data over three hail pads during a hail event in France. Note in the two bottom panels how the peaks in Z are accompanied by dips in Z_{dr} to negative values (minimum reaching -1.4 dB). The bottom two panels also show that the hail pads detected hail with maximum sizes of 20-23 mm with number per square meter of 1400-3850. These are among the first attempts to validate the radar signatures in hail.

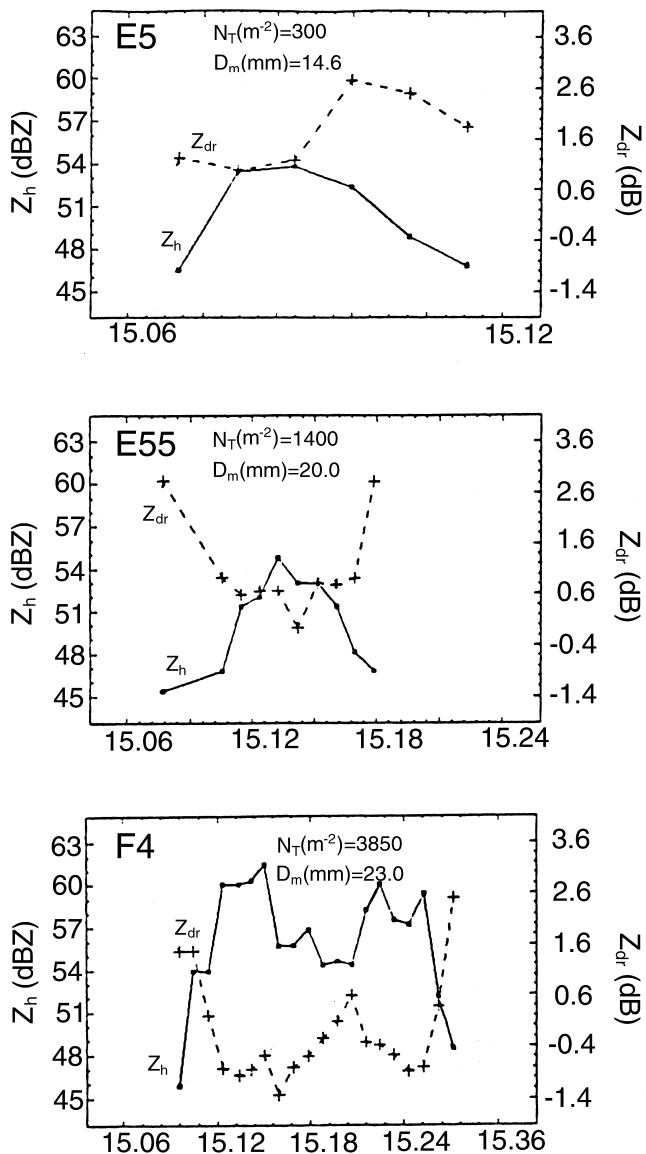


Fig. 7.15: Time variation of Z and Z_{dr} above three hail pads as measured by the S-band ANATOL radar in France. N_T refers to the number of hailstones per m^2 and D_m is the maximum hail size as recorded by the hail pads, from Husson and Pointin (1989).

The full complement of radar measurements in a supercell storm event and their evolution with time as it moved across a hail chase van is shown in Fig. 7.16. In the ρ_{co} panel (c), the hydrometeor types actually observed as a function of time are annotated at the top. Note the signatures during the time of golf ball hail falling on the chase van especially the enhanced *LDR* reaching -16 to -18 dB and lowered ρ_{co} values dipping to 0.91. Note also that the observed hydrometeor types and the radar signature values are in reasonable accord with the boundaries shown in Fig. 7.1. Panel (d) shows the accumulated rainfall for the entire event based on a Young

capacitance gage on the van and using the standard $Z-R$ relation (see equation (6.9d); here max Z is limited to 55 dBZ) as well as the $R=40.5 K_{dp}^{0.85}$ (similar to equation (6.9e)). The power of K_{dp} to estimate the rainfall in the presence of large hail is clearly evident from this panel.

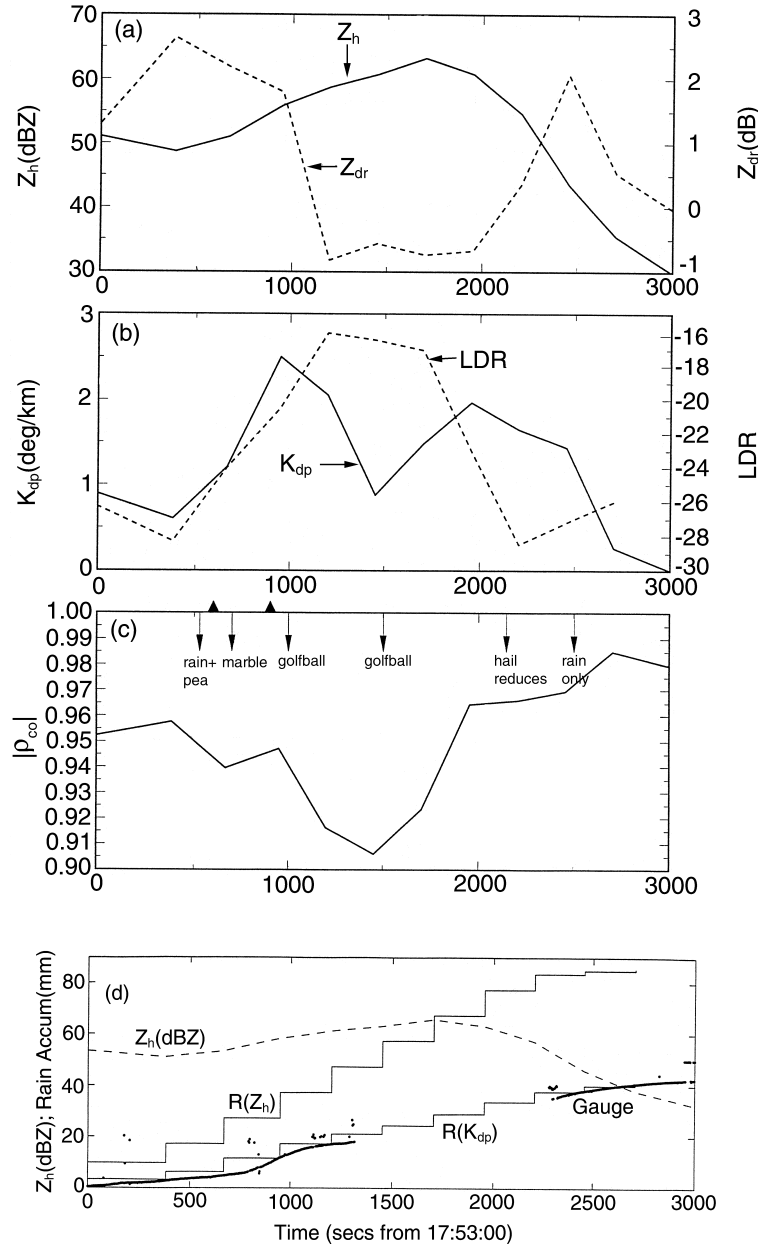


Fig. 7.16: (a-c) Time series of polarimetric data over a chase van location. Data from the CSU-CHILL radar at 1° elevation angle. Visual observations of hydrometeor type are marked in panel (c). (d) Rain accumulation measured by gage on the van (the gap in data was caused by power supply problem), from Hubbert et al (1998).

Fig. 7.17 shows PPI data of Z , Z_{dr} , K_{dp} and ρ_{co} from the prototype WSR-88D as well as the Version 2 ‘warm season’ Classification results in the last panel. Data are from a severe hailstorm with reports of very large hail. Three hail cells can be noted centered at (-10,-90 km), (10,-100) and (20,-120). The classification results show hail around these areas surrounded by heavy rain.

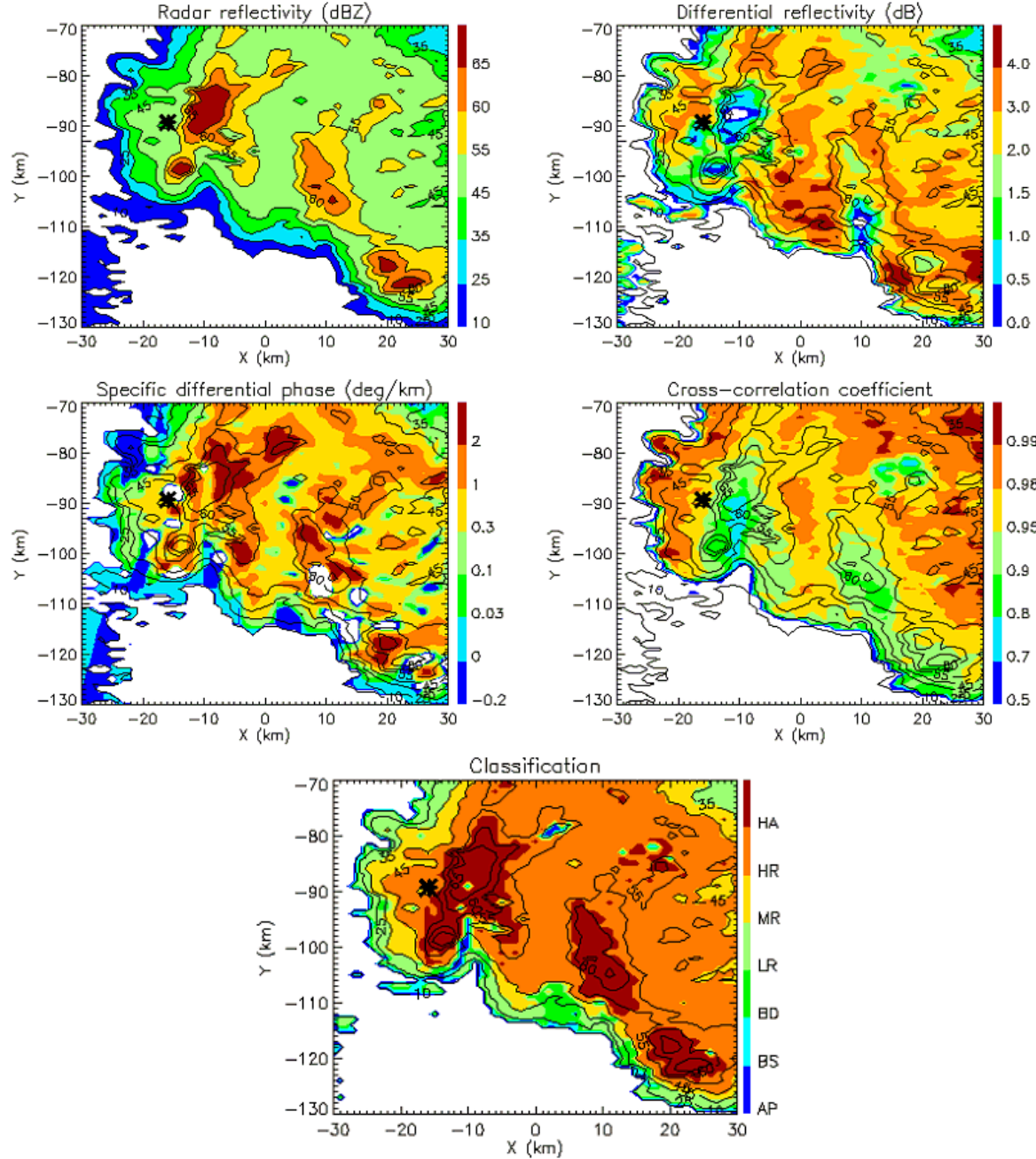


Fig. 7.17: PPI data at 0.5° elevation angle from the dual-polarized WSR-88D radar located in Norman, Oklahoma for the hail event on 14 May 2003. The location of the large hail report is shown by the ‘star’ mark. For the classes (HA, HR, etc.) see Table 7.1. Image from Schuur et al (2003) and from Schuur et al (2005a).

Ryzhkov et al. (2005a) have used an enhanced version 2 of their ‘warm season’ fuzzy logic classifier which included $SD(Z)$, $SD(\Phi_{dp})$ and mean Doppler velocity for verification of hail from 4 storm events using two chase van teams (total of 74 hail intercept observations from the 4 events). They compared the fuzzy logic scheme results with the standard WSR-88D hail detection algorithm (Witt et al 1998) which uses Z , vertical storm structure and environmental conditions . They found that the polarimetric-based fuzzy logic method gave 100% probability of hail detection (POD) with false alarm rate (FAR) of 11% and critical success index (CSI) of 0.89. In comparison, the standard WSR-88D hail algorithm gave POD=88%, FAR=39% and CSI=0.56. The reduction in FAR and increase in CSI are significant, demonstrating the advantage to be gained by the additional measurements of Z_{dr} and ρ_{co} . Of more importance to the forecaster is the detection of damaging hail (e.g., diameters > 20 mm) rather than detecting the occurrence of any size hail. There is evidence that large hail depolarizes more than small hail, thus LDR in combination with Z and Z_{dr} may show more promise in detecting damaging hail near the surface (Kennedy et al 2003).

There are a number of S-band research fuzzy logic versions that use different sets of input observations as well as a different and much larger set of output hydrometeor classes. These research versions can be applied to give a vertical cross section of hydrometeor types (based on RHI or full volume PPI scans) as opposed to only the 0.5° and 1.5° PPI scans for the WSR-88D application. More notably, the research versions have an additional input: in the NSSL research version it was the environmental temperature profile modified so that the height of the 0° isotherm was forced to coincide with the height locating the minimum in ρ_{co} (Zrnic et al 2001). In the CSU research version the height of the melting level was input but is determined from the vertical profile of Z_{dr} (i.e., finds the height where the slope of Z_{dr} changes rapidly in the transition from isotropic wet ice to oriented oblate rain). The details of the research versions are very sophisticated and can be found in the corresponding references (for S-band: Zrnic et al 2001; Vivekanandan et al 1999; Lim et al 2005).

An important sensitivity study by Zrnic et al (2001) concluded that the combination of Z and Z_{dr} possesses the ‘strongest discriminating power’ and that inclusion of the temperature profile (or knowing the height of the melting level) put an important constraint on the allowable hydrometeor types above (or, below) the melting level (e.g., rain was excluded at heights well above the melting level). This implies that ρ_{co} is an important input variable. At the current time it appears that the LDR measurement is perhaps not important in ‘warm’ season classification and that ρ_{co} is a suitable alternative (perhaps because they are simply related if the particles’ canting angles are randomly oriented in the plane of polarization). However, it appears that LDR might be more useful in ‘cold’ season classification when the 0° level might be near or ‘below’ the surface.

7.4.2 Classification for ‘cold season’

The hydrometeor classes for the WSR-88D Version 3 ‘cold season’ were given previously in Table 7.1. The membership functions are shown in Fig. 7.18; for clarity only the dry snow (DR), wet snow (WS), stratiform rain (SR) and convective rain (CR)

membership functions are shown. Distinction between dry snow and stratiform rain is difficult using only Z_h , Z_{dr} and ρ_{co} , even within the fuzzy logic scheme, as the membership functions overlap considerably. Fig. 7.19 shows scatter plot of Z_{dr} versus Z_h obtained from measurements with the prototype WSR-88D radar for three different types of snow in Norman, Oklahoma as well as the boundaries for the rain class to illustrate the overlap between light rain and snow.

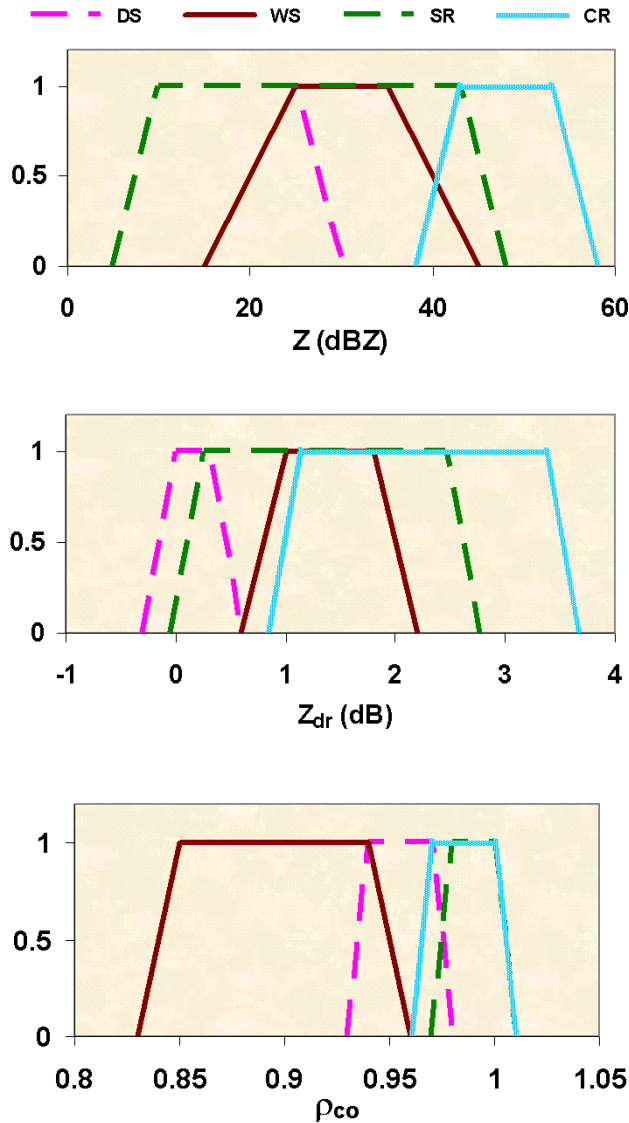


Fig. 7.18: Membership functions for four classes in Version 3 of the WSR-88D classification (“Cold season”): dry snow (DS), wet snow (WS), stratiform rain (SR), and convective rain (CR) shown as a function of Z_h (top), Z_{dr} (middle), ρ_{co} (bottom), from Schuur et al (2003). The other cold season classes are omitted for clarity of the display.

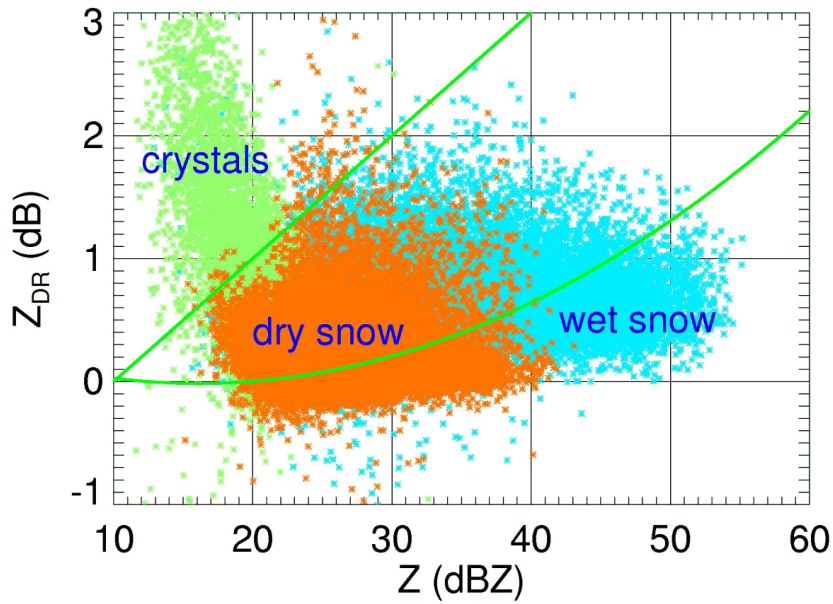


Fig. 7.19: Scatter plots of data from the prototype WSR-88D in three different types of snow in Norman, Oklahoma, from Ryzhkov and Zrnic (2003). The two green curves are the rain boundaries and confine the rain class in the $Z-Z_{dr}$ plane.

For cold season classification it is important to determine the height of the bright-band (BB) which separates snow above the BB, wet snow in the BB and stratiform rain below the BB. The ρ_{co} and LDR parameters are the important polarimetric variables that can be used to locate the BB even when the reflectivity bright-band is too weak to be detected. In particular, the ρ_{co} reaches its minimum value closer to the base of the BB whereas the peak in LDR occurs above it and is closer to the maximum of Z . Fig. 7.20 shows 4-panels of RHI scan data taken during a stratiform event at close range with the CSU-CHILL S-band radar located in Greeley, Colorado. The low values of ρ_{co} and the enhanced LDR are due to the variety of ‘shapes’ present in the BB caused by various degrees of partially wetted snow. Note that the maximum in LDR and the minimum of ρ_{co} are similar in magnitudes to what can occur in a severe hail storm (see Fig. 7.16); however, the reflectivity and Z_{dr} magnitudes are, of course, very different in the two cases.

There is a large amount of polarimetric data available for stratiform rain events with BB at S and C-bands. Fig. 7.21 shows histograms of ρ_{co} in drizzle and the BB obtained in Southern England using the RAL S-band radar system. Note how well separated the BB is from drizzle when using the ρ_{co} variable.

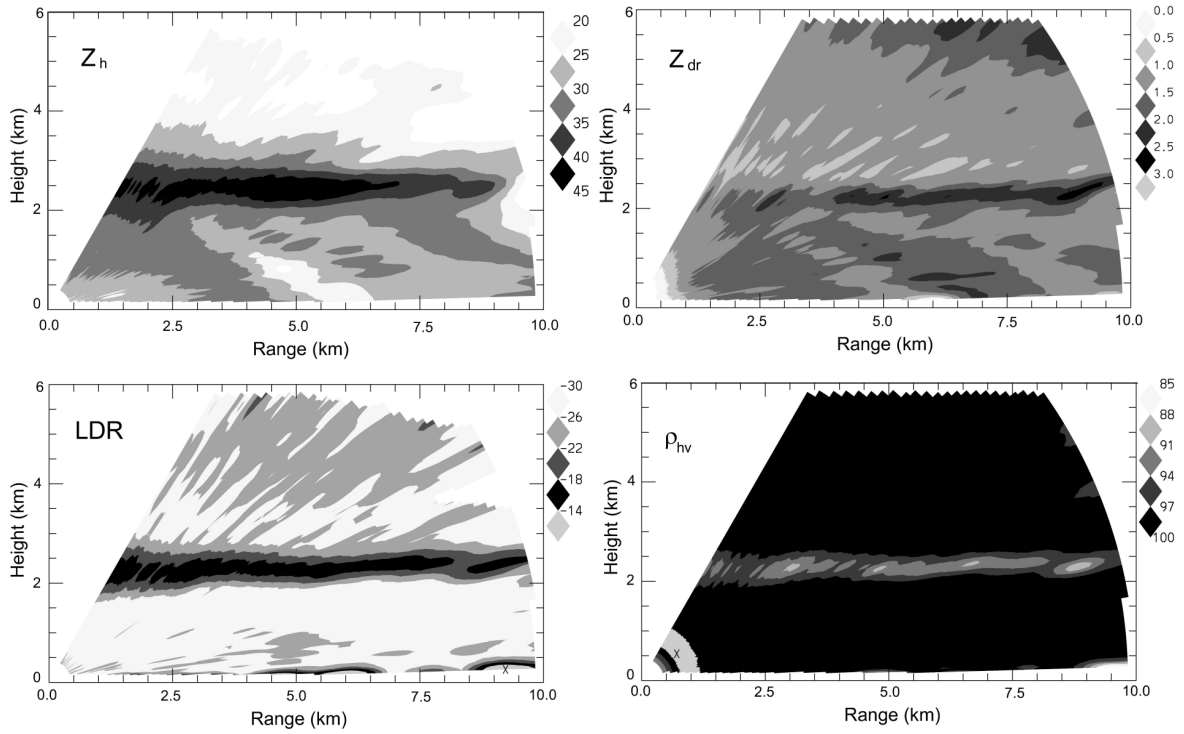


Fig. 7.20: RHI scan data using the CSU-CHILL radar depicting Z_h , Z_{dr} , LDR and ρ_{hv} (same as ρ_{co}) in a stratiform event. From Beaver and Bringi (1997), ©copyright 1997 IEEE.

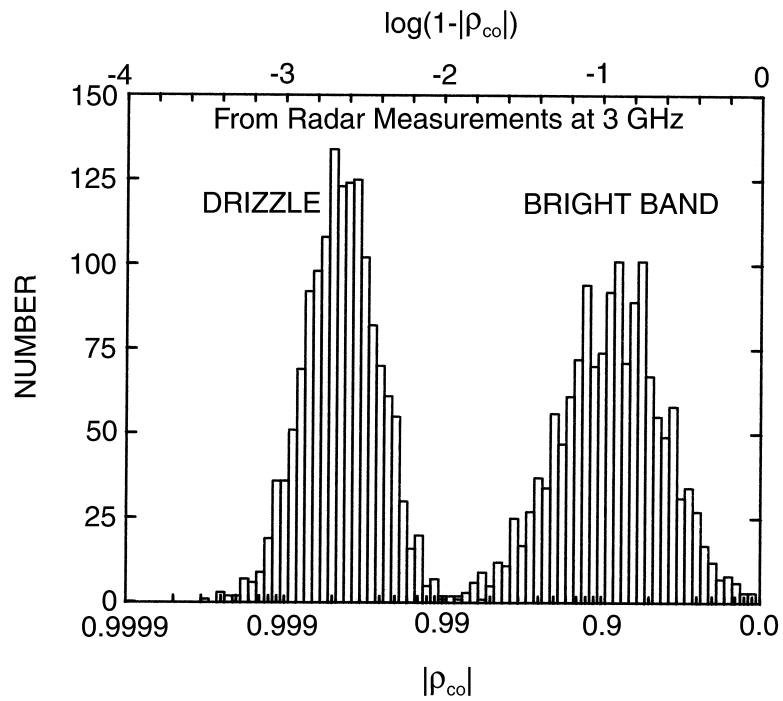


Fig. 7.21: Histogram of ρ_{co} in drizzle and in bright band using the RAL S-band radar located in Chilbolton, U.K., from Illingworth and Caylor (1991).

The WSR-88D algorithm locates the minimum of ρ_{co} at every azimuth angle using data from range profiles at the 1.5° elevation angle sweep. Generally as one progresses along range, the precipitation changes from rain to wet snow in the BB to dry snow at longer ranges. Correspondingly, there is a sharp decrease in ρ_{co} from 0.99 in rain to < 0.95 in the wet snow, after which it tends to increase in the dry snow at longer ranges. However, this increase in the dry snow region is often masked by a general lowering of ρ_{co} due to lowered SNR when SNR falls below about 15-20 dB. Thus, noise correction is important for ρ_{co} at the further ranges. Referring to equation (2.30), the measured power levels in the H and V receivers have to be corrected for noise, prior to normalization by the signal powers (i.e. the square root term in the denominator). After detecting the drop in ρ_{co} during the transition from rain to wet snow at each azimuth angle in the 1.5° sweep, a ‘bright band’ contour is generated for the sweep. Note that such a contour is expected to be circular around the radar in very homogeneous events, but deviations from circularity often occur because of embedded convection or other sources of spatial inhomogeneity. To illustrate this difference, Fig. 7.22 shows PPI data of Z , Z_{dr} , ρ_{co} and the Version 3 Classification results. Note that rain and clutter/AP are prohibited at ranges beyond the BB contour and snow is prohibited below the BB. The left 4 panels show data from a winter storm event with stratiform rain classification and BB contour showing more or less good symmetry about the radar location. The right 4-panels show similar data about 9 hours later when there is noticeable asymmetry in BB contour about the radar, mainly to the N-NW, implying a drop in the height of the BB. On the other hand, in the southern sector the BB contour is similar to 9 hours earlier. During this event the BB was slowly lowering in height due to cold pool of air advecting from the N-NW. Details of this event can be found in Ryzhkov and Zrnic (2003) and Scharfenberg and Maxwell (2003).

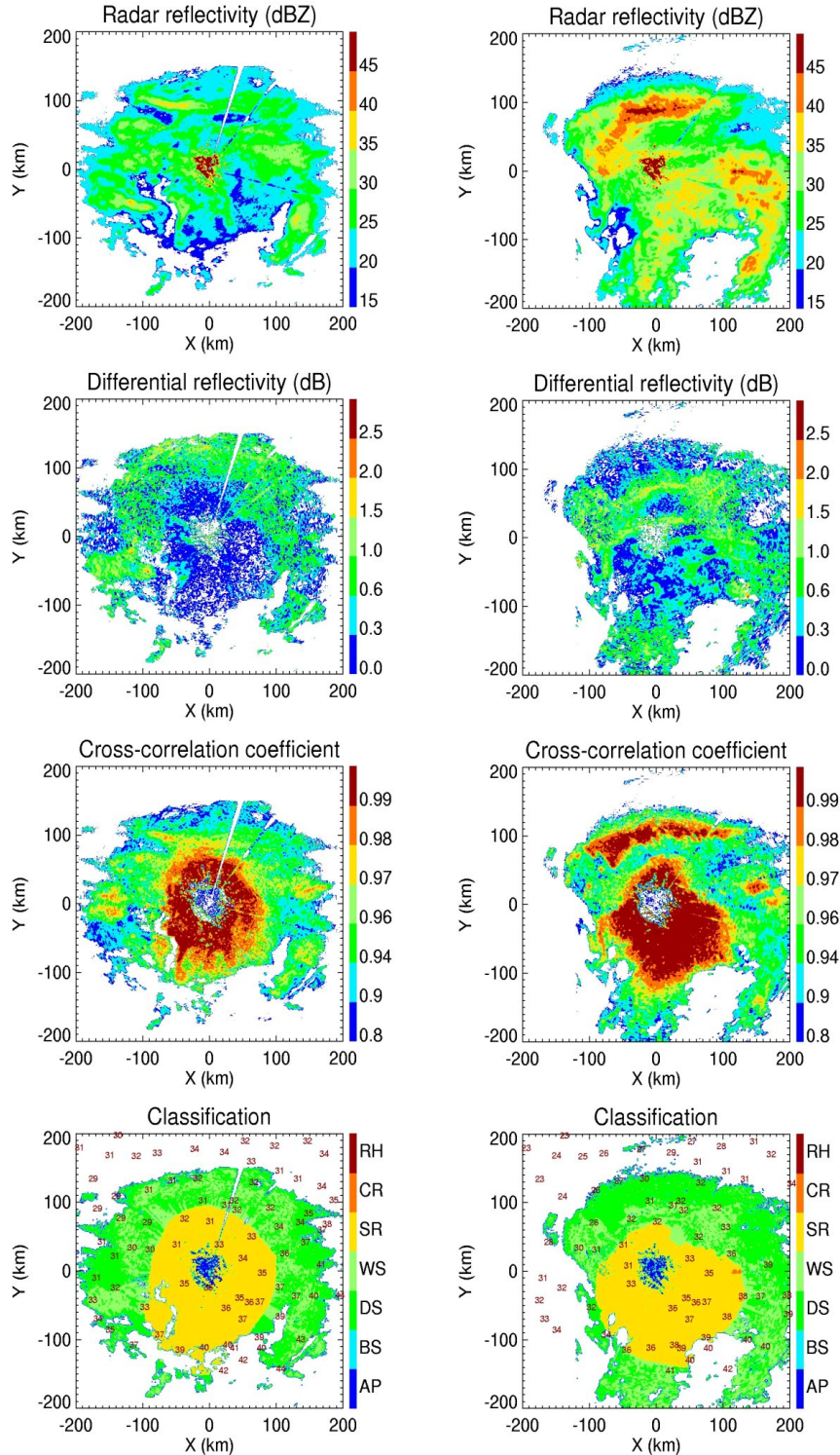


Fig. 7.22: PPI scan data from the prototype WSR-88D radar in a winter storm event of 3 Dec 2002 at 18:03 UTC (left panels) and 4 Dec 2002 at 03:02 UTC (right panels) in Norman, Oklahoma. Compared to the left 4-panels with more circular BB contour around the radar, the right 4-panels show very asymmetric BB contour due to cold air advection from the N-NW.

Surface temperatures in °F are shown in the classification panels, from Ryzhkov and Zrnic (2003).

7.4.3 The HDR method and combined HDR-LDR methods

The Hail Detection Ratio (HDR) is a parameter which has been used in the past to indicate the presence of hail ever since the earliest measurements of Z_h and Z_{dr} at S-band in the UK by Hall et al. (1984). This signature indicates the extent to which the observed Z_h deviates from the rain-hail boundary in the $Z_h - Z_{dr}$ plane. At S-band, the HDR has been formulated by Aydin et al. (1986) as:

$$\text{HDR} = Z_h - f(Z_{dr}) \quad (\text{dB}) \quad (7.1)$$

where $f(Z_{dr})$ is given by:

$$f(Z_{dr}) = \begin{cases} 27 & Z_{dr} \leq 0 \text{ dB} \\ 19Z_{dr} + 27 & 0 < Z_{dr} \leq 1.74 \text{ dB} \\ 60 & Z_{dr} > 1.74 \text{ dB} \end{cases} \quad (7.2)$$

Hail is indicated if HDR is greater than 3 dB. Similar results were obtained in an earlier study by Leitao and Watson (1984) in the UK. Referring back to Fig. 7.14, the third panel corresponds to the largest values of HDR (of ~ 30 dB), with maximum hail size of 23 mm.

By combination of HDR and LDR, effectively a three-parameter non-fuzzy classification method is applied. At S-band, Kennedy et al. (2001) have used the so-called ‘hail quadrature parameter’ term, abbreviated to HQP. This term is defined as the length of a ‘vector’ whose orthogonal components are HDR and LDR, both in dB. The HQP domain ($5 < \text{HDR} < 50$ dB and $-25 < \text{LDR} < -10$ dB) covers the expected range of HDR and LDR values for hail.

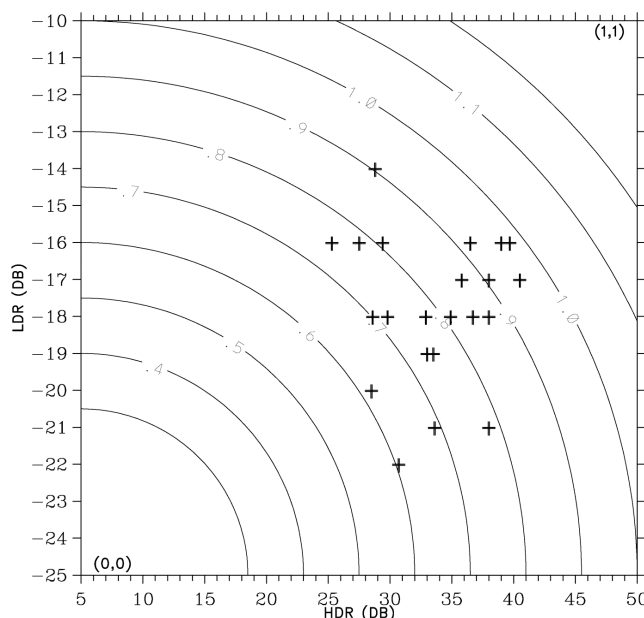


Fig. 7.23: Contours of HQP in the LDR - HDR plane. The ‘+’ marks locations of reported hail. From Kennedy et al (2003).

Fig. 7.23 shows contours of HQP in the HDR-LDR domain including the signatures of hail-damaged areas (marked by the '+'). The elliptical contours in the figure represent constant values of HQP given by:

$$HQP = \sqrt{\left(\frac{HDR - 5}{45}\right)^2 + \left(\frac{LDR + 25}{15}\right)^2} \quad (7.3)$$

High HQP value (≥ 0.9) indicates the occurrence of large hail ($\sim > 2$ cm).

An application of the HQP-derived hail swath is given in Fig. 7.24, which shows the swath for a severe storm on which the contours of the maximum HQP in each pixel (over the duration of the storm) are overlaid. The inner most contour corresponds to HQP-maximum of 0.9, the middle one to 0.6 and the outer most one to 0.3. Post storm damage survey locations are marked by crosses and locations with documented structural hail damage are marked by circles. Golf-ball size hailstones were reported for this event.

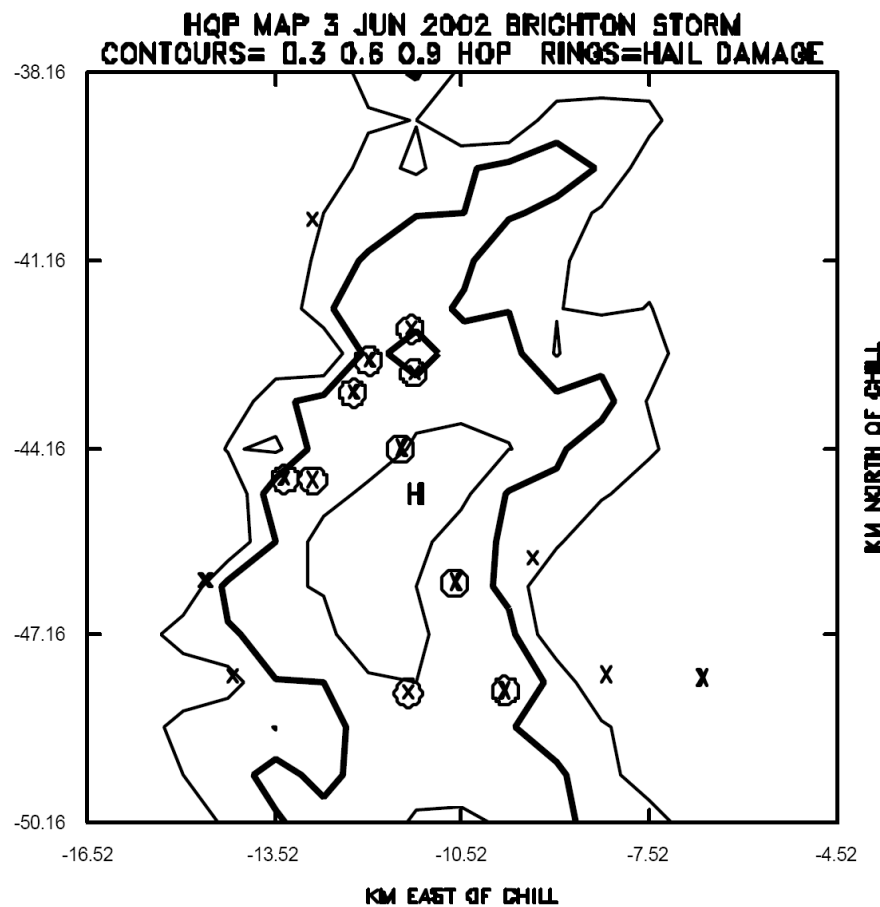


Fig. 7.24: HQP hail swath map using data from the CSU-CHILL radar, with reported large hail marked by circles. From Kennedy et al. (2003).

7.5 Echo classification algorithms for C-band – an overview

It is only in the past several years that operational agencies have begun to evaluate C-band polarimetric radar for echo classification. One of the earliest C-band polarimetric radars is the C-POL operated by the BMRC, Australia, from which examples were shown in Chapters 3 and 6 in the context of Φ_{dp} filtering, K_{dp} estimation and rainfall estimation. In addition, a primitive non-fuzzy logic method of separating meteorological from non-meteorological echoes was described in Fig. 3.2. The classification of precipitation types using fuzzy logic in near real-time and ‘tuned’ for tropical convection has been on-going with the C-POL radar along with some preliminary attempts at validation (Keenan 2003; May and Keenan, 2005). The main differences between S and C-bands are related to K_{dp} (which is larger by a factor of around two for the same rain rate) as well as Z_{dr} (large values due to non-Rayleigh scattering for $D \geq 7$ mm) and ρ_{co} values which can be much lower in the bright-band and in rain/hail mixtures, again due to non-Rayleigh scattering.

Among the operational agencies, notable examples are the on-going efforts at MeteoFrance using the radar located in Trappes, at Environment Canada using the King City radar, at ARPA Emilia-Romagna and ARPA Piemonte in Italy, the ARMOR radar operated by the University of Alabama in Huntsville (in cooperation with NASA and a local TV station), the University of Helsinki radar used primarily for winter precipitation studies, and the UK Met Office radar located in Thurnham primarily for hydrology. While the echo classification algorithms being implemented and evaluated by these radars are all different, yet they are all based on fuzzy logic schemes as described in Section 7.1. A clear consensus approach has not been identified at C-band as yet whether it be for the simpler classification of meteorological versus non-meteorological echoes or for the more sophisticated warm season/cold season precipitation type classification. Here we will describe some of the approaches along with their ‘pros/cons’ and how they differ from the WSR-88D S-band fuzzy logic methods described in earlier sections.

The following three Sections (7.6, 7.7 and 7.8) describe the various C-band methods used for separating meteo echoes from non-meteo echoes, as well as hydrometeor classification using fuzzy and non-fuzzy logic schemes. A summary of the different methods together with their pros and cons is given in Table 7.3 and Table 7.4 prior to describing them in detail. For fuzzy-logic schemes described in Section 7.7, Table 7.4 also gives the method of aggregation (Q-value in Fig.7.2) and the basis for forming the membership functions (with the exception of the BMRC approach, the table references do not provide details of the construction of the membership functions).

Table 7.3: Summary of meteo versus non-meteo classification at C-band

Reference	Input vector	Membership functions	Method of Aggregation (Q)	Output classes	Pros, cons, and comments
Meteo-France approach Gourley et al (2007) Section 7.6.1	<ul style="list-style-type: none"> • ρ_{co} • texture of Z_{dr} • texture of Φ_{dp} 			<ul style="list-style-type: none"> • Precipitation • non-precipitation (such as ground clutter and/or anomalous propagation, clear-air echoes) 	<ul style="list-style-type: none"> • Membership functions derived from data acquired for each output class, as identified by an expert. • Weights derived objectively from the membership function overlap regions using Cho et al. (2006). • Implemented on the operational Trappes radar • Suppresses erroneous classification using additional input features as in Table 7.6 • Membership functions are conditional density functions which are different from the classical ones described in Section 7.1. • Non-precip. membership functions are not transportable to other locations. • Qualitative and indirect validation of non-precipitation class accuracy using absence of artifacts in long-period (~ 24 h) Z-R based rain accumulation maps.
Sea clutter identification Sugier and Tabary (2006) Section 7.6.2.	<ul style="list-style-type: none"> • SD (Φ_{dp}) • ρ_{co} 			<ul style="list-style-type: none"> • Precipitation • AP / sea clutter 	<ul style="list-style-type: none"> • Uses simple Boolean-logic scheme with 'hard' thresholds, since negligible overlap with precipitation. • Simple to incorporate into a fuzzy logic scheme with other classes. • Limited testing with BMRC C-POL and UK Met. Office Thurnham radars. • Other non-polarimetric based methods are also available for AP/sea clutter.

Reference	Input vector	Membership functions	Method of Aggregation (Q)	Output classes	Pros, cons, and comments
Chaff identification Zrnic and Ryzhkov (2004) Section 7.6.3. See also Section 7.3.3.	<ul style="list-style-type: none"> SD (ϕ_{dp}) LDR ρ_{co} 			<ul style="list-style-type: none"> Precipitation, chaff 	<ul style="list-style-type: none"> Uses simple Boolean-logic scheme with 'hard' thresholds, since negligible overlap with precipitation. Simple to incorporate into a fuzzy logic scheme with other classes. Applicable to resonant or non-resonant chaff, according to model results. Validation data have been reportedly collected by Meteo France but not yet published Ideally, LDR is required to differentiate from other non-precip. classes. (Normal dual-polarized antenna quality is sufficient.)

Table 7.4: Summary of precipitation classification at C-band

Reference	Input vector	Membership functions	Method of Aggregation (Q)	Output classes	Pros, cons, and comments
Italian operational approach 1 Cremonini et al. (2004): Algorithm 1 Section 7.7.1	• Z_h • Z_{dr} T-profile using std. atmos. with measured surface temperature	• Trapezoidal shape • 'Tuned' from NSSL S-band research version • 2-D (Z_h, Z_{dr}) • 1-D (T)	$Q_i = \sum_j [P_j(Z_h, Z_{dr}) + P_j(T)]$ • Weights=1 • Class selection: max (Q_i) • Threshold: max(Q_i)> 0.55 • Q from 'sum' maximizes probability of detection • i refers to hydro. class • j refers to input vector	• Light rain • Moderate rain • Heavy rain • Large drops • Rain+hail • Graupel/small hail • Hail • Dry snow • Wet snow • Ice crystals	<ul style="list-style-type: none"> • Uses the three most important input parameters for classification (Z_h, Z_{dr} and T) • Uses 2-D membership functions for Z_h, Z_{dr}. • Alberoni et al. (2002) scheme is used on an operational basis. (These Italian operational radars are being upgraded for ρ_{co} and K_{dp} measurements) • No attenuation correction. • Weights are ad hoc. • Too many output classes relative to number of input parameters. • Gives rise to noisy classification images. • Generally not validated by in-situ data.
Italian operational approach 2 Alberoni et al. (2002) Section 7.7.1	• Z_h • Z_{dr}	• Same as above (except no T)	As above except exclude $P_j(T)$	As above except replace last class by: <ul style="list-style-type: none"> • Horiz. oriented crystals • Vertical oriented crystals⁴ 	As above
Italian operational approach 3 Marzano et al. (2006) Section 7.7.1	• Z_h • Z_{dr} T-profile from sounding or standard atmosphere	• Trapezoidal shape • 1-D (T) from Zrnic et al. (2001) 2-D MBFs using (Z_h, Z_{dr}) for each hydro class based on scattering calculations assuming a priori models for size, shape, orientation and dielectric constant for that class	$Q_i = \prod_j [P_j(Z_h, Z_{dr}) + P_j(T)]$ • Weights = 1 • Class selection: max(Q_i) • 'Not Classified' category if any of two Q_i 's give same max value • Q from 'product' reduces erroneous classification • i refers to hydro class • j refers to input vector	As in Cremonini et al. (2004)	As for Cremonini et al. (2004) above

⁴ cannot be classified without K_{dp} as additional input vector

Reference	Input vector	Membership functions	Method of Aggregation (Q)	Output classes	Pros, cons, and comments
BMRC Australian approach Keenan et al. (2003) May and Keenan (2005) Section 7.7.2	• Z_h • Z_{dr} • ρ_{co} • K_{dp} T-profile from Rawinsonde	• Beta functions defined in equation (7.7) • All 1-D functions	$Q_i = \sum_j [P_j(v_j) + P_j(T)]$ • v_j are the input vector components • Equal weights • Class selection: $ \max(Q_i) - \bar{Q} \geq 1.75\sigma$ • σ is the std. dev. of Q_i • j refers to input vector • i refers to hydro class	• Drizzle • Rain • Dry low density snow • Dry high density snow • Wet snow • Dry graupel • Wet graupel • Small wet hail • Large wet hail • Rain+hail mix	<ul style="list-style-type: none"> • Limited validation with profiler data. • Particularly useful for detecting R/H Mix below the melting level. • Used on a semi-operational basis. • Weights are ad hoc. • Too many output classes. • Tuned for tropical convection. • Uses only 1-D membership functions for all input parameters.
University of Alabama (ARMOR) method Petersen et al (2005) Deierling et al (2007) Section 7.7.3	• Z_h • Z_{dr} • ρ_{co} • K_{dp} • LDR • $SD(V_r)$ • $SD(Z_{dr})$ • $SD(\Phi_{dp})$ T-profile	• Trapezoidal shape • All 2-D with respect to Z_h except for T(1-D) • ‘Tuned’ from NSSL-NCAR research version at S-band	<ul style="list-style-type: none"> • Similar to above except the membership functions are 2-D with respect to Z_h, except for T. • User input variable weights • Class selection: $\max(Q_i)$ • If LDR not available, then its weight is set to zero. • Several thresholds applied to prevent unrealistic classes. 	<ul style="list-style-type: none"> • Cloud drops • Drizzle • Light rain • Moderate rain • Heavy rain • Hail • Hail/rain mix • Graupel / small hail • Graupel / small hail / rain • Dry snow • Wet snow • Irregular ice crystals • Horiz. oriented ice • Supercooled liquid drops • Insects • Second trip • Ground clutter 	<ul style="list-style-type: none"> • Does Meteo versus non-Meteo classes, in addition to summer/winter seasonal classes in the same scheme • Z_{dr}, LDR, ρ_{co}, K_{dp}, are 2-D membership functions with respect to Z_h. • Used operationally for TV weather broadcast (mainly for hail detection). • LDR data are not routinely used, but the scheme allows for LDR input, as needed. (ARMOR radar recently upgraded with high-quality antenna.) • Weights are ad hoc. • Too many output classes. • Tuned for local weather events. • No routine validation, but uses occasional NWS hail reports.

Reference	Input vector	Membership functions	Method of Aggregation (Q)	Output classes	Pros, cons, and comments
Environment Canada Hudak et al (2006) Section 7.7.4	As in Table 7.2	<ul style="list-style-type: none"> Trapezoidal shape 2-D (Z_h, Z_{dr}) 'Tuned' from NEXRAD operational version at S-band (Ryzhkov et al 2005a). 3 schemes used: Meteo vs. non Meteo, cold season, warm season. 	<ul style="list-style-type: none"> Class selection based on $\max(Q_i)$. Q_i's are different for the three schemes. User input variable weights. 	As in Table 7.1	<ul style="list-style-type: none"> Uses 2-D membership functions for Z_h, Z_{dr}. On-going research-type validation over well-instrumented site and some aircraft in-situ probes. Like NEXRAD, has 3 schemes, viz. Meteo vs. non-meteo, warm season, cold-season Output classes are compressed and more in-line with practical requirements. Particularly efficient for detecting moving/advection rain-snow boundaries. Antenna 3-dB beamwidth of 0.6° gives high spatial resolution. Implemented on operational radar, with regular evaluation by weather forecasters. Does not need temperature profile. Weights are ad hoc. Implemented for low level sweeps only. No published classification articles in the open literature, as yet.
DLR hail detection Höller et al (1994) Höller (1998) Fehr et al (2004) Section 7.8.1	<ul style="list-style-type: none"> Z_{dr} LDR melting height 	Non-Fuzzy Algorithm	Non-Fuzzy Algorithm	<ul style="list-style-type: none"> Small drops Large drops Dry small graupel / snow Wet melting graupel / Dry large graupel / Dry small hail Dry hail Wet ail Large wet hail Rain and small hail Rain and large hail 	<ul style="list-style-type: none"> Good for detection of damaging hail Updrafts located using detection of large drops above the freezing level. Has been extended to derive empirically-based hydrometeor mass content. Independent of Z_h calibration. Requires LDR with high-quality antenna. Non-fuzzy scheme, based on Boolean-logic with 'hard' thresholds. Too many output classes relative to number of input parameters. Tuned generally for supercell /thunderstorms

Reference	Input vector	Membership functions	Method of Aggregation (Q)	Output classes	Pros, cons, and comments
HDR HDR–LDR combination Nanni et al (2000) Aydin and Giridhar (1991) Section 7.8.2	<ul style="list-style-type: none"> • Z_h • Z_{dr} • LDR 	Non-Fuzzy Algorithm	Non-Fuzzy Algorithm	<ul style="list-style-type: none"> • Rain • small hail • large or damaging hail 	<ul style="list-style-type: none"> • HDR only needs two parameters; no need for phase measurements. • Good for damaging hail detection. • Validation has been attempted for some cases. • Second method (HDR-LDR) requires high quality antenna for LDR. • Non-fuzzy scheme, based on Boolean-logic with 'hard' thresholds. • HDR-LDR method has not been tested at C-band.

7.6 Discrimination between meteorological and non-meteorological echoes – algorithms for C-band

7.6.1 The MeteoFrance approach

The MeteoFrance approach described in Gourley et al. (2007) separates precipitation echo from non-precipitation echo (which includes clear air and ground clutter/AP) using an observational-based methodology. Many hours of polarimetric data (Z_h , Z_{dr} , Φ_{dp} and ρ_{co}) were collected at low elevation angles (~ 1.5 deg) under conditions where the echo was known a priori to be dominated by ground clutter/AP or clear air or precipitation (as determined by an ‘expert’).

a) Input feature vector

The input feature vector was selected to be ρ_{co} and the textures of Φ_{dp} and Z_{dr} (note that the only common features with Table 7.2 version 1 at S-band are ρ_{co} and $SD(\Phi_{dp})$, whereas the output classes are more or less the same (see Table 7.1 Version 1). The texture parameter differs from the standard deviation (SD) in Table 7.2. The texture of Z_{dr} or Φ_{dp} is calculated in a polar area centered at (r_o, θ_o) whose ‘bounds’ are three resolution volumes in range (i.e. $r_o - \Delta_r$, r_o , $r_o + \Delta_r$) and three in azimuth ($\theta_o - \Delta$, θ_o , $\theta_o + \Delta$) where Δ_r is 240 m and Δ is 0.5 deg for their system. The data from 9 resolution volumes are used to define the texture at (r_o, θ_o) in a root mean square sense, i.e., the deviation squared from the value at the center of the polar area to the surrounding values are calculated, normalized by the total number of resolution volumes (9 here) and then the square root is taken. Because the polar area increases with range, the texture parameters have to be range normalized in an empirical manner and are not expected to be the same for radars at other locations or using different ‘bounds’ for the polar areas. Table 7.5 summarizes the input feature vector and output classes. Note however that the ‘clear air’ and ‘ground clutter/AP’ classes are later combined into one ‘non-precipitation’ class.

Table 7.5: Input feature vector and output classes for the MeteoFrance fuzzy logic classifier. From Gourley et al. (2007).

Input feature vector	Output classes ⁵
ρ_{co}	precipitation
texture (Z_{dr})	ground clutter/AP
texture (Φ_{dp})	clear air

b) Membership functions

The next step is to compute the probability density function (referred to as density functions) which is based on the converged histograms of ρ_{co} , texture(Z_{dr}) and texture(Φ_{dp}) for each output class (i.e., precipitation, ground clutter/AP and clear air). From the histogram, a ‘smoothed’ density function is generated using the Gaussian kernel density estimation procedure which essentially creates a Gaussian curve at each ‘bin’ of the histogram and then sums them up:

⁵ Note: the ‘ground clutter/AP’ and ‘clear air’ classes are combined later into a single ‘non-precipitation’ class

$$f(x) = \frac{1}{\sigma\sqrt{2\pi}} \sum_{i=1}^n e^{-\left\{\frac{1}{2}\left(\frac{X_i-x}{\sigma}\right)^2\right\}} \quad (7.4)$$

where $f(x)$ is the density function, σ is the smoothing parameter, n is the total number of data points, X_i is the i th observation of ρ_{co} , texture of Z_{dr} or texture of Φ_{dp} , and x is the independent variable. The σ is calculated according to Silverman's rule (Silverman 1986). All density functions are normalized so that the area under the curve is unity.

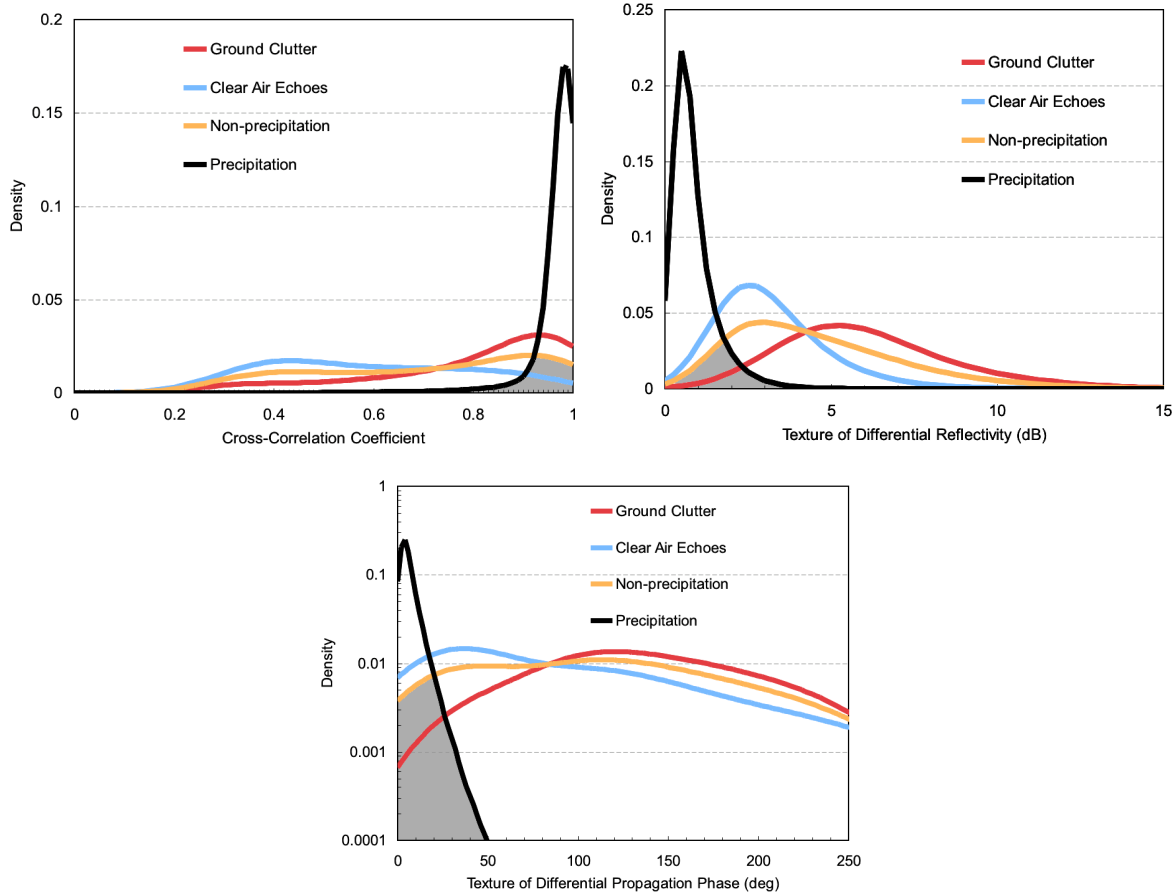


Fig. 7.25: Smoothed density functions from observations with the MeteoFrance radar. Specific classes were identified by an expert. The shaded area is used to calculate the weighting functions for the input vector components. From Gourley et al. (2007).

Fig. 7.25 shows the density functions of ρ_{co} , texture(Z_{dr}) and texture(Φ_{dp}) in three panels. In each panel the different curves correspond to the three output classes i.e., ground clutter/AP, clear air or precipitation echoes. The curve for the non-precipitation class is simply the average of the density functions of ground clutter and clear air. In essence, there are only two output classes corresponding to 'precipitation' and 'non-precipitation' which earlier was referred to as 'meteo' and 'non-meteo' classes. Examination of Fig. 7.25 shows that the 'width' of the density

function for precipitation is much less than for non-precipitation echo regardless of the input variable. In particular, the texture of Φ_{dp} shows that it is a powerful discriminator between ‘meteo’ and ‘non-meteo’ echoes in general agreement with the bottom panel in Fig. 7.5. There is also general agreement between the density function of ρ_{co} (top panel) of Fig. 7.25 and the third panel of Fig. 7.5. Note, however, that Fig. 7.5 illustrates (un-normalized) trapezoidal membership functions whereas Fig. 7.25 refers to density functions based on observations.

A novel assertion is made by Gourley et al. (2007) that the observation-based density functions can be used as membership functions in a fuzzy logic scheme. No proof or justification is offered for such an assertion. Recall from Section 7.1 that membership functions are related to (but not the same as) the conditional probability, i.e., $P(\text{echo class is precipitation} / \rho_{co} = \text{observed value})$, and not to the density function $P(\rho_{co} / \text{echo class=precipitation})$. Nevertheless, the MeteoFrance scheme does ‘work’ in spite of this difference from the ‘classical’ definition of membership functions since the principal differences between these two approaches are not very large.

c) Membership weights

Recall from Fig. 7.2 that weights W are assigned for each of the input features (i.e., ρ_{co} , $\text{texture}(Z_{dr})$ and $\text{texture}(\Phi_{dp})$). In Version 1 of the prototype WSR-88D algorithm, equal weights are given to the 5 input variables (see Table 7.2). Such weighting is subjective and the classification is quite sensitive to the selected weights. An objective procedure for selecting the weights is described in Cho et al. (2006). To illustrate this approach, a qualitative description is given by referring to the simple schematic membership functions previously shown in Fig. 7.2. Note first that for the input variable Z_{dr} , the overlapping area in membership function values between the rain and hail classes is the least as compared with the overlap area for Z_h which is the largest and intermediate overlap for LDR . It follows that most weight should be given to Z_{dr} , followed by lesser weight for LDR and least weight to Z_h . These three weights are easily calculated as follows. Let the individual overlap areas be defined as $A_{Z_{dr}} = (\text{overlap area between rain \& hail for } Z_{dr})$; $A_{LDR} = (\text{overlap area between rain \& hail for } LDR)$; and $A_{Z_h} = (\text{overlap area between rain \& hail for } Z_h)$. Define the normalization factor $1/S$ as:

$$\frac{1}{S} = \frac{1}{A_{Z_{dr}}} + \frac{1}{A_{LDR}} + \frac{1}{A_{Z_h}} \quad (7.5)$$

Then the weights for Z_{dr} , LDR and Z_h follows as:

$$W(Z_{dr}) = \frac{1}{A_{Z_{dr}}} / \frac{1}{S} \quad (7.6a)$$

$$W(LDR) = \frac{1}{A_{LDR}} / \frac{1}{S} \quad (7.6b)$$

$$W(Z_h) = \frac{1}{A_{Z_h}} / \frac{1}{S} \quad (7.6 b)$$

It follows that the sum of the weights is 1.

In Fig. 7.25, the shaded areas are the overlapping areas between the ‘precipitation’ and ‘non-precipitation’ classes corresponding to the three input variables. These areas are, respectively, 0.243, 0.203 and 0.081 for ρ_{co} , texture(Z_{dr}), and texture(Φ_{dp}). Thus, the corresponding weights are, respectively, 0.19, 0.23 and 0.58. Note that these weights are based on density functions derived from radar observations with the C-band MeteoFrance radar located in Trappes and are not applicable to other locations where the ground clutter/AP might be different.

d) Additional thresholding

Once the weights and membership functions are known then the aggregation value for each output class (denoted by Q in Fig. 7.2) is calculated and the maximum value is taken. The class with $\max(Q)$ is then selected as the final output class. Further, to suppress erroneous classification, empirical thresholds are used based on a larger set of input variables as given in Table 7.6. Use of such thresholds overrides the $\max(Q)$ -based output classification. These thresholds may need to be ‘fine-tuned’ for radars in other locations (mainly for ground clutter/AP).

Table 7.6: Empirical thresholds used to suppress erroneous class assignments in the MeteoFrance scheme

Parameter	Threshold	Suppressed Class
ρ_{co}	< 0.7	precipitation
Texture (Φ_{dp})	> 100 deg	precipitation
Z_h	< 5 dBZ	precipitation
Pulse-to-pulse fluctuation in Z_h ⁶	> 5 dB	Ground clutter
Mean Doppler velocity	> 5 m/s	Ground clutter

⁶ Most Doppler radars do not measure the pulse-to-pulse fluctuation in Z_h as it is related to the width of the Doppler power spectrum.

7.6.2 Identification of sea clutter at C-band

Previously in Section 7.3.2 the identification of sea clutter, marine boundary clouds and precipitation was described using a fuzzy logic scheme described by Ryzhkov et al. (2002b) using data from an S-band radar. To the best of our knowledge a fuzzy logic scheme to classify sea clutter/AP and precipitation at C-band using polarimetric input variables has not yet been developed (though fuzzy logic schemes are available for non-polarimetric radar at C-band, see Berenguer et al. 2006). Sugier and Tabary (2006) comment that the standard deviation of Φ_{dp} at C-band clearly identifies sea clutter/AP from precipitation using a simple threshold in accord with the S-band results of Ryzhkov et al. (2002b).

Here, we illustrate C-band data from the C-POL radar located in Darwin, Australia and operated by the BMRC. Darwin is located near the coast and is frequently affected by sea clutter/AP. Fig. 7.26 shows three panels of PPI data at 0.4 deg elevation angle of (a) Z_h , (b) ρ_{co} , (c) standard deviation of Φ_{dp} or $SD(\Phi_{dp})$. The SD here is calculated based on 10 consecutive range gates of Φ_{dp} . It is similar to the texture of Φ_{dp} except a polar area is not used and hence no range normalization is necessary as in the MeteoFrance approach. In panels (b) and (c), a region of sea clutter is noted in the azimuth sector 240-300°, and range sector 5-40 km where ρ_{co} is very low (~0.3) and $SD(\Phi_{dp})$ is very high (~70°). The precipitation echoes are clearly demarcated by high values of ρ_{co} (> 0.85) and low $SD(\Phi_{dp}) < 15^\circ$. This is not different from the S-band data described by Ryzhkov et al. (2002b).

In Fig. 7.26 there appears to be a region of sea clutter due to AP where the $Z_h \sim 40$ dBZ, the ρ_{co} is large (>0.8) and the $SD(\Phi_{dp})$ is large (~50-60°). It could not have been identified without $SD(\Phi_{dp})$. To clearly illustrate this point, Fig. 7.27 shows the range profile of Z_h , ρ_{co} and $SD(\Phi_{dp})$ along the azimuth 330° within the region of inferred AP. We note that in AP-induced ground clutter, the ρ_{co} values overlap with precipitation as in the top panel of Fig. 7.25 or the third panel in Fig. 7.5.

The histograms of $SD(\Phi_{dp})$ and ρ_{co} are shown in Fig. 7.28 for data in the region of sea clutter (the sector 240°<azimuth<300° and 5<range<40 km), and for data from precipitation echoes elsewhere with large ρ_{co} (>0.9) and low $SD(\Phi_{dp}) < 20^\circ$. These histograms clearly show that there is no overlap between sea clutter and precipitation echoes in $SD(\Phi_{dp})$ or in ρ_{co} . For AP-induced sea clutter there will be some overlap in ρ_{co} but not in $SD(\Phi_{dp})$ as mentioned earlier.

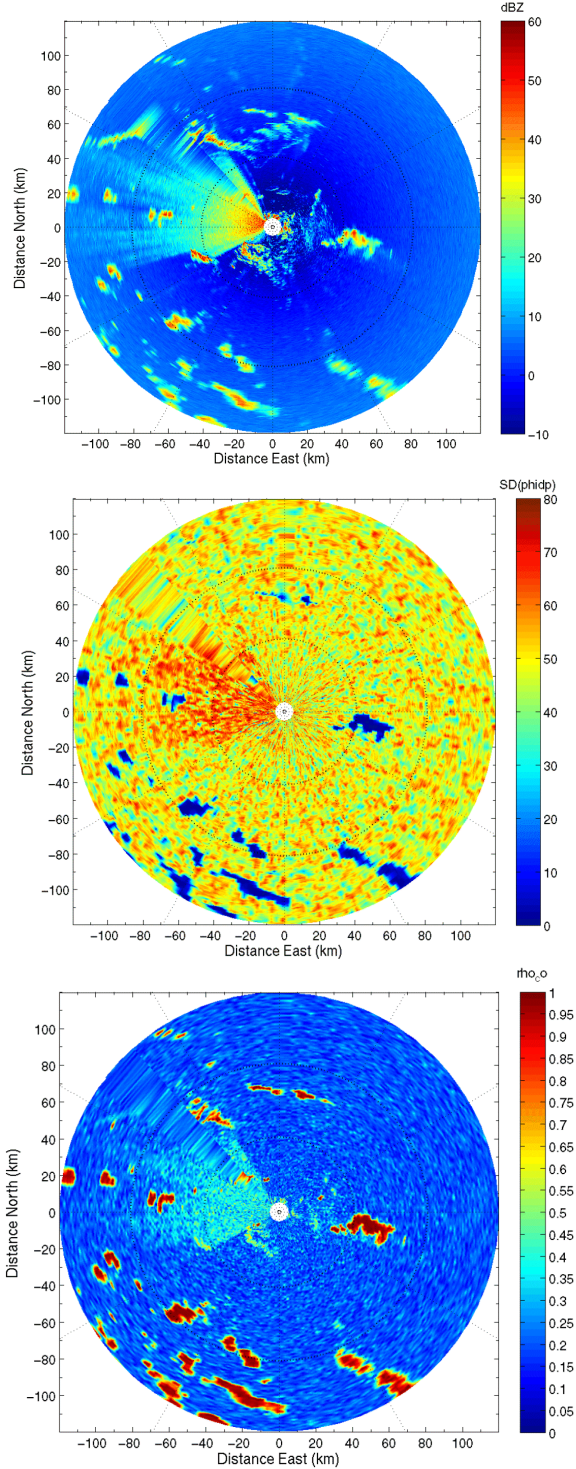


Fig. 7.26: PPI data from C-POL radar in Darwin, Australia. Top panel: Z_h ; middle panel $SD(\Phi_{dp})$; bottom panel: ρ_{co} . Range rings at 40 km. Sea-clutter is in $260^\circ < az < 300^\circ$, $0 < r < 40$ km and what appears to be AP-induced sea-clutter near $az = 330^\circ$, $50 < r < 60$ km. Data courtesy of Thomas Keenan of the BMRC.

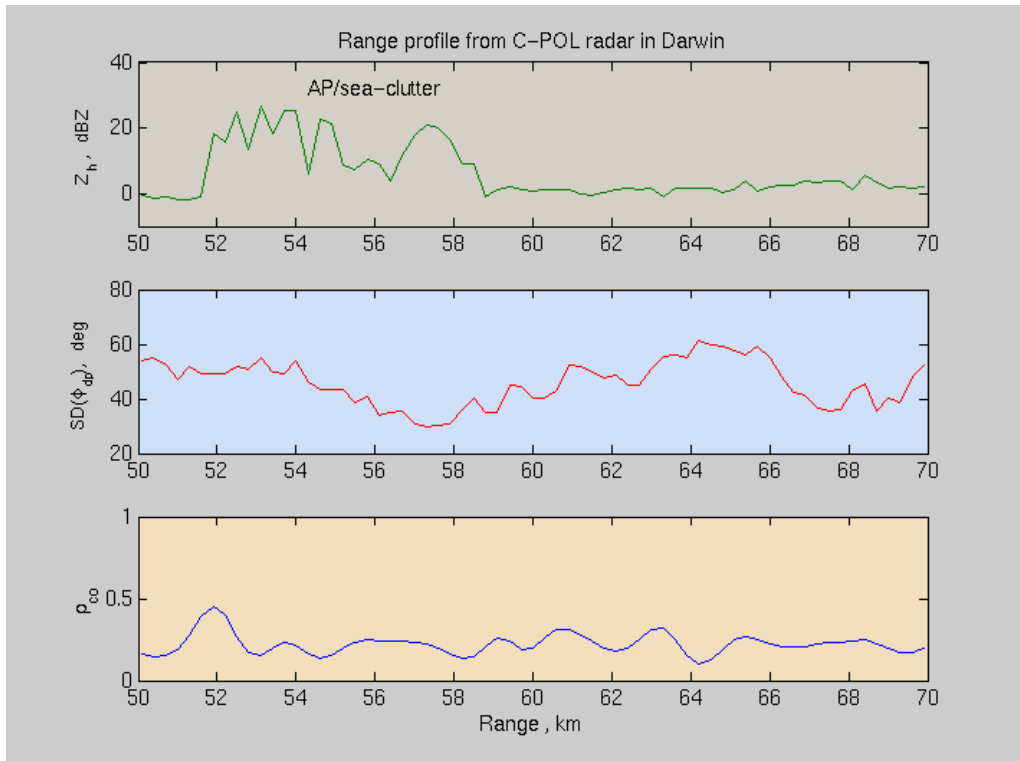


Fig. 7.27: Range profiles along $\text{az}=330^\circ$ (see PPI in previous figure) to illustrate the radar parameters in what appears to be AP-induced sea clutter.

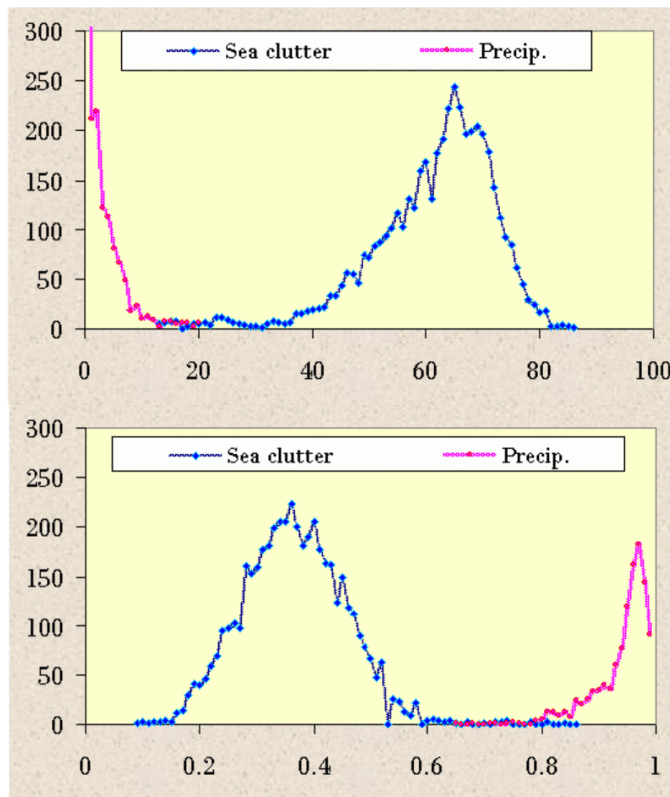


Fig. 7.28: Histograms from PPI data in Fig. 7.26. Top panel shows histogram of $\text{SD}(\phi_{dp})$ for sea clutter and from precipitation echoes. Similarly for bottom panel, except histogram of ρ_{co} . Note negligible overlap area between the two classes.

7.6.3 Identification of chaff

Observations of chaff with polarimetric C-band weather radars have not appeared in the archived literature (to the best of the authors' knowledge), although anecdotal evidence of high LDR observations of around -5 dB with the DLR radar exist. Simulations performed by Zrnic and Ryzhkov (2004) show that the polarimetric properties of chaff at C-band are very similar to those at S-band, whether the chaff is resonant or not (see fuller description in Section 7.3.3).

It appears that an observational-based methodology such as that used by MeteoFrance would lead to a robust classification of chaff with input variables being ρ_{co} , $SD(\Phi_{dp})$ and LDR . Such data in chaff (except LDR) have been collected by MeteoFrance but not reported upon yet.

7.7 Classification between hydrometeor types – algorithms for C-band using fuzzy logic schemes

7.7.1 The Italian operational approach using Z_h , Z_{dr} , and temperature

The Italian operational C-band radars are configured for measurement of Z_h and Z_{dr} using 'fast' switchable ferrite circulators to alternately change the transmitted polarization state from H to V on a pulse-to-pulse basis. A single receiver is used for processing the copolar HH and VV signals (such a configuration is termed as a polarization agile/single receiver system by Bringi and Chandrasekar 2001; their Chapter 6). In addition, the mean Doppler velocity and spectral width are also available from the HH signals. The signal processors in these radars have not yet been modified to calculate Φ_{dp} and ρ_{co} but it appears that such an upgrade is imminent.

The fuzzy logic schemes in the Italian operational radars (e.g., ARPA Emilia-Romagna or ARPA Piemonte) are thus focused on the input vector being Z_h and Z_{dr} with the option of temperature profile input either measured by rawinsonde or by assuming a standard atmosphere profile of 6.5 deg/km starting from available surface temperature at ground stations. Generally, the fuzzy logic schemes used are 'tuned' C-band versions of the research NSSL scheme of Zrnic et al (2001) (as opposed to the prototype WSR-88D versions in Section 7.2). They use two-dimensional membership functions (Z_h - Z_{dr} plane) for the various classes based on Fig. 7.1 given earlier. Fig. 7.29 gives the basic block diagram of the fuzzy logic scheme. It should be mentioned that since Φ_{dp} is not measured by the operational radars to correct the measured Z_h and Z_{dr} for rain-induced attenuation, it is a serious draw back, especially in convective storms.

Zrnic et al. (2001) comment that the most important input feature vectors are Z_h , Z_{dr} and temperature profile for hydrometeor classification (ρ_{co} and/or LDR play important roles if the temperature profile is either unavailable or soundings are not

representative of the storm interior). We must add that ρ_{co} and $SD(\Phi_{dp})$ are absolutely necessary for classification between ‘meteo’ and ‘non-meteo’ echoes.

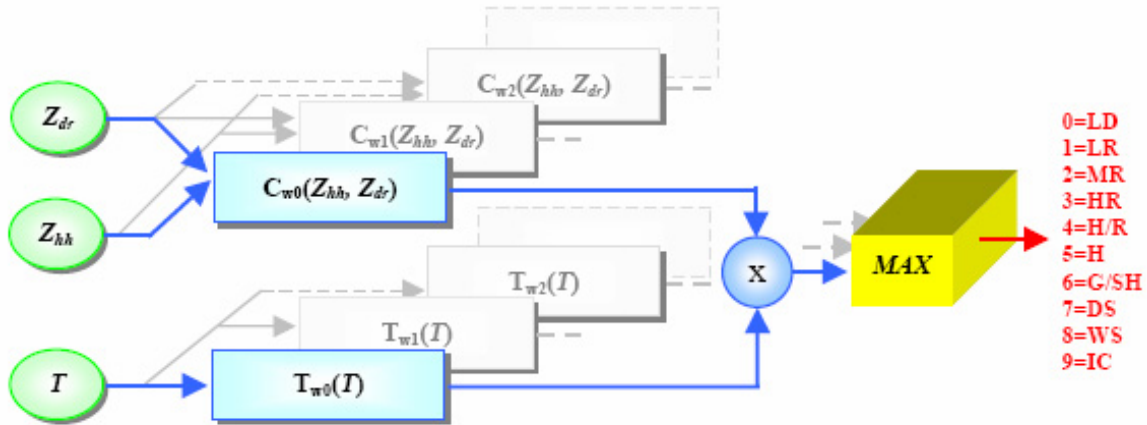


Fig. 7.29: Schematic diagram of the fuzzy logic scheme using Z_h , Z_{dr} and temperature (T) as the input vector. 2-D membership functions for each class are based on (Z_h, Z_{dr}) while the temperature for each class is based on 1-D membership functions. The output classes are LD=large drops, LR=light rain rate, MR=medium rain rate, HR=high rain rate, H/R=hail+rain mix, H=hail, G/SH=graupel/small hail, DS=dry snow, WS=wet snow, IC=ice crystals. From Marzano et al. (2006); image ©copyright Frank Marzano.

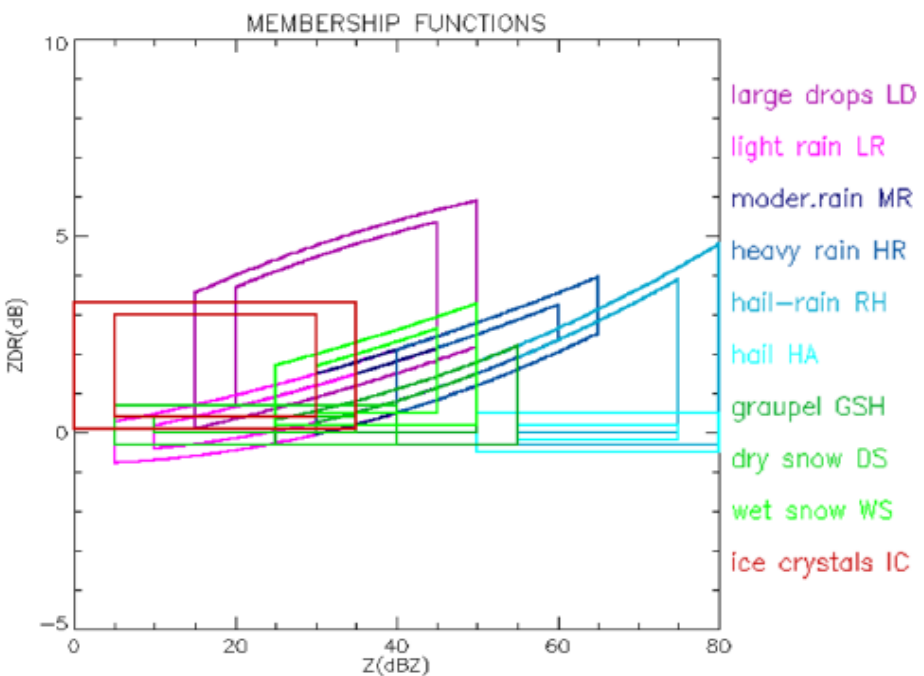


Fig. 7.30: Trapezoidal membership functions in the Z_h , Z_{dr} plane for various classes listed ‘tuned’ for C-band based on Zrnic et al. (2001). From Cremonini et al. (2004); image ©copyright Copernicus GmbH.

An example of the basis of the 2-D membership functions for the various classes is given in Fig. 7.30. It shows the considerable overlap between the various classes. In fact it can be argued that with only 3 input features it is perhaps impossible to output 10 hydrometeor classes; combining classes may be preferable for operation applications.

Fig. 7.31 shows the classification by Cremonini et al. (2004) in the simplest case of stratiform rain and it is clear that a ‘reasonable’ classification is possible in this case, i.e., rain below the bright-band (BB) and wet snow above. It could be argued that dry aggregated snow should have been detected above the wet snow layer.

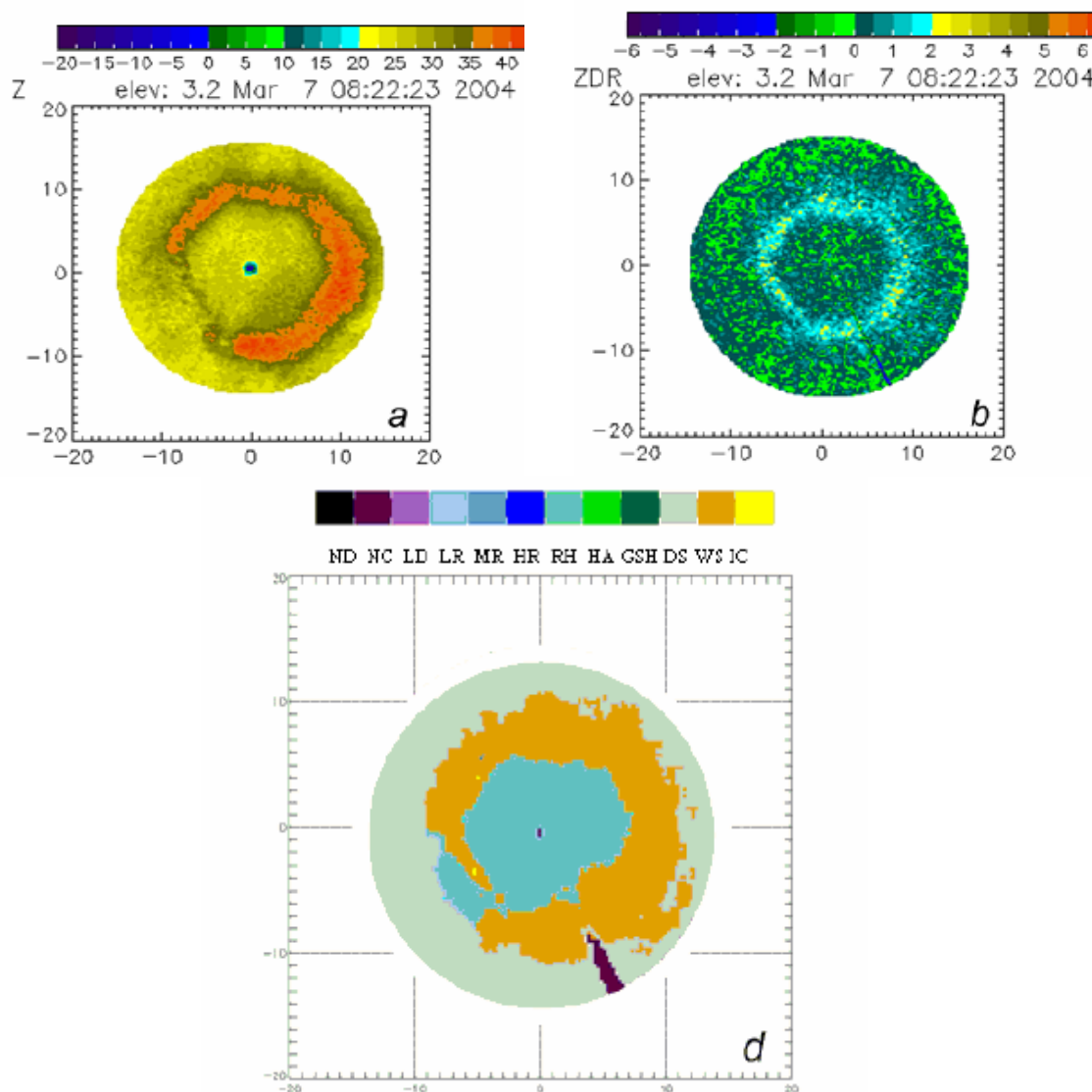


Fig. 7.31: PPI of Z_h (top left panel), Z_{dr} (top right panel) and classification result. From Cremonini et al. (2004); their algorithm 1; image ©copyright Copernicus GmbH.

A convective storm example from Marzano et al. (2006) is shown in Fig. 7.32 as a RHI scan with Z_h from 2 radars (scan taken along the baseline) in the top panel along with the classification from both radars in the bottom two panels. The authors claim that the classification results though ‘noisy’ are ‘reasonable’ and in accord with expected microphysical regimes in convective storms. Note the hail core in the left panel below extending to in altitude to 4 km, with graupel/small hail extending to 7 km.

The classification from both radars are not always identical because the Z_h and Z_{dr} data have not been corrected for attenuation and because of the different resolution volumes. Spatial smoothing would improve the image presentation for operational applications.

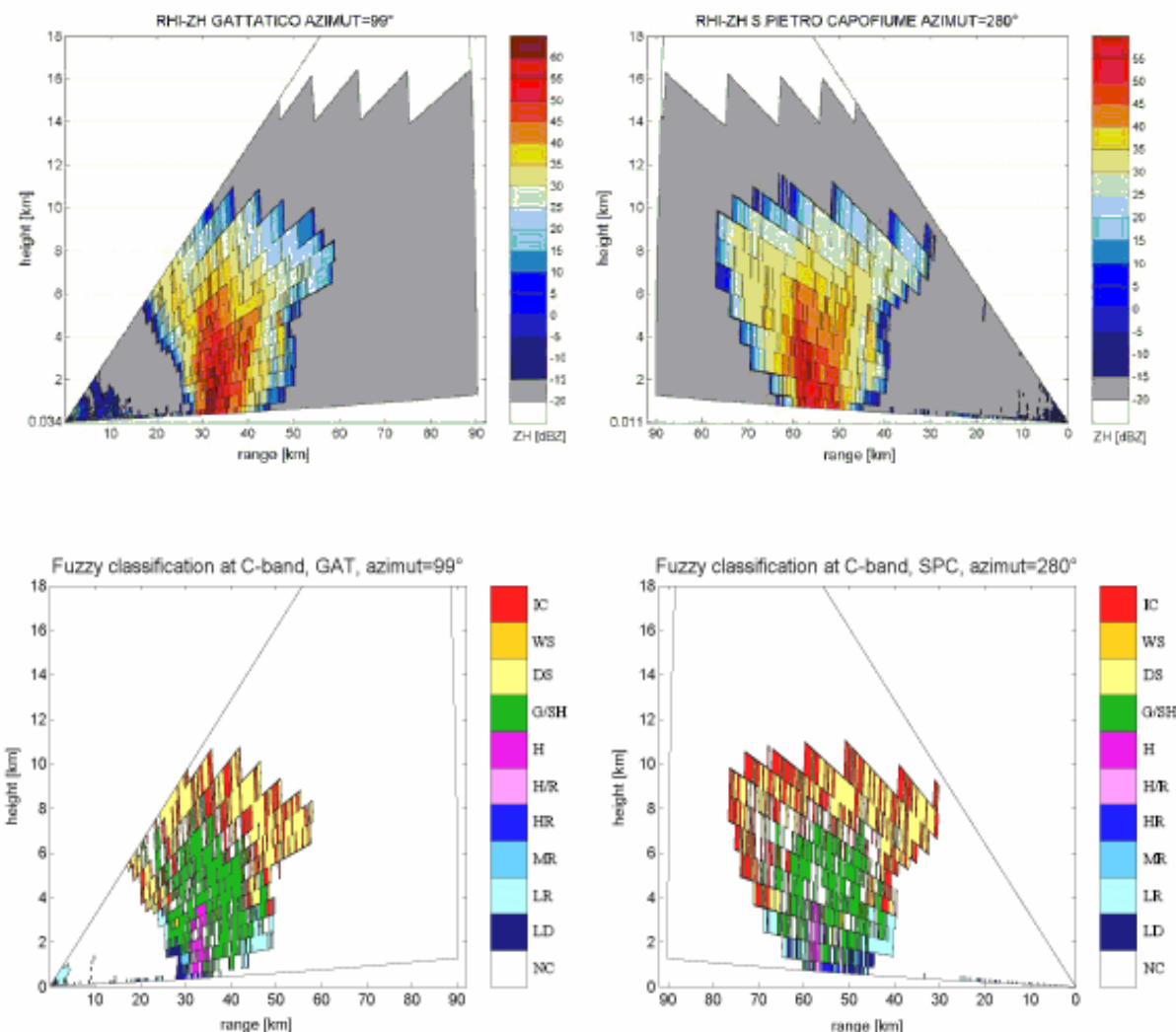


Fig. 7.32: RHI scans of reflectivity from 2 radar along their baseline. Bottom panels show results of classification. From Marzano et al. (2006); image ©copyright Frank Marzano.

7.7.2 The Australian BMRC C-POL scheme

The Australian Bureau of Meteorology Research Center (BMRC) C-POL scheme has ten output classes, namely, (1) drizzle, (2) rain, (3) dry low density snow, (4) high density snow , (5) wet snow, (6) dry graupel, (7) wet graupel, (8) small wet hail, (9) large wet hail and (10) rain hail mixture. The input vector is Z_h , Z_{dr} , ρ_{co} and K_{dp} . Attenuation correction has been performed for Z_h using the I-ZPHI method (see Section 4.3) and for Z_{dr} using the A_h -scaled method (see Section 5.2). To avoid gross misclassification, the environmental temperature profile is used as an additional input vector component.

1-D membership functions, analogous to conditional probability, $P_i(v_j)$ for each class i and input variable v_j (e.g., $v_1 = Z_h$, $v_2 = Z_{dr}$, etc) is given by the function:

$$P_i(v_j) = \frac{1}{1 + \left\{ \frac{v_j - \langle v_j^i \rangle}{\sigma(v_j^i)} \right\}^{12}} \quad (7.7)$$

where $\langle v_j^i \rangle$ is the mid-point of the symmetric function and $\sigma(v_j^i)$ is related to the ‘width’. These are given in Table 7.7 for each class (i: row) and for the four radar parameters and temperature (j: column). They are derived from the range of values originally given in Table 1 of Keenan et al. (2003) for the ten classes. The corresponding functions are plotted in Fig. 7.33 for all 10 classes.

Table 7.7: Values of $\langle v \rangle$ and $\sigma(v)$ for the 10 classes and the 5 input vector components. All membership functions are one dimensional.

	Drizzle	Rain	Dry LD snow	Dry HD snow	Wet Snow	Dry Graupel	Wet Graupel	Wet Hail, < 2 cm	Wet Hail, > 2 cm	Rain-Hail-Mix
Z_h										
	17.5	42.5	12.5	12.5	32.5	27.5	40	55	60	62.5
	7.5	17.5	22.5	22.5	12.5	7.5	10	5	5	17.5
Z_{dr}										
	0.45	2.25	0	0.5	1.75	0.25	0.75	0	-0.25	2.5
	0.25	1.75	0.5	0.5	1.25	0.75	1.25	0.5	0.75	3.5
K_{dp}										
	0.03	10	0	0.2	0.5	0.5	1.5	0	0.5	10
	0.03	10	1	0.2	0.5	0.5	1.5	1	1.5	10
ρ_{co}										
	0.985	0.975	0.975	0.975	0.7	0.975	0.975	0.935	0.91	0.95
	0.015	0.025	0.025	0.025	0.2	0.025	0.025	0.015	0.01	0.05
T										
	10	10	-10	-15	2.5	-10	2.5	2.5	2.5	7.5
	20	20	10	15	2.5	10	17.5	17.5	17.5	17.5

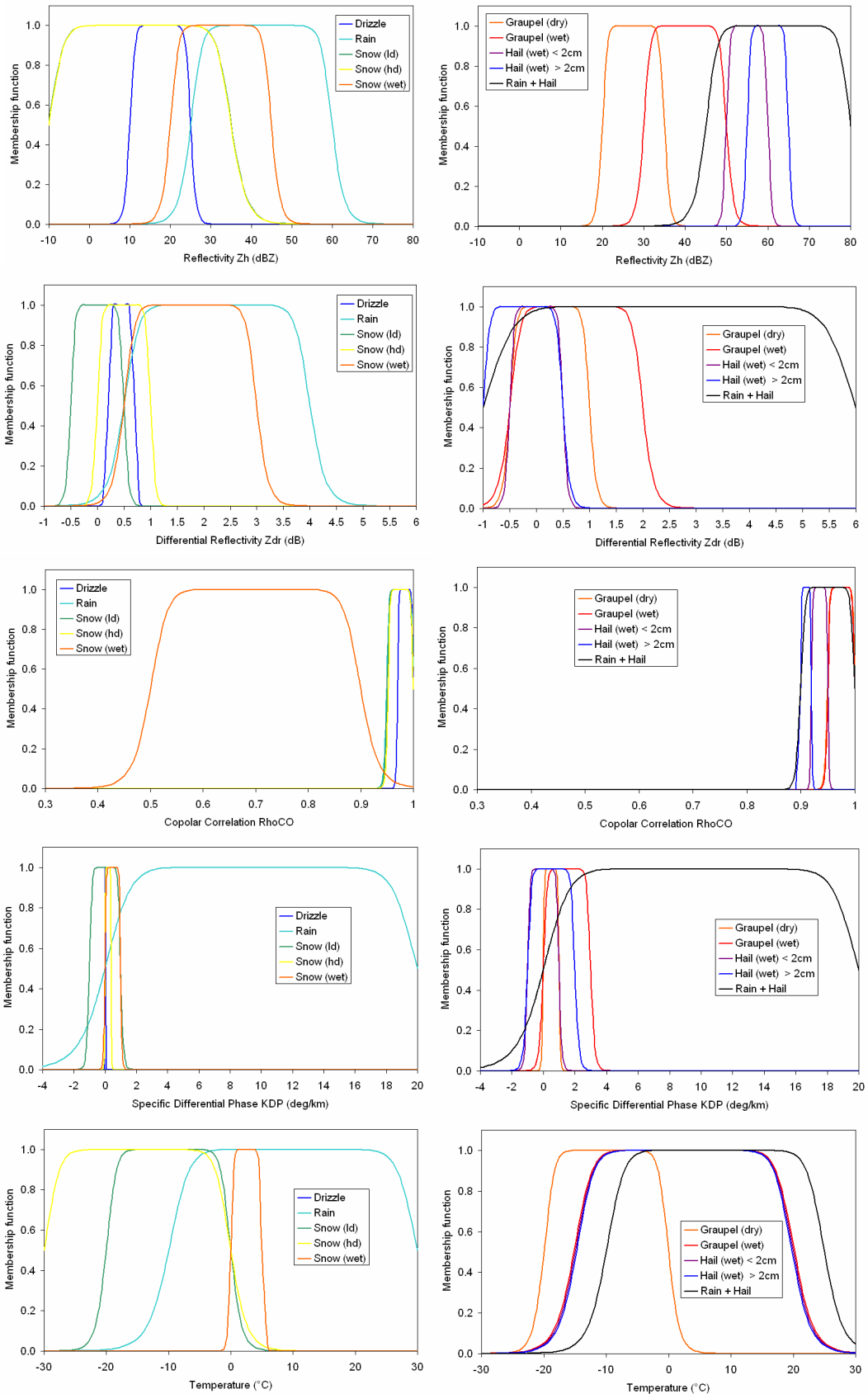


Fig. 7.33: Membership functions for all ten hydrometeors classes, with input feature vector (from top to bottom) (a) Z_h , (b) Z_{dr} , (c) ρ_{co} , (d) K_{dp} , (e) temperature.

An example of using the above scheme is given in Fig. 7.34 for a squall line with leading convective cells and trailing stratiform region in Darwin, Australia. The lower panel shows the presence of rain/hail mixture extending well below the freezing level along the leading edge, with wet graupel just above it and dry graupel changing to snow at higher altitudes. Between 30 and 40 km in the trailing stratiform region, the melting snow class is detected just below the freezing level height, with dry snow above and rain below.

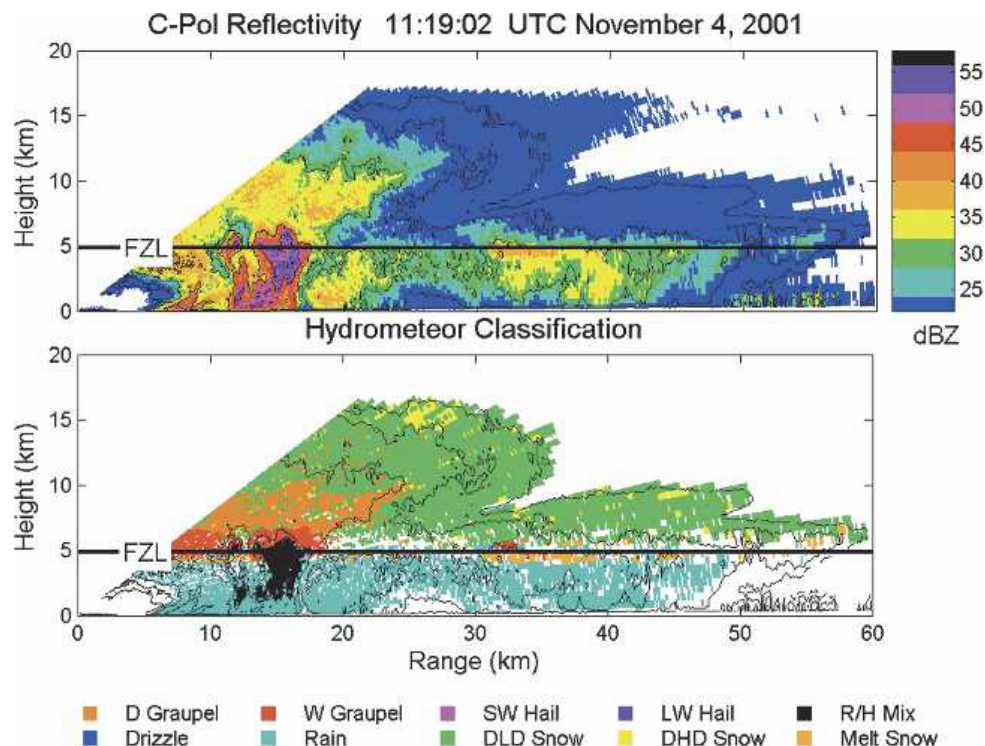


Fig. 7.34: RHI through a squall line using the C-POL BMRC radar. Top panel shows attenuation-corrected Z_h ; bottom panel shows results the classification. From May and Keenan (2005).

7.7.3 The University of Alabama ARMOR scheme

The University of Alabama in Huntsville and WHNT-TV station operate an Advanced Radar for Meteorological and Operational Research (ARMOR). This is the first C-band operational polarimetric radar in the US which operates 24 hrs a day (Petersen et al. 2005). One of the main interests is hydrometeor classification especially hail and heavy rainfall mapping. Their fuzzy logic scheme is a C-band ‘tuned’ version (Dieseling et al. 2007) of the S-band NCAR/NSSL research algorithm described in Vivekanandan et al. (1999). In general, the ‘tuning’ of the trapezoidal membership functions was based on polarimetric measurements reported in the literature (e.g., Doviak and Zrnic, 1993; Hoeller et al., 1994; Bringi and Chandrasekar, 2001, Ryzhkov et al. 2005a).

The input feature vector to the algorithm are shown in Table 7.4 above and include the radar measurements, temperature as well as SD of radial velocity, Z_{dr} and Φ_{dp} . The SD fields are analogous to the texture of the fields and are computed over a small polar area of data. The texture parameters are included to separate ground clutter and clear air echoes (mainly insects) from precipitation echoes. Currently 17 output classes are identified by this scheme, 14 of which are hydrometeor related (see Table 7.4).

The membership functions for Z_{dr} , LDR , K_{dp} and ρ_{co} are two-dimensional with reflectivity as the independent variable (the exact membership functions are not yet published). Membership function outputs are weighted and summed to obtain the Q-value as given in Fig. 7.2. If LDR is not measured, for instance, then its weighting is set to zero. Also, several thresholds are applied to prevent unrealistic outputs (similar to Table 7.6 above). For example drizzle is not allowed at temperatures below 0 C. The algorithm chooses the output class with the maximum of the weighted sum (max Q) as the output.

Some examples of classification are shown in Fig. 7.35 for a stratiform event (RHI scan) and Fig. 7.36 for a convective storm with hail (sector PPI scan at elevation angle of 2.7 deg). For the stratiform event, note the wet snow layer depicting the bright band, with rain below and dry snow above. For the convective event, note a small hail core centered at 58 km/105° surrounded by a larger region of rain/hail mixture and small region of heavy rain to the north of the hail core.

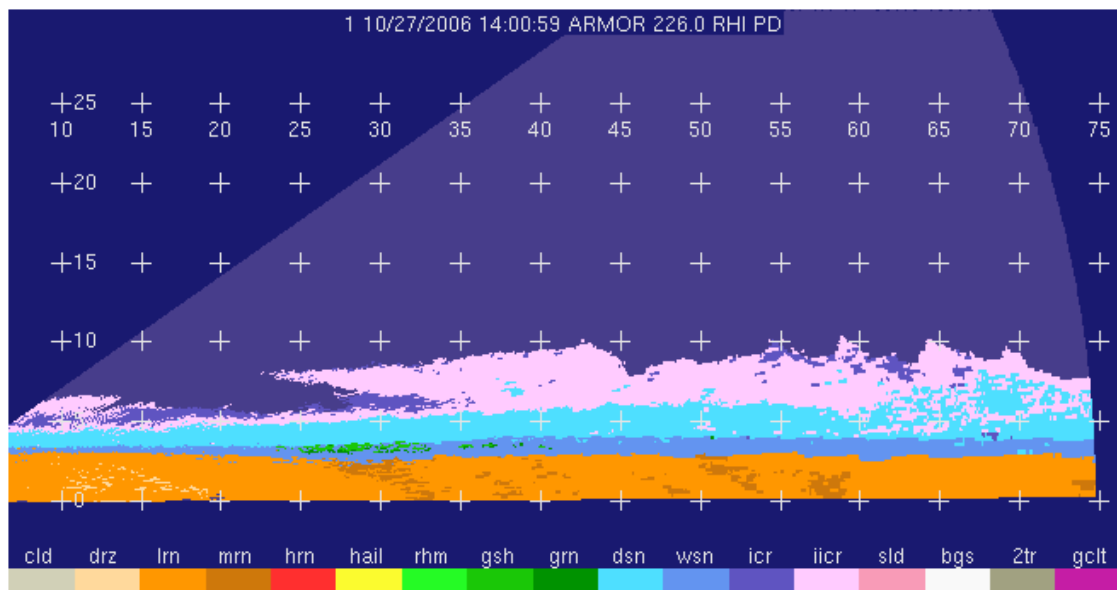


Fig. 7.35: Classification example using the ARMOR radar RHI scan in a stratiform event near Huntsville, Alabama. Figure courtesy of Walt Petersen and Wiebke Deierling.

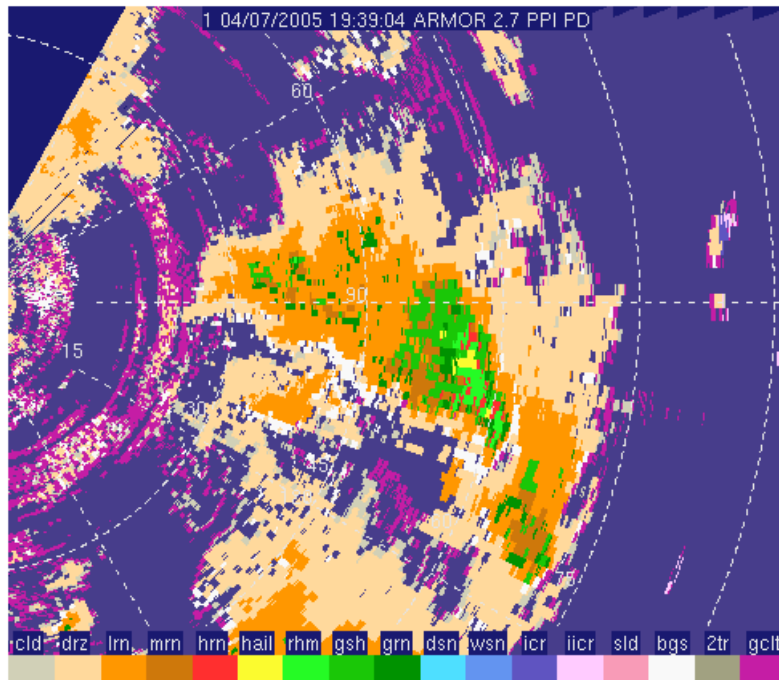


Fig. 7.36: Classification example from sector PPI scan at 2.7° elevation angle from the ARMOR radar. Range rings are 15 km. Adapted from Petersen et al. (2005).

7.7.4 The Environment Canada approach

The Environment Canada operational radar, located in King City, Ontario, has been applying a hydro-classification method based on the fuzzy logic principles developed for the S-band NEXRAD system (Ryzhkov et al. 2005a). The input vector and output classes were listed earlier in Table 7.1 and Table 7.2, respectively. Extension to C-band is currently being implemented, taking into account resonant scattering and attenuation effects (Ryzhkov et al. 2006). Details of this scheme are not yet available in the literature; however, Hudak et al. (2006) have conducted winter precipitation studies and shown that rain/snow boundary can be efficiently detected using Z_{dr} and ρ_{co} .

Fig. 7.37 shows a PPI example of a precipitation transition case which occurred during a cold front passing along the lower Great Lakes. The enhancement in Z_{dr} along the northeast to southwest oriented line correlates well with a significant reduction in ρ_{co} , and together, they indicate the rain/snow boundary. Temperature recordings taken at various sites at the scan time (not shown here but given in Fig. 2b of Hudak et al., 2006) corroborate this. Further validation of this transition was provided by a vertically-pointing X-band radar and a hydrometeor velocity and size detector probe, both located 30 km north of the radar, and both providing time series data. Soon after the rain/snow boundary (from the PPI images) traversed the instrumented site, the X-band radar recorded the sudden disappearance of the bright-band, coupled with much reduced fall velocities at the lowest range gates, indicating clearly that the cold front had passed through and had given rise to precipitation transition to dry snow. This was supported further by analysis of the detector probe data.

The King City radar is one of the few operational radars which has a well instrumented site at close range (30 km) enabling continuous evaluation (and improvement) of hydrometeor classification algorithms in a wide variety of precipitation types. It also allows for data-based construction of membership functions and objective weighting factors, similar to those described in Section 7.6.1. Its high resolution antenna (0.6° beamwidth) enables the acquisition of high quality polarimetric data at low elevation angles and in the presence of high reflectivity gradients, as compared to conventional 1° beamwidth antennas.

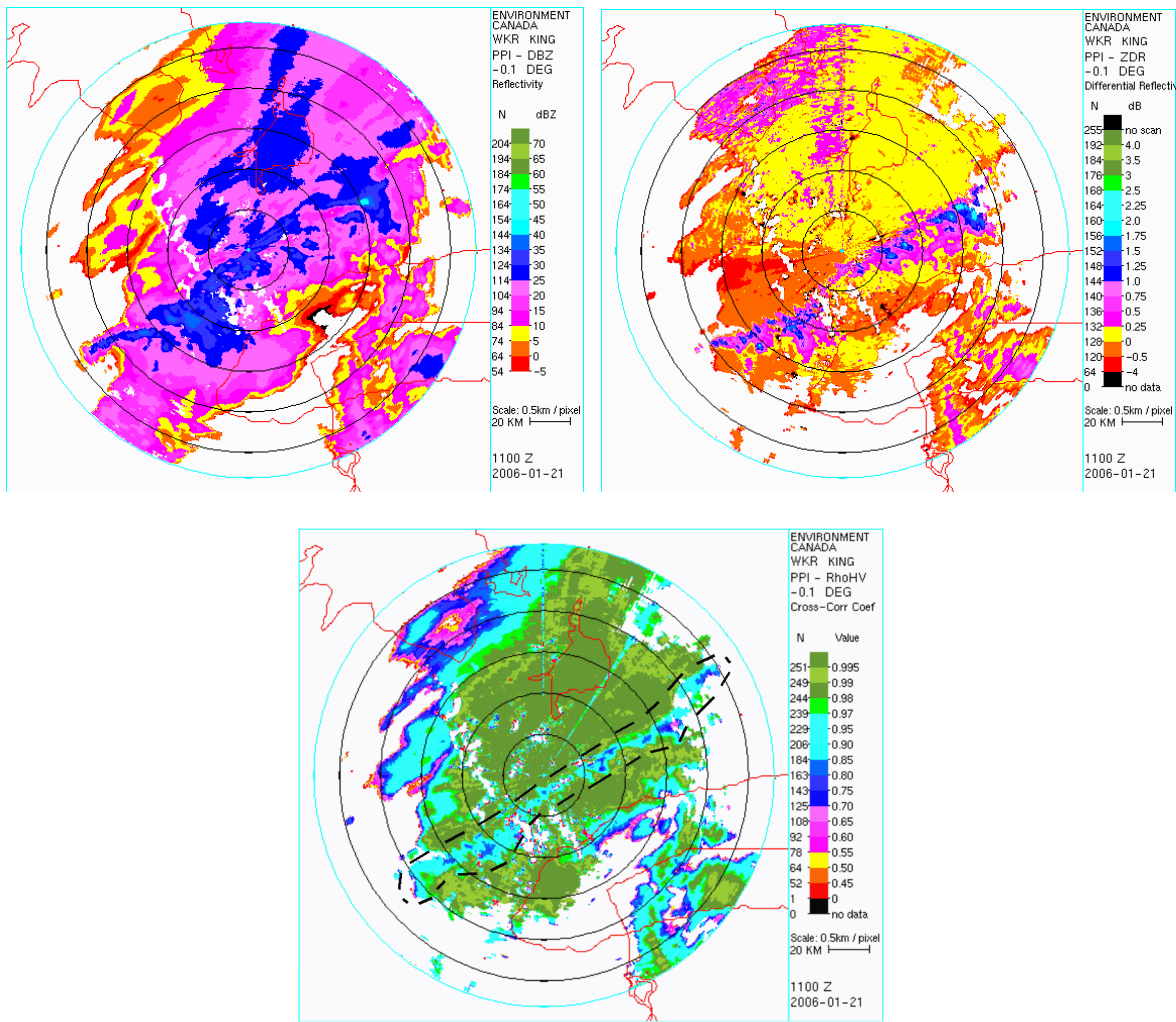


Fig. 7.37: PPI sweeps at low elevation angle (0.1°) from the King City radar operated by Environment Canada. Top left: reflectivity; top right: differential reflectivity; bottom: co-polar correlation coefficient. Range rings are 15 km. The dashed line in the bottom panel encircles the rain/snow boundary, with rain to the south and snow to the north. From Hudak et al. (2006); image ©copyright David Hudak.

7.8 Classification between hydrometeor types – algorithms for C-band using non-fuzzy logic schemes

7.8.1 DLR scheme

In the category of non-fuzzy-logic schemes for hydrometeor identification (mainly for severe hailstorms) at C-band, the Höller et al. (1994) method seems the most quoted one in the literature. It uses Z_{dr} and LDR as well as the freezing level height as its input and classifies the hydrometeors into several classes including rain, graupel and hail. Table 7.8 summarizes the categories and conditions associated with them. The limits are given pictorially in Fig. 7.38.

Table 7.8: Limits of Z_{dr} and LDR used for hydrometeor identification using the Höller scheme. H_{melt} refers to the melting level height.

Hydrometeors	Z_{dr} threshold	LDR threshold	Height threshold
Small raindrops	$Z_{dr} < +1$ dB	$LDR^7 < -35$ dB	$H \leq H_{melt}$
Large raindrops	$Z_{dr} \geq +1$ dB	$LDR < -25$ dB	
Graupel (dry, small), Snow	$Z_{dr} \leq +1$ dB	$LDR < -35$ dB	$H > H_{melt}$
Graupel (wet, melting, small), graupel (dry, large), hail (dry, small)	$-1 \leq Z_{dr} < +1$ dB	$-35 < LDR \leq -25$ dB	
Hail (dry)	$-1 \leq Z_{dr} < +1$ dB	$-25 < LDR \leq -20$ dB	
Hail (wet)	$-1 \leq Z_{dr} \leq +1$ dB	$-20 < LDR \leq -15$ dB	
Large wet hail (spongy or water shell)	$Z_{dr} \leq +1$ dB	$LDR > -15$	
Rain + small hail	$Z_{dr} \geq +1$ dB	$-25 < LDR \leq -20$ dB	
Rain + large hail	$Z_{dr} \geq +1$ dB	$LDR > -20$ dB	

Much of these limits are based on scattering calculations at C-band. Höller et al. (1994) however also include qualitative (cloud model-based) reasons for the threshold values used in their classification scheme, but they note that owing to the lack of verification/validation and lack of complete scattering calculations, there is some degree of subjectivity in the definition of hydrometeor categories and the ‘hard’ separation boundaries of their Z_{dr} and LDR values. It is possible to fuzzify this method by generating 2-D membership functions in the Z_{dr} - LDR plane from Table 7.8. The inclusion of other polarimetric parameters such as K_{dp} and ρ_{co} was attempted for a few storm events and was found to refine the output classes.

⁷ Note that the DLR radar uses an offset feed antenna with LDR system limit ~ -35 dB.

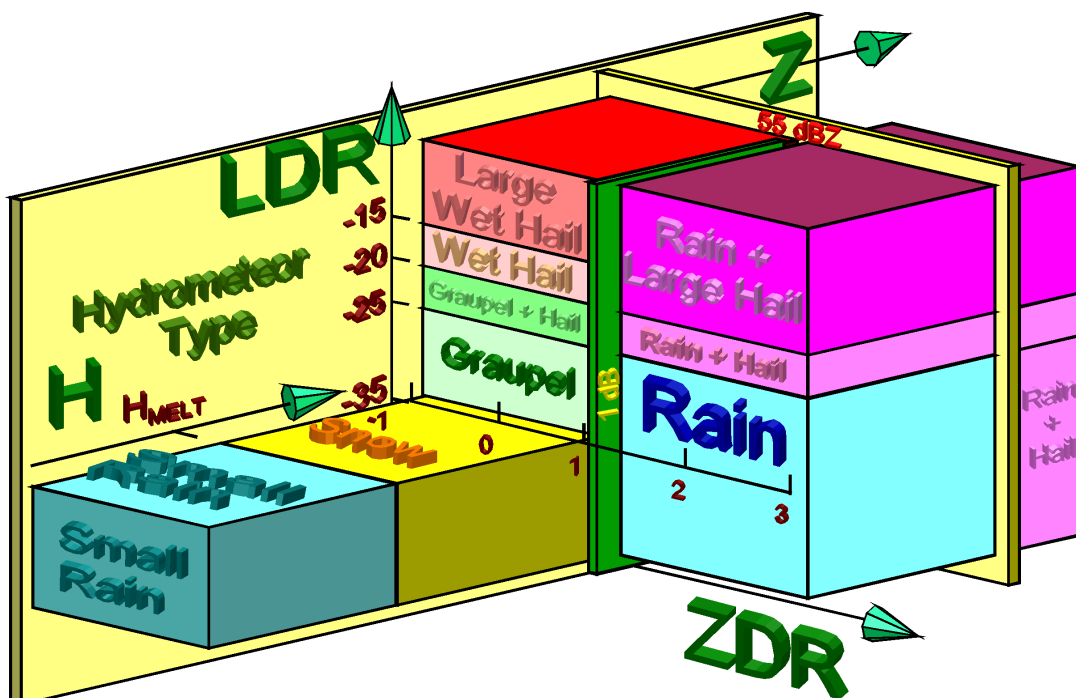


Fig. 7.38: 3-D depiction of the hydrometeor classification scheme by Höller et al. (1994). Image courtesy Hartmut Höller, DLR.

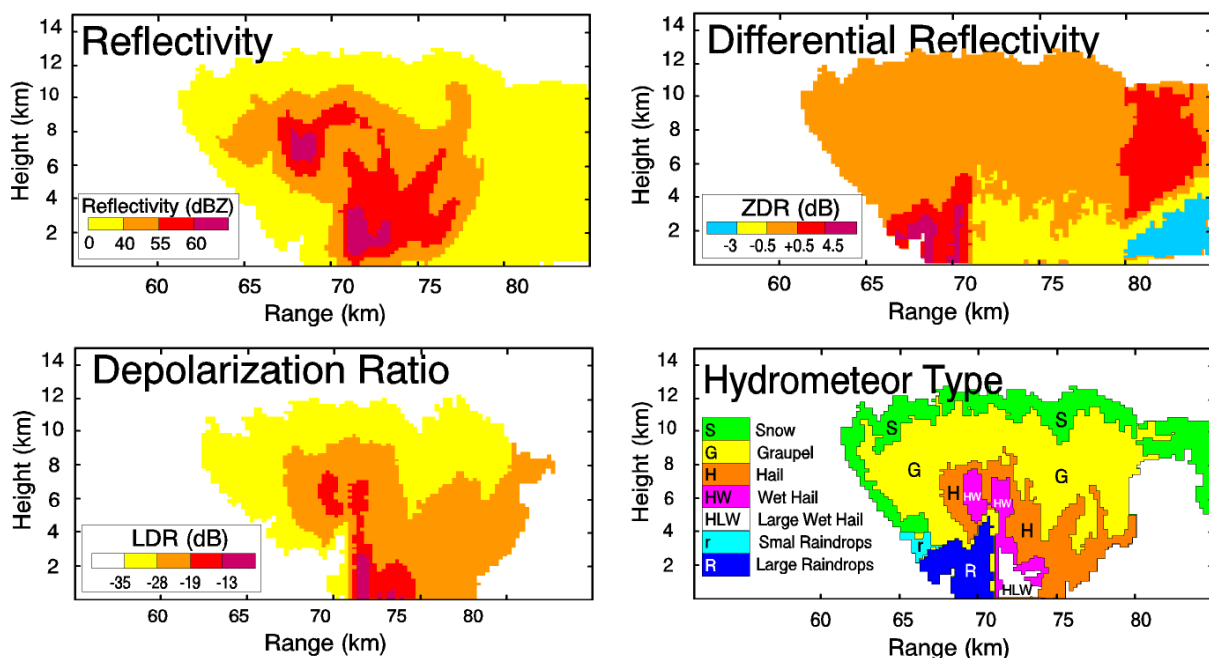


Fig. 7.39: Höller et al. (1994) classification scheme applied to an RHI taken during its vigorous growth phase during a damaging hail event in South Germany. The storm was monitored by DLR's POLDIRAD for several hours. Image courtesy Hartmut Höller, DLR.

An example of the application of Höller's table-based method is given in Fig. 7.39, taken during a damaging hail event of 30 June, 1990. The RHI was taken through the storm core during its vigorous growth phase. The reflectivity panel shows the area of hail initiation as an overhanging echo region with a core at 6 to 8 km altitude at a distance of 67 to 69 km. In this area, LDR is increased (-19 to -13 dB) and slightly negative ZDR is observed. At a distance of about 72 km, very high reflectivity is associated with a strong precipitation shaft of a decaying cell. The combination of very high reflectivity and ZDR around 0 dB in that area indicates hail. This interpretation is supported by quite high LDR above -13 dB. Hail on ground was observed in that area, with a mean size of approximately 1.5 to 2.5 cm.

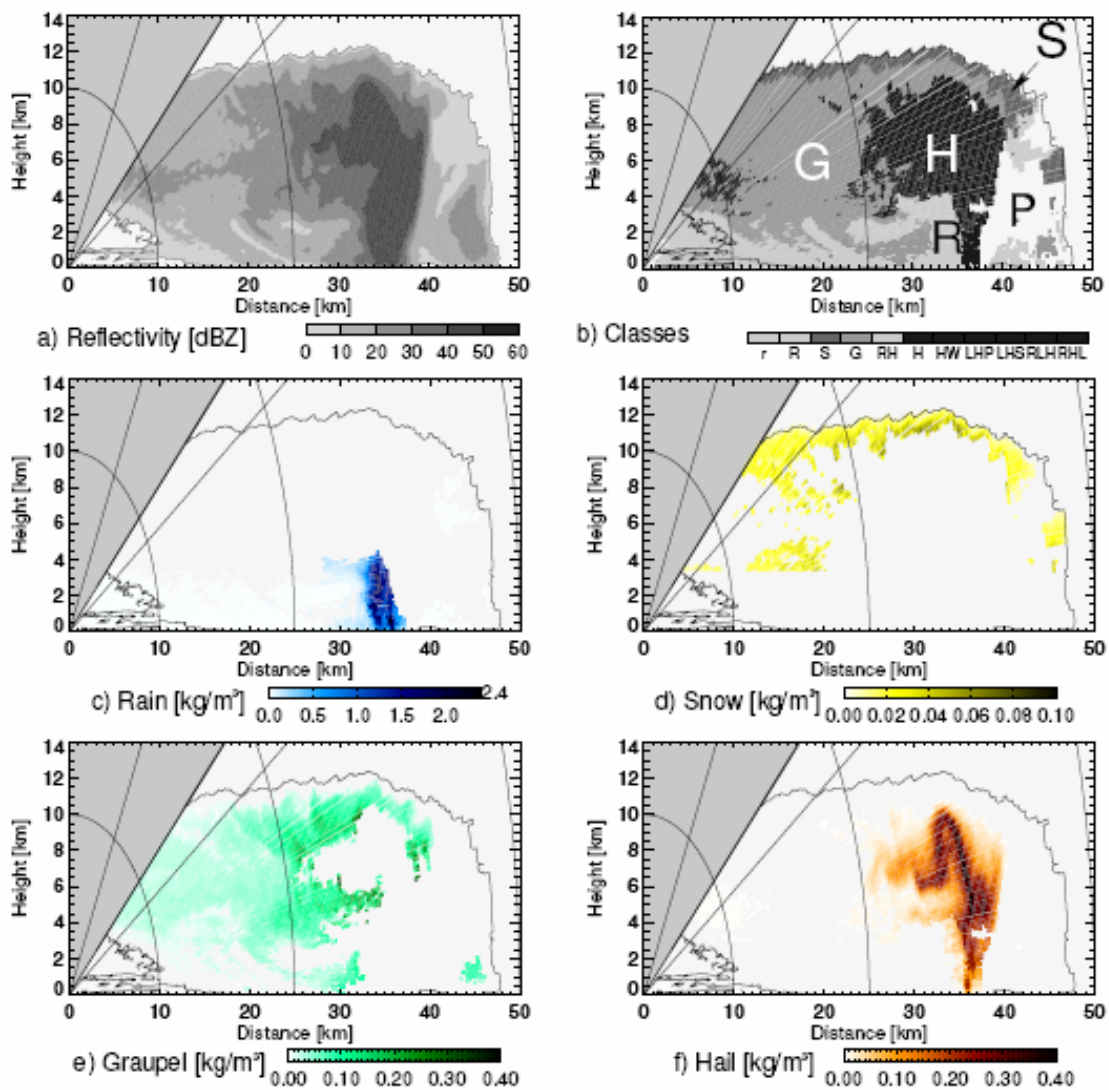


Fig. 7.40: An extension of Höller's classification scheme applied to a supercell storm along with empirical estimates of their mass contents. From Fehr et al (2004); ©copyright 2004 Elsevier.

Fehr et al (2004) have applied Höller's scheme to different types of convective systems (e.g., supercell, multi-cell complex and squall-line). The storms were long-lived and were monitored by DLR's C-band dual-polarization Doppler radar (POLDIRAD). An empirical model-based Z_h – mass content relation was derived for each class. One RHI example is shown in Fig. 7.40, taken during a 1998 supercell storm in South Germany. Note that after classification, the relative intensity of the various classes in terms of spatial distribution of mass content (even though approximate) may be potentially used for nowcasting. Note that the Z_h - mass relations used are based on model microphysical simulations, are empirical and furthermore tuned for thunderstorms in certain types of environmental conditions. Nonetheless, they give spatial variations of relative intensities within the various hydrometeor classes. Such information, while not being accurate, may assist in the forecasting of severe weather.

7.8.2 The HDR method and combined HDR-LDR methods

The Hail Detection Ratio (HDR) can not only be used for S-band (see Section 7.4.3), but also for C-band radar. The equivalent formulas are not as well established by direct observations; however, based on DSD data from Darwin, Australia, scattering calculations have been used to derive the $f(Z_{dr})$ in a similar way as given in equations (7.1) and (7.2):

$$f(Z_{dr}) = \begin{cases} 32 & Z_{dr} < 0 \text{ dB} \\ 19.5 Z_{dr} + 32 & 0 < Z_{dr} < 1.74 \text{ dB} \\ 60 & Z_{dr} > 1.74 \text{ dB} \end{cases} \quad (7.8)$$

The boundaries are shown for S-band (according to equation (7.2)) and C-band (according to equation (7.8)) in Fig. 7.41.

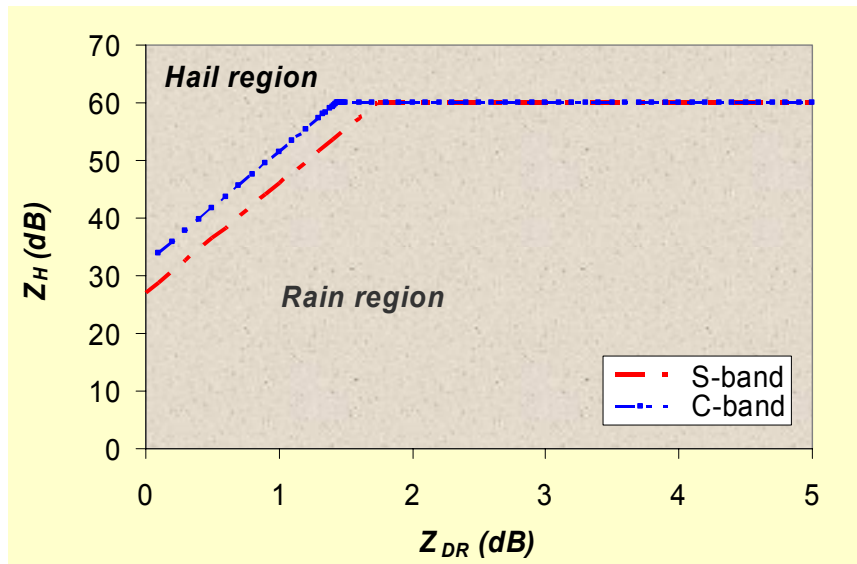


Fig. 7.41: Rain/hail boundaries shown for S and C bands in the Z_h - Z_{dr} plane, according to equations (7.1), (7.2), and (7.8).

Nanni et al. (2000) have assessed the use of the HDR hail-indicator with a C-band operational radar. The assessment was performed by comparing against the ‘ground-truth’ from a hailpad network. Despite the frequent occurrence of differential attenuation which affects the measured Z_{dr} , the comparisons have indicated that ‘HDR gives a high probability of hail detection as well as acceptable number of false alarms’ (Nanni et al., 2000). Analyses of four events have indicated that the HDR threshold may need to be increased to 13 dB for better hail/rain discrimination. It should be noted however that this study utilizes the S-band version of HDR (on the basis of the C-band calculations of Aydin and Giridhar, 1991). Furthermore, the study had been selective in the events chosen for the analysis. For example, cases with negative Z_{dr} over the pad area were not included since the differential attenuation was considered too high for accurate correction methods to be applied.

Work at C-band on the combined use of HDR and LDR has not been, so far, carried out. Compared to the combined HDR-LDR methods for S-band (Section 7.4.3), the LDR values for hail are expected to be slightly higher at C-band (e.g. see Höller limits in Table 7.8) and the corresponding HDR values are expected to be slightly smaller (as inferred from Fig. 7.41). An additional consideration at C-band is the attenuation-correction for Z_h and, more importantly, for Z_{dr} as well as LDR (which requires one-way differential attenuation correction for the return signal).

7.9 Preliminary results for echo classification at X-band

The use of X-band for weather radars has gained momentum in the past few years. This is primarily due to dual-polarization capabilities added to such radars which improved attenuation-correction methods by the differential propagation phase integration (as discussed in Chapter 4). These radars are generally short range (typically up to 50 km) and the primary applications at this stage appear to be in hydrology or as gap-filler radars in an operational network. As opposed to S-band and C-band radars, which are operated with dual-polarization capabilities since many years, algorithms for classification of 'meteo' and 'non-meteo' echoes, or of classification between different hydrometeor types have not yet appeared in the literature at X-band to a significant extent. This situation will no doubt change in the next few years as X-band polarimetric radars become more widely deployed. But for now, echo classification results are of rather preliminary nature for X-band, and a lot of research on that matter is continuing. In this section, two examples of recent results are presented, firstly an example for the classification of clutter and meteorological targets, and secondly an example for mid-latitude wintertime precipitation classification.

7.9.1 Classification between meteorological and non-meteorological echoes and identification of sea clutter

In this Section we give a brief description of data from a polarimetric radar located in Athens close to the Mediterranean (XPOL⁸: Anagnostou et al. 2004) from the viewpoint of distinguishing between sea-clutter, ground-clutter and 'meteo' echoes similar to what was done in Section 7.6.2. In accord with the fact that the standard deviation of Φ_{dp} , or $SD(\Phi_{dp})$, and ρ_{co} are the main variables for classification of 'meteo' versus 'non-meteo' echoes we give here examples of data from regions known apriori to be from sea-clutter, land clutter, and 'meteo' echoes.

Fig. 7.42 gives four panels of sector PPI at low elevation angle of reflectivity, $SD(\Phi_{dp})$ and ρ_{co} , respectively. In the reflectivity panel, the regions of sea clutter, land clutter and 'meteo' echoes are marked. It is immediately evident that 'meteo' echoes have low $SD(\Phi_{dp}) < 20$ deg and high $\rho_{co} > 0.9$ as opposed to sea-clutter which has corresponding values of $SD(\Phi_{dp}) \sim 30\text{--}60^\circ$ and $\rho_{co} < 0.6$. These values are not very different from the C-band data shown earlier in Section 7.6.2.

Fig. 7.43 shows range profiles along the 235° azimuth that show in more detail the values of reflectivity, $SD(\Phi_{dp})$ and ρ_{co} in sea-clutter. Again, the significant features are the very low values of ρ_{co} and variable but high values of $SD(\Phi_{dp})$. This figure may be compared with the C-band data in Fig. 7.27 which is inferred to be from AP/sea-clutter.

⁸ Operated by National Observatory of Athens, Institute of Environmental Research and Sustainable Development (IERSD).

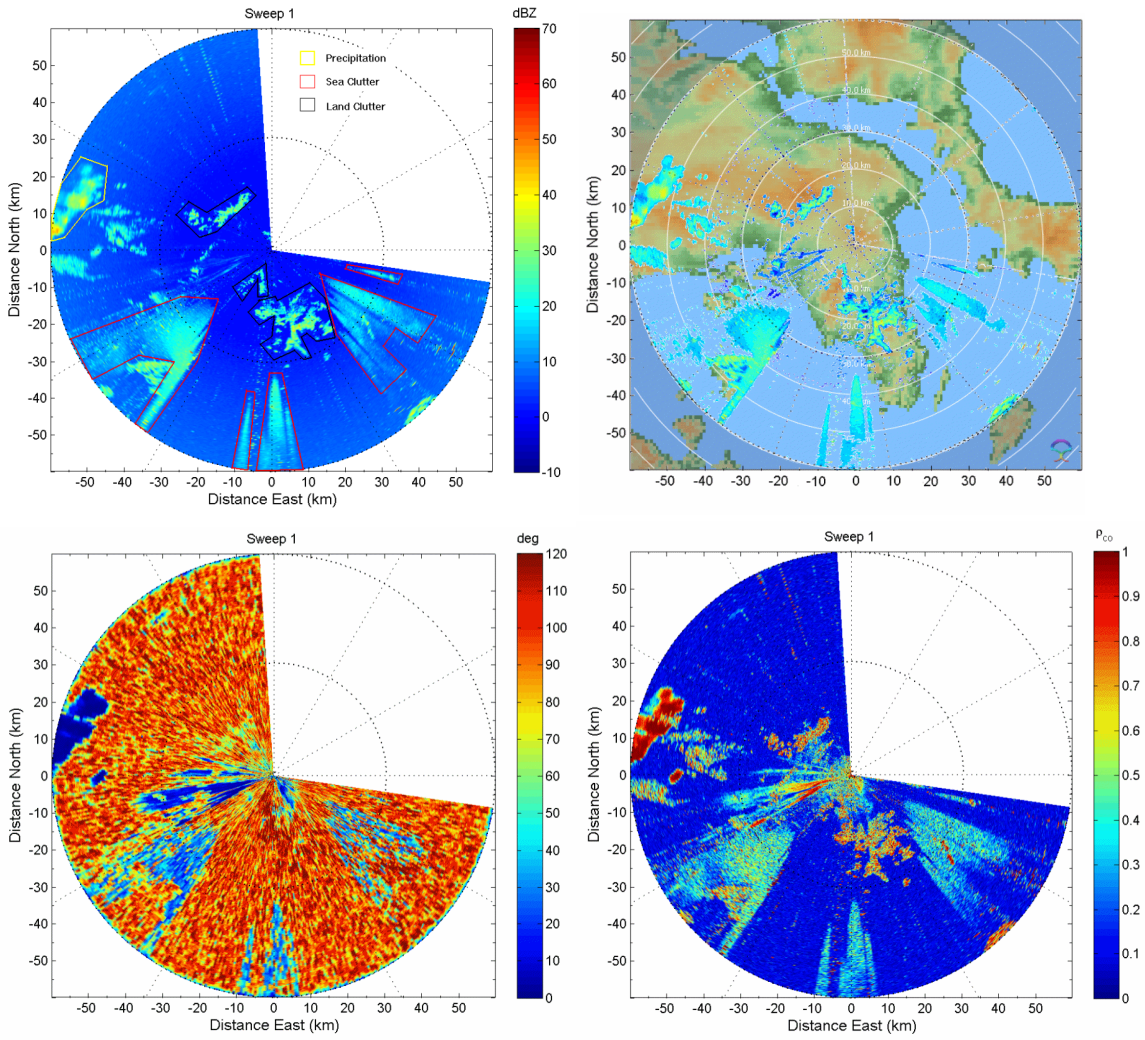


Fig. 7.42: Sector PPI data (elevation 1° ; range 60 km) from XPOL radar in Athens, Greece. Top left panel: Z_h ; top right panel: Z_h (high-level), overlaid to map around the radar site; bottom left panel: $SD(\Phi_{dp})$; bottom right panel: ρ_{co} . Sea-clutter, land-clutter and ‘meteo’ echoes are marked in the top panel. XPOL radar data courtesy of M.N. and E.N. Anagnostou.

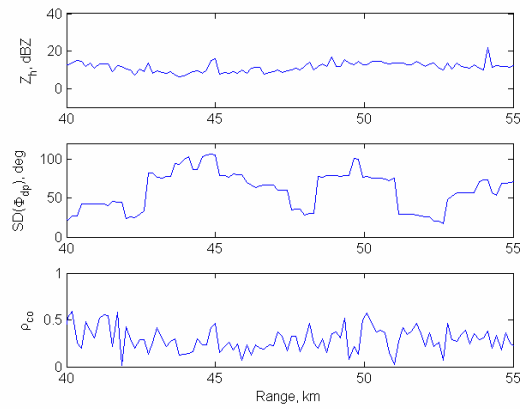


Fig. 7.43: Range profiles along azimuth angle of 235° to illustrate the radar parameters in sea clutter, top panel: Z_h ; middle panel: $SD(\Phi_{dp})$; bottom panel: ρ_{co} .

Fig. 7.44 shows relative frequency histograms of $SD(\Phi_{dp})$ and ρ_{co} from the marked regions in the top left panel of Fig. 7.42. These histograms clearly show that there is very little overlap between sea-clutter and precipitation echoes in $SD(\Phi_{dp})$ or in ρ_{co} . In fact, they are quite similar to the C-band histograms shown in Fig. 7.28. Hence, it follows that an X-band fuzzy-logic scheme could be 'tuned' from the C-band MeteoFrance methodology described in Section 7.6.1. Alternately, the NEXRAD approach as described in Section 7.3.1 could be used. Note that there is more overlap in ρ_{co} values between 'meteo' echoes and land clutter (see Fig. 7.44; see for comparison also Fig. 7.28). On the other hand, this is not the case for 'meteo' echoes versus sea-clutter. Since the coastline is always well known with respect to the radar site, it is possible to develop two classifiers for 'meteo' versus 'non-meteo', i.e., one for land and one for sea. In the case of the latter, a simple threshold scheme might work since the overlap is negligible (cf. also Table 7.3 under Sugier and Tabary 2006).

Fig. 7.45 shows a set of preliminary trapezoidal membership functions at X-band for three classes, namely, 'meteo', land clutter and sea-clutter, with $SD(\Phi_{dp})$ and ρ_{co} as input vector elements. Note that ρ_{co} in precipitation must be corrected for system noise if the SNR < 15 dB. The membership functions are based on the histograms in Fig. 7.44 and require testing at other sites.

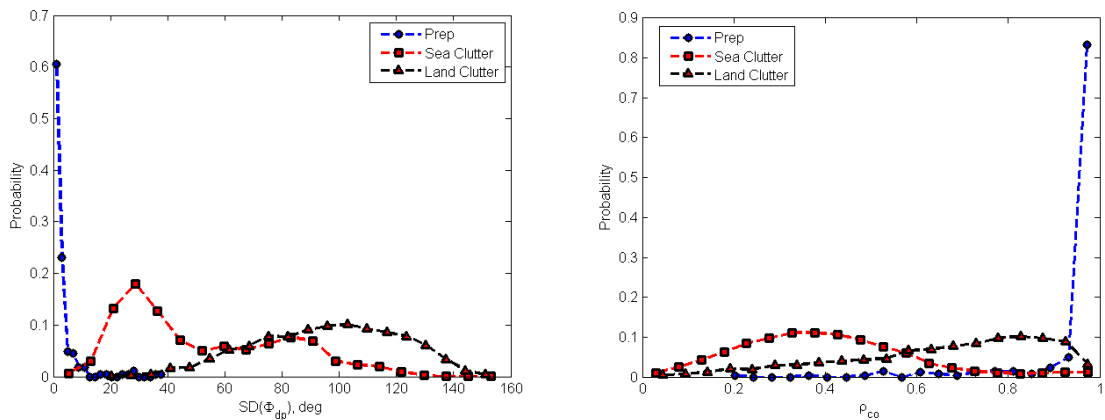


Fig. 7.44: Relative frequency histograms using data from the sector PPI sweep shown in Fig. 7.42. Left panel shows histogram of $SD(\Phi_{dp})$ for precipitation, sea and land clutter. Similarly for right panel, except histogram of ρ_{co} . Note negligible overlap area between the 'meteo' and sea-clutter classes.

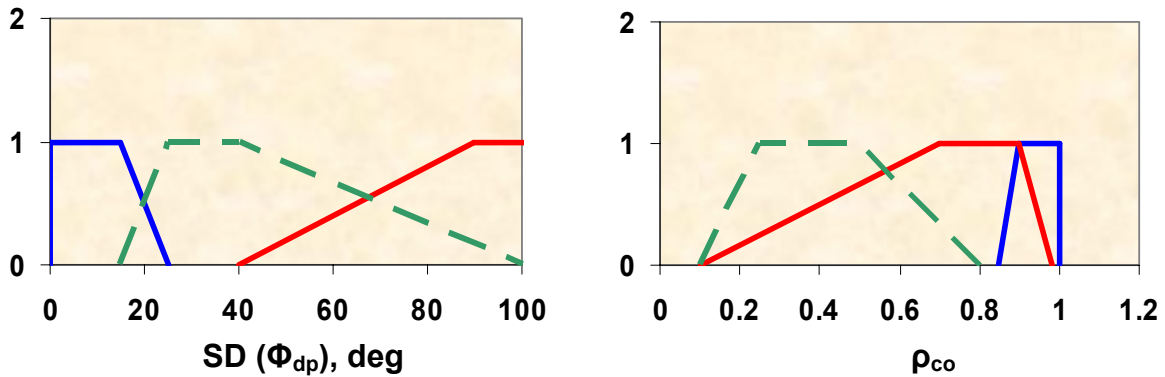


Fig. 7.45: Membership functions for the three classes : ‘meteo’ echoes (blue), sea-clutter (dashed green) and ground clutter (red), shown as a function of $\text{SD}(\Phi_{dp})$ (left) and ρ_{co} (right).

7.9.2 Recent research on hydrometeor classification

Developmental work on hydrometeor classification schemes for X-band systems has only recently begun. The work includes both theoretical calculations and experimentally-based observations. In the former case, Dolan and Rutledge (2007) have performed simulations based on numerical scattering calculations at X-band of different type of hydrometeors with varying size, shape, orientation and dielectric constant distributions. Their classes include rain, drizzle, snow and graupel. Hail was excluded because of complicating Mie affects at X-band. The numerical results were used to form the basis for the beta membership functions to be used within an X-band fuzzy logic methodology.

On the experimental side, Iwanami et al. (2007) have reported results of hydrometeor type classification in winter clouds. The classification scheme uses a fuzzy-logic technique as proposed by Lim et al. (2005). Simultaneous observations from NIED’s X-band polarimetric radar and in-situ measurements with balloon-borne hydrometeor videosonde and rawinsonde were used first to derive the histograms of Z_h , Z_{dr} , ρ_{co} and temperature for five identified classes, namely : rain (R), sleet (S), graupel (G), aggregates (A) and ice crystals (X). The histograms are given in Fig. 7.46. The videosonde images used for a priori selection of regions with different classes were often composed of mixed particle types. Most information content appears to be in the Z_{dr} and temperature input variables. As with the MeteoFrance approach discussed in Section 7.6.1, the histograms are directly used to construct the membership functions, which in this case are beta functions with the mean located at the maximum, and the width being at the 70% cumulative frequency level (on both sides of the histogram peak).

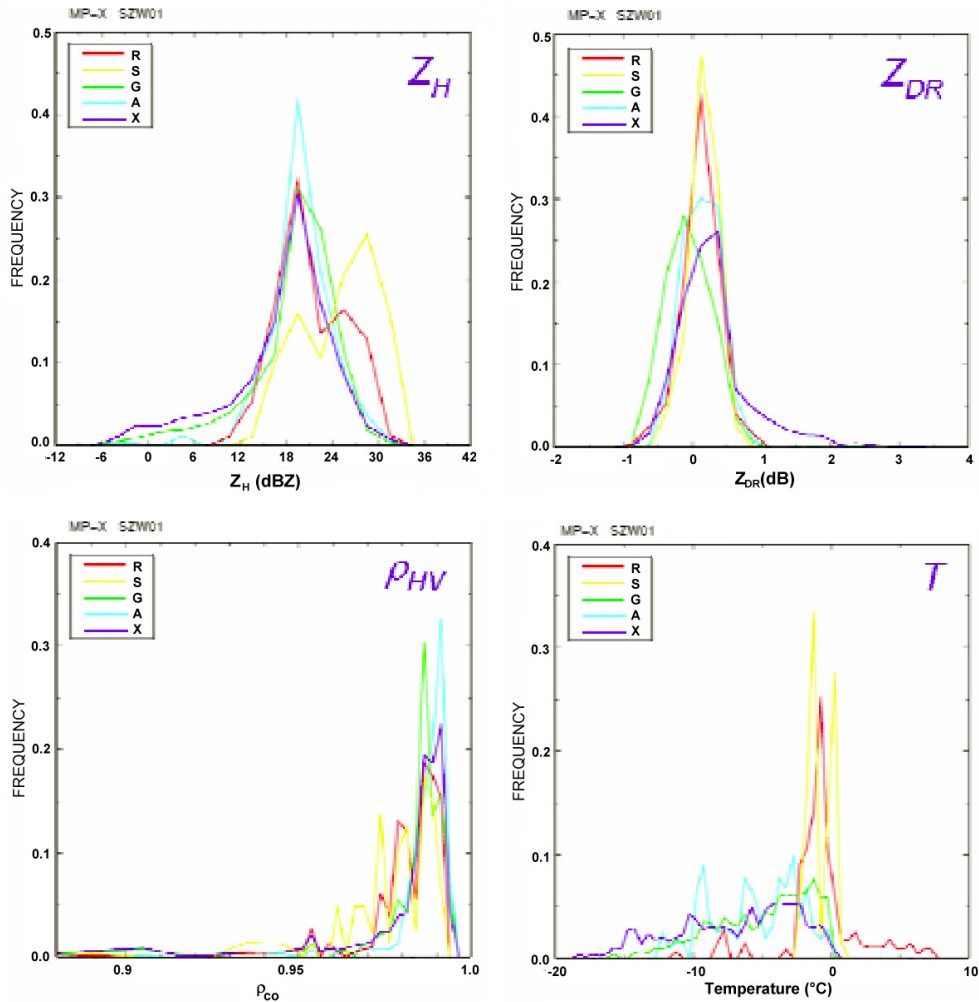


Fig. 7.46: Histograms of Z_h , Z_{dr} , ρ_{co} (same as ρ_{co}) and temperature for various classes. R = rain, S = sleet, G = graupel, A = aggregates and X = ice crystals. From Iwanami et al. (2007).

One example, based on an RHI scan, is shown in Fig. 7.47. The four panels show Z_h (top left), Z_{dr} (top right), ρ_{co} (bottom left) and the results of the classification (bottom right). Superimposed on the plots is the track of the videosonde, the images of which were in turn used to check the performance of the fuzzy-logic method. Note the region aloft (at around 3 km height) with relatively low Z_h and high Z_{dr} values indicative of horizontally-oriented plate-like crystals. This has also been observed and verified at S- and C-bands (Bader et al, 1987; Vivekanandan et al.). In contrast, aggregation processes generally lead to regions of relatively high Z_h with Z_{dr} of ~ 0 - 0.5 dB. However, the classification results of Fig. 7.47 do not show this latter feature. Moreover, a distinct bright-band is also absent in this particular example.

Preliminary results of Iwanami et al. (2007) have indicated that rain, sleet and graupel were significantly better classified than aggregates or crystals. The stated reasons were, (a) aggregates were normally mixed with other hydrometeor types and (b) their ice crystal class included four different types (plate, dendrite, needle, column). These results support the general concept that winter season classification

is more difficult than summer. It is anticipated that the addition of LDR and K_{dp} into the input vector will improve the identification of graupel versus aggregates and different types of oriented crystals (plate-like versus needle/column-like), respectively.

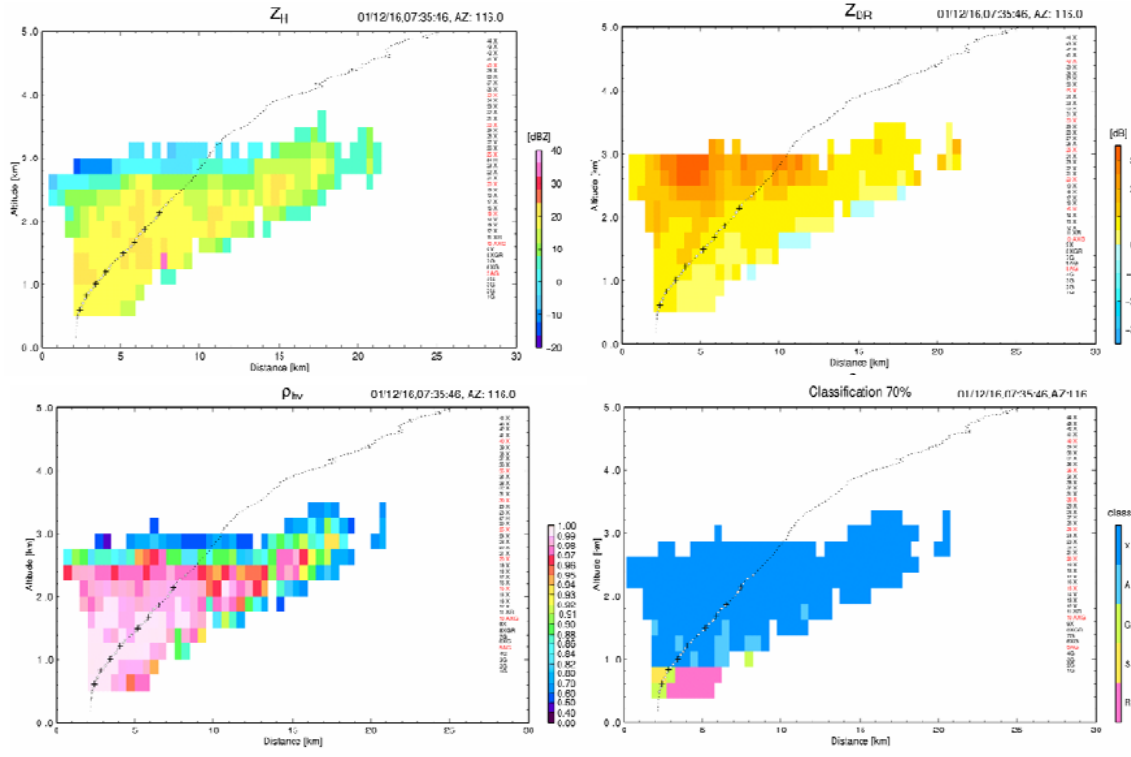


Fig. 7.47: RHI scan data of Z_h (top left panel), Z_{dr} (top right), ρ_{hv} (bottom left) and classification results (bottom right; R = rain, S = sleet, G = graupel, A = aggregates and X = ice crystals). Dashed line shows the ascent of the balloon-borne videosonde and rawinsonde. From Iwanami et al. (2007).

8 APPENDIX A – Iterative Φ_{dp} Filtering

The differential propagation phase (Φ_{dp}) is known to be a monotonically increasing function of range in rainfall. The measured differential phase between H and V polarizations ($\tilde{\Psi}_{dp}$), however, is the sum of Φ_{dp} and the scattering differential phase (δ):

$$H^*V = \tilde{\Psi}_{dp} = \Phi_{dp} + \arg(S_{hh}^*S_{vv}) \quad (\text{A.1a})$$

$$= \Phi_{dp} + \delta \quad (\text{A.1b})$$

where H and V are the received complex signals (i.e., $H = I + jQ$) and S_{hh} , S_{vv} are the diagonal elements of the scattering matrix at range r . For Rayleigh scattering $\delta = 0$ and we do not need to distinguish between $\tilde{\Psi}_{dp}$ and Φ_{dp} . However, at C and X-bands the δ term may become significant mainly due to Mie scattering effects from melting hail which can, at times, 'appear' as very large raindrops. This 'resonance' is quite strong at C-band whereas at X-band it appears to be 'damped' due to larger absorption effects. Recent data from three dual-polarized radars suggest that the scattering differential phase in rain may not be significant at X-band (Park et al. 2004, Matrosov et al. 2002, Anagnostou et al. 2004) though other system errors could cause an effect similar to δ fluctuations. At C-band the δ effect has been documented (varies from 5°–20° due to large drops or partially melted hail around 7-10 mm; e.g., Meischner et al 1991; Keenan et al 1997; May et al 1999). The δ effect, which appears as 'local' phase perturbations on an otherwise monotonic increasing $\tilde{\Psi}_{dp}$ function with range, must be removed before the K_{dp} can be calculated. There are two different approaches to δ 'correction', (a) the iterative range filtering method of Hubbert and Bringi (1995) and, (b) the 'consensus' estimator described by May et al. (1999). Note that the retrieved δ can also be used for detecting Mie scattering effects from non-meteorological echoes such as birds (Zrnić and Ryzhkov 1999). Here we describe in more detail the iterative filtering method of Hubbert and Bringi (1995) which has been applied at C and X-bands with very little modification. Note that for S-band, only two iterations are sufficient since $\delta \approx 0^\circ$ for Rayleigh scattering.

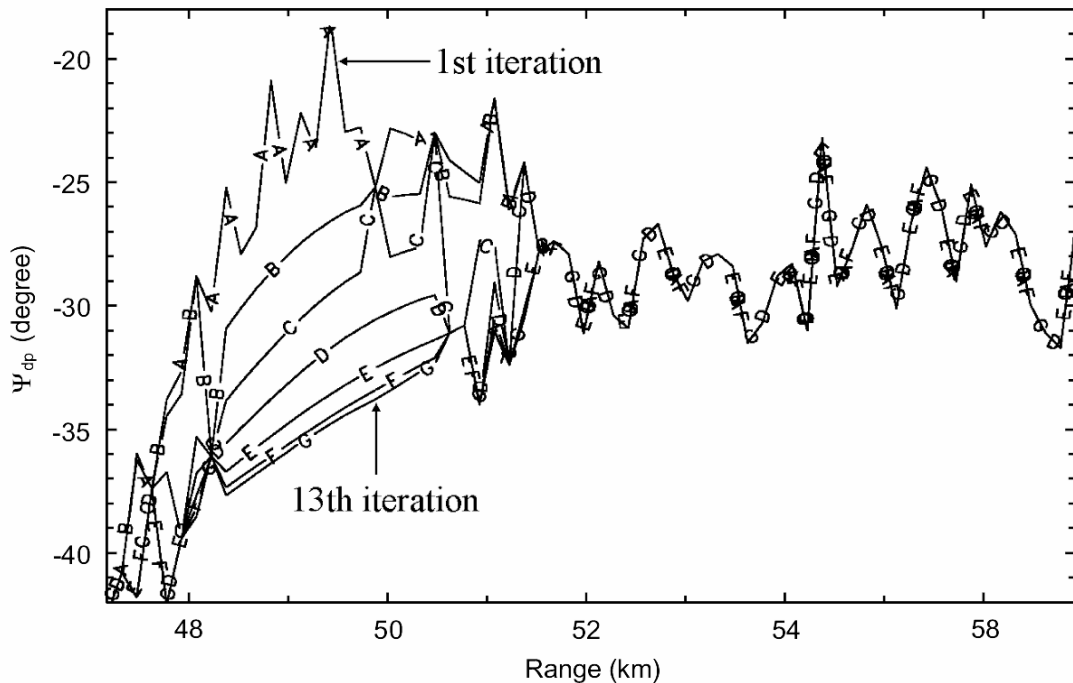


Fig. A.1: An example of iterative filtering technique showing $\tilde{\Psi}_{dp}$ after 1, 3, 5, 7, 9, 11 and 13 iterations, corresponding to curves A-G, respectively, of the filtering process. The original unfiltered curve is seen in Fig. 3.7 (dashed curve). From Hubbert and Bringi (1995).

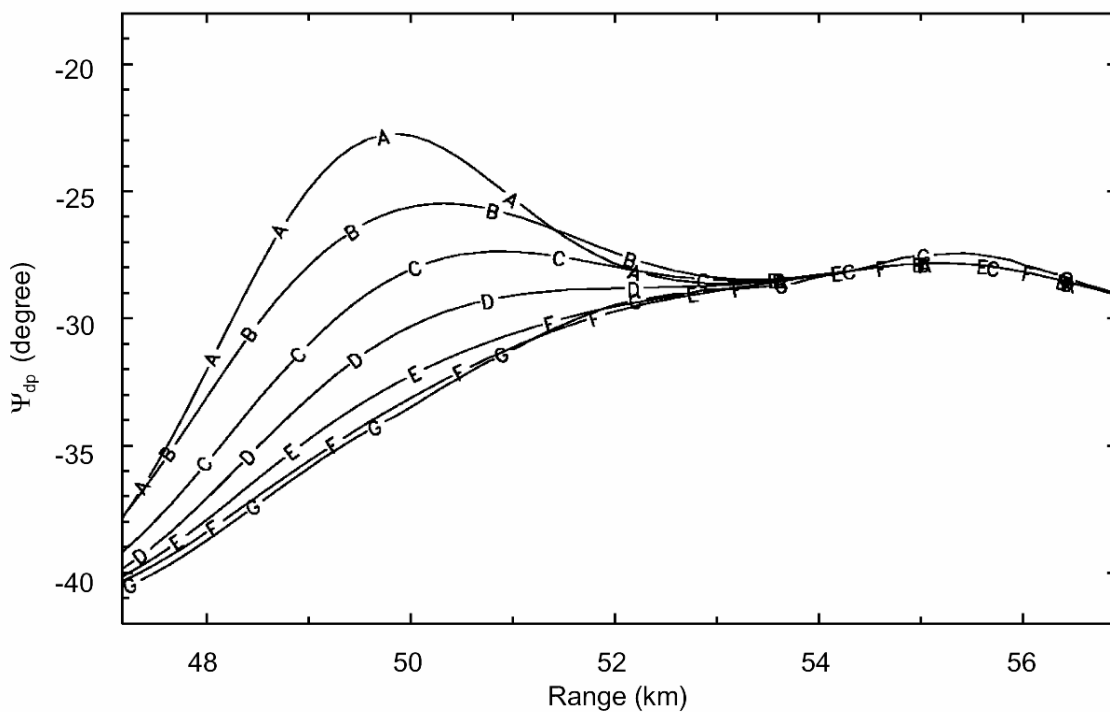


Fig. A.2: As in Fig. A.1 except filtered $\tilde{\Psi}_{dp}$ is shown (i.e. curve A results after curve A of Fig. A.1 is smoothed with the filter). From Hubbert and Bringi (1995).

The basis of the method is an iterative application of a finite impulse response (FIR) range filter which has the desired frequency response, i.e., attenuating the 'high' frequency gate-to-gate spatial fluctuations while preserving the monotonic increasing trend in $\tilde{\Psi}_{dp}$. It is basically a weighted moving average filter. The magnitude response of a 20th order FIR filter was shown in Fig. 3.5 which is designed for 150 m gate spacing. This design strongly attenuates spatial fluctuations of 1.5 km or less by 12 dB or more. The -3 dB point is chosen at 2.85 km. Practically, this design was chosen because it performed well. The goal is to preserve the monotonic increasing trend of $\tilde{\Psi}_{dp}$ due to the propagation medium while attenuating statistical fluctuations and perturbations due to δ .

The iterative filter works as follows. The 'raw' $\tilde{\Psi}_{dp}$ is shown as curve A in Fig. A.1. The curve marked A in Fig. A.2 is the result of the first application of the FIR filter. A new range profile (marked as curve B in Fig. A.1) is constructed by selecting data points from either the 'raw' profile or its filtered version as determined by a threshold. This threshold is set according to the expected standard deviation of the differential phase measurement (3°–5°). The 'raw' $\tilde{\Psi}_{dp}$ (curve A in Fig. A.1) and the filtered $\tilde{\Psi}_{dp}$ (curve A in Fig. A.2) are differenced at each range gate. If the absolute value of the difference at any gate is less than the pre-selected threshold, the 'raw' $\tilde{\Psi}_{dp}$ is selected for the next iterated $\tilde{\Psi}_{dp}$ range profile, otherwise the filtered $\tilde{\Psi}_{dp}$ is selected. In this way the next iterated range profile of $\tilde{\Psi}_{dp}$ (curve B in Fig. A.1) is created. The process is then repeated by filtering curve B in Fig. A.1 which results in curve B in Fig. A.2. These two curves are differenced and after application of the threshold it results in curve C in Fig. A.1 and so on until curve G is generated in Fig. A.1. Convergence is determined by requiring that the change in $\tilde{\Psi}_{dp}$ from one iteration to the next is within some tolerance. It was found that repeating the filtering process 10–15 times produced 'good' results. The last iteration results in curve G in Fig. A.1 and its filtered version is curve G in Fig. A.2 (or the solid line in Fig. 3.8). In effect, curve G 'replaces' the 'raw' $\tilde{\Psi}_{dp}$ data between 48.5 km and 51 km with a smooth monotonic curve in the region where significant δ exists.

The K_{dp} is obtained by taking the range derivative of the solid line in Fig. 3.8 or curve G in Fig. A.2 using the slope of a linear least squares fit to a varying number of consecutive range samples based on the reflectivity value as explained in Chapter 3. In this way an estimate of K_{dp} is available within the region of significant δ . Finally, the difference between the 'raw' $\tilde{\Psi}_{dp}$ and curve G in Fig. A.2 is the profile of δ shown in Fig. A.3. A simplified flow diagram is illustrated in Fig. A.4.

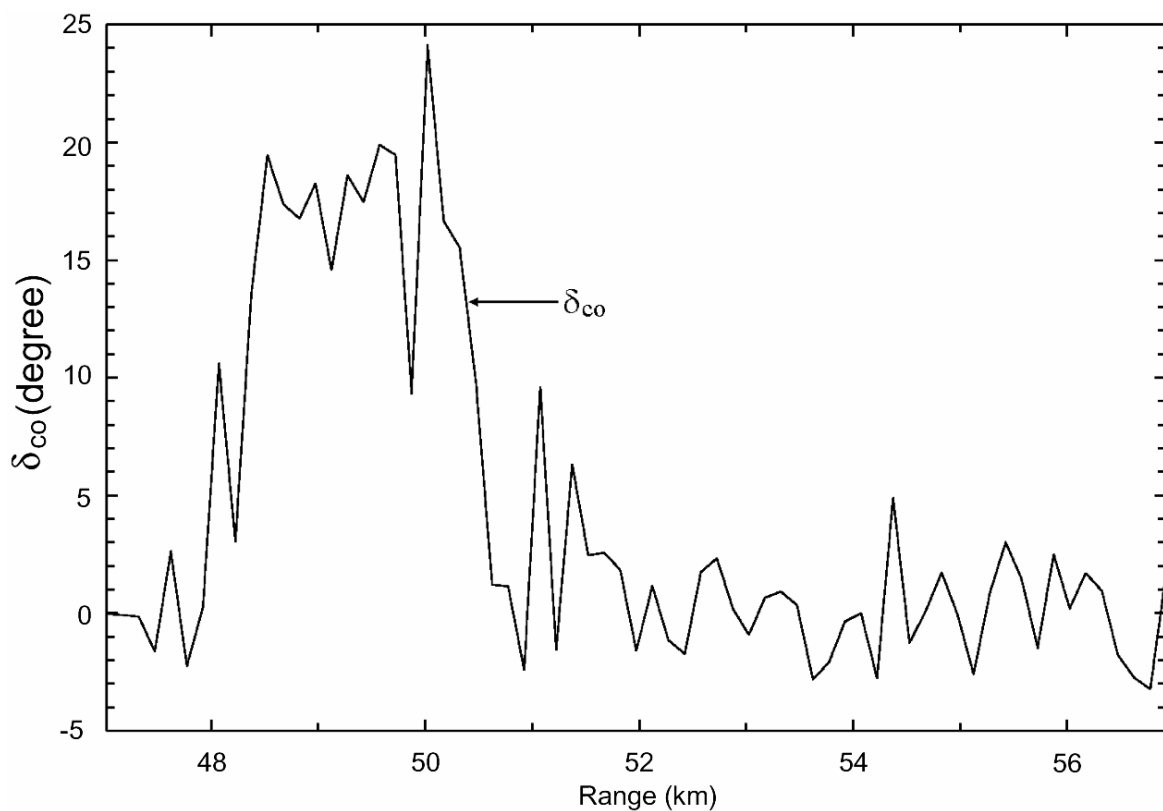


Fig. A.3: The estimate of δ present in the $\tilde{\Psi}_{dp}$ range profile. From Hubbert and Bringi (1995).

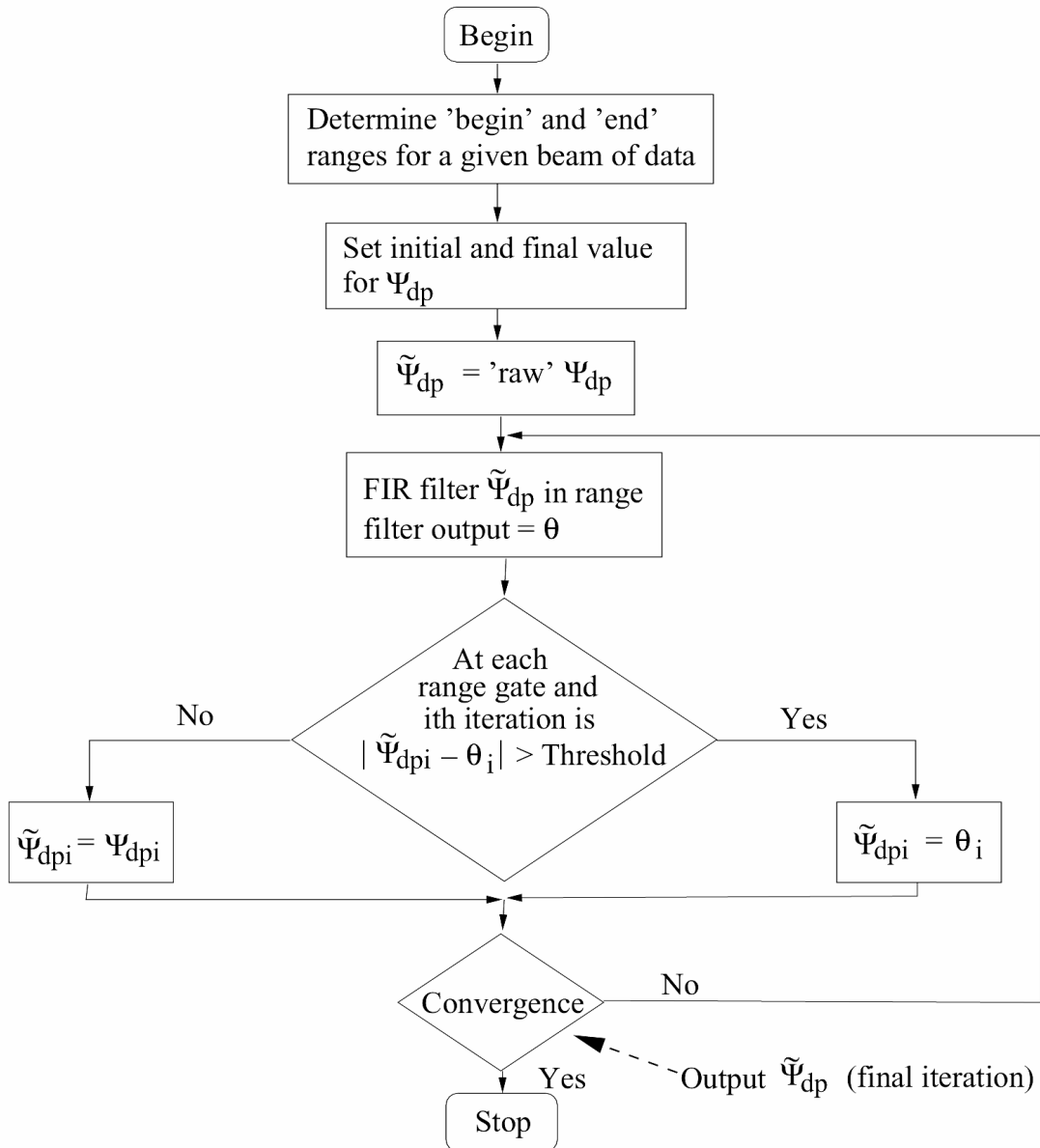


Fig. A.4: Simplified flow diagram for the iterative filtering methodology. Adapted from Hubbert and Bringi (1995).

9 APPENDIX B – List of Symbols and Acronyms

Roman character symbols

A	specific attenuation
A_{dp}	specific differential attenuation
A_h	specific attenuation for horizontal polarization
A_v	specific attenuation for vertical polarization
b	exponent of the power law relationship between specific attenuation and specific differential phase
c	speed of light
D	diameter of a spherical rain drop
D_e	equivalent spherical diameter
D_m	mass weighted mean diameter of a drop size distribution
D_0	median volume diameter
\vec{f}	forward scattering amplitude vector
G_0	radar antenna gain
H, h	horizontal polarization
\hat{h}	unit vector along horizontal polarization direction
$K_{dp} / K_w /^2$	specific differential phase
	dielectric factor of water
k_0	wave number in free space
N	number of range samples in path length L
$N(D)$	drop size distribution ; number of drops per unit volume in the diameter interval D to $D + \delta D$
N_T	zeroth moment of drop size distribution
N_w	intercept parameter of a normalized gamma drop size distribution
N_0	intercept parameter of the drop size distribution $N(D)$
$P_i(j)$	value of the membership for jth radar observable and for the i th hydrometeor class
P_r	power received
P_t	transmitter pulse power
Q_i	aggregation value derived from the radar data, used for hydrometeor classification
R	rainfall rate
S_{hh}, S_{vh}	first column of the 2×2 amplitude scattering matrix
S_{vv}, S_{hv}	second column of the 2×2 amplitude scattering matrix
V, v	vertical polarization
\hat{v}	unit vector along vertical polarization direction
$V(D)$	terminal velocity of rain drop with diameter D
W	liquid water content
W_j	weight appropriate for $P_i(j)$
Z	radar reflectivity
Z_{dr}	differential reflectivity
Z_e	equivalent radar reflectivity factor
$Z_{h,v}$	equivalent reflectivity factor for H and V – polarization
$Z_{dr'}$	measured differential reflectivity
Z_h'	observed / measured reflectivity

Greek character symbols

α	coefficient of the power law relationship between specific attenuation and specific differential phase
β	coefficient of the power law relationship between back scatter differential phase
δ, δ_{co}	back scatter differential phase
Δr	radar range sampling interval
φ_1	antenna beamwidth in the azimuth plane
Φ_{dp}	differential propagation phase
λ	radar wavelength
Λ	slope of an exponential drop size distribution or slope parameter of gamma drop size distribution
μ	parameter of gamma drop size distribution
θ_i	IR filter output for the i th iteration
θ_1	antenna beamwidth in the elevation plane
ρ_{co}	correlation coefficient
ρ_{xh}	co-cross correlation coefficient for horizontal polarization
ρ_{xv}	co-cross correlation coefficient for vertical polarization
ρ_w	density of water
σ_b	back scatter (radar) cross-section
σ_{ext}^h	extinction cross-section for horizontal polarization
σ_{ext}^v	extinction cross-section for vertical polarization
σ_{dp}	specific differential attenuation and specific differential phase
τ_0	transmitter pulse duration
$\tilde{\Psi}_{dp}$	measured differential phase between horizontal and vertical polarisations

Acronyms

ANATOL	S-band radar in France
AP	anomalous propagation
AR	areal rainfall
BB	bright band in stratiform rain
BMRC	Bureau of Meteorology Research Centre
C-band	radar frequency around 5 GHz
C-POL	BMRC C-band polarization radar
CSI	critical success index
CSU	Colorado State University
CSU-CHILL	Colorado State University, Chill radar (S-band)
DLR	German aerospace research establishment
FAR	false alarm ratio
FIR	finite impulse response
LDR	linear depolarization ratio
MCS	mesoscale convective system
MP-X	multi-parameter, X-band (NIED, Japan)

NCAR	National Center for Atmospheric Research (US)
NEXRAD	Next generation weather radar belonging to NOAA
NIED	National Institute for Earthquake and Disaster Prevention (Japan)
NSSL	National Severe Storms Laboratory (US)
PIA	path integrated attenuation
POD	probability of detection
PPI	plan position indicator
PRT	pulse repetition time
RAL	Rutherford Appleton Laboratory (UK)
RHI	range-height indicator
RMS	root mean square
S-band	radar frequency around 3 GHz
SD	standard deviation
SNR	signal-to-noise ratio
SPOL	S-band polarimetric radar operated by NCAR
WSR-88D	Weather Surveillance Radar 88 Doppler
X-band	radar frequency around 10 GHz

10 References

- [1] Alberoni, P.P., D. Zrnic, A. Ryzhkov and L. Guerrieri, 2002: Use of a fuzzy logic classification scheme with a C-band polarimetric radar: First results, Proc. of ERAD 2002, 324-327.
- [2] Anagnostou, E.M., M.N. Anagnostou, W.F. Krajewski, A. Kruger and B. Miriovsky, 2004: High resolution rainfall estimation from X-band polarimetric radar measurements, *J. Hydrometeor.*, vol. 5, 110-128.
- [3] Andsager, E., K.V. Beard and N.F. Laird, 1999: Laboratory measurements of axis ratios for large raindrops., *J. Atmos. Sci.*, vol. 56, 2673-2683.
Beard, K.V. and C. Chuang, 1987: A new model for the equilibrium shape of raindrops, *J. Atmos. Sci.*, vol. 44, 1509-1524.
- [4] Aydin K. and C. Tang, 1997: Relationships between IWC and Polarimetric Radar Measurands at 94 and 220 GHz for Hexagonal Columns and Plates, *J Atmos and Oceanic Tech*, vol. 14, 1055–1063.
- [5] Aydin, K. and V.Giridhar, 1991: C-band dual polarization radar observables in rainfall: implications on differentiating hydrometeor phase and estimating rainfall rate, *Preprints 25th Conf. on Radar Meteorol.*, Amer. Meteor. Soc., Boston, 670-673.
- [6] Aydin, K., T.A. Seliga and V. Balaji, 1986: Remote sensing of hail with a dual linear polarization radar, *J. Appl. Meteor.*, vol. 25, 1475-1484.
- [7] Bader M.J., S.A. Clough and G.P. Cox, 1987: Aircraft and dual polarization radar observations of hydrometeors in light stratiform precipitation. *Quarterly J. of Royal Met. Soc.*, vol. 133, 491-515.
- [8] Balakrishnan, N. and D.S. Zrnic, 1990: Use of Polarization to Characterize Precipitation and Discriminate Large Hail. *J Atmos Sci*, vol. 47, 1525–1540.
- [9] Beard, K.V. and C. Chuang, 1987: A new model for the equilibrium shape of raindrops, *J. Atmos. Sci.*, vol. 44, 1509-1524.
- [10] Beaver, J. and V.N. Bringi, 1997: The application of S-band polarimetric radar measurements to Ka-band attenuation prediction, *Proc IEEE*, vol. 85, 893-909.
- [11] Berenguer, M., Daniel Sempere-Torres, Carles Corral, and Rafael Sánchez-Diezma, 2006: A Fuzzy Logic Technique for Identifying Nonprecipitating Echoes in Radar Scans, *J. Atmos. Oceanic Tech.*, vol. 23, 1157–1180.
- [12] Brandes, E.A., G. Zhang and J. Vivekanandan, 2002: Experiments in rainfall estimation with a polarimetric radar in a sub-tropical environment, *J. Appl. Meteor.* vol. 41, 674-684.
- [13] Bringi, V.N., T.A. Seliga and K. Aydin, 1984: Hail detection with a differential reflectivity radar, *Science*, vol. 225, 1145-1147.
- [14] Bringi, V.N., V. Chandrasekar, N. Balakrishnan and D.S. Zrnić, 1990: An examination of propagation effects in rainfall on radar measurements at microwave frequencies, *J. Atmos. Oceanic Tech.*, vol. 7, 829-840.
- [15] Bringi, V.N. and V. Chandrasekar, 2001: *Polarimetric Doppler Weather Radar*, Cambridge Univ. Press, p636

- [16] Bringi, V.N., T.D. Keenan and V. Chandrasekar, 2001a: Correcting C-band radar reflectivity and differential reflectivity data for rain attenuation: A self-consistent method with constraints, IEEE Trans. Geosci. Remote Sens., vol. 39, 1906-1915.
- [17] Bringi, V.N., G. Huang, V. Chandrasekar, T.D. Keenan, 2001b: An areal rainfall estimator using differential propagation phase: Evaluation using a C-band radar and a dense gage network in the Tropics, J. Atmos. Oceanic Tech., vol. 18, 1810-1818.
- [18] Bringi, V.N., T. Tang and V. Chandrasekar, 2004: Evaluation of a new polarimetrically based Z-R relation, J. Atmos. Oceanic Tech., vol. 21, 612-623.
- [19] Burk, S.D., T. Haack, L.T. Rogers and L.J. Wagner, 2003: Island Wake Dynamics and Wake Influence on the Evaporation Duct and Radar Propagation, J Appl Meteor, vol. 42, 349–367.
- [20] Carey, L.D., S.A. Rutledge, D.A. Ahijevych and T.D. Keenan, 2000: Correcting propagation effects in C-band polarimetric radar observations of tropical convection using differential propagation phase, J. Appl. Meteor., vol 39, 1405-1433.
- [21] Cho, Y.H., Gyuwon Lee, K.E. Kim and I. Zawadzki, 2006: Identification and removal of ground echoes and anomalous propagation using the characteristics of radar echoes, J. Atmos. Oceanic Tech., vol. 23, 1206–1222.
- [22] Cremonini, R., R. Bechini, P.P. Alberoni and M. Celano, 2004: Which hydrometeor classification scheme is realistic using Z_h , Z_{dr} and temperature in complex orography? A study based on operational C-band polarimetric weather radar in Northern Italy, Proc. of ERAD 2004, Vissby, Sweden, 393-397.
- [23] Deierling, W., W.A. Petersen, J. Latham, S.M. Ellis, J.E. Dye and H. J. Christian, 2007: The relationship between total lightning and ice mass fluxes. (in preparation) to be submitted to J. Geophys. Res.
- [24] Dolan B. and S.A. Rutledge, 2007: Microphysical and kinematic analysis algorithms for a network of x-band radars. Proceedings 33rd Int. Conf. Radar Meteor., AMS, Cairns, Australia.
- [25] Doviak R.J. and D. S, Zrnic, 1993: Doppler radar and weather observations, Academic Press, New York, 562 pp.
- [26] Fehr, T., N. Dotzek and H. Höller, 2005: Comparison of lightning activity and radar-retrieved microphysical properties in EULINOX storms, Atmospheric Research, vol. 76, 167-189.
- [27] Fulton, R., A. Ryzhkov and D. Zrnic, 1999: Areal rainfall estimation using conventional and polarimetric radar methods, Preprints 29th Int. Conf. Radar Meteor., AMS, Montreal, 293-296.
- [28] Guili D., Ghererdelli M, Freni A, Seliga T A and Aydin K (1991). Rainfall and clutter discrimination by means of dual-linear polarization radar measurements, J. Atmos. Oceanic Tech. vol 8, 777-789.
- [29] Goddard, J.W.F., J. D. Eastment and M. Thurair, 1994: The Chilbolton Advanced Meteorological Radar: A Tool for Multidisciplinary Atmospheric Research, IEE Electronics and Comms. Eng. Journal, vol 6, No. 2, 77-86.

- [30] Goddard, J.W.F., K.L. Morgan, A.J. Illingworth and H. Sauvageot, 1995: Dual-wavelength polarization measurements in precipitation using the CAMRA and Rabelais radars, Preprint 27th Int. Conf. Radar Meteor., AMS, Vail, CO., 196-198.
- [31] Gorgucci E., G. Scarchilli, V. Chandrasekar and V.N. Bringi, 2001: Rainfall estimation from polarimetric radar measurements: composite algorithms independent of rain drop shape-size relation, *J. Atmos. Oceanic Tech.*, vol. 18, 1773-1786.
- [32] Gourley, J.J., P. Tabary and J. Parent du Chatelet, 2006: Data quality of the Meteo-France C-band polarimetric radar. *J. Atmos. Oceanic Technol.*, vol. 23, 1340-1356
- [33] Gourley, J.J., P. Tabary and J. Parent du Chatelet, 2007: A fuzzy logic algorithm for the separation of precipitation from non-precipitating echoes using polarimetric radar observations, *J. Atmos. Oceanic Tech* (in press).
- [34] Hall, M.P.M, S.M. Cherry, J.W.F. Goddard and G.R. Kennedy, 1980: Raindrop sizes and rainfall rate measured by dual-polarisation radar, *Nature*, vol. 285, 195-198.
- [35] Hall, M.P.M, J.W.F. Goddard and S.M. Cherry, 1984: Identification of hydrometeors and other targets by dual-polarization radar, *Radio Sci*, vol. 19, 132-140.
- [36] Hendry A, G.C. McCormick and B.L. Barge 1976: The degree of common orientation of hydrometeors observed by polarization diversity radars, *J. Appl. Meteor.* vol 15, 633-640.
- [37] Höller, H., V.N. Bringi, J. Hubbert, M. Hagen and P.F. Meischner, 1994: Life cycle and precipitation formation in a hybrid-type hailstorm revealed by polarimetric and Doppler radar measurements, *J. Atmos. Sci.*, vol. 51, 2500-2522.
- [38] Höller, H., 1998: Hochreichende Konvektion, *Annalen der Meteorologie*, vol. 38, DWD, Herbstschule Radarmeteorologie, Oberpfaffenhofen, 2-6 Nov. 1998.
- [39] Hubbert, J. and V.N. Bringi, 1995: An iterative filtering technique for the analysis of copolar differential phase and dual-frequency radar measurements, *J. Atmos. Oceanic Technol.*, vol. 12, 643-648.
- [40] Hubbert, J., V.N. Bringi, H. Hoeller and P. Meischner, 1995: C-band polarimetric signatures from a convective storm during CLEOPATRA, Preprints 27th Int. Conf. Radar Meteor, American Meteor Soc, Vail, Colorado, 443-446.
- [41] Hubbert, J., V. N. Bringi, L. D. Carey and S. Bolen, 1998: CSU-CHILL Polarimetric Radar Measurements from a Severe Hail Storm in Eastern Colorado, *J Appl Meteor*, vol. 37, 749–775.
- [42] Hudak, D., P. Rodriguez, G.W. Lee, A. Ryzhkov, F. Fabry and N. Donaldson, 2006: Winter precipitation studies with a dual polarized C-band radar, 4th European conference on Radar in Meteorology and Hydrology (ERAD), Barcelona, Spain, 18-22 Sept.
- [43] Husson, D. and Y. Pointin, 1989: Quantitative estimation of hailfall intensity with a dual-polarization radar and a hailpad network, Preprints 24th Int Conf Radar Meteor, American Meteor Soc, Tallahassee, Florida, 318-325.

- [44] Illingworth, A.J. and I.J. Caylor, 1991: Correlation measurements of precipitation, Preprints 25th Int Conf Radar Meteor, American Meteor Soc, Paris, France, 650-653.
- [45] Illingworth, A.J. and T.M. Blackman, 2002: The need to represent raindrop size spectra as normalized gamma distributions for the interpretation of polarization radar observations, *J. Appl. Metero.*, vol. 41, 286-297.
- [46] Iwanami, K., R. Misumi, M. Maki, T. Wakayama, K. Hata and S. Watanabe, 2001: Development of a multiparameter radar system on mobile platform, Preprints 30th Int. Conf. Radar Meteor., AMS, Munich, 104-106.
- [47] Iwanami, K., K. Kusunoki, N. Orikasa, M. Maki, R. Misumi, and M. Murakami, 2007: Hydrometeor type classification in winter clouds using X-band polarimetric radar measurements - Comparison of X-band polarimetric radar data with in-situ measurements by HYVIS. Proceedings 33rd Int. Conf. Radar Meteor., AMS, Cairns, Australia.
- [48] Jameson, A.R., 1992: The effect of temperature on attenuation correction schemes in rain using polarization propagation differential phase shift, *J. Appl. Metero.*, vol. 31, 1106-1118.
- [49] Keenan, T.D., D. Zrnić, L. Carey, P. May and S. Rutledge, 1997: Sensitivity of C-band polarimetric variables to propagation and backscatter effects in rain, Preprint 28th Int. Conf. Radar Meteor., AMS, Austin, TX., 13-14.
- [50] Keenan, T.D., K. Glasson, F. Cummings, T.S. Bird, R.J. Keeler and J. Lutz, 1998: The BMRC/NCAR C-band polarimetric (C-POL) radar system, *J. Atmos. Oceanic Technol.*, vol. 15, 871-886.
- [51] Keenan, T.D., 2003: Hydrometeor classification with a C-band polarimetric radar, *Aust. Meteor. Mag.*, vol. 52, 23-31.
- [52] Kennedy, P C., S. A. Rutledge, W. A. Petersen, and V. N. Bringi, 2001: Polarimetric Radar Observations of Hail Formation, *J. Appl. Meteor.*, vol. 40, 1347–1366.
- [53] Kennedy, P., T.K. Depue, R. Cifelli, D. Barjenbruch, C. Gimmetstad, D.A. Brunkow and S.A. Rutledge, 2003: Ground truth verification of the hail quadrature parameter (HQP), 31st Conf Radar Meteor, American Meteor Soc, Seattle, Washington, 577-580.
- [54] Kitchen, M., R. Brown and A. Davies, 1994: Real-time correction of weather radar data for the effects of bright band range and orographic growth in widespread precipitation, *Q. J. Roy. Met. Soc.*, vol 120, 1231-1254.
- [55] Kruger, A. and W. Krajewski, 2002: Two-dimensional video disdrometer: a description, *J Atmos and Oceanic Tech*, Vol. 19, pages 602-617.
- [56] Lang, T.J., S.A. Rutledge and J.L. Stith, 2004: Observations of Quasi-Symmetric Echo Patterns in Clear Air with the CSU-CHILL Polarimetric Radar, *J Atmos Oceanic Tech*, vol. 21, 1182–1189.
- [57] Le Bouar, E., J. Testud and T.D. Keenan, 2001: Validation of the rain profiling algorithm ZPHI from the C-band polarimetric weather radar in Darwin, *J. Atmos. Oceanic Tech.*, vol. 18, 1819-1837.

- [58] Le Bouar E, E. Moreau, J. Testud, R. Ney, H. Poulima, and O. Deudon, 2005: An extensive validation experiment of algorithm ZPHI applied to radar HYDRIX, 32nd Conference on Radar Meteorology, American Meteorological Society, Albuquerque, NM, 22-29 Oct.
- [59] Leitao, M. J. and Watson P. A., 1984: Application of dual linearly polarized radar data to prediction of microwave path attenuation at 10-30 GHz, *Radio Sci.*, vol. 19, 209-221.
- [60] Lim, S., V.Chandrasekar and V.N. Bringi, 2005: Hydrometeor classification system using dual-polarization radar measurements: Model improvements and in situ verification, *Trans IEEE Geosci Remote Sens*, vol. 43, 792-801.
- [61] Liu, H and V. Chandrasekar, 2000: Classification of hydrometeors based on polarimetric radar measurements: Development of fuzzy logic and neuro-fuzzy systems and in situ verification, *J Atmos Oceanic Tech*, vol. 17, 140-164.
- [62] Maki, M., S.G. Park and V.N. Bringi, 2004: Statistical error of rain rate estimation due to natural variations of rain drop size distributions for 3 cm wavelength polarimetric radar, submitted to *J. Meteor. Soc. Japan*.
- [63] Maki, M, K Iwanami, R. Misumi, S-G. Park, H. Moriwaki, K. Maruyama, I. Watabe, D-I. Lee, M. Jang, H-K. Kim, V. N. Bringi, H. Uyeda, 2005: Semi-operational rainfall observations with X-band multiparameter radar, *Atmos. Sci. Letters*, vol 6, issue 1, 12-18.
- [64] Marzano, F.S., D. Scaranari, M. Celano, G. Vulpiani and M. Montopoli, 2006: Hydrometeor classification from dual polarized weather radar: extending fuzzy logic from S-band to C-band data, *Advances in Geosciences*, vol. 7, 109-114.
- [65] Matrosov, S.Y., K.A. Clark, B.E. Martner and A. Tokay, 2002: X-band polarimetric radar measurement of rainfall, *J. Appl. Metero.*, vol. 41, 941-952.
- [66] May, P.T., T.D. Keenan, D.S. Zrnić, L.D. Carey, and S.A. Rutledge, 1999: Polarimetric radar measurements of tropical rain at a 5-cm wavelength, *J. Appl. Meteor.*, vol. 38, 750-765.
- [67] May, P. T. and T. D. Keenan, 2005: Evaluation of microphysical retrievals from polarimetric radar with wind profiler data, *J. Appl. Meteor.*, vol. 44, 827-838.
- [68] McCormick G. C. and A. Hendry 1979: Techniques for the determination of the polarization properties of precipitation, *Radio Science*, vol 14, 1027-1040.
- [69] Meischner, P., V.N. Bringi, D. Heimann and H.A. Hoeller, 1991: A squall line in S-Germany: Kinematics and precipitation formulation as deduced by advanced polarimetric and Doppler radar measurements, *Mon. Wea. Rev.*, vol. 119, 678-701.
- [70] Mueller, E.A. and R.P. Larkin, 1985: Insects observed using dual-polarization radar, *J Atmos Oceanic Tech*, vol. 2, 49–54.
- [71] Nanni, S., P. Mezzasalma and P. P. Alberoni, 2000: Detection of hail by means of polarimetric radar data and hailpads: results from four storms, *Meteor. Appl.*, vol. 7, 121-128.
- [72] Parent-du-Châtelet, J., J. Testud, H. Andrieu and P. Tabary, 2004: First dual-polarisation weather radar in the French Network: test of its usefulness for

- hydrology, Proceedings 3rd European Conf. on Radar in Meteor. and Hydrol. ERAD vol. 2, 6-10 Sept, Visby, Sweden, 421-424.
- [73] Park, S.G., M. Maki, K. Iwanami and V.N. Bringi, 2004: Correction of radar reflectivity and differential reflectivity for rain attenuation and estimation of rainfall at X-band wavelength, 6th Int. Symp. Hydro. App. Weather Radar, Melbourne, Australia, 2-4 February.
 - [74] Park, S.G., M. Maki, K. Iwanami, V.N. Bringi and V. Chandrasekar, 2005: Correction of radar reflectivity and differential reflectivity for rain attenuation at X-band. Part II: Evaluation and Application, J Atmos. Oceanic Tech, vol 22, 1633-1655.
 - [75] Petersen, W. A., K. Knupp, J. Walters, W. Deierling, M. Gauthier, B. Dolan, J. P. Dice, D. Satterfield, C. Davies, R. Blakeslee, S. Goodman, S. Podgorny, J. Hall, M. Budge and A. Wooton, 2005: The UAH-NSSTC/WHNT ARMOR C-band dual polarimetric radar: a unique collaboration in research, education and technology transfer, 32nd Conf. Radar Meteor., Amer. Met. Soc., Albuquerque, New Mexico.
 - [76] Pointin Y, D. Ramond and J. Fournet-Fayard 1988: Radar differential reflectivity Z_{DR} : a real case evaluation of errors induced by antenna characteristics. J. Atmos. Oceanic Tech. vol 5, 416-423.
 - [77] Pruppacher, H.R. and K.V. Beard, 1970: A wind tunnel investigation of the internal circulation and shape of water drops fall at terminal velocity in air, Quart J Roy Meteor Soc, vol. 96, 247-256.
 - [78] Randeu, W. L., und W. Riedler, 1985: Über die Entwicklung und den Bau eines mehrparametrischen frequenzagilen Wetterradars im Rahmen der Erforschung von Ausbreitungsstörungen auf Satellitenfunkstrecken. Habilitationsschrift TU Graz, Nov. 1986.
 - [79] Randeu, W.L., M. Schönhuber and G. Lammer, 2002: Real-time measurements and analyses of precipitation micro-structure and dynamics, Proc. of ERAD(2002), 78-83.
 - [80] Ryzhkov, A. and D.S. Zrnić, 1995: Precipitation and attenuation measurements at 10 cm wavelength, J. Appl. Metero., vol. 34, 2121-2134.
 - [81] Ryzhkov, A. and D.S. Zrnić, 1998: Polarimetric rainfall estimation in the presence of Anomalous Propagation, J. Atmos. Oceanic Technol., vol. 15, 1320-1330.
 - [82] Ryzhkov, A., D.S. Zrnić, and R. Fulton, 2000: Areal rainfall estimates using differential phase, J. Appl. Metero., vol. 39, 263-268.
 - [83] Ryzhkov, A., D.S. Zrnic, J.C. Hubbert, V.N. Bringi, J. Vivekanandan and E.A. Brandes, 2002a: Polarimetric Radar Observations and Interpretation of Co-Cross-PolarCorrelation Coefficients. J Atmos and Oceanic Tech, vol. 19, 340–354.
 - [84] Ryzhkov, A., P. Zhang, R. Doviak and C. Kessinger, 2002b: Discrimination between weather and sea clutter using Doppler and dual-polarization weather radars, XXVII General Assembly of the International Union of Radio Science, Maastricht, The Netherlands, CD-ROM, paper # 1383.
 - [85] Ryzhkov, A., 2003: Rainfall measurements with the polarimetric WSR-88D radar, CIMMS report, National Severe Storms Laboratory, Norman, Oklahoma.

- [86] Ryzhkov, A. and D.S Zrnić, 2003: Discrimination between rain and snow with a polarimetric NEXRAD radar, 31st Conf Radar Meteor, American Meteor Soc, Seattle, Washington, 635- 638.
- [87] Ryzhkov, A., S. Giangrande and T.J. Schuur, 2003: Rainfall estimation with a polarimetric prototype of the operational WSR-88D radar, Preprints 31th Int. Conf. Radar Meteor., AMS, Seattle, 6-12 August, 208-211.
- [88] Ryzhkov, A., T.J. Schuur, D.W. Burgess, P.L. Heinselman, S.E. Giangrande and D. S. Zrnić, 2005a: The Joint Polarization Experiment: Polarimetric Rainfall Measurements and Hydrometeor Classification, Bull Amer Meteor Soc, vol. 86, 809–824.
- [89] Ryzhkov, A., S.E. Giangrande and T.J. Schuur, 2005b: Rainfall estimation with a polarimetric prototype of WSR-88D, J Appl. Meteor, vol. 44, 502–515.
- [90] Ryzhkov, A., D. Hudak and J. Scott, 2006: A new polarimetric scheme for attenuation correction at C-band, 4th European conference on Radar in Meteorology and Hydrology (ERAD), Barcelona, Spain, 18-22 Sept.
- [91] Sachidananda, M. and D.S. Zrnic, 1985: ZDR measurement considerations for a fast scan capability radar, Radio Sci, vol. 20, 907-922.
- [92] Sachidananda, M. and D.S. Zrnic, 1986: Differential propagation phase shift and rainfall rate estimation, Radio Sci, vol. 21, 235-247.
- [93] Scharfenberg, K. and E. Maxwell, 2003: Operational use of a hydrometeor classification algorithm to detect the snow melting level, 31st Conf Radar Meteor, American Meteor Soc, Seattle, Washington, 639- 641.
- [94] Schroth A, M. Chandra and P. Meischner, 1988: A C-band coherent polarimetric radar for propagation and cloud physics research, J. Atmos. Oceanic Tech. vol 5, 803-822.
- [95] Schuur, T., A. Ryzhkov and P. Heinselman, 2003: Observations and classification of echoes with the polarimetric WSR-88D radar, NOAA National Severe Storms Laboratory Tech Report, Norman, Oklahoma, USA.
- [96] Seliga T.A. and V.N. Bringi, 1976: Potential use of radar differential reflectivity measurements at orthogonal polarizations for measuring precipitation, J. Appl. Meteor. vol 15, 69-76.
- [97] Seliga T.A. and V.N. Bringi, 1978: Differential reflectivity and differential phase shift: applications in Radar Meteorology, Radio Science, vol 13, 271-275.
- [98] SIGMET Inc. (2001): Antenna mounted receiver (AMR) for dual-polarization applications, Boston, MA, 2001.
- [99] Silverman, B.W., 1986: Density estimation for statistics and data analysis. Chapman and Hall, 175 pp.
- [100] Smyth, T.J. and A.J. Illingworth, 1998: Correction for attenuation of radar reflectivity using polarization data, Quart. J. Roy. Meteor. Soc., vol. 124, 2393-2415.
- [101] Straka, J.M. and D.S. Zrnic, 1993: An algorithm to deduce hydrometeor types and contents from multiparameter radar data, Preprints 26th Int. Conf. Radar Meteor, American Meteor Soc, Norman, Oklahoma, 513-515.

- [102] Straka, J., D.S. Zrnić and A.V. Ryzhkov, 2000: Bulk hydrometeor classification and quantification using polarimetric radar data: Synthesis of Relations, *J Appl Meteor*, vol. 39, 1341–1372.
- [103] Sugier J. and P. Tabary, 2006: Evaluation of dual-polarisation technology at C-band for operational weather radar network, Section 6.2, OPERA-2 work packages 1.4 &1.5.
- [104] Testud, J., E. Le Bouar, E. Obligis and M. Ali-Mehenni, 2000: The rain profiling algorithm applied to polarimetric weather radar, *J. Atmos. Oceanic Technol.*, vol. 17, 322-356.
- [105] Testud, J., S. Oury, P. Amayenc and R.A. Black, 2001: The concept of "normalized" distributions to describe raindrop spectra: A tool for cloud physics and cloud remote sensing, *J. Appl. Metero.*, vol. 40, 1118-1140.
- [106] Thurai, M. and V.N. Bringi, 2005: Drop Axis Ratios from a 2D Video Disdrometer, *J Atmos and Oceanic Tech*, Vol. 22, No. 7, pages 963–975.
- [107] Timothy, K.I., T. Iguchi, Y. Ohsaki, H. Horie, H. Hanado and H. Kumagai, 1999: Test of the specific differential propagation phase shift (K_{dp}) technique for rain-rate estimation with a Ku-band rain radar, *J. Atmos. Oceanic Technol.*, vol. 16, 1077-1091.
- [108] Tragi, K., 1990: Polarimetric radar backscattering from reciprocal random targets, *Trans IEEE Geosci Remote Sens*, vol. 8, 856-864.
- [109] Vivekanandan, J., V.N. Bringi, M. Hagen and P. Meischner, 1994: Polarimetric radar studies of atmospheric ice particles. *Trans. IEEE Geosci Remote Sens*, vol. 32, No. 1, 1-10.
- [110] Vivekanandan, J., S. M. Ellis, R. Oye, D. S. Zrnic, A. V. Ryzhkov and J. Straka. 1999: Cloud Microphysics Retrieval Using S-band Dual-Polarization Radar Measurements, *Bull Amer Meteor Soc*, vol. 80, No. 3,381–388.
- [111] Wakimoto, R.M. and V.N. Bringi, 1988: Dual-polarization observations of microbursts associated with intense convection: The 20 July storm during the MIST project, *Mon. Wea. Rev.*, vol. 116, 1521-1539.
- [112] Zrnić, D.S. and A. Ryzhkov, 1998: Observations of insects and birds with a polarimetric radar, *Trans IEEE Geosci Remote Sens*, vol. 36, 661-668.
- [113] Zrnić, D.S. and A.V. Ryzhkov, 1999: Polarimetry for weather surveillance radars, *Bull. Am. Meteor. Soc.*, vol. 80, 389-406.
- [114] Zrnić, D.S., A.Ryzhkov, J. Straka, Yidi Liu and J. Vivekanandan, 2001: Testing a procedure for automatic classification of hydrometeor types, *J Atmos and Oceanic Tech*, vol. 18, 892–913.
- [115] Zrnić, D.S and A. V. Ryzhkov, 2004: Polarimetric Properties of Chaff, *J. Atmos. Oceanic Tech.*, vol. 21, 1017–1024.

11 About the Authors

V.N. Bringi received his PhD from Ohio State University in 1976 and is currently Professor of Electrical and Computer Engineering at Colorado State University. He is a Fellow of the American Meteorological Society and co-author of "Polarimetric Doppler Weather Radar" published in 2001 by Cambridge University Press.

M. Thurai received her PhD from King's College, London in 1985 and has previously worked at Rutherford Appleton Laboratory, UK and the Communications Research Laboratory, Japan. She is currently at Colorado State University.

R. Hannesen received his PhD from University of Karlsruhe in 1999. Since then, he is working in Selex–Gemtronik's Sensor Data Processing group.